MULTIPARTICLE PRODUCTION IN HADRON-NUCLEUS COLLISIONS AT HIGH ENERGIES

by

CHARLES C. YOUNG

B.S., California Institute of Technology (1973)

Submitted in Partial Fulfillment of the Requirements
for the Degree of Doctor of Philosophy at the
Massachusetts Institute of Technology
May 13, 1977

Signature of Author...
Department of Physics, May 13, 1977

Certified by...
Thesis Supervisor

Accepted by...
Chairman, Departmental Committee on
Graduate Students

E-178

MULTIPARTICLE PRODUCTION IN HADRON-NUCLEUS COLLISIONS AT HIGH ENERGIES

by

CHARLES C. YOUNG

Submitted to the Department of Physics on
May 13, 1977, in partial fulfillment of the
requirements for the degree of Doctor of Philosophy

ABSTRACT

Particle production at high energies was investigated by measuring the charged multiplicity and pseudorapidity distribution in hadron-nucleus interactions in the energy range 50 to 200 GeV. The results are compared with the predictions of the hydrodynamic, energy flux cascade, parton-multiperipheral and two-fireball models. None of these are in perfect agreement with the data.

Thesis Supervisor: W. Busza
Title: Associate Professor of Physics

TABLE OF CONTENTS

CHAPTER I

INTRODUCTION

Many ideas have been put forward in an attempt to understand or at least demystify the various aspects of strong interactions. There are the hydrodynamic,[1] quark[2] and multiperipheral[3] models. Some, for example, the quark model, focus on the systematic trends in the properties of hadrons, while others are more concerned with the dynamics of interactions. To date, however, there is not one model which is in agreement with all of the data.

The conventional attempts at verifying or refuting theories test their asymptotic predictions. In this particular context, "asymptotic" refers to time scales large compared with the characteristic time scales of strong interactions, i.e. $>> 10^{-23}$ second. Little effort has gone into investigating the early behavior ($\sim 10^{-23}$ second) of hadronic interactions.

This experiment (Fermilab experiment number 178) was an attempt to fill this gap. The experiment consisted of two distinct parts. The first part measured the average charged multiplicity in π^--nucleus interactions and found a very weak atomic number dependence -- the π^--Uranium multiplicity is approximately twice that of a π^--nucleon interaction at beam energies of 100 and 175 GeV. A crude

angular distribution indicates that the increase in multiplicity is confined to the region $\theta \gtrsim 26°$.

These interesting results prompted the second part of the experiment where the pseudorapidity distributions in hadron-nucleus interactions were measured for p, $\bar{p}$, K^+, π^+, and π^- beams at 50, 100 and 200 GeV.

If the results are considered as functions of the parameter $\bar{\nu}$, the different beam particles exhibit surprisingly similar behavior. The common features include a weak dependence on the atomic number of the target, a weak energy dependence ($\sim \ln(s)$) and the apparent similarity between the results of hadron-nucleon and hadron-nucleus collisions in the region of high pseudorapidity.

Physics Motivation

Reasonable estimates of the characteristic distance in strong interactions in the 100 GeV range indicate that it is of the order of 10 fermis or greater. For example, from the uncertainty principle one can estimate the center-of-mass time scale to be $\tau^* \sim \frac{1}{m_\pi}$, where m_π is the mass of the pion, the lightest known hadron. A 100 GeV proton-proton interaction in the laboratory frame of reference has a time dilation factor $\gamma \sim 7$ when compared to the center-of-mass system. Therefore the characteristic length scale in the laboratory is $\tau = \gamma\tau^* \sim 10$ fermis.

Since the width of unstable hadrons is of the same order as the mass of the pion, one would obtain a similar result by considering the strong decay of such a particle. Similar numbers would be obtained also in the context of some models, e.g. the multiperipheral model.[4]

Further confirmation of these estimates is furnished by the ideas on and the calculations of a formation zone[5] in analogy to the theory of Bremsstrahlung radiation. Landau and Pomeranchuk[6] noticed in 1953 that the Bremsstrahlung radiation decreased if the successive scatterings were closer than some characteristic time τ.

Consider Bremsstrahlung radiation from an electron. The intensity of radiation is given by

$$\frac{d^3I}{dk^3} \sim \left| \int \vec{j}(\vec{x},t)\, e^{i(\vec{k}\cdot\vec{x}-\omega t)}\, d^3x\,dt \right|^2$$

where $\vec{j}$ = current density of the electron

ω = frequency of radiated photon

$\vec{k}$ = wave number of radiated photon

and the integral is to be evaluated over the path of the electron. Since $\omega = |\vec{k}|$, the exponential factor can be written as $e^{-it/\tau}$ where

$$\tau = \frac{1}{\omega(1-\hat{k}\cdot\vec{v})}$$

If there are two successive scatters separated in time by t where t is much smaller than τ, then the integral vanishes to lowest order in (t/τ). Thus successive scatters are ineffective in producing radiation if the time separation is small.

The formation time τ has a ready physical interpretation.

$$\tau = \frac{E}{E\omega(1-\hat{k}\cdot\vec{v})} = \frac{E}{Kp}$$

where $P = (\vec{p},E)$ = 4-momentum of the electron

and $K = (\vec{k},\omega)$ = 4-momentum of the photon

Kp is the usual dot product of 4-vectors. Evaluating the scalar dot product in the rest frame of the electron,

$$\tau = \left(\frac{E}{m}\right)_{\text{electron}} \left(\frac{1}{\omega_0}\right)$$

where ω_0 = frequency of photon as seen in the electron's rest frame.

So the formation time τ is just the period of the photon (as seen in the emitting electron's rest frame) after it has been transformed to the moving frame. The formula becomes quite plausible.

This can be translated into the language of hadronic physics simply by evaluating the invariant dot product for the case of a hadron radiating a meson. The formula becomes

$$\tau = \frac{2\ Ex}{(Mx)^2 + \mu^2}$$

where E = beam energy

M = mass of beam particle

x = fraction of beam energy taken by radiated meson

μ = transverse mass of radiated meson.

For a typical 100 GeV proton-proton interaction, this estimate gives $\tau \sim 20$ fermis.

There is, therefore, compelling evidence that in interactions of 100 GeV hadrons, the region within 10 fermis of the interaction contains states that may be quite different from the more familiar asymptotic states of hadrons. So it is reasonable, and indeed necessary, to investigate the early properties of hadronic systems if one is to understand the strong interaction.

In order to investigate the early behavior of hadronic systems, one is faced with the problem of having to make measurements within 10 fermis of the interaction (if one is not willing to wait for new accelerators to be built which are so powerful as to make this distance a macroscopic one). This task requires equipment which is capable of interacting with hadrons in distances short compared with 10 fermis. The only material known to have this property

is nuclear matter. The hadronic absorption lengths in nuclear matter are of the order of 2 fermis. This is to be compared with the diameter of, say, a Uranium nucleus ($\sim$15 fermis). It appears, therefore, that hadron-nucleus interactions can be of great help in discerning the early development of a hadronic interaction and in discriminating among the many theories.

Take the following extreme case as an example. Suppose that the time scale of hadronic production is actually much shorter than our estimates. Let the final state hadrons (mostly pions) materialize in, say, 0.01 fermi. These pions, on encountering successive nucleons within a nucleus, will interact and bring about an intra-nuclear hadronic cascade. An obvious manifestation of this phenomenon is a greatly increased multiplicity. A naive calculation yields

$$\langle n\rangle_{hA} \sim \langle n\rangle_{hp}^{(A^{1/3})}$$

where $\langle n\rangle_{hA}$ and $\langle n\rangle_{hp}$ are the average multiplicities in hadron-nucleus and hadron-nucleon collisions respectively. A is the atomic number of the nucleus. At 100 GeV, the ratio of $\langle n\rangle_{hA}$ to $\langle n\rangle_{hp}$ reaches 10^4 for a Uranium target. A more realistic calculation incorporating energy conservation and the leading particle effect still gives ratios of the order of 100.

This is also the rapidity of one frame as seen by the other. It takes on the values 2.3, 2.65 and 3.0 for beam energies of 50, 100 and 200 GeV.

It is well known that in general a given angle in the center-of-mass cannot be associated with a unique angle in the laboratory frame. However, this is possible for a β=1 particle. A β=1 particle produced at 90° in the center-of-mass frame of a 50 GeV proton-proton interaction has a laboratory angle of 11.3°. The corresponding angles for 100 and 200 GeV proton-proton interactions are 8.1° and 5.7° respectively. The pseudorapidities of these angles are precisely the values of u calculated above.

The kinematically allowed range of rapidity for the secondary particles depends not only on the center-of-mass energy but also on the mass and the transverse momentum of the particle. The limits are discussed and tabulated in Appendix II, which contains a detailed discussion of the rapidity and pseudorapidity variables.

A crude estimate of the rapidity range is straight forward. In the laboratory frame of reference, the minimum rapidity is approximately 0, the rapidity of the target. The maximum rapidity is approximately that of the beam particle, i.e. $\ln(\frac{2E}{m_b})$ where m_b is the mass of the beam particle. For a proton beam, this is twice the center-of-mass rapidity u calculated above.

CHAPTER III

PART I OF THE EXPERIMENT

Introduction

The first part of this experiment was carried out near the second focus of the M6 beam line in the Meson Detector Building of the Fermi National Accelerator Laboratory (Fermilab).

The initial testing of the apparatus was performed at the Brookhaven National Laboratory (BNL) and the equipment was first set up in the M6 beam line in October 1973. The data were not taken until June 1974. There were several reasons for this delay. Most of the time, the experiment had to be run "parasitically," i.e. the equipment could be inserted into the beam only with the consent of the primary user of the beam line. FNAL experiment numbers 69 and 96 were the primary users of the M6 beam line at various times during the course of this experiment. This arrangement resulted in sporadic running, and necessitated frequent testing and calibration as the beam conditions changed. A fire in the M6W tunnel (December 1973) introduced a further delay.

The data presented here were obtained in a period of 5 days (the 14th to the 18th of June 1974) when the beam line was temporarily in the control of this experiment.

The interaction of 100 and 175 GeV/c π^- on nuclear targets producing n charged particles was studied:

$$\pi^- + A \rightarrow n \text{ charged particles.}$$

Targets ranged from carbon (atomic number A = 12) to uranium (atomic number A = 238). Data on hydrogen target were obtained by subtracting the carbon data from the polyethylene (CH_2) data.

Experimental Set-Up

The beam was not a separated π^- beam, but contained a small admixture of e^-, μ^-, K^- and $\bar{p}$. Even though the beam line was instrumented with 3 gas Cherenkov counters for identifying beam particles, they were situated downstream of and were therefore of no use to this experiment. At 100 and 175 GeV/c, the beam was predominantly π^- (see Table III-1).[18]

The electron contamination of the beam was effectively eliminated by inserting 4/3 radiation lengths of lead at the first focus of the beam -- see Figure III-1. The severe degradation of the electron's energy prevented it from reaching the second focus where this experiment was performed. The effects of the other beam contaminations were taken into account during the analysis.

Typical beam intensities were 0.5 10^6 particles per

second. There were no observable changes in the data as the beam intensity varied from 0.1 10^6 to 1.0 10^6 particles per second.

The apparatus is shown schematically in Figure III-2. A counter telescope (consisting of scintillation counters BT1, V1, V2 and T1) defined beam particles. Other counters were used to trigger the data-acquisition system. The remaining counters, 13 in all, measured the multiplicity in two angular bins.

An acceptable beam particle satisfied the following requirements:

(1) BT1 and T1 registered counts in coincidence,

(2) V1 and V2 did not fire,

(3) The pulse height in BT1 did not exceed 1.5 times minimum ionizing, and

(4) No other beam candidate (satisfying requirements (1) through (3) above) was within 150 nano-seconds (nsec) of this beam particle.

A block diagram of the electronics used to impose these requirements is shown in Figure III-3.

Requirements (1) and (2) insured that the beam particle was properly incident on the target. The effects of doubly-occupied RF buckets were minimized by (3). The last requirement was necessitated by the wide pulse width

(~100 nsec) of the counter C. This counter was situated in the beam and therefore responded to every beam particle as well as interaction secondaries. See Appendix I for details of this counter.

The data acquisition system was triggered whenever all the following requirements were satisfied:

(1) there was an acceptable beam particle as defined above,

(2) either dE/dx_1 or W_1 fired,

(3) either dE/dx_2 or W_2 fired,

(4) BT2 did not register a count, and

(5) the data acquisition system was last triggered no sooner than 22 μsec before.

The dE/dx_1 and dE/dx_2 counters had high thresholds of 1.5 times minimum ionizing. So (2) and (3) together required either a wide-angle particle or more than 1 particle in the forward direction. The effect of delta-rays on triggering was reduced by the presence of the 3/4" of aluminum placed in front of the W_2 counter. The aluminum plate had a 2-inch diameter hole to allow passage of the beam.

The counter BT2 was placed about 100 meters downstream of the target and was isolated from the rest of the equipment by beam-line bending magnets, which deflected beam particles 51.18 milliradians (mrad). Triggering by energetic delta-rays was therefore reduced. The otherwise

uninteracted beam particle would trigger BT2 and hence fail requirement (4). The momentum acceptance of the bending magnets was sufficiently small ($\Delta p/p \simeq 1.5\%$) so that a beam particle which had undergone a hadronic interaction had a negligible chance of reaching BT2. The last requirement guaranteed that the data acquisition system was not busy processing the previous event.

The multiplicity detector consisted of 13 counters, the 12 H counters and the C counter, arranged as shown in Figure III-2. They were made of ultra-violet transmitting (UVT) lucite, which imposed a velocity acceptance of $\beta \gtrsim 0.85$ -- see Appendix III.

The 12 H counters were arranged to give a hodoscope in the shape of a truncated cone. The inside of this cone was lined with a 1/2" layer of carbon, which served to absorb delta-rays produced in the target.

The 13th counter, C, was a 12-sided bevelled slab of UVT lucite which fitted into the hole of the truncated cone. See Appendix III for details of the design of this counter. It measured multiplicity with a novel pulse-height technique. Details of this method can be found in Appendix IV.

The targets were mounted on two styrofoam wheels, one of which was used at any given time. Targets were selected and positioned by remote control. The target wheel, illustrated in Figure III-4, was turned until a digital readout on the wheel agreed with the numbers previously determined with the aid of surveying equipment. A closed circuit television camera furnished a check on the choice and position of the target.

Data

The data acquisition system consisted of two parts -- scalers and a pulse-height analyzer. The scalers were used for

(1) counting the number of beam particles and triggers to yield cross-sections,

(2) estimating "dead-time" corrections to cross-sections, and

(3) other diagnostic functions, such as alignment of the apparatus relative to the beam.

The amount of charge in a pulse from the C count was digitized by the pulse-height analyzer and stored in one of eight octants. If none of the 12 H counters forming the cone-shaped hodoscope registered a count, the first octant was selected. If one of the 12 H counters fired, the second octant was used, and so on. Events with 7 or more H counters firing were stored in the last (eighth) octant. This routing was done by a "home-made" device which first summed the information from the 12 H counters and then compared the result with eight preset values (0 through 7).

The appropriate signal was then sent to the pulse-height analyzer to route the data.

Most of the data were obtained with the apparatus in the configuration shown in Figure III-2, where the H hodoscope subtended the angular range 26°<θ<110° and the C counter covered θ<26°. The rest of the data were from a different geometry. The entire target assembly, including the target wheel, the dE/dx_1, the W_1 and the last two beam-defining counters (V_2 and T_1), was moved upstream approximately 36 inches. Data were obtained for new angular bins with the C counter covering the forward most 3.5°. In all, data were obtained at the points given in Table III-2.

Several thicknesses of target were used at each point to allow an extrapolation of the data to zero target thickness in order to correct for extra-nuclear cascades, conversion of gamma rays, production of delta rays etc. Several different thicknesses of radiators were used on the C counter to ascertain the effects, if any, that the radiator thickness might have on the observed multiplicity. No discernable effects were found.

At the end of each run, the information stored in the 4096-channel pulse-height analyzer and the scalers was put on magnetic tape. Hence the only information available was the 8 spectra (stored in the 8 octants of the analyzer) integrated over an entire run. Of course, the scaler information had been similarly integrated. No event-by-event information was available. Typical runs lasted approximately 15 to 30 minutes.

So, in summary, the experiment produced data covering these two areas:

(1) the atomic number dependence of the charged multiplicity in the region $\theta<110°$ in π^--A interactions at 100 and 175 GeV/c, and

(2) (crude) angular distributions of the secondary particles in these interactions.

Analysis

The first step in the data analysis was the removal of those events with three or fewer charged secondaries. This was necessary because of the loose trigger requirements. They accepted events where the beam particle interacted in the C counter (which was measured to be about 10% of an interaction length) rather than in the target, provided that it had deposited more than 1.5 times the minimum ionization energy in the counter dE/dx_1 or had produced a delta ray incident on the W_1 counter. The low-multiplicity data were dominated by these spurious events. A correction was later applied in order to account for the missing (legitimate) low-multiplicity events. This cut on the data was performed by fitting to the pulse height distributions and then statistically removing those events with less than four charged secondaries.

The average multiplicity and dispersion (<n> and D) of each of the eight spectra in each run were then evaluated. See Appendix IV for details of this calculation. The results from the eight spectra are summed together irrespective of which octant the information was stored in to give the average multiplicity and dispersion for the forward small-angle region. Corrections were applied for the missing low-multiplicity events, acceptance, systematic bias in calibration, etc. See Appendix V for details. These two quantities were then extrapolated to zero target thickness with a linear extrapolation to give the final results.

The average multiplicity of the large-angle region was obtained by examining the frequency distribution of struck H counters. The probability that more than one particle might have been incident on the same H counter was allowed for under the assumption that there was no azimuthal correlation among the wide-angle particles going into the H hodoscope. Since the information stopped at a maximum of 7 H counters firing simultaneously (the limitation being imposed by the 8 octants of the pulse-height analyzer), all events with at least 7 active H counters were assumed to have fired exactly 7 out of the 12 H counters. The mathematical details of this calculation are presented in Appendix VI.

The results for the entire region $\theta<110°$ were obtained by adding together the results of the 2 regions.

Multiplicity distributions (as opposed to the first two moments of these distributions) could not be determined with sufficient accuracy to warrant reporting the results. The difficulties are explained in Appendix V.

The data, analyzed as outlined above, are summarized in Tables III-3 and III-4. The errors quoted in the tables do not include systematic effects such as cutting off the multiplicity distribution at 7 in the angular region $26°<\theta<110°$. These effects were estimated to introduce an uncertainty of no more than 3%. It is not understood why the π^--Uranium multiplicity is lower than the π^--Lead multiplicity at 100 GeV/c.

Discussion of Results

Figure III-5 shows the measured absorption cross-sections and those reported in Reference 19. Table III-5 shows the hydrogen-target results of this experiment, which were obtained by subtracting the carbon data from the polyethylene (CH_2) data. In the same table are the results from hydrogen bubble chamber experiments.[20,21,22,23] The agreement is satisfactory.

One can see from Figure III-6 that the multiplicity is a relatively weak function of the atomic number of the

target. If the data are considered in the form of R_A versus $\bar{\nu}$, an apparently energy-independent linear relationship is observed as shown in Figure III-7. Straight lines have been fitted to the 100 GeV and the 175 GeV data separately as well as to the combined data. In all cases, uncertainties in $\bar{\nu}$ have been included in the fit. However, scale uncertainties, due to errors in the average multiplicity for a hydrogen target in the case of R_A and errors in the pion-nucleon cross-section in the case of $\bar{\nu}$, have not been included. The results of these fits are given in Table III-6. The three fitted straight lines are consistent with being the same line. Cosmic ray experiments (using mostly proton projectiles) also observe a similar weak energy dependence in R_A versus $\bar{\nu}$ over a much wider energy range though with greater uncertainty.[18] The results are summarized in Table III-7.

This weak energy dependence has been pointed out by many other authors, working mostly with emulsions and cosmic rays.[24,25,26,27] Figure III-8(a) shows that the data of this experiment are compatible with data obtained with a proton beam if R_A versus $\bar{\nu}$ is used as the measure. The straight line $R_A=0.62+0.40\ \bar{\nu}$ is the best linear fit to the combined 100 and 175 GeV data of this experiment. It should be noted that this apparent similarity between protons and pions is destroyed if the atomic number A is used as the independent variable instead of $\bar{\nu}$. This is shown in Figure III-8(b), where the solid curve is a hand drawn line through the data of this experiment. It should also be emphasized that the values of R_A, which has a very small range, are taken from many different experiments with possibly very different systematic errors and biases. The observed feature may be purely coincidental.

Several features of the angular distributions (Figure III-9) are worth noticing. For $\theta<3.5°$, the multiplicity does not depend on the target nucleus. As the angle increases, R_A, for any given $\bar{\nu}$, also increases. For angles between 26° and 110°, R_A reaches a value of 5 for a Uranium target. So the increase in multiplicity as a function of the atomic number of the target is predominantly in the region of large angles.

The dispersion in multiplicity, $D=\sqrt{\langle n^2\rangle-\langle n\rangle^2}$, is plotted against the average multiplicity, $\langle n\rangle$, in Figure III-10. Also plotted in the same figure are the data of π^-p[21,22,23,28] interactions. All the points appear to lie on the same straight line: $D\sim0.5\langle n\rangle$. The possible significance and interpretation of this feature is not definite.[29,30] While one might expect D^2 to vary linearly with $\langle n\rangle$ in a model where particles are produced independently, resulting in a Poisson-like distribution, the averaging over various categories of events could obscure

such a dependence. The averaging over different impact parameters would have a similar effect. To illustrate the deviation from a Poisson distribution, Figure III-11 shows the topological cross-sections in 200 GeV/c proton-proton interactions[31] and a Poisson distribution with a mean equal to the average multiplicity. The Poisson distribution has been arbitrarily normalized to the data at n=6. Since emulsion experiments and neon bubble chamber experiments have established the phenomenological validity of KNO scaling,[32,33,34] this comparison also applies to interactions with nuclear targets.

Therefore the results of the first part of the experiment can be summarized as follows:

(1) The average charged multiplicity in π^--nucleous interactions is linear in the parameter $\bar{\nu}$.

(2) The multiplicity ratios, $R_A=\langle n\rangle_A/\langle n\rangle_p$, can be adequately parameterized by $R_A=0.62+0.40\,\bar{\nu}$. This parameterization appears to be energy independent.

(3) The increase in multiplicity as a function of the target nucleus appears to be excluded from the region $\theta\lesssim26°$.

(4) The dispersion of the multiplicity distribution in π^--nucleus interactions seems

to be linearly related to the average multiplicity. Furthermore, this linear dependence is consistent with an extrapolation of the dependence observed in π-p interactions.

However, this part of the experiment left several intriguing questions unanswered; such as

(1) Would proton-nucleus and pion-nucleus interactions yield results that lie on a common R_A versus $\bar{\nu}$ curve as suggested by data from different groups?

(2) Is R_A energy independent as indicated by the data?

(3) How is the extra multiplicity in excess of a hadron-nucleon collision distributed? Are these particles, independent of energy, confined to the region $\theta \gtrsim 26°$?

The answers to these questions can be used to discriminate between the models of strong interaction. These constraints are discussed further in Chapters V and VI.

TABLE CAPTIONS

III-1 The hadronic composition at 100 and 175 GeV/c of the M6 beam line with the polarity set for negative particles. The numbers are from Reference 18.

III-2 Points where data were taken.

III-3 The average multiplicities and dispersions in 100 GeV/c π^--nucleus interactions. Data on hydrogen target were obtained by subtracting the Carbon data from the Polyethylene data.

III-4 The average multiplicities and dispersions in 175 GeV/c π^--nucleus interactions. Data on hydrogen target were obtained by subtracting the Carbon data from the Polyethylene data.

III-5 Comparison of the average multiplicities and dispersions in π^--proton interactions of this experiment with bubble chamber results. The 50, 100, 147 and 205 GeV/c data are from References 20, 21, 22 and 23 respectively. Because of the velocity cut in this experiment ($\beta \gtrsim 0.85$), the observed average multiplicity should be approximately 0.5 particle less than that in a bubble chamber experiment.[35]

III-6 The results of fitting R_A versus $\bar{\nu}$ with a straight line $(a+b\bar{\nu})$. The errors on a and b are highly correlated as shown by the error matrices. The chi-squared per degree of freedom of each fit is also given.

III-7 R_A as a function of beam energy in proton-Emulsion and proton-Carbon interactions. The numbers are from Reference 8.

FIGURE CAPTIONS

III-1 The location of the experiment in the M6 beam line of Fermilab. Quadrupole magnets are shown schematically as convex lenses; dipole magnets are not shown.

III-2 Layout of the equipment.

III-3 Block diagram of the electronics. Note circuitry used to define acceptable beam particles.

III-4 Illustration of the target wheel.

III-5 The pion absorption cross-sections measured in this experiment (·) and those in Reference 19 (x).

III-6 Average charged multiplicities in π^--nucleus interactions at 100 and 175 GeV/c. Secondary particles with laboratory angles greater than 110° were not measured.

III-7 R_A versus $\bar{\nu}$ at 100 and 175 GeV/c. The line is the best linear fit to the combined data.

III-8 (a) Comparison of R_A versus $\bar{\nu}$ with other experiments.
(b) Comparison of R_A versus A with other experiments.
The data for this experiment are given by the solid lines. The data points are:
40 GeV/c π-Carbon, Reference 27 (□)
200 GeV/c π-Neon, Reference 34 (x)
200 GeV/c p-Emulsion, Reference 7 (Δ)

300 GeV/c p-Chromium (in emulsion), Reference 36 (∇)

300 GeV/c p-Tungsten (in emulsion), Reference 36 (▼)

Echo Lake data, Reference 9 (○).

The projectiles are 70% p and 30% π at an average energy of 250 GeV. Targets are Carbon, Aluminum, Iron, Tin and Lead.

III-9 R_A versus $\bar{\nu}$ for the 100 GeV/c π^- data in different angular bins. The errors shown do not include normalization uncertainties due to errors of the hydrogen point.

III-10 Dispersion versus the average multiplicity in πp and πA interactions. Low energy πp data (○) are from a compilation by A. Wroblewski, Reference 28. The 100 (▲), 147 (△) and 200 (□) GeV πp data are from References 21, 22 and 23 respectively. The high multiplicity data (•) are from the π^-A interactions of this experiment.

III-11 Deviation of the topological cross-sections from a Poisson distribution. The data are from Reference 31. The Poisson distribution has a mean of 6.94, the average charged multiplicity in 200 GeV/c proton-proton interactions. The curve has been arbitrarily normalized to the data at n=6.

TABLE III-1

Beam Composition

Momentum	π^{-*}	K^-	$\bar{p}$
100	94.2±.8%	3.8±.2%	2.0±.15%
175	96.5±1.%	3.4±.2%	0.3±.05%

*The π^- component contains approximately 1% of e^- and 1% of μ^- at both momenta.

TABLE III-2

Points Where Data Were Obtained

Atomic No. of Target	Target Position	100 GeV/c	175 GeV/c
12	nominal	x	x
	moved upstream	x	
"14" (polyethylene)	nominal	x	x
	moved upstream	x	
27	nominal	x	
	moved upstream	x	
64	nominal	x	x
	moved upstream	x	
108	nominal	x	
	moved upstream	x	
207	nominal	x	x
	moved upstream	x	
238	nominal	x	
	moved upstream	x	

TABLE III-3

100 GeV/c π^--Nucleus Interactions

Target	$\bar{\nu}$	Average Multiplicities				Dispersion
		$0<\theta<3.5°$	$0<\theta<26°$	$26<\theta<110°$	$0<\theta<110°$	
H	1.00	3.32 ±.30	5.72 ±.30	0.83 ±.20	6.55 ±.20	2.9 ±.1
C	1.36	3.37 ±.10	6.19 ±.10	1.66 ±.10	7.85 ±.10	3.7 ±.1
Al	1.70	3.38 ±.20	6.24 ±.30	2.07 ±.10	8.31 ±.10	4.3 ±.2
Cu	2.14	3.30 ±.25	6.89 ±.30	2.83 ±.10	9.72 ±.10	4.8 ±.2
Ag	2.48	3.22 ±.30	7.23 ±.30	3.47 ±.20	10.7 ±.20	5.4 ±.3
Pb	2.96	3.23 ±.20	7.98 ±.30	4.20 ±.10	12.2 ±.20	5.8 ±.2
U	3.07	3.25 ±.30	7.48 ±.30	4.25 ±.20	11.7 ±.20	6.0 ±.3

TABLE III-4

175 GeV/c π^--Nucleus Interactions

Target	$\bar{\nu}$	Average Multiplicity			Dispersion
		$0° \leq \theta \leq 26°$	$26° \leq \theta \leq 110°$	$0° \leq \theta \leq 110°$	
H	1.00	6.80±.20	1.02±.20	7.82±.30	3.5±.15
C	1.36	7.54±.23	1.78±.10	9.22±.10	4.5±.15
Cu	2.14	8.57±.30	2.82±.11	11.39±.20	5.6±.25
Pb	2.96	9.72±.32	4.55±.15	14.27±.15	7.0±.25

TABLE III-5

Comparison of $\pi^- p$ Data With Bubble Chamber (HBC) Results

Energy (GeV)	<n>	D
50 (HBC)	5.78±.04	2.70±.03
100 (this expt)	6.55±.20	2.90±.10
100 (HBC)	6.79±.08	3.16±.04
147 (HBC)	7.34±.10	3.58±.05
175 (this expt)	7.82±.30	3.50±.15
205 (HBC)	8.02±.12	3.91±.11

TABLE III-6

Results of Fitting to $R_A = a+b\bar{\nu}$

Beam	a	b	Error Matrix	χ^2
100 GeV	0.62±.04	0.40±.02	$\begin{pmatrix} .002 & -.001 \\ -.001 & .001 \end{pmatrix}$	1.3
175 GeV	0.63±.05	0.40±.03	$\begin{pmatrix} .002 & -.001 \\ -.001 & .001 \end{pmatrix}$	0.7
100 and 175 GeV	0.62±.03	0.40±.02	$\begin{pmatrix} .001 & -.001 \\ -.001 & .000 \end{pmatrix}$	0.9
100 and 175 GeV*	0.61±.01	0.39±.01	---	1.2

*This fit is constrained to go through the point ($\bar{\nu}=1, R_A=1$).

TABLE III-7

Energy Dependence of R_A for Emulsion and Carbon

	Energy (GeV)	R_A
Emulsion	67	1.65 ± .04
	200	1.73 ± .04
	200	1.68 ± .06
	∼1000	1.71 ± .31
	∼3000	1.81 ± .17
	∼8000	1.63 ± .12
Carbon	110	1.18 ± .10
	200	1.10 ± .08
	290	1.15 ± .11
	410	1.16 ± .21
	670	1.33 ± .19

FIGURE III-1

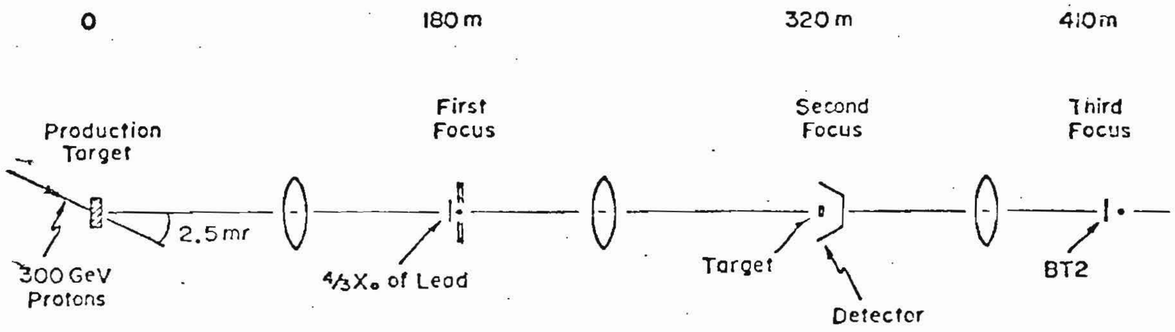

NAL M6 BEAM LINE

FIGURE III-2

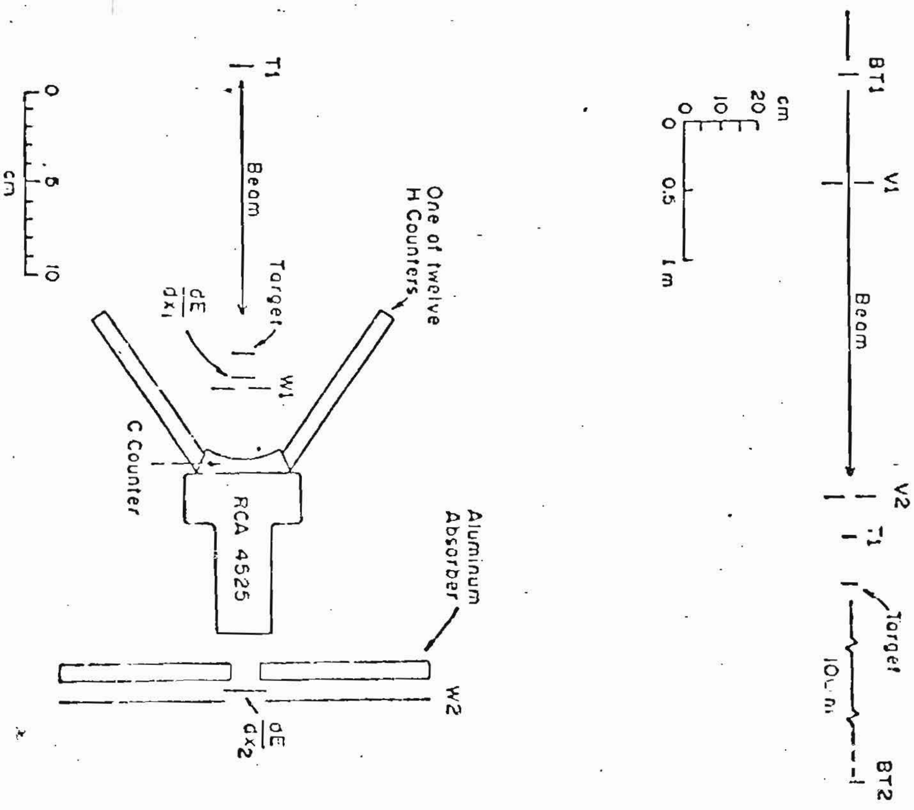

FIGURE III-3

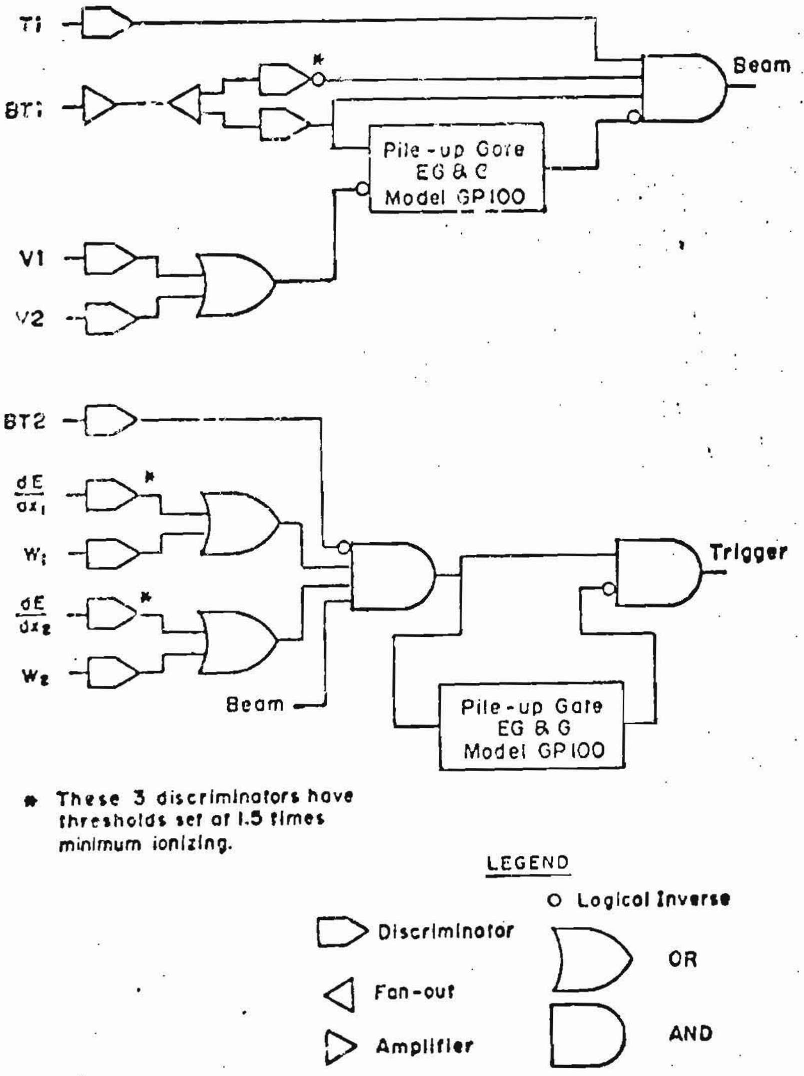

* These 3 discriminators have thresholds set at 1.5 times minimum ionizing.

FIGURE III-4

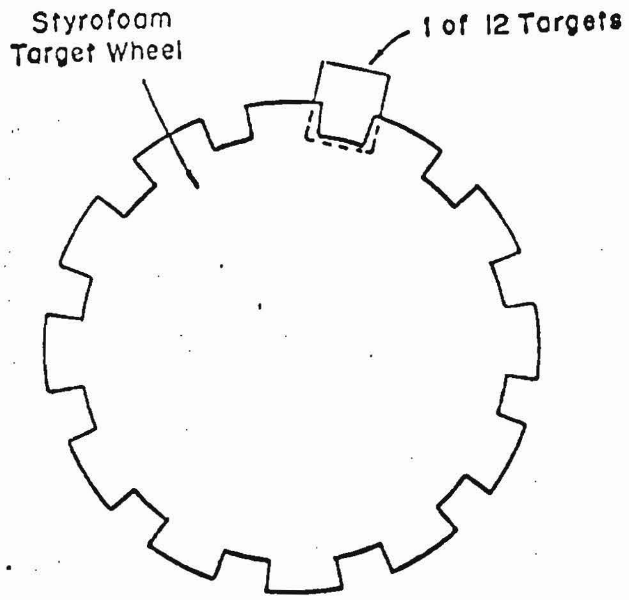

FIGURE III-5

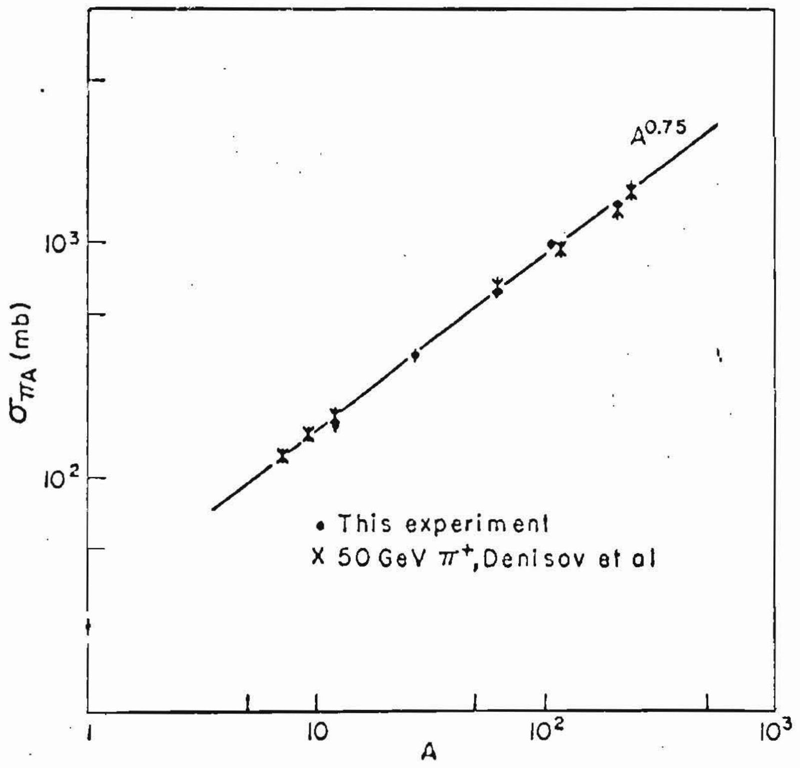

FIGURE III-6

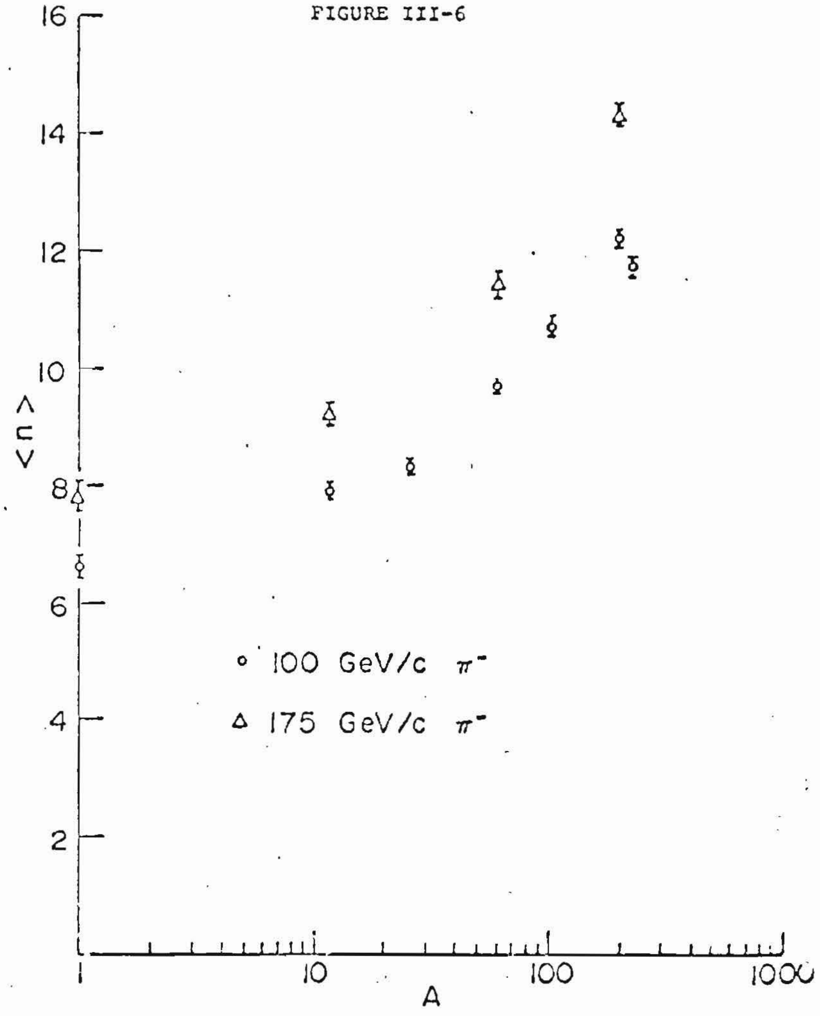

FIGURE III-7

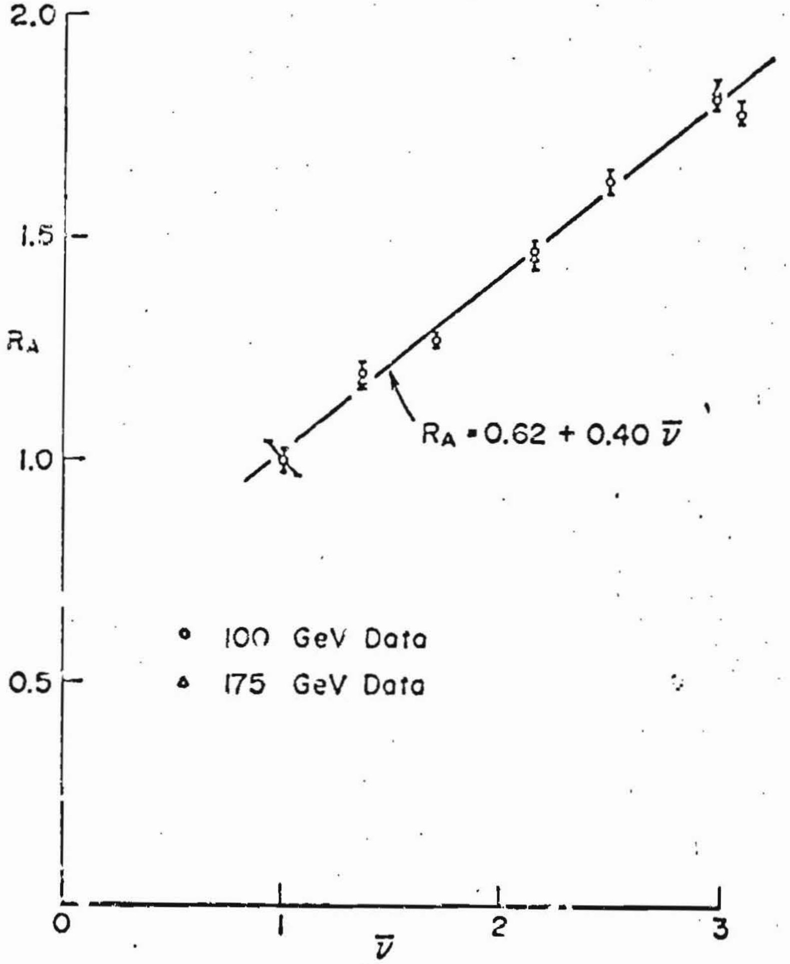

FIGURE III-8

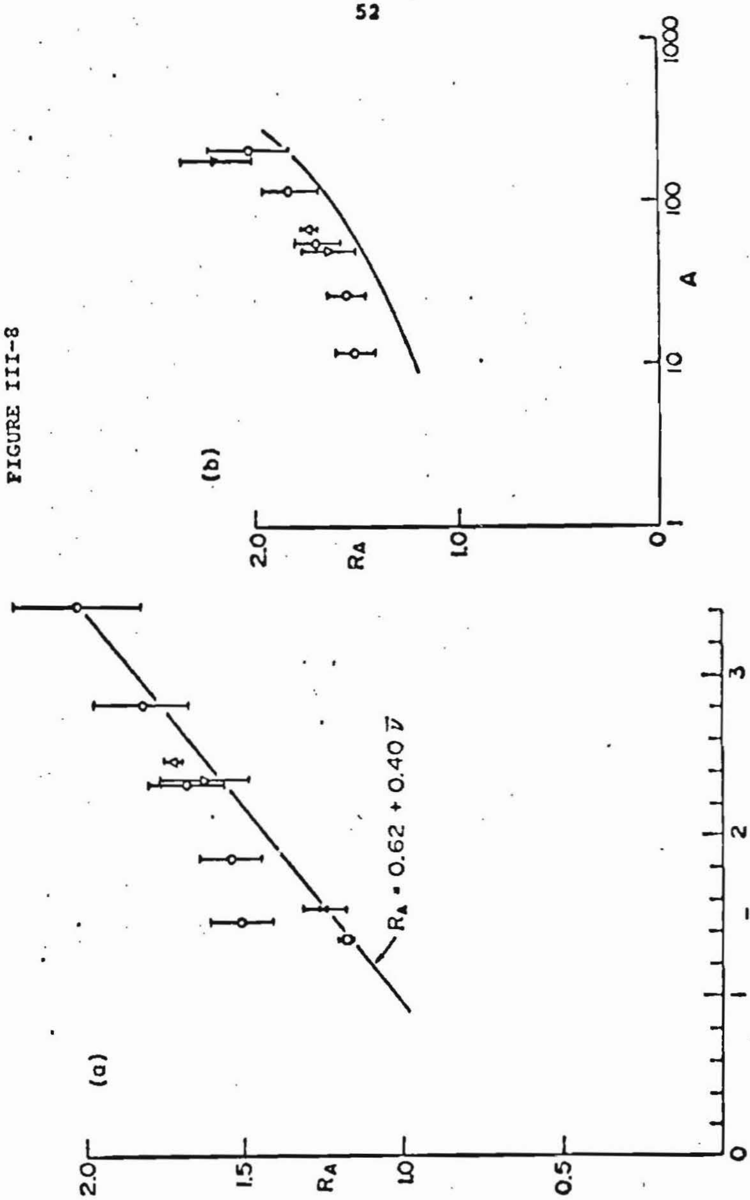

FIGURE III-9

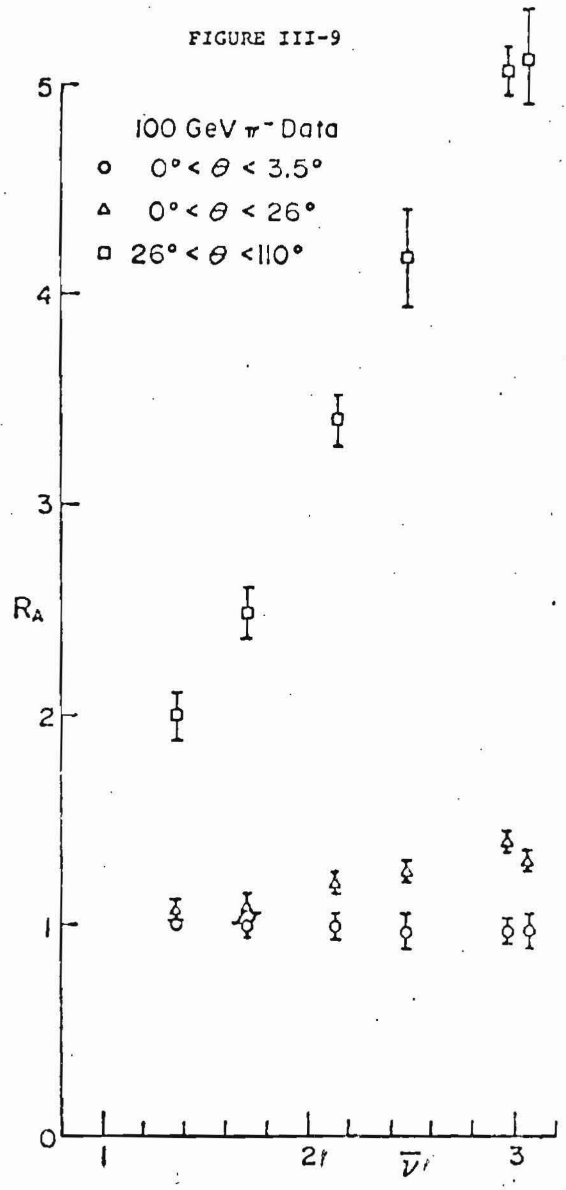

FIGURE III-10

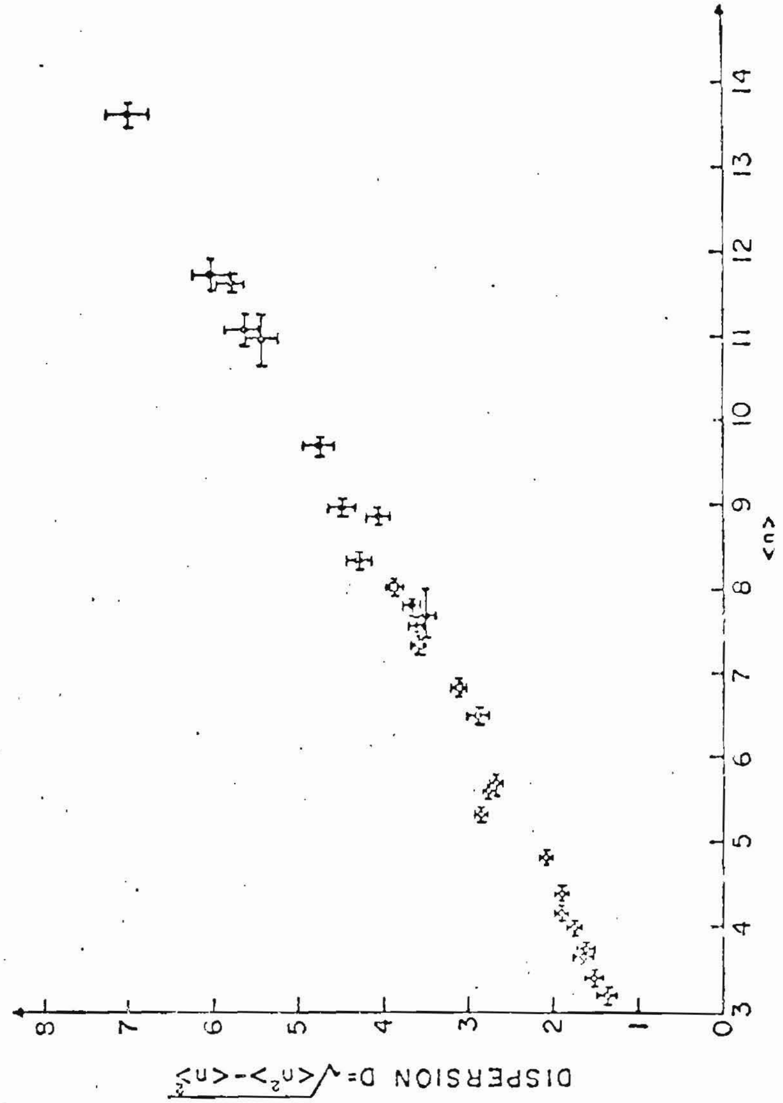

FIGURE III-11

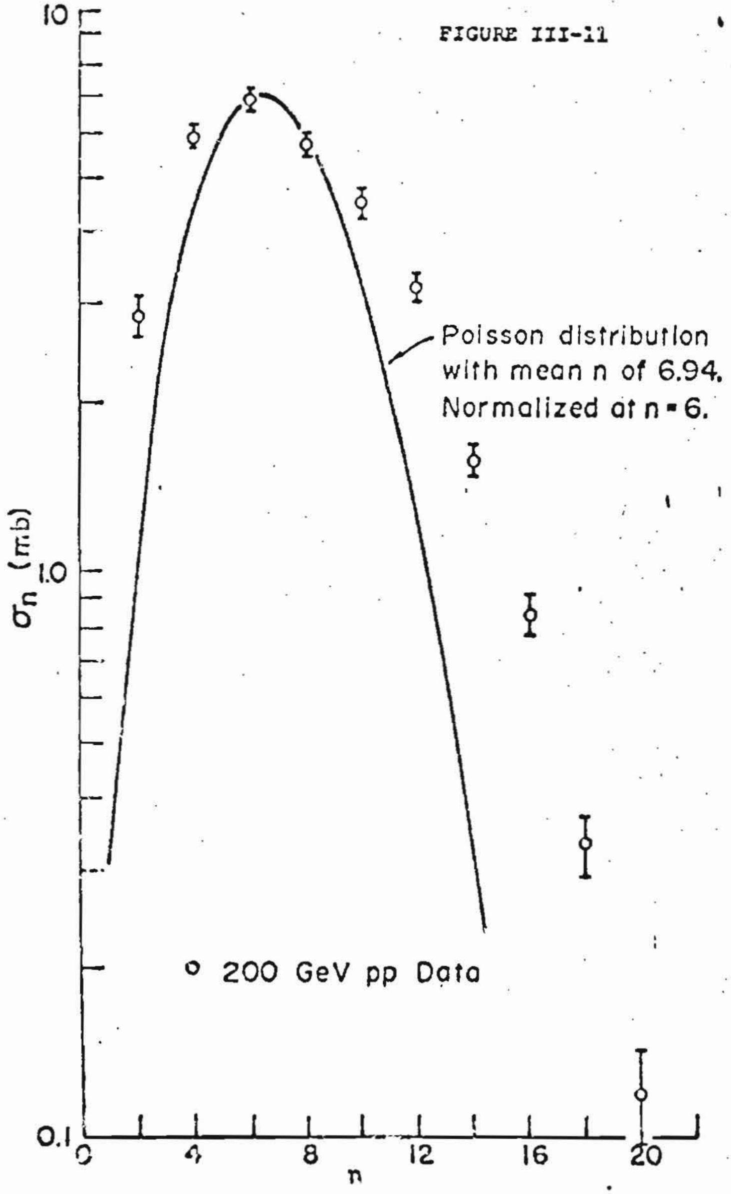

CHAPTER IV

PART II OF THE EXPERIMENT

Motivation

The first part of FNAL experiment number 178[37] yielded several pieces of interesting information. First, the average charged multiplicity per inelastic collision increases slowly with the atomic number A of the target. This was a confirmation of emulsion results.[8]

Comparison with experiments[9,26] performed with proton beams suggests that this behavior is similar for both π-A and p-A interactions, provided that one uses R_A and $\bar{\nu}$ as the relevant parameters. It was decided to explore this apparent similarity further within one experiment in order to minimize any systematic biases that might occur.

Another feature of the data is the confinement of the increase in multiplicity to the region of low pseudorapidity. Therefore another goal of this experiment was to determine the pseudorapidity (or angular) distribution of the charged secondaries in hadron-nucleus collisions. The differences between proton and pion induced reactions might manifest themselves in the pseudorapidity distribution. K and $\bar{p}$ beams would also be used.

Over the very limited energy range of 100 to 175 GeV, R_A appeared to be independent of energy. This point would be investigated further. The energy dependence of the pseudorapidity distribution would be examined also.

In summary, the pseudorapidity or angular distributions of charged secondaries in hadron-nucleus collisions would be investigated as a function of the energy of the incident beam particle and the identity of the beam particle as well as the target.

Experimental Set-up

The second part of this experiment (FNAL Experiment Number 178) was carried out at the fourth focus of the M6W beam line in the Meson Laboratory of Fermilab. The equipment was situated approximately 600 meters from the meson production target -- see Figure IV-1.

Setting up and testing occupied April through June of 1975. The data to be presented here were obtained in a period of 10 days -- August 3 to August 14 with two days lost to regularly scheduled maintenance of the accelerator.

Running conditions during this period were poor. Beam availability was sporadic. Having just attined a 400 GeV/c proton beam and attempting to commision the "capacitor tree," the accelerator was experiencing reliability problems, which were often exacerbated by the summer heat. Beam quality was also poor. The spill time was 350 milliseconds (msec) with a repetition cycle of 13 seconds. "Debunching" was far from complete as almost 4% of the RF "buckets" were doubly occupied at a beam intensity of only $2\ 10^5$ per spill. This was much higher than that observed under previous experimental conditions with a 300 GeV/c proton beam incident on the meson production target.[38]

The detectors were based on the previous setup with three 12-element hodoscopes added for increased angular resolution. Relative to the target, the cone-shaped hodoscope H was essentially unmoved. The UVT lucite counter C was moved downstream to accommodate the 3 new ring-shaped hodoscopes. See Figure IV-2.

The construction of one of the ring-shaped hodoscopes is illustrated in Figures IV-3 and IV-4, which are the front and side views respectively. It was made of two layers of 6 counters each. Each counter subtends 60° of the azimuth. The two layers were rotated 30° relatively to one another so that the cracks between adjacent counters do not line up. The front or upstream layer was made of 3/4-inch thick UVT lucite, while the back or downstream layer was made of 1/4-inch plastic scintillator.

There were several reasons for such a construction. The front lucite layer imposed a velocity selection of $\beta \geq 0.85$, the same as that imposed by the C counter and by the H hodoscope. Its thickness also served to prevent delta-rays from reaching the downstream scintillator layer unless their energies exceeded approximately 8-10 MeV.

The three gas-filled Cherenkov counters used to identify beam particles are shown schematically in Figure IV-1. C1 was a threshold Cherenkov counter used to identify pions, C2 was a differential Cherenkov counter used to tag protons, and C3 was a DISC (Differential Isochronous Cherenkov Counter)[39] set to identify kaons. Details of these counters, including their performance characteristics, are given in References 39 and 40. These counters made it possible to take proton, kaon and pion data simultaneously.

An acceptable beam particle was defined by:

(1) the counters T, TX and TY registered counts in coincidence,

(2) veto counters V0, V1 and V2 were not hit,

(3) the pulse height from the T counter did not exceed 1.5 times minimum ionizing, and

(4) there was no other signal in the T counter $\sim$120 nsec before or after the coincidence signal.

The reasons for these requirements are as discussed in Chapter III in connection with the first part of this experiment.

The beam rate was monitored by a scaler. The coincidence rates between this beam signal and each of the three

gas-filled Cherenkov counters were also scaled. Thus the beam rate of each particle type was known. Unfortunately, during the time when the 200 GeV data were obtained, the DISC counter was not functioning after being drenched by a broken water pipe. Therefore there were no data on 200 GeV/c K^+ or K^- reactions.

Targets were mounted on the cut-out bottom of plastic cups, which were manually changed whenever it was necessary to change targets. The construction of these targets and their holder is illustrated in Figure IV-5. A photograph of one such target, a 4-inch long block of polyethylene used only in testing, is reproduced in Figure IV-6.

The trigger requirements were as follows:

(1) there was an acceptable beam particle as defined above,

(2) there was at least one coincidence count (between front and back layers) in one of the three ring-shaped hodoscopes, or there were large pulses (greater than 1.5 times minimum ionizing) in both the dE/dx_1 and the dE/dx_2 counters, and

(3) the data acquisition system was ready to process this event.

For each event, the on/off state of the 48 hodoscope counters (12 from the H hodoscope and 12 each from the three ring-shaped hodoscopes), the V3 counter which covered the region $\eta \gtrsim 7$, and the 3 particle-identifying Cherenkov counters were stored in CAMAC devices. The pulse heights of the dE/dx_1, dE/dx_2 and C counters were digitized and stored in CAMAC units also. The combined information was then transferred to a magnetic tape. The contents of the scalers were recorded on tape periodically.

Figures IV-7 and IV-8 are schematic diagrams of the electronics used to impose the requirements discussed above.

The PDP11/10 computer used to transfer data from CAMAC units to magnetic tape also performed diagnostic functions. The number of events that were induced by protons, kaons or pions as well as the number of untagged or multiply-tagged events were available on-line. The frequencies at which the hodoscope counters were struck were also available. Any asymmetry around the azimuth was an indication of malfunctioning counters or a misalignment of the apparatus relative to the beam. The three pulse height distributions were also displayed on-line. Frequent visual inspections ascertained that there was no drift in the pedestal or the gain. Off-line analyses have confirmed this.

A profile monitor, designed, manufactured, maintained and supplied by Fermilab, was used to check the beam alignment in addition to its general well-being. It

was located within the beam defining telescope -- see Figure IV-2. This device provided a spill-by-spill profile of the beam in each of the two directions transverse to the beam line. Any significant change in the fields of the beam line magnets showed up instantly as a distorted profile.

Data

The targets used in this experiment are listed in Table IV-1. Several thicknesses of each material were used to allow an extrapolation to zero target thickness. Hydrogen-target data were obtained by subtracting the carbon data from the polyethylene (CH_2) data.

In order to obtain finer angular bins than those subtended by individual hodoscopes, the relative positions of the detectors and the target were varied. One of these positions is shown in Figure IV-2. The pseudorapidity coverage of the detectors in each of these geometries is tabulated in Table IV-2. Three positions were used.

The available data are summarized in Table IV-3. Note that there is no kaon data at 200 GeV/c due to malfunctioning of the DISC counter.

Typical beam intensities were 1-3 10^5 beam particles per 350-msec spill. A typical run lasted 10-30 minutes with approximately [illegible]0000 triggers.

The fraction of events that were proton (or kaon or pion) induced depended on the composition of the beam, which varied with the momentum as well as the polarity. The ratios of identified beam particles are given in Table IV-4. Notice that the fractions of the beam that were K^+ or $\bar{p}$ are very small. The data on these beam particles have much poorer statistical accuracy than the proton or pion data.

Analysis

The first step in the analysis was the selection of those events which satisfied the following three points:

(1) there was an unambiguous identification of the beam particle as a proton, kaon or pion,

(2) the counter V3 was off -- this counter covered the region $\eta \geq 7.0$.

(3) there were at least 3 charged secondaries.

The second requirement was used primarily to reject elastic scattering and non-interacting beam particles which deposited relatively large amounts of energy in the dE/dx counters. The third requirement was motivated as in the first part of this experiment. It helped to reject those events which had a hadronic interaction in the C counter only.

This cut on the data was done without any fitting. The clear separation between 1, 2 and 3 particle peaks in the pulse height spectrum of the C counter allowed a

straight forward cut. The now missing 0-, 1- and 2-prong events would be corrected for later in the analysis.

The resulting events were then separated into three groups depending on the beam particle identity. They were treated individually but in identical fashion from this point on.

The contribution from target empty interactions were subtracted. Empty target runs were taken at regular and frequent intervals for this purpose. Approximately 10% of the data were on an empty target.

The algorithms used to find the average multiplicities in the C counter and in the H hodoscope were unchanged from the first part of this experiment. Details are given in Appendices IV and VI.

With the assumption of no azimuthal correlations within each ring hodoscope, its multiplicity distribution was obtained by a fitting procedure. The method is detailed in Appendix VII, which also offers reasons for the assumption.

Corrections for the missing 0-, 1-, and 2-prong events as well as for acceptance were then applied. See Appendix VIII. The average multiplicity for each pseudorapidity bin was then extrapolated to zero target thickness. The data from the three different positions are given in Tables IV-5(a) through IV-5(x). The errors shown in these tables do not include uncertainties in the shape of the psuedorapidity distribution introduced when correcting for low-multiplicity events. This effect is estimated to change the multiplicity of each pseudorapidity bin by no more than 2-3%.[41]

In order to obtain multiplicities for non-overlapping pseudorapidity bins, the data were averaged over the 3 geometries as outlined in Appendix VIII. These results are given in Tables IV-6(a) through IV-6(j). Since data were not obtained for all targets at all positions, only part of the data could be treated this way. This is the explanation for having no more than 5 targets in each of these tables.

The errors in Tables IV-6(a) through IV-6(j) do not include uncertainties that may have been introduced in the correction for low-multiplicity events and those that may have resulted from the algorithm used in averaging the data over the different geometries. Their combined effect is estimated to be less than 3%.

Another approach was also used in the final steps of the analysis. After the extrapolation to zero target thickness, but before averaging the data from the three available geometries, the average multiplicity in each pseudorapidity bin was fitted with a polynomial in $\bar{\nu}$. The point-to-point uncertainties in $\bar{\nu}$ were included in the fits. Some of these fits are illustrated in Figures IV-9

and IV-10. Higher order polynomials were tried until an optimal fit was obtained as measured by the chi-squared per degree of freedom. To prevent the choice of unreasonable fits, a minimum of 2 degrees of freedom was required. Provided that the average multiplicity in each pseudorapidity bin is a continuous function of the atomic number A of the target, these fits could be used to determine the pseudorapidity distribution and hence the average multiplicity at all values of $\bar{\nu}$. Polynomials were used in the fits for ease of computation. No special significance should be attached to this choice. The shapes of the fitted lines are not intended to convey any special significance either; the only purpose of the fits is to allow an estimate of the rapidity distribution and the average multiplicity that one would have obtained using some other target.

These fitted numbers were then averaged over the three available positions in exactly the same way as the original data. The final results of this procedure are given in Tables IV-7(a) through IV-7(j). The errors quoted in these tables (Tables IV-7) do not include the possible systematic biases that may have been introduced by the algorithm of smoothing the data as a function of $\bar{\nu}$, nor do they include the uncertainties discussed in connection with Tables IV-5 and IV-6. However, the combined effect of these uncertainties is expected to be no more than 5%

for each pseudorapidity bin.

A comparison of the numbers given in Tables IV-6(a) through IV-6(j) with those given in Tables IV-7(a) through IV-7(j) shows that they are compatible. So the procedure for smoothing and interpolating the data for each pseudorapidity bin as a function of $\bar{\nu}$ is probably acceptable. This interpolation scheme is necessary in order that proton, kaon and pion reactions may be compared at the same value of $\bar{\nu}$.

Discussion of Results

The data on hydrogen target were obtained by a polyethylene-carbon subtraction, i.e. the data on carbon targets were treated as background for the data on polyethylene (CH_2) targets. This has the unfortunate consequence of having a background greater than the signal -- the absorption cross-section of proton on carbon is approximately 240 millibarns (mb) while that on hydrogen is about 30 mb. Thus the data on hydrogen targets were poorly determined. And since the hydrogen data will often be used as a reference for the data from other targets, e.g. the average multiplicity on hydrogen is the denominator in the ratio R_A, trends of the data can be obscured by the poorly determined Hydrogen point. Therefore all references to the hydrogen data will be based on the results obtained by the

second technique mentioned at the end of the last section. In other words, the continuity of the data as a function of the atomic number of the target was used to arrive at a slightly better determined result for the data on hydrogen.

Except for the average charged multiplicities, which are summarized in Table IV-8, and the ratio R_A, all discussions will be based on the results obtained by the second method, i.e. the numbers in Tables IV-7(a) through IV-7(j). Without this technique, it would be impossible to test the validity of the use of $\bar{\nu}$ as the independent variable instead of the atomic number A.

An inspection of Tables IV-5(t) through IV-5(x) and Table IV-8 reveals that the 200 GeV/c π^+ and π^- data are consistent with one another. However, the π^- data were usually better determined. This resulted from the fact that at 200 GeV/c, the negatively charged particles in the beam line were predominantly π^- whereas the positively charged particles were mostly protons. Unless otherwise stated, all references to the 200 GeV/c pion data refer to the π^- data.

The comparison of averaged charged multiplicities with hydrogen bubble chamber results[20,21,22,31,42,43,44,45] is given in Table IV-9. The agreement is satisfactory. Figures IV-11 through IV-13 are comparisons of the (pseudo) rapidity distributions from hydrogen targets. In the case of the 100 GeV/c proton-proton data,[46] the bubble chamber results have been treated in exactly the same way as this experiment's, i.e. there was a velocity cut of $\beta>0.85$ and all events with any track having $\eta>7$ were removed. The agreement is excellent. In the other cases,[45,47] the bubble chamber results have not been similarly treated. These distributions are given as a function of rapidity instead of pseudorapidity. Two points need to be emphasized. The velocity cut of $\beta>0.85$ imposed in this experiment is expected to result in an average multiplicity that is lower by about 0.5 particles.[35] Interaction secondaries, in the laboratory frame of reference, tend to have higher values of pseudorapidity than their rapidities. (See Appendix II for details on these variables.) Hence one would expect the pseudorapidity distributions to be slightly lower and shifted to the right relative to the corresponding rapidity distributions. With these cautionary remarks in mind, one can see that the agreement between the results of this experiment and those of bubble chamber experiments is satisfactory.

Figures IV-14 and IV-15 are comparisons of the pseudorapidity distributions of the 200 GeV emulsion data of this experiment with those obtained from the optical scanning of emulsion stacks.[48] The average multiplicities are compared in Table IV-10.[15,48,49,50,51] Note that some

of the emulsion results of this experiment are based solely on interpolated values. The agreement is quite good.

It should be pointed out that in the comparison of (pseudo)rapidity distributions, the normalizations are absolute. The distributions have not been arbitrarily normalized to one another; the area under each distribution corresponds to the reported average multiplicity of that reaction.

The results are now compared with those obtained in the first part of this experiment. The average charged multiplicities are summarized in Table IV-11. Except for the data on Uranium target, the agreement is acceptable. The fact that the previous measurement gave a multiplicity smaller for a Uranium target than for a Lead target already renders that particular data point suspect. Note that the average multiplicities tabulated in Table IV-11 do not agree with those given in Table IV-6. The numbers in Table IV-11 are smaller because only the multiplicity in the region $\theta<110°$ has been included in order to make a fair comparison.

If one ignores the Uranium data, there still appears to be a systematic difference. The new measurements give results higher than the old measurements by 0.3 to 0.5 particles. While these numbers are within the systematic errors estimated at $\lesssim 5\%$ (not included in the tables), this slight discrepancy is discomforting. For the region $\theta<3.5°$ ($\eta>3.5$), the two measurements agree. However, it is difficult to inspect the regions $\theta<26°$ and $26°<\theta<110°$. $\theta=26°$ and $110°$ correspond to η of 1.47 and -.36 respectively. In both cases, especially in the latter case, the pseudorapidity distribution is varying rapidly as a function of η. Uncertainties in the angular boundaries become greatly magnified when one inspects the multiplicity.

While this slight discrepancy cannot be completely resolved, it can be understood on the basis of small mismeasurements of the polar angles.

In the region of $\eta>5$, the multiplicities reported here do not decrease as the atomic number of the target increases. This is in apparent contradiction to the results of emulsion experiments,[52,53] where a decrease in multiplicity has been noticed as N_h increases. N_h is defined as the number of heavily ionizing tracks, i.e. those charged particles with $\beta\lesssim 0.7$. A more detailed comparison (see Appendix IX) shows that the data are indeed quite compatible. The apparent disagreement is simply a manifestation that N_h is not an equivalent measure of the target as its atomic number.

Having established the validity of the data by comparison, where possible, with other experiments, attention will now be focussed on some features of the data. The $\bar{\nu}$

dependence, the beam particle dependence and the energy dependence of the average charged multiplicities as well as the pseudorapidity distributions will be discussed.

As has been pointed out previously by many authors, the average charged multiplicity is a weak function of the atomic number A of the target. Figure IV-16 shows the average multiplicity in proton nucleus collisions at 50, 100 and 200 GeV as a function of $\bar{\nu}$. $\bar{\nu}$ is defined as the average number of absorption mean free paths that the target nucleus presents to the beam particle. For protons, $\bar{\nu}\sim A^{1/3}$. Details on $\bar{\nu}$ can be found in Appendix I. The data on reactions initiated by anti-protons, kaons and pions show similar weak atomic number dependences.

The rise in multiplicity as a function of $\bar{\nu}$ appears to be excluded from the region of high pseudorapidity. This is illustrated in Figures IV-17 through IV-19, where the pseudorapidity distributions for $\bar{\nu}=1$, 2 and 3 have been plotted for pion beams of 50, 100 and 200 GeV/c. The proton, anti-proton and kaon results, which are not shown, exhibit similar trends.

The similarities and differences of the data for the various beam particles will now be discussed. It has been noticed previously that the proton and pion data look remarkably similar if one uses the scaled multiplicity R_A and the parameter $\bar{\nu}$ as the variables. Figure IV-20 shows the best linear fits to the data of R_A versus $\bar{\nu}$ for proton, kaon and pion induced reactions at 50 and 100 GeV/c. The parameters of the fitted straight lines are given in Table IV-12.

It appears that the kaon data is significantly different from the proton and pion data, which are consistent with being identical. However, such a conclusion may be premature. First, it should be pointed out that in fitting the straight lines to R_A versus $\bar{\nu}$ only point-to-point errors have been included. Uncertainties in both R_A and $\bar{\nu}$ have been taken into account. However, overall normalization uncertainties were not included. For example, the uncertainties in the multiplicities of hadron-hydrogen interactions were not included in the errors of R_A. It would enter as a scale uncertainty. Similarly, uncertainties in the hadron-nucleon cross-sections were not included in the errors on $\bar{\nu}$. It would enter as an uncertainty in the scale of $\bar{\nu}$. It is unlikely that the first effect can account for the observed differences. The second effect is far more important in this comparison of different beam particles. The scale uncertainties in $\bar{\nu}$ are 2%, 13% and 3% for proton, kaon and pion beams respectively. See Appendix I and Table A-I-1 for further details. A change in the $\bar{\nu}$ scale for the kaon data by one standard deviation (i.e. 13%) would make the fit to R_A versus $\bar{\nu}$

for kaon-initiated reactions compatible with those for proton and pion beams. A more definitive comparison has to await a better measurement of the kaon-proton absorption cross-section in the energy range of 50 to 100 GeV.

The comparison of anti-proton data also have to be postponed. There are no published data on the absorption cross-sections of anti-protons on nuclei. If one assumes as in Appendix I that the values of $\bar{\nu}$ are identical for proton and anti-proton beams, one can conclude that the proton and anti-proton data are indistinguishable in R_A versus $\bar{\nu}$.

Some models make predictions for the average multiplicity using power law dependences on the atomic number A. To facilitate future comparisons, the data have also been fitted to the form $R_A=R_1A^{\alpha}$. The results are summarized in Table IV-13. These fits gave chi-squared per degree of freedom systematically higher than those in fits to $R_A=a+b\bar{\nu}$. The errors on R_A have been treated the same way as in the previous fits: normalization uncertainties on R_A were not included in the fits. The fitted values of α appear to depend on the identity of the beam particle.

A further comparison of the three different beam particles is the comparison of the pseudorapidity distributions. Figures IV-21 through IV-23 are the pseudorapidity distributions for $\bar{\nu}=2$ at 50, 100 and 200 GeV/c. In the first two cases, proton, kaon and pion data were available, while in the last instance there was no kaon data. The distributions for the three beam particles have similar shapes. Their normalization differences are due to the different multiplicities in hadron-nucleon collisions. In particular, the multiplicities in the forward angular region ($5<\eta<7$) are independent of the target nucleus and are consistent with the results from hydrogen bubble chambers. It should be emphasized that in this comparison of different beam particles, the value of $\bar{\nu}$ is only precise to within the scale uncertainties mentioned above.

Attention will now be turned to the energy dependence of the results. Emulsion experiments have shown that R_A is practically independent of energy[8] above ∿70 GeV. See Table III-7. Figure IV-24 is a comparison of the results of this experiment and emulsion experiments[26,49,54] performed with incident protons. They are in fair agreement, although the results of this experiment appear to favor a stronger energy dependence.

Figure IV-25 shows the best fits to R_A versus $\bar{\nu}$ in proton- and pion-nucleus interactions at 50, 100 and 200 GeV/c. The parameters of these fits are given in Table IV-11. Taking into account possible normalization differences in R_A, i.e. uncertainties in the average multiplicities for hydrogen targets, the lines are compatible with being energy independent.

Figure IV-26 shows the π-Carbon[27] and p-Emulsion[26,49,5 average multiplicities as a function of beam energy. Low energy data have also been included.[25,55,56,57] The data are compatible with a ln(s) behavior, similar to proton-proton data.

Figure IV-27 shows the pseudorapidity distributions of the proton data for $\bar{\nu}=2$ at 50, 100 and 200 GeV. The increase in multiplicity as a function of beam energy is predominantly in the region of higher pseudorapidity. Figure IV-28 shows the pion data at $\bar{\nu}=3$.

It has been pointed out earlier that the rise in multiplicity as a function of $\bar{\nu}$ is confined to regions of low rapidity. The critical value of pseudorapidity for this increase becomes larger as the beam energy increases. This is demonstrated in Figure IV-29. The proton data for a $\bar{\nu}=3$ target with the pseudorapidity distributions from a hydrogen target subtracted are displayed for 50, 100 and 200 GeV. The increase in width in pseudorapidity of the excess multiplicity over hydrogen is now more apparent.

Thus in summary,

(1) The linear dependence between R_A and $\bar{\nu}$ seems to be independent of the identity of the beam particle, with the possible

exceptions of kaon and anti-proton.

(2) R_A is at most a weak function of energy in the range 50 to 200 GeV.

(3) For the same value of $\bar{\nu}$, the shapes of the pseudorapidity distributions are similar for proton, kaon, pion and anti-proton beams. There are slight differences in their heights, which are compatible with the differences in the multiplicities of the different beam particles on hydrogen.

(4) As the beam energy is increased, there is a corresponding (though slow) increase in multiplicity which is predominantly in the region of high pseudorapidity.

(5) At a fixed beam energy, the rise in multiplicity as a function of the atomic number of the target is confined to the region of low pseudorapidity.

(6) The extent in pseudorapidity where this rise occurs increases with the beam energy. The left edge of this enhancement is energy independent, while the right edge goes to higher values of η.

TABLE CAPTIONS

IV-1	List of targets used in the second part of this experiment.
IV-2	Pseudorapidity bins covered in the 3 different geometries. The range and size of each pseudorapidity bin are given.
IV-3	Summary of available data. Note that there is no kaon data at 200 GeV/c.
IV-4	Beam composition at various momenta and polarity. Only those beam particles which were unambiguously identified have been included. The total has been normalized to 100%. At 200 GeV/c, kaons were not detected as a result of equipment failure.
IV-5	(a) through (x)-Observed average charged multiplicities in each pseudorapidity bin for all the reactions investigated. Uncertainties are also included. The quoted errors do not include possible biases introduced by the correction for the low-multiplicity events. This η-dependent effect is estimated to be less than 3% -- see text.
IV-6	(a) through (j)-Average charged multiplicities in each pseudorapidity bin after averaging over the 3 geometries. The quoted errors include all effects that were included in Table IV-5. Note

that this table represents less data than Table IV-5 -- in many instances there were not enough data over the different geometries to allow a meaningful average.

IV-7 (a) through (j)-Average charged multiplicities in each of 12 non-overlapping pseudorapidity bins. These numbers were obtained by an interpolation -- see text for details. The indicated errors do not include systematic biases due to interpolation. The systematic effects are expected to total no more than 5%.

IV-8 Summary of average charged multiplicities.

IV-9 Comparison of hadron-proton average charged multiplicities with other experiments. The hydrogen bubble chamber data are from:

a V.V. Ammosov et al, Reference 42
b J. Erwin et al, Reference 43
c C. Bromberg et al, Reference 44
d S. Barish et al, Reference 31
e G.A. Akopdjanov et al, Reference 20
f E.L. Berger et al, Reference 21
g D. Bogert et al, Reference 22
h V.E. Barnes et al, Reference 45

Because of the velocity cut used in this experiment, the measured average charged multiplicities are expected to be $\sim$0.5 less than bubble chamber results.[35]

IV-10 Comparison of average charged multiplicities in hadron-emulsion experiments. The emulsion data are from:

a S.A. Azimov et al, Reference 49
b J. Babecki et al, Reference 26
c P.L. Jain et al, Reference 50
d Alma-Ata-Gatchina-Moscow-Tashkent Collaboration, Reference 48
e I. Otterlund, Reference 51

See Appendix IX for a definition of $\langle n_s \rangle$; it is similar to the average charged multiplicity of this experiment.

IV-11 Comparison of the average charged multiplicities in 100 GeV/c π-nucleus interactions measured in the first and second parts of this experiment. Note that the numbers in this table do not agree with those in Tables IV-6 or IV-7. The numbers here refer to the angular range $\theta<110°$.

IV-12 Results of fitting R_A versus $\bar{\nu}$ with a straight line of the form $a+b\bar{\nu}$. The quoted errors on a and b are highly correlated. The typical errors on R_A that one would have obtained using the full error matrix are given in the column "errors on R_A".

The chi-squared per degree of freedom are also listed.

IV-13 Results of fitting to $R_A=R_1A^\alpha$. For an explanation of the errors, see above, Table IV-12.

FIGURE CAPTIONS

IV-1 Location of the experiment. The M6 beam line splits into 2 branches near the third focus. This experiment was carried out in the west branch.

IV-2 Layout of the equipment.

IV-3 Front view of a ring-shaped hodoscope. The solid lines outline the 6 UVT lucite counters; the dashed lines are for the scintillation counters.

IV-4 Side view of a ring hodoscope.

IV-5 The construction of a typical target in its holder.

IV-6 Picture of an actual target holder. The target shown in the picture is a 4-inch thick piece of polyethylene (CH_2), which was only used for testing; actual targets did not exceed 1/8-inch.

IV-7 Block diagram of electronics for the beam defining logic.

IV-8 Block diagram of electronics for the trigger logic.

IV-9 An illustration of the polynomial interpolation of the average multiplicity in each pseudorapidity bin as a function of $\bar{\nu}$ in 50 GeV/c π-nucleus collisions. The points are the actual data and the solid lines are the best fits as defined in the text.

IV-10 An illustration of the polynomial interpolation of the average charged multiplicity in each pseudorapidity bin as a function of $\bar{\nu}$ in 100 GeV/c π-nucleus collisions.

IV-11 Comparison of the pseudorapidity distribution of 100 GeV/c proton-proton interaction with bubble chamber results. The solid line is from this experiment; the dashed line is from the Michigan-Rochester Collaboration, Reference 46. Cuts have been applied to the bubble chamber data to simulate the conditions of this experiment. Only tracks with $\beta > 0.85$ were considered. Events with any track having $\eta > 7$ and those with less than 3 charged secondaries were also rejected.

IV-12 Comparison of the 200 GeV/c proton-proton pseudorapidity distribution with the rapidity distribution obtained in a bubble chamber experiment, Reference 47. The bubble chamber results were only presented for the region $y_{cm} < 0$ and have been reflected about the center-of-mass rapidity to give the entire distribution. Note that the bubble chamber results (dashed lines) are in rapidity and do not have any cuts imposed.

IV-13 Comparison of the 100 GeV/c K^+-p pseudorapidity distribution of this experiment (solid lines) with the rapidity distribution in a bubble chamber experiment, Reference 45. The bubble chamber results (dashed lines) have no cuts imposed.

IV-14 Comparison of 200 GeV/c proton-Emulsion pseudorapidity distributions. The solid lines are from this experiment and the dashed lines are from Reference 48.

IV-15 Same as IV-14 but for 200 GeV/c π^--Emulsion interactions.

IV-16 Average charged multiplicities in proton-nucleus interactions. The solid lines are the best linear fits to $\langle n \rangle$ versus $\bar{\nu}$.

IV-17 $\bar{\nu}$-dependence of the pseudorapidity distributions in 50 GeV/c π^+-nucleus interactions. Note that the increase in multiplicity is confined to the region $\eta < 3.5$.

IV-18 $\bar{\nu}$-dependence of the pseudorapidity distributions in 100 GeV/c π^+-nucleus interactions. Note that the increase in multiplicity is confined to the region $\eta < 4$.

IV-19 $\bar{\nu}$-dependence of the pseudorapidity distributions in 200 GeV/c π^--nucleus interactions. Note that the increase in multiplicity is confined to the region $\eta < 5$.

IV-20 Best linear fits to R_A versus $\bar{\nu}$ in 50 and 100 GeV/c hadron-nucleus interactions. Typical errors on the fitted values of R_A are shown.

IV-21 Comparison of the 50 GeV/c proton, kaon and pion pseudorapidity distributions for $\bar{\nu}=2$. Typical errors are shown.

IV-22 Comparison of the 100 GeV/c proton, kaon and pion pseudorapidity distributions for $\bar{\nu}=2$. Typical errors are shown.

IV-23 Comparison of the 200 GeV/c proton and pion pseudorapidity distributions for $\bar{\nu}=2$. There was no kaon data at this beam momentum. Typical errors are shown.

IV-24 R_A versus beam energy in proton-Emulsion interactions. Results of other experiments (•) are from References 26, 49 and 54.

IV-25 Best linear fits to R_A versus $\bar{\nu}$ for 50, 100 and 200 GeV/c proton- and pion-nucleus interactions. Typical errors on the fitted values of R_A are shown.

IV-26 Average charged multiplicities in π-Carbon and p-Emulsion interactions as a function of beam energy. Results of other experiments are from References 25, 26, 27, 49, 54, 55, 56 and 57.

IV-27 Energy dependence of the pseudorapidity distributions for $\bar{\nu}=2$ in proton-nucleus interactions. Note that the increase in multiplicity is mainly in the region of higher pseudorapidity.

IV-28 Energy dependence of the pseudorapidity distributions for $\bar{\nu}=3$ in pion-nucleus interactions. Note that the increase in multiplicity is mainly in the region of higher pseudorapidity.

IV-29 Pseudorapidity distributions of the proton data for $\bar{\nu}=3$ at 50, 100 and 200 GeV. The corresponding pseudorapidity distributions from a hydrogen target have been subtracted. The excess multiplicity moves to regions of higher pseudorapidity as the beam energy increases. This rate is approximately the same as that of the kinematic limit on rapidity.

TABLE IV-1

Targets Used in the Second Part of This Experiment

Target	Atomic Number	Number of Thicknesses Available
beryllium	9	3
carbon	12	5
polyethylene	"14"	3
aluminum	27	5
titanium	48	2
copper	64	3
molybdenum	96	4
silver	108	5
tungsten	184	2
lead	207	5
uranium	238	5
emulsion		2

TABLE IV-2

Pseudorapidity Coverage in the 3 Geometries

	Range of η	$\Delta\eta$
Position 1:		
H hodoscope	-0.38 to 1.31	1.69
Ring hodoscope 1	1.47 to 2.17	0.70
Ring hodoscope 2	2.30 to 3.06	0.76
Ring hodoscope 3	3.20 to 3.96	0.76
C counter	4.06 to 7.00*	2.94
Position 2:		
H hodoscope	-0.67 to 0.68	1.35
Ring hodoscope 1	1.15 to 1.81	0.66
Ring hodoscope 2	2.16 to 2.92	0.76
Ring hodoscope 3	3.14 to 3.91	0.77
C counter	5.28 to 7.00*	1.72
Position 3:		
H hodoscope	0.56 to 2.39	1.83
Ring hodoscope 1	2.14 to 2.87	0.73
Ring hodoscope 2	2.65 to 3.41	0.76
Ring hodoscope 3	3.35 to 4.12	0.77
C counter	4.15 to 7.00*	2.85

*$\eta \geq 7.0$ is the region covered by the V3 counter. See text.

TABLE IV-3

Summary of Available Data

		Position 1	Position 2	Position 3
50 GeV/c	π^+	x	x	
	K^+	x	x	
	p	x	x	
100 GeV/c	π^+	x	x	x
	K^+	x	x	x
	p	x	x	x
200 GeV/c	π^+	x	x	x
	K^+			
	p	x	x	x
200 GeV/c	π^-	x	x	
	K^-			
	$\bar{p}$	x	x	

TABLE IV-4

Beam Composition

Momentum	Polarity	$p(\bar{p})$	$K^+(K^-)$	$\pi^+(\pi^-)$
50 GeV/c	+	14.6±.2%	2.60±.04%	82.8±.2%
100 GeV/c	+	36.9±.1%	3.72±.02%	59.3±.1%
200 GeV/c	+	28.6±.3%	---	71.4±.1%
200 GeV/c	-	7.47±.10%	---	92.5±.2%

TABLE IV-5(a)

50 GEV/C PROTON MULTIPLICITIES

NU BAR	PSEUDORAPIDITY RANGE				
	-0.38 1.34	1.47 2.20	2.30 3.07	3.19 3.97	4.06 7.00
1.00 0.00	0.98 0.47	1.74 0.25	1.06 0.23	0.91 0.17	0.93 0.09
1.50 0.01	1.11 0.07	1.06 0.08	1.44 0.09	0.99 0.07	0.90 0.06
2.50 0.02	2.50 0.22	1.72 0.14	1.82 0.14	1.15 0.09	0.90 0.17
2.95 0.03	3.13 0.28	2.12 0.18	1.91 0.16	1.03 0.09	0.97 0.10
3.61 0.04	4.21 0.44	2.56 0.27	1.88 0.19	0.88 0.10	0.85 0.16

TABLE IV-5(b)

50 GEV/C PROTON MULTIPLICITIES

NU BAR	PSEUDORAPIDITY RANGE				
	-0.67 0.72	1.16 1.85	2.17 2.94	3.14 3.92	5.29 7.00
1.00 0.00	-0.17 0.32	0.94 0.18	0.67 0.20	1.33 0.20	0.29 0.04
1.50 0.01	0.48 0.08	0.97 0.07	1.51 0.09	1.01 0.06	0.25 0.01
2.50 0.02	1.23 0.15	1.67 0.13	1.86 0.13	1.18 0.09	0.30 0.10
3.61 0.04	2.01 0.26	2.40 0.26	2.02 0.19	1.13 0.11	0.25 0.03

TABLE IV-5(c)

100 GEV/C PROTON MULTIPLICITIES

NU BAR	PSEUDORAPIDITY RANGE				
	-0.38 1.34	1.47 2.20	2.30 3.07	3.19 3.97	4.06 7.00
1.00 0.00	0.55 0.15	0.85 0.17	1.22 0.19	1.14 0.16	1.51 0.25
1.37 0.01	0.92 0.03	1.17 0.03	1.53 0.04	1.36 0.04	1.76 0.06
1.50 0.01	1.10 0.02	1.20 0.02	1.56 0.02	1.31 0.02	1.63 0.02
1.92 0.01	1.64 0.04	1.51 0.04	1.93 0.04	1.52 0.04	1.88 0.06
2.50 0.02	2.26 0.11	1.97 0.09	2.06 0.10	1.53 0.08	1.24 0.16
2.45 0.03	2.41 0.10	2.07 0.10	2.24 0.10	1.67 0.08	2.10 0.10
2.95 0.03	3.20 0.10	2.39 0.09	2.52 0.09	1.80 0.06	1.91 0.09
3.61 0.04	4.15 0.12	2.86 0.11	2.59 0.09	1.71 0.06	1.64 0.09
3.76 0.05	4.60 0.24	3.24 0.20	2.60 0.15	1.78 0.10	1.89 0.18

TABLE IV-5(d)

100 GEV/C PROTON MULTIPLICITIES

NU BAR	PSEUDORAPIDITY RANGE				
	-0.67 0.72	1.16 1.85	2.17 2.94	3.14 3.92	5.29 7.00
1.00 0.00	0.64 0.12	0.64 0.16	1.32 0.21	1.28 0.19	0.55 0.14
1.50 0.01	0.49 0.02	0.97 0.03	1.60 0.04	1.40 0.03	0.48 0.02
2.50 0.02	1.18 0.12	1.77 0.14	2.25 0.14	1.79 0.12	0.50 0.04
3.61 0.04	2.30 0.09	2.74 0.14	2.66 0.11	1.81 0.07	0.55 0.05
3.76 0.05	2.62 0.14	2.83 0.23	2.88 0.16	1.92 0.10	0.48 0.07

TABLE IV-5(e)

100 GEV/C PROTON MULTIPLICITIES

NU BAR	PSEUDORAPIDITY RANGE				
	0.56 2.35	2.13 2.90	2.65 3.42	2.35 4.13	4.16 7.00
1.00 0.00	3.76 0.78	1.76 0.41	1.41 0.49	1.54 0.39	2.21 0.21
1.37 0.01	2.67 0.11	1.52 0.08	1.66 0.09	1.30 0.09	1.54 0.02
1.50 0.01	2.54 0.15	1.42 0.10	1.60 0.13	1.23 0.08	1.41 0.00
2.29 0.02	4.53 0.45	2.27 0.27	2.15 0.27	1.38 0.19	1.57 0.08
2.50 0.02	4.46 0.45	2.14 0.25	2.01 0.24	1.52 0.18	1.64 0.04
2.95 0.03	5.53 0.42	2.41 0.24	2.28 0.21	1.58 0.16	1.72 0.02
3.61 0.04	6.41 0.62	2.46 0.31	2.26 0.29	1.46 0.20	1.60 0.03
3.76 0.05	6.60 0.87	2.77 0.49	2.52 0.34	1.60 0.26	1.71 0.00

TABLE IV-5(f)

200 GEV/C PROTON MULTIPLICITIES

NU BAR	PSEUDORAPIDITY RANGE				
	-0.38 1.34	1.47 2.20	2.30 3.07	3.19 3.97	4.06 7.00
1.00 0.00	0.22 0.12	0.66 0.13	1.13 0.16	1.27 0.17	2.54 0.30
1.37 0.01	0.82 0.03	1.02 0.03	1.52 0.04	1.51 0.04	2.78 0.04
1.50 0.01	1.06 0.01	1.21 0.02	1.70 0.02	1.65 0.02	2.87 0.03
1.92 0.01	1.65 0.04	1.61 0.05	2.05 0.05	1.96 0.05	3.17 0.08
2.29 0.02	1.84 0.12	1.79 0.13	2.23 0.14	1.93 0.12	3.21 0.12
2.50 0.02	2.34 0.15	2.03 0.13	2.42 0.14	2.22 0.14	3.39 0.28
2.45 0.03	2.17 0.09	1.93 0.12	2.25 0.10	2.01 0.08	3.25 0.08
2.84 0.03	2.62 0.22	2.38 0.24	2.47 0.22	2.24 0.17	3.26 0.20
2.95 0.03	2.72 0.13	2.29 0.18	2.54 0.16	2.20 0.12	2.92 0.15
3.47 0.04	3.90 0.33	2.81 0.30	3.03 0.27	2.27 0.23	3.33 0.03
3.61 0.04	4.26 0.12	3.12 0.14	3.10 0.11	2.47 0.08	3.45 0.13
3.76 0.05	4.71 0.17	3.48 0.16	3.32 0.14	2.59 0.11	3.25 0.18

TABLE IV-5(g)

200 GEV/C PROTON MULTIPLICITIES

NU BAR	PSEUDORAPIDITY RANGE				
	-0.67 0.72	1.16 1.85	2.17 2.94	3.14 3.92	5.29 7.00
1.00 0.00	0.10 0.11	0.75 0.14	1.31 0.21	1.46 0.19	0.97 0.16
1.50 0.01	0.45 0.02	0.87 0.03	1.61 0.04	1.65 0.04	0.89 0.03
2.50 0.02	1.26 0.06	1.78 0.11	2.55 0.14	2.26 0.10	0.93 0.06
2.95 0.03	1.61 0.08	2.07 0.15	2.61 0.14	2.32 0.10	0.95 0.06
3.61 0.04	2.40 0.09	2.95 0.20	3.12 0.16	2.54 0.11	1.07 0.06

TABLE IV-5(h)

200 GEV/C PROTON MULTIPLICITIES

NU BAR	PSEUDORAPIDITY RANGE				
	0.56 2.35	2.13 2.90	2.65 3.42	2.35 4.13	4.16 7.00
1.00 0.00	2.14 0.41	1.25 0.28	1.38 0.30	1.31 0.28	2.50 0.09
1.37 0.01	2.38 0.05	1.37 0.05	1.65 0.04	1.55 0.04	2.52 0.07
1.50 0.01	2.62 0.07	1.51 0.06	1.74 0.06	1.66 0.06	2.51 0.03
1.92 0.02	3.45 0.10	1.88 0.09	2.12 0.08	1.89 0.07	2.68 0.11
2.50 0.02	4.70 0.15	2.33 0.11	2.49 0.10	2.15 0.08	2.84 0.15
2.95 0.03	5.51 0.17	2.60 0.14	2.66 0.11	2.16 0.08	3.00 0.12
3.61 0.04	6.02 0.31	3.04 0.26	2.89 0.20	2.29 0.15	3.09 0.04
3.76 0.05	7.16 0.26	2.97 0.19	2.94 0.13	2.32 0.11	3.02 0.17

TABLE IV-5(i)

200 GEV/C ANTI-PROTON MULTIPLICITIES

NU BAR	PSEUDORAPIDITY RANGE				
	-0.39	1.47	2.30	3.19	4.06
	1.34	2.20	3.07	3.97	7.00
1.37	0.78	1.05	1.60	1.44	3.18
0.01	0.34	0.34	0.44	0.46	0.05
1.50	0.78	1.00	1.47	1.58	2.91
0.01	0.16	0.13	0.18	0.18	0.38
1.92	1.82	1.09	1.38	1.94	3.70
0.01	0.46	0.35	0.47	0.47	0.20
2.50	2.83	2.71	3.48	1.61	2.72
0.02	1.70	1.29	1.49	0.96	0.54
2.75	3.64	3.42	3.29	2.65	3.45
0.03	1.40	1.20	1.22	0.96	0.23
3.61	3.17	2.82	2.10	1.15	1.09
0.04	1.43	1.04	1.00	0.62	1.47
3.76	6.21	2.68	1.37	2.23	2.91
0.05	2.93	1.79	1.74	1.31	1.34

TABLE IV-5(j)

200 GEV/C ANTI-PROTON MULTIPLICITIES

NU BAR	PSEUDORAPIDITY RANGE				
	-0.67	1.16	2.17	3.14	5.29
	0.72	1.85	2.94	3.97	7.00
1.50	1.01	0.71	1.49	1.56	1.19
0.01	0.20	0.18	0.28	0.29	0.29
2.50	0.99	1.99	1.78	2.52	0.93
0.02	0.97	0.79	1.01	1.03	0.10
2.95	2.33	2.30	3.03	2.17	1.15
0.03	0.75	0.85	1.05	0.88	0.50
3.61	3.44	3.64	4.01	2.38	1.96
0.04	0.75	0.91	0.97	0.68	0.51

TABLE IV-5(k)

50 GEV/C K-PLUS MULTIPLICITIES

NU BAR	PSEUDORAPIDITY RANGE				
	-0.38 1.34	1.47 2.20	2.30 3.07	3.19 3.97	4.06 7.00
1.19 0.02	0.83 0.29	0.90 0.21	1.26 0.28	1.04 0.21	1.04 0.19
1.75 0.04	2.37 0.60	1.28 0.36	1.75 0.40	1.36 0.30	1.48 0.52
1.98 0.05	2.88 0.64	1.38 0.41	1.73 0.42	1.15 0.28	1.64 0.55
2.30 0.08	3.81 1.11	1.76 0.64	1.87 0.56	1.11 0.35	1.37 0.34

TABLE IV-5(l)

50 GEV/C K-PLUS MULTIPLICITIES

NU BAR	PSEUDORAPIDITY RANGE				
	-0.67 0.72	1.16 1.85	2.17 2.94	3.14 3.92	5.29 7.00
1.19 0.02	0.37 0.18	1.14 0.19	1.41 0.26	1.24 0.21	0.31 0.01
1.75 0.04	0.94 0.33	1.47 1.32	1.62 0.34	1.45 0.27	0.45 0.33
2.30 0.08	1.91 0.61	2.18 0.63	1.81 0.53	1.30 0.34	0.42 0.20

TABLE IV-5(m)

100 GEV/C K-PLUS MULTIPLICITIES

NU BAR	PSEUDORAPIDITY RANGE				
	-0.38 1.34	1.47 2.70	2.30 3.07	3.19 3.97	4.06 7.00
1.10 0.02	0.71 0.10	0.86 0.08	1.22 0.11	1.19 0.11	1.90 0.25
1.19 0.02	0.90 0.06	0.90 0.05	1.26 0.06	1.30 0.06	2.06 0.11
1.43 0.02	1.30 0.13	1.06 0.09	1.47 0.11	1.24 0.10	2.25 0.24
1.75 0.04	1.97 0.37	1.79 0.26	1.75 0.29	1.46 0.24	1.83 0.64
1.74 0.05	2.07 0.35	1.75 0.25	1.76 0.28	1.65 0.23	2.55 0.41
1.98 0.05	2.57 0.31	1.79 0.21	2.03 0.21	1.54 0.17	1.97 0.36
2.30 0.08	3.96 0.37	2.05 0.23	2.15 0.23	1.78 0.17	2.11 0.36
2.38 0.09	4.01 0.73	2.24 0.42	2.41 0.40	1.57 0.29	1.54 0.69

TABLE IV-5(n)

100 GEV/C K-PLUS MULTIPLICITIES

NU BAR	PSEUDORAPIDITY RANGE				
	-0.67 0.72	1.16 1.85	2.17 2.94	3.14 3.92	5.29 7.00
1.19 0.02	0.41 0.08	0.62 0.07	1.17 0.11	1.06 0.10	0.41 0.10
1.75 0.04	0.64 0.36	0.76 0.30	1.54 0.39	1.36 0.35	0.70 0.04
2.30 0.08	2.03 0.27	1.56 0.24	1.97 0.25	1.64 0.20	0.38 0.19
2.38 0.09	1.96 0.42	2.01 0.42	2.00 0.38	1.87 0.32	0.37 0.25

TABLE IV-5(o)

50 GEV/C PI-PLUS MULTIPLICITIES

NU BAR	PSEUDORAPIDITY RANGE				
	-0.38	1.47	2.30	3.19	4.06
	1.34	2.20	3.07	3.97	7.00
1.00	0.84	1.25	1.74	1.54	0.99
0.00	0.23	0.23	0.31	0.24	0.29
1.36	1.06	1.05	1.35	1.14	1.05
0.02	0.04	0.04	0.05	0.05	0.01
2.14	2.20	1.64	1.78	1.30	1.13
0.04	0.09	0.08	0.08	0.06	0.09
2.48	2.55	1.74	1.80	1.19	1.14
0.06	0.11	0.10	0.08	0.05	0.08
2.96	3.52	2.02	1.86	1.15	1.13
0.09	0.17	0.16	0.10	0.07	0.02

TABLE IV-5(p)

50 GEV/C PI-PLUS MULTIPLICITIES

NU BAR	PSEUDORAPIDITY RANGE				
	-0.67	1.16	2.17	3.14	5.29
	0.72	1.85	2.94	3.92	7.00
1.00	0.13	0.75	1.46	1.26	0.32
0.00	0.16	0.19	0.29	0.28	0.01
1.36	0.48	0.91	1.41	1.15	0.25
0.02	0.03	0.04	0.05	0.05	0.01
2.14	1.98	1.48	1.83	1.29	0.34
0.04	0.06	0.07	0.08	0.06	0.05
2.96	2.04	2.15	1.96	1.21	0.32
0.09	0.10	0.19	0.10	0.06	0.01

TABLE IV-5(q)

100 GEV/C PI-PLUS MULTIPLICITIES

NU BAR	PSEUDORAPIDITY RANGE				
	-0.38 1.34	1.47 2.20	2.30 3.07	3.19 3.97	4.06 7.00
1.00 0.00	0.63 0.14	0.98 0.14	1.33 0.17	1.41 0.19	2.21 0.27
1.26 0.02	0.96 0.03	1.02 0.03	1.39 0.03	1.38 0.03	1.90 0.06
1.36 0.02	1.01 0.01	1.06 0.02	1.42 0.02	1.41 0.02	1.95 0.03
1.70 0.02	1.40 0.03	1.27 0.03	1.67 0.03	1.54 0.03	2.21 0.05
2.14 0.04	1.75 0.07	1.61 0.07	1.77 0.08	1.58 0.07	1.63 0.15
2.17 0.05	2.10 0.07	1.66 0.09	1.99 0.10	1.66 0.07	2.49 0.11
2.48 0.06	2.66 0.07	1.98 0.06	2.09 0.06	1.75 0.05	2.26 0.09
2.96 0.09	2.54 0.09	2.36 0.09	2.27 0.07	1.81 0.05	1.95 0.06
3.07 0.10	3.74 0.18	2.35 0.13	2.29 0.11	1.83 0.09	2.36 0.16

TABLE IV-5(r)

100 GEV/C PI-PLUS MULTIPLICITIES

NU BAR	PSEUDORAPIDITY RANGE				
	-0.67 0.72	1.16 1.85	2.17 2.94	3.14 3.92	5.29 7.00
1.00 0.00	0.18 0.12	0.75 0.13	1.40 0.19	1.51 0.20	0.72 0.14
1.36 0.02	0.48 0.02	0.83 0.02	1.42 0.04	1.44 0.03	0.45 0.02
2.14 0.04	1.07 0.09	1.18 0.10	1.84 0.13	1.67 0.11	0.63 0.03
2.96 0.09	2.03 0.07	2.17 0.11	2.28 0.08	1.74 0.06	0.61 0.04
3.07 0.10	2.38 0.11	2.47 0.17	2.44 0.12	1.86 0.09	0.62 0.06

TABLE IV-5(s)

100 GEV/C PI-PLUS MULTIPLICITIES

NU BAR	PSEUDORAPIDITY RANGE				
	0.56	2.13	2.65	2.35	4.16
	2.35	2.90	3.42	4.13	7.00
1.00	1.60	1.10	1.24	1.00	2.31
0.00	0.63	0.35	0.40	0.41	0.15
1.26	2.34	1.39	1.56	1.40	1.83
0.02	0.09	0.06	0.07	0.06	0.02
1.36	2.56	1.36	1.63	1.42	1.75
0.02	0.11	0.08	0.08	0.09	0.03
1.98	3.46	1.41	1.64	1.52	2.06
0.03	0.39	0.18	0.17	0.19	0.08
2.14	3.96	1.93	2.03	1.67	2.11
0.04	0.31	0.17	0.18	0.16	0.01
2.48	4.49	2.03	2.02	1.67	2.29
0.06	0.28	0.17	0.16	0.13	0.15
2.96	4.60	1.82	1.82	1.45	2.17
0.09	0.40	0.23	0.18	0.15	0.00
3.07	5.54	2.17	2.13	1.69	2.34
0.10	0.59	0.28	0.26	0.22	0.04

TABLE IV-5(t)

200 GEV/C PI-PLUS MULTIPLICITIES

NU BAR	PSEUDORAPIDITY RANGE				
	-0.38	1.47	2.30	3.10	4.06
	1.34	2.20	3.07	3.97	7.00
1.00	0.16	0.17	0.07	0.61	2.85
0.00	0.42	0.19	0.21	0.23	1.29
1.26	1.07	1.03	1.51	1.53	3.45
0.02	0.11	0.08	0.11	0.12	0.10
1.36	0.96	1.02	1.48	1.61	3.38
0.02	0.04	0.03	0.04	0.05	0.11
1.70	1.51	1.25	1.92	1.88	3.95
0.02	0.12	0.10	0.13	0.13	0.29
1.98	1.60	1.34	1.53	1.65	4.04
0.03	0.30	0.28	0.32	0.31	0.44
2.14	2.16	1.74	2.11	2.03	4.52
0.04	0.44	0.31	0.38	0.35	1.07
2.12	2.36	1.86	2.24	2.11	4.11
0.05	0.29	0.24	0.26	0.24	0.14
2.40	2.42	1.95	2.22	2.24	4.10
0.06	0.65	0.50	0.52	0.51	0.08
2.48	2.31	1.77	2.32	1.67	3.54
0.06	0.39	0.30	0.34	0.29	0.55
2.86	2.71	2.03	2.49	2.73	4.38
0.09	0.36	0.60	0.63	0.57	0.41
2.96	3.69	2.59	2.51	2.26	3.79
0.09	0.31	0.22	0.22	0.18	0.40
3.07	3.97	3.12	2.79	2.64	4.52
0.10	0.47	0.34	0.31	0.27	0.64

TABLE IV-5(u)

200 GEV/C PI-PLUS MULTIPLICITIES

NU BAR	PSEUDORAPIDITY RANGE				
	-0.67 0.72	1.16 1.33	2.17 2.94	3.14 3.92	5.29 7.00
1.00 0.00	-0.15 0.43	0.30 0.17	0.90 0.31	1.18 0.32	-0.04 0.71
1.36 0.02	0.44 0.08	0.86 0.06	1.52 0.10	1.61 0.11	1.13 0.12
2.14 0.04	1.01 0.11	1.39 0.18	2.04 0.22	2.18 0.23	1.25 0.21
2.48 0.06	1.49 0.33	1.80 0.36	2.36 0.42	2.09 0.37	1.21 0.21
2.96 0.09	1.94 0.25	1.77 0.25	1.66 0.24	1.82 0.22	1.15 0.22

TABLE IV-5(v)

200 GEV/C PI-PLUS MULTIPLICITIES

NU BAR	PSEUDORAPIDITY RANGE				
	0.56 2.35	2.13 2.90	2.65 3.42	2.35 4.13	4.16 7.00
1.00 0.00	2.80 1.39	0.71 0.39	1.75 0.43	1.48 0.42	2.72 0.64
1.26 0.02	2.27 0.18	1.34 0.10	1.47 0.11	1.52 0.12	3.11 0.26
1.36 0.02	2.38 0.23	1.38 0.13	1.59 0.15	1.50 0.15	3.25 0.19
1.70 0.02	3.10 0.30	1.62 0.17	1.90 0.18	1.76 0.18	3.27 0.42
2.14 0.04	4.06 0.43	2.05 0.22	2.02 0.22	1.84 0.20	3.84 0.47
2.48 0.06	5.18 0.48	2.22 0.23	2.70 0.23	1.97 0.21	3.82 0.45
2.96 0.09	6.52 0.88	2.67 0.44	3.17 0.43	2.01 0.34	3.83 0.09
3.07 0.10	6.95 0.75	2.80 0.33	3.37 0.34	2.10 0.27	3.82 0.60

TABLE IV-5(w)

200 GEV/C PI-MINUS MULTIPLICITIES

NU BAR	PSEUDORAPIDITY RANGE				
	-0.38	1.47	2.30	3.19	4.06
	1.34	2.20	3.07	3.97	7.00
1.00	0.54	0.96	1.28	1.44	3.55
0.00	0.12	0.12	0.15	0.16	0.34
1.26	0.84	0.75	1.35	1.49	3.18
0.02	0.03	0.04	0.05	0.06	0.01
1.36	0.94	1.01	1.42	1.50	3.11
0.02	0.01	0.01	0.02	0.02	0.03
1.70	1.44	1.37	1.79	1.76	3.48
0.02	0.04	0.04	0.05	0.05	0.05
2.14	2.16	1.68	2.14	2.08	3.48
0.04	0.13	0.11	0.12	0.12	0.21
2.48	2.56	1.88	2.20	1.98	3.84
0.06	0.11	0.12	0.11	0.09	0.17
2.96	3.62	2.52	2.54	2.26	3.70
0.09	0.11	0.12	0.09	0.08	0.14
3.07	4.20	2.82	2.80	2.43	4.00
0.10	0.22	0.20	0.17	0.14	0.01

TABLE IV-5(x)

200 GEV/C PI-MINUS MULTIPLICITIES

NU BAR	PSEUDORAPIDITY RANGE				
	-0.67	1.16	2.17	3.14	5.27
	0.72	1.85	2.74	3.92	7.00
1.00	0.15	0.51	0.90	0.93	1.09
0.00	0.10	0.11	0.15	0.17	0.16
1.36	0.42	0.81	1.46	1.61	1.06
0.02	0.02	0.02	0.03	0.03	0.03
2.14	0.97	1.37	1.97	1.79	1.07
0.04	0.10	0.10	0.10	0.12	0.08
2.48	1.33	1.61	2.16	2.02	1.12
0.06	0.06	0.11	0.11	0.09	0.00
2.96	1.93	2.30	2.53	2.12	1.18
0.09	0.06	0.11	0.09	0.06	0.05

TABLE IV-6(a)

MULTIPLICITIES IN PROTON-NUCLEUS INTERACTIONS AT 50 GEV/C

NU BAR	PSEUDORAPIDITY RANGE												AV MULT
	-0.57 -0.38	-0.38 0.56	0.56 0.92	0.92 1.39	1.39 1.99	1.99 2.25	2.25 2.76	2.76 3.08	3.08 3.38	3.38 4.08	4.08 5.28	5.28 7.00	
1.03 0.0	-0.06 0.12	0.0 0.24	0.17 0.15	0.56 0.15	1.23 0.19	0.46 0.11	0.56 0.15	0.36 0.10	0.44 0.09	1.02 0.16	0.64 0.16	0.29 0.03	5.69 0.51
1.50 0.01	0.04 0.03	0.35 0.36	0.26 0.04	0.52 0.06	0.94 0.09	0.49 0.05	1.01 0.10	0.59 0.06	0.46 0.04	0.85 0.07	0.64 0.11	0.26 0.01	6.40 0.23
2.50 0.02	0.14 0.06	0.93 0.12	0.57 0.08	0.98 0.12	1.55 0.15	0.69 0.08	1.26 0.13	0.71 0.08	0.56 0.05	0.97 0.09	0.60 0.23	0.31 0.07	9.27 0.43
3.61 0.04	0.24 0.10	1.60 0.23	0.92 0.15	1.52 0.21	2.28 0.27	0.89 0.12	1.36 0.16	0.70 0.10	0.51 0.06	0.80 0.10	0.59 0.24	0.26 0.02	11.67 0.57

TABLE IV-6(b)

MULTIPLICITIES IN PROTON-NUCLEUS INTERACTIONS AT 100 GEV/C

NU BAR	PSEUDORAPIDITY RANGE												AV MULT
	-0.67 -0.38	-0.38 0.56	0.56 0.92	0.92 1.39	1.39 1.99	1.99 2.25	2.25 2.76	2.76 3.08	3.08 3.38	3.38 4.08	4.08 5.28	5.28 7.00	
1.00 0.0	-0.01 0.04	0.05 0.08	0.24 0.09	0.52 0.16	0.93 0.19	0.47 0.10	0.97 0.14	0.57 0.12	0.51 0.11	1.14 0.16	1.33 0.20	0.56 0.08	7.35 0.46
1.50 0.01	0.05 0.01	0.34 0.03	0.26 0.03	0.55 0.05	0.98 0.06	0.50 0.04	1.04 0.06	0.67 0.05	0.59 0.04	1.17 0.06	1.06 0.06	0.49 0.02	7.72 0.16
2.50 0.02	0.13 0.05	0.82 0.09	0.55 0.07	1.04 0.12	1.71 0.15	0.78 0.08	1.47 0.11	0.87 0.08	0.75 0.07	1.42 0.10	0.96 0.10	0.51 0.03	11.33 0.32
3.61 0.04	0.27 0.05	1.65 0.12	0.93 0.09	1.65 0.17	2.52 0.20	1.05 0.10	1.76 0.12	1.00 0.09	0.83 0.07	1.44 0.10	1.09 0.09	0.55 0.03	14.75 0.38
3.76 0.05	0.32 0.07	1.87 0.16	1.00 0.12	1.74 0.21	2.69 0.25	1.13 0.13	1.89 0.17	1.07 0.10	0.85 0.09	1.53 0.12	1.34 0.12	0.48 0.04	15.94 0.53

TABLE IV-6(c)

MULTIPLICITIES IN PROTON-NUCLEUS INTERACTIONS AT 200 GEV/C

NU BAR	PSEUDORAPIDITY RANGE												AV MULT
	-0.57 -0.33	-0.33 0.56	0.56 0.92	0.92 1.39	1.39 1.69	1.69 2.25	2.25 2.76	2.76 3.09	3.09 3.38	3.38 4.08	4.08 5.26	5.29 7.00	
1.00 0.0	-0.01 0.04	0.0 0.07	0.15 0.05	0.37 0.10	0.71 0.12	0.37 0.07	0.81 0.12	0.56 0.09	0.54 0.08	1.23 0.14	1.57 0.22	0.98 0.10	7.29 0.33
1.50 0.01	0.04 0.01	0.32 0.03	0.27 0.02	0.53 0.04	0.96 0.05	0.51 0.03	1.08 0.06	0.72 0.04	0.67 0.04	1.50 0.07	1.82 0.11	0.90 0.03	9.34 0.18
2.50 0.02	0.14 0.03	0.87 0.06	0.58 0.05	1.06 0.09	1.76 0.12	0.84 0.07	1.64 0.11	1.05 0.08	0.94 0.07	1.99 0.11	2.21 0.20	0.94 0.04	14.01 0.34
2.95 0.03	0.19 0.04	1.07 0.09	0.68 0.06	1.25 0.11	2.02 0.14	0.93 0.08	1.74 0.12	1.09 0.08	0.93 0.07	1.99 0.11	2.04 0.16	0.97 0.05	14.95 0.34
3.61 0.04	0.28 0.05	1.69 0.12	0.97 0.08	1.74 0.15	2.71 0.19	1.18 0.09	2.09 0.14	1.25 0.09	1.09 0.08	2.16 0.12	2.23 0.15	1.05 0.05	18.47 0.40

TABLE IV-6(d)

MULTIPLICITIES IN ANTI PROTON-NUCLEUS INTERACTIONS AT 200 GEV/C

NU BAR	PSEUDORAPIDITY RANGE												AV MULT
	-0.67 -0.33	-0.33 0.56	0.56 0.92	0.92 1.39	1.39 1.69	1.69 2.25	2.25 2.76	2.76 3.09	3.09 3.38	3.38 4.08	4.08 5.28	5.28 7.00	
1.50 0.01	0.14 0.08	0.55 0.12	0.28 0.07	0.42 0.11	0.77 0.14	0.45 0.10	0.98 0.19	0.65 0.12	0.63 0.12	1.43 0.22	1.69 0.71	1.20 0.22	9.19 0.65
2.50 0.02	0.09 0.34	0.82 0.80	0.60 0.51	1.22 0.60	2.09 0.87	0.91 0.51	1.75 0.87	1.06 0.59	0.92 0.46	1.79 0.81	1.27 0.79	0.94 0.08	13.47 2.23
2.95 0.03	0.29 0.27	1.53 0.64	0.87 0.42	1.47 0.58	2.59 0.86	1.22 0.50	2.16 0.81	1.26 0.54	1.06 0.42	2.10 0.76	2.27 0.82	1.16 0.36	17.35 2.12
3.61 0.04	0.42 0.27	1.78 0.66	1.04 0.44	1.82 0.61	3.00 0.84	1.29 0.45	2.13 0.72	1.14 0.47	0.92 0.30	1.40 0.53	-0.88 2.19	1.97 0.38	16.04 2.33

TABLE IV-6(e)

MULTIPLICITIES IN KAON-NUCLEUS INTERACTIONS AT 50 GEV/C

NU BAR	PSEUDORAPIDITY RANGE												AV MULT
	-0.67 -0.38	-0.38 0.56	0.56 0.92	0.92 1.39	1.39 1.99	1.99 2.25	2.25 2.76	2.76 3.06	3.06 3.38	3.38 4.08	4.08 5.28	5.28 7.00	
~~1.19~~ 0.02	0.02 0.05	0.24 0.14	0.23 0.09	0.52 0.13	0.90 0.18	0.43 0.11	0.89 0.20	0.56 0.13	0.50 0.10	1.00 0.18	0.72 0.28	0.31 0.01	6.31 0.52
1.75 0.04	0.10 0.09	0.83 0.26	0.51 0.21	0.86 0.70	1.26 0.86	0.57 0.19	1.12 0.25	0.69 0.17	0.61 0.14	1.23 0.24	1.02 0.74	0.46 0.03	9.26 1.45
2.30 0.08	0.23 0.22	1.53 0.52	0.85 0.34	1.33 0.43	1.80 0.54	0.71 0.26	1.24 0.39	0.70 0.26	0.56 0.16	1.02 0.28	0.94 0.56	0.42 0.15	11.35 1.29

TABLE IV-6(f)

MULTIPLICITIES IN KAON-NUCLEUS INTERACTIONS AT 100 GEV/C

NU BAR	PSEUDORAPIDITY RANGE												AV MULT
	-0.67 -0.38	-0.38 0.56	0.56 0.92	0.92 1.39	1.39 1.99	1.99 2.25	2.25 2.76	2.76 3.06	3.06 3.38	3.38 4.08	4.08 5.28	5.28 7.00	
1.19 0.02	0.04 0.03	0.30 0.05	0.20 0.05	0.37 0.05	0.69 0.07	0.39 0.05	0.82 0.09	0.53 0.06	0.47 0.05	1.07 0.09	1.64 0.26	0.41 0.07	6.92 0.33
1.75 0.04	0.08 0.13	0.60 0.23	0.32 0.14	0.41 0.18	1.16 0.25	0.60 0.15	1.12 0.26	0.68 0.17	0.61 0.14	1.24 0.23	1.12 0.91	0.71 0.04	8.89 1.10
2.30 0.05	0.27 0.10	1.64 0.21	0.83 0.14	1.16 0.17	1.64 0.22	0.75 0.12	1.39 0.19	0.84 0.13	0.73 0.10	1.51 0.17	1.77 0.59	0.39 0.14	12.92 0.79
2.39 0.09	0.24 0.15	1.53 0.36	0.86 0.23	1.34 0.30	1.93 0.37	0.82 0.19	1.48 0.29	0.88 0.17	0.76 0.15	1.49 0.26	1.16 1.03	0.39 0.18	12.73 1.33

TABLE IV-6(g)

MULTIPLICITIES IN PI PLUS-NUCLEUS INTERACTIONS AT 50 GEV/C

NU BAR	PSEUDORAPIDITY RANGE												AV MULT
	-0.67 -0.36	-0.36 0.55	0.55 0.92	0.92 1.39	1.39 1.99	1.99 2.25	2.25 2.76	2.76 3.08	3.08 3.38	3.38 4.03	4.03 5.28	5.28 7.00	
1.00 0.0	0.0 0.06	0.13 0.12	0.17 0.06	0.41 0.12	0.91 0.18	0.51 0.12	1.06 0.22	0.68 0.15	0.61 0.12	1.22 0.22	0.66 0.41	0.33 0.01	5.73 0.63
1.36 0.02	0.05 0.01	0.34 0.03	0.25 0.02	0.49 0.05	0.90 0.07	0.46 0.04	0.93 0.07	0.57 0.05	0.50 0.04	1.00 0.07	0.60 0.08	0.25 0.01	5.54 0.18
2.14 0.04	0.26 0.05	1.17 0.02	0.59 0.05	0.90 0.08	1.40 0.11	0.66 0.06	1.23 0.10	0.72 0.07	0.59 0.05	1.11 0.08	0.78 0.17	0.34 0.04	9.76 0.33
2.96 0.09	0.23 0.05	1.48 0.12	0.82 0.08	1.31 0.15	1.91 0.20	0.78 0.08	1.31 0.11	0.72 0.07	0.56 0.05	0.99 0.08	0.61 0.09	0.32 0.01	11.26 0.35

TABLE IV-6(h)

MULTIPLICITIES IN PI PLUS-NUCLEUS INTERACTIONS AT 100 GEV/C

NU BAR	PSEUDORAPIDITY RANGE												AV MULT
	-0.67 -0.36	-0.36 0.56	0.56 0.92	0.92 1.39	1.39 1.99	1.99 2.25	2.25 2.76	2.76 3.08	3.08 3.38	3.38 4.03	4.03 5.28	5.28 7.00	
1.00 0.0	0.09 0.04	0.33 0.05	0.20 0.05	0.38 0.13	0.72 0.15	0.40 0.08	0.65 0.12	0.58 0.10	0.55 0.10	1.19 0.17	1.56 0.20	0.73 0.07	7.58 0.42
1.36 0.02	0.03 0.01	0.33 0.02	0.27 0.02	0.52 0.04	0.90 0.05	0.46 0.03	0.94 0.06	0.64 0.04	0.60 0.04	1.29 0.06	1.42 0.07	0.46 0.02	7.86 0.15
2.14 0.04	0.13 0.04	0.76 0.07	0.47 0.05	0.82 0.09	1.35 0.11	0.65 0.06	1.25 0.09	0.79 0.07	0.72 0.06	0.47 0.09	1.24 0.10	0.64 0.02	10.29 0.26
2.96 0.09	0.25 0.05	1.48 0.10	0.76 0.07	1.30 0.12	1.96 0.14	0.84 0.07	1.44 0.10	0.86 0.07	0.75 0.06	1.47 0.09	1.48 0.09	0.62 0.03	13.21 0.30
3.07 0.10	0.29 0.06	1.62 0.13	0.95 0.09	1.46 0.16	2.17 0.19	0.91 0.09	1.56 0.12	0.93 0.09	0.81 0.07	1.59 0.11	1.76 0.13	0.53 0.04	14.57 0.39

TABLE IV-6(i)

MULTIPLICITIES IN PI PLUS-NUCLEUS INTERACTIONS AT 200 GEV/C

NU BAR	PSEUDORAPIDITY RANGE												AV MULT
	-0.67 -0.37	-0.36 0.55	0.56 0.91	0.92 1.38	1.39 1.49	1.49 2.25	2.25 2.75	2.76 3.06	3.08 3.39	3.33 4.04	4.03 5.28	5.28 7.00	
1.00 0.0	-0.03 0.15	-0.05 0.27	0.15 0.18	0.32 0.27	0.50 0.30	0.26 0.15	0.55 0.16	0.50 0.12	0.45 0.12	1.02 0.21	2.85 0.88	-0.03 0.41	5.43 1.17
1.36 0.02	0.04 0.03	0.33 0.05	0.25 0.03	0.49 0.06	0.88 0.07	0.46 0.04	0.97 0.07	0.66 0.05	0.63 0.05	1.44 0.09	2.21 0.19	1.15 0.08	9.45 0.27
2.14 0.04	0.11 0.04	0.77 0.13	0.50 0.10	0.69 0.14	1.46 0.18	0.70 0.10	1.38 0.16	0.80 0.12	0.81 0.11	1.84 0.19	2.99 0.62	1.27 0.13	13.61 0.77
2.48 0.05	0.13 0.12	0.97 0.23	0.62 0.11	1.11 0.18	1.74 0.23	0.80 0.13	1.56 0.21	1.07 0.14	0.88 0.12	1.71 0.20	2.50 0.42	1.22 0.13	14.31 0.73
2.96 0.09	0.25 0.04	1.46 0.19	0.82 0.13	1.40 0.21	2.12 0.25	0.90 0.12	1.53 0.17	1.03 0.13	0.95 0.11	1.85 0.17	2.69 0.29	1.17 0.13	16.17 0.61

TABLE IV-6(j)

MULTIPLICITIES IN PI MINUS-NUCLEUS INTERACTIONS AT 200 GEV/C

NU BAR	PSEUDORAPIDITY RANGE												AV MULT
	-0.67 -0.37	-0.36 0.55	0.56 0.91	0.92 1.39	1.39 1.99	1.49 2.25	2.25 2.75	2.76 3.07	3.08 3.39	3.35 4.05	4.06 5.28	5.28 7.00	
1.00 0.0	0.01 0.04	0.10 0.07	0.12 0.04	0.30 0.07	0.65 0.10	0.36 0.06	0.71 0.12	0.48 0.05	0.44 0.05	1.11 0.15	2.43 0.60	1.10 0.13	7.81 0.67
1.36 0.02	0.04 0.01	0.29 0.02	0.22 0.02	0.44 0.04	0.83 0.06	0.45 0.04	0.94 0.07	0.64 0.05	0.61 0.05	1.43 0.09	2.03 0.24	1.07 0.04	8.99 0.29
2.14 0.04	0.11 0.04	0.76 0.08	0.47 0.05	0.83 0.09	1.39 0.13	0.69 0.07	1.36 0.12	0.88 0.08	0.82 0.08	1.64 0.15	2.38 0.41	1.08 0.07	12.60 0.52
2.48 0.06	0.15 0.03	0.92 0.08	0.50 0.05	0.98 0.10	1.59 0.14	0.76 0.08	1.45 0.13	0.91 0.03	0.82 0.07	1.80 0.13	2.69 0.37	1.14 0.04	13.36 0.48
2.96 0.09	0.23 0.04	1.41 0.10	0.83 0.07	1.40 0.13	2.20 0.18	0.97 0.09	1.70 0.13	1.03 0.09	0.92 0.07	1.95 0.13	2.49 0.35	1.20 0.06	16.31 0.49

MULTIPLICITIES IN PROTON NUCLEUS INTERACTIONS AT 50 GEV/C

TABLE IV-7(a)

NU BAR	PSEUDORAPIDITY RANGE												AV MULT
	-0.67 -0.33	-0.38 0.55	0.55 0.92	0.92 1.34	1.37 1.99	1.99 2.25	2.25 2.75	2.76 3.08	3.08 3.38	3.38 4.08	4.08 5.28	5.28 7.00	
1.00 0.00	-0.01 0.04	0.09 0.12	0.14 0.08	0.36 0.08	0.74 0.09	0.38 0.06	0.75 0.11	0.46 0.07	0.45 0.04	0.93 0.06	0.65 0.09	0.26 0.01	5.24 0.27
1.37 0.01	0.01 0.01	0.27 0.06	0.23 0.05	0.50 0.05	0.94 0.07	0.46 0.05	0.90 0.09	0.55 0.06	0.47 0.04	0.91 0.07	0.65 0.09	0.25 0.01	6.17 0.21
1.50 0.01	0.04 0.01	0.33 0.03	0.26 0.04	0.55 0.05	1.01 0.09	0.49 0.05	0.95 0.09	0.57 0.06	0.47 0.04	0.91 0.07	0.65 0.09	0.26 0.01	6.50 0.21
1.92 0.01	0.05 0.01	0.56 0.07	0.38 0.03	0.72 0.07	1.23 0.13	0.57 0.05	1.09 0.09	0.63 0.06	0.49 0.04	0.59 0.07	0.65 0.09	0.26 0.01	7.56 0.23
2.00 0.02	0.07 0.03	0.60 0.05	0.40 0.05	0.75 0.05	1.28 0.13	0.59 0.05	1.11 0.09	0.64 0.06	0.50 0.04	0.89 0.07	0.65 0.09	0.25 0.01	7.77 0.23
2.29 0.02	0.12 0.04	0.77 0.07	0.49 0.06	0.86 0.09	1.44 0.11	0.65 0.06	1.19 0.10	0.67 0.07	0.51 0.04	0.88 0.06	0.65 0.09	0.26 0.01	8.50 0.26
2.50 0.02	0.14 0.04	0.90 0.10	0.55 0.07	0.97 0.13	1.55 0.13	0.69 0.06	1.24 0.11	0.69 0.07	0.51 0.04	0.87 0.06	0.65 0.09	0.26 0.01	9.04 0.28
2.65 0.03	0.13 0.04	0.87 0.10	0.56 0.05	0.95 0.10	1.53 0.12	0.68 0.06	1.23 0.10	0.67 0.07	0.51 0.04	0.87 0.06	0.65 0.09	0.26 0.01	8.91 0.27
2.84 0.03	0.17 0.05	1.12 0.11	0.65 0.07	1.13 0.11	1.75 0.15	0.75 0.07	1.32 0.11	0.71 0.07	0.52 0.04	0.86 0.06	0.65 0.09	0.25 0.01	9.71 0.31
2.95 0.03	0.11 0.06	1.19 0.12	0.70 0.08	1.18 0.12	1.81 0.16	0.77 0.08	1.34 0.12	0.72 0.07	0.53 0.04	0.85 0.06	0.65 0.09	0.25 0.01	10.19 0.32
3.00 0.04	0.19 0.05	1.23 0.12	0.72 0.06	1.23 0.12	1.84 0.15	0.78 0.08	1.35 0.12	0.72 0.07	0.53 0.04	0.86 0.06	0.65 0.09	0.26 0.01	10.32 0.33
3.47 0.04	0.24 0.03	1.56 0.14	0.88 0.12	1.42 0.16	2.10 0.20	0.86 0.09	1.41 0.14	0.74 0.09	0.54 0.04	0.85 0.06	0.65 0.09	0.26 0.01	11.52 0.41
3.61 0.04	0.25 0.03	1.65 0.21	0.93 0.14	1.47 0.17	2.17 0.21	0.89 0.10	1.43 0.15	0.74 0.10	0.54 0.04	0.85 0.06	0.65 0.09	0.26 0.01	11.88 0.45
3.76 0.05	0.25 0.04	1.74 0.24	0.99 0.16	1.57 0.19	2.27 0.22	0.91 0.10	1.44 0.17	0.74 0.11	0.54 0.04	0.84 0.06	0.65 0.09	0.26 0.01	12.27 0.49
4.00 0.05	0.27 0.13	1.97 0.29	1.08 0.20	1.59 0.22	2.41 0.24	0.95 0.11	1.45 0.20	0.75 0.13	0.54 0.04	0.84 0.05	0.65 0.09	0.26 0.01	12.89 0.57

MULTIPLICITIES IN PROTON NUCLEUS INTERACTIONS AT 100 GEV/C

TABLE IV-7(b)

NU BAR	PSEUDORAPIDITY RANGE												AV MULT
	-0.67 -0.33	-0.33 0.56	0.55 0.92	0.92 1.34	1.39 1.99	1.99 2.25	2.25 2.75	2.76 3.08	3.08 3.38	3.38 4.08	4.08 5.28	5.23 7.00	
1.00 0.00	0.01 0.01	0.05 0.03	0.15 0.02	0.33 0.04	0.69 0.06	0.39 0.03	0.86 0.05	0.57 0.04	0.52 0.04	1.07 0.07	1.12 0.07	0.50 0.02	6.24 0.16
1.37 0.01	0.03 0.01	0.24 0.01	0.25 0.02	0.31 0.04	0.93 0.05	0.48 0.03	1.02 0.05	0.66 0.04	0.58 0.04	1.17 0.06	1.14 0.07	0.50 0.02	7.55 0.15
1.50 0.01	0.04 0.01	0.33 0.03	0.29 0.02	0.37 0.05	1.02 0.06	0.52 0.04	1.07 0.05	0.69 0.04	0.61 0.04	1.21 0.06	1.15 0.07	0.50 0.02	8.01 0.15
1.92 0.01	0.09 0.02	0.58 0.04	0.41 0.03	0.75 0.05	1.31 0.07	0.63 0.04	1.24 0.07	0.78 0.05	0.67 0.04	1.31 0.07	1.16 0.07	0.50 0.02	9.47 0.18
2.00 0.02	0.10 0.02	0.63 0.04	0.44 0.03	0.82 0.06	1.37 0.08	0.65 0.04	1.27 0.07	0.79 0.05	0.69 0.04	1.32 0.07	1.17 0.07	0.50 0.02	9.74 0.18
2.29 0.02	0.11 0.02	0.83 0.06	0.52 0.04	0.95 0.07	1.57 0.09	0.72 0.05	1.39 0.08	0.85 0.05	0.73 0.05	1.38 0.07	1.18 0.07	0.50 0.02	10.74 0.21
2.50 0.02	0.16 0.03	0.93 0.06	0.59 0.04	1.07 0.06	1.72 0.10	0.78 0.05	1.45 0.08	0.85 0.05	0.75 0.05	1.41 0.08	1.19 0.07	0.50 0.02	11.45 0.22
2.65 0.03	0.15 0.03	0.90 0.06	0.57 0.04	1.05 0.08	1.69 0.10	0.77 0.05	1.44 0.08	0.80 0.05	0.75 0.05	1.43 0.08	1.19 0.07	0.50 0.02	11.78 0.22
2.84 0.03	0.19 0.04	1.15 0.08	0.69 0.05	1.25 0.09	1.97 0.12	0.87 0.05	1.58 0.09	0.94 0.06	0.79 0.05	1.45 0.08	1.21 0.07	0.50 0.02	12.59 0.25
2.95 0.03	0.24 0.04	1.22 0.08	0.73 0.05	1.30 0.10	2.05 0.12	0.90 0.06	1.62 0.09	0.95 0.06	0.80 0.05	1.46 0.08	1.21 0.07	0.50 0.02	12.96 0.26
3.00 0.04	0.21 [illegible]	1.25 0.08	0.74 0.05	1.33 0.10	2.09 0.11	0.92 0.06	1.61 0.09	0.96 0.06	0.81 0.05	1.47 0.08	1.21 0.07	0.50 0.02	13.13 0.26
3.47 [illegible]	0.25 0.05	1.57 0.11	0.89 0.07	1.58 0.12	2.44 0.15	1.04 0.07	1.79 0.11	1.07 0.07	0.85 0.05	1.49 0.08	1.24 0.07	0.50 0.02	14.87 0.31
3.61 0.04	0.25 0.04	1.67 0.17	0.94 0.07	1.65 0.13	2.54 0.16	1.07 0.08	1.83 0.11	1.05 0.07	0.85 0.06	1.50 0.08	1.26 0.07	0.50 0.02	15.13 0.32
3.76 0.05	0.27 0.05	1.75 0.13	0.99 0.08	1.73 0.14	2.60 0.17	1.11 0.08	1.87 0.11	1.06 0.06	0.86 0.06	1.50 0.09	1.25 0.07	0.50 0.07	15.52 0.34
4.00 0.05	0.32 0.06	1.93 0.14	1.07 0.09	1.86 0.15	2.84 0.19	1.18 0.09	1.94 0.12	1.08 0.08	0.88 0.07	1.50 0.10	1.26 0.07	0.50 0.02	15.97 0.37

MULTIPLICITIES IN PROTON NUCLEUS INTERACTIONS AT 200 GEV/C

TABLE IV-7(c)

NJ BAR	PSEUDORAPIDITY RANGE												AV MULT
	-0.67 -0.34	-0.33 0.55	0.56 0.92	0.92 1.33	1.33 1.99	1.99 2.25	2.25 2.75	2.75 3.05	3.05 3.38	3.38 4.08	4.08 5.28	5.28 7.33	
1.00 0.00	0.0 0.07	-0.02 0.05	0.14 0.03	0.33 0.05	0.61 0.06	0.35 0.03	0.83 0.06	0.57 0.04	0.51 0.05	1.15 0.04	1.68 0.12	0.86 0.01	6.96 0.23
1.37 0.01	0.03 0.01	0.24 0.02	0.26 0.02	0.47 0.04	0.87 0.05	0.46 0.03	1.30 0.06	0.69 0.04	0.64 0.04	1.42 0.07	1.81 0.11	0.89 0.03	8.76 0.18
1.50 0.01	0.04 0.01	0.31 0.03	0.27 0.02	0.53 0.04	0.95 0.05	0.50 0.03	1.37 0.06	0.72 0.04	0.64 0.04	1.50 0.07	1.85 0.11	0.90 0.03	9.36 0.19
1.92 0.01	0.09 0.02	0.53 0.04	0.39 0.03	0.73 0.05	1.27 0.07	0.64 0.04	1.29 0.07	0.85 0.05	0.79 0.05	1.72 0.08	1.96 0.11	0.93 0.03	11.18 0.21
2.00 0.02	0.09 0.02	0.57 0.04	0.41 0.03	0.77 0.06	1.33 0.07	0.66 0.04	1.33 0.07	0.87 0.05	0.81 0.05	1.75 0.08	1.98 0.12	0.93 0.03	11.52 0.21
2.29 0.02	0.12 0.03	0.72 0.05	0.49 0.04	0.91 0.07	1.55 0.09	0.75 0.05	1.48 0.08	0.95 0.06	0.87 0.05	1.95 0.09	2.05 0.12	0.95 0.03	12.71 0.23
2.50 0.02	0.14 0.03	0.82 0.06	0.55 0.04	1.02 0.07	1.72 0.10	0.82 0.05	1.54 0.09	1.01 0.06	0.91 0.05	1.91 0.09	2.09 0.12	0.97 0.03	13.56 0.25
2.65 0.03	0.14 0.03	0.90 0.06	0.54 0.04	1.00 0.07	1.68 0.09	0.80 0.05	1.56 0.09	0.99 0.06	0.90 0.05	1.90 0.09	2.08 0.12	0.96 0.03	13.38 0.25
2.84 0.03	0.14 0.03	1.02 0.07	0.66 0.05	1.21 0.09	2.01 0.11	0.93 0.06	1.75 0.10	1.07 0.06	0.97 0.06	2.00 0.10	2.14 0.12	0.97 0.03	14.96 0.23
2.95 0.03	0.17 0.04	1.34 0.09	0.73 0.05	1.28 0.09	2.11 0.12	0.96 0.06	1.80 0.10	1.12 0.07	0.99 0.06	2.02 0.10	2.15 0.13	1.03 0.03	15.42 0.28
3.00 0.04	0.29 0.04	1.13 0.08	0.72 0.05	1.31 0.09	2.15 0.12	0.98 0.06	1.82 0.10	1.13 0.07	1.00 0.05	2.03 0.10	2.16 0.13	1.03 0.04	15.53 0.29
3.47 0.04	0.25 0.05	1.52 0.10	0.91 0.06	1.64 0.12	2.58 0.15	1.13 0.08	2.03 0.12	1.23 0.08	1.07 0.06	2.13 0.10	2.20 0.13	1.03 0.04	17.73 0.34
3.61 0.04	0.23 0.05	1.60 0.12	0.97 0.07	1.76 0.13	2.72 0.17	1.18 0.08	2.09 0.12	1.26 0.09	1.10 0.07	2.16 0.11	2.20 0.13	1.06 0.04	18.43 0.36
3.76 0.05	0.32 0.06	1.83 0.13	1.05 0.08	1.36 0.15	2.87 0.18	1.23 0.08	2.15 0.13	1.29 0.08	1.32 0.07	2.19 0.12	2.21 0.14	1.05 0.04	19.15 0.39
4.00 0.05	0.33 0.07	2.16 0.17	1.18 0.09	2.07 0.17	3.11 0.21	1.30 0.09	2.25 0.14	1.33 0.09	1.16 0.09	2.25 0.15	2.21 0.15	1.07 0.03	20.42 0.45

MULTIPLICITIES IN ANTI-PROTON NUCLEUS INTERACTIONS AT 200 GEV/C

TABLE IV-7(d)

NJ BAR	PSEUDORAPIDITY RANGE												AV MULT
	-0.67 -0.34	-0.33 0.55	0.56 0.92	0.92 1.34	1.33 1.99	1.99 2.25	2.25 2.75	2.75 3.05	3.05 3.39	3.38 4.08	4.08 5.28	5.28 7.33	
1.00 0.00	0.07 0.11	0.22 0.13	0.09 0.11	0.08 0.16	0.25 0.22	0.26 0.14	0.71 0.26	0.54 0.17	0.55 0.14	1.40 0.26	2.22 0.30	1.01 0.03	7.41 0.55
1.37 0.01	0.12 0.03	0.46 0.11	0.23 0.07	0.34 0.11	0.63 0.15	0.40 0.10	0.90 0.20	0.63 0.13	0.50 0.12	1.45 0.22	2.22 0.30	1.03 0.03	9.00 0.54
1.50 0.01	0.13 0.07	0.35 0.12	0.23 0.07	0.43 0.11	0.77 0.14	0.45 0.10	0.97 0.19	0.65 0.12	0.62 0.11	1.47 0.21	2.22 0.30	1.01 0.08	9.56 0.51
1.92 0.01	0.18 0.07	0.82 0.13	0.45 0.08	0.71 0.13	1.20 0.17	0.61 0.10	1.19 0.19	0.75 0.12	0.68 0.11	1.52 0.19	2.22 0.30	1.01 0.03	11.35 0.51
2.00 0.02	0.14 0.04	0.93 0.14	0.43 0.04	0.77 0.14	1.25 0.18	0.64 0.11	1.23 0.20	0.77 0.13	0.69 0.11	1.53 0.19	2.22 0.30	1.01 0.08	11.73 0.54
2.29 0.02	0.22 0.04	1.36 0.14	0.59 0.12	0.97 0.18	1.58 0.25	0.75 0.14	1.38 0.24	0.84 0.15	0.74 0.11	1.57 0.20	2.22 0.30	1.01 0.04	12.35 0.63
2.50 0.02	0.25 0.11	1.20 0.23	0.65 0.15	1.11 0.22	1.79 0.30	0.83 0.17	1.49 0.28	0.89 0.18	0.77 0.12	1.60 0.21	2.22 0.30	1.01 0.08	13.35 0.72
2.65 0.03	0.25 0.11	1.17 0.22	0.65 0.14	1.38 0.21	1.76 0.29	0.81 0.16	1.47 0.27	0.86 0.17	0.76 0.12	1.60 0.21	2.22 0.30	1.01 0.08	13.53 0.70
2.84 0.03	0.23 0.14	1.42 0.30	0.81 0.19	1.34 0.29	2.14 0.39	0.96 0.21	1.67 0.35	0.97 0.23	0.82 0.14	1.65 0.25	2.22 0.30	1.01 0.08	13.31 0.89
2.95 0.03	0.30 0.15	1.33 0.32	0.85 0.21	1.42 0.31	2.25 0.42	1.03 0.23	1.73 0.39	1.33 0.25	0.83 0.15	1.66 0.26	2.22 0.30	1.01 0.08	15.78 0.95
3.00 0.04	0.35 0.15	1.53 0.33	0.87 0.22	1.45 0.32	2.31 0.43	1.02 0.24	1.75 0.40	1.01 0.24	0.84 0.16	1.67 0.27	2.22 0.30	1.01 0.08	16.00 0.97
3.47 0.04	0.34 0.23	1.94 0.44	1.06 0.28	1.77 0.42	2.79 0.57	1.20 0.31	2.03 0.52	1.12 0.34	0.91 0.20	1.73 0.33	2.22 0.30	1.01 0.03	18.01 1.24
3.61 0.04	0.34 0.21	1.93 0.47	1.11 0.30	1.87 0.45	2.93 0.63	1.25 0.33	2.08 0.55	1.13 0.36	0.93 0.21	1.75 0.36	2.22 0.30	1.01 0.08	18.62 1.32
3.76 0.05	0.39 0.23	2.03 0.50	1.17 0.33	1.97 0.48	3.09 0.65	1.31 0.36	2.16 0.59	1.14 0.36	0.95 0.22	1.77 0.38	2.22 0.30	1.01 0.08	19.26 1.40
4.00 0.05	0.47 0.25	2.14 0.54	1.26 0.36	2.14 0.53	3.33 0.77	1.40 0.39	2.29 0.65	1.25 0.47	0.98 0.26	1.81 0.42	2.22 0.30	1.01 0.08	20.29 1.54

MULTIPLICITIES IN K-PLUS NUCLEUS INTERACTIONS AT 50 GEV/C

TABLE IV-7(e)

NU BAR	PSEUDORAPIDITY RANGE												AV MULT
	-0.67 -0.39	-0.38 0.55	0.55 0.92	0.92 1.33	1.33 1.99	1.99 2.25	2.25 2.75	2.75 3.08	3.08 3.38	3.38 4.08	4.08 5.28	5.28 7.00	
1.00 0.03	-0.01 0.08	0.02 0.14	0.13 0.12	0.38 0.17	0.75 0.22	0.35 0.13	0.82 0.24	0.54 0.16	0.51 0.08	1.10 0.13	0.87 0.23	0.31 0.01	5.82 0.56
1.10 0.02	0.00 0.07	0.13 0.16	0.18 0.10	0.45 0.15	0.83 0.20	0.41 0.12	0.85 0.22	0.55 0.14	0.52 0.08	1.09 0.13	0.87 0.23	0.31 0.01	6.22 0.51
1.19 0.02	0.02 0.06	0.21 0.14	0.23 0.09	0.52 0.13	0.90 0.18	0.43 0.11	0.93 0.20	0.57 0.12	0.52 0.08	1.09 0.13	0.87 0.23	0.31 0.01	6.58 0.43
1.43 0.02	0.06 0.05	0.30 0.12	0.36 0.08	0.69 0.13	1.03 0.17	0.49 0.09	0.97 0.16	0.62 0.10	0.53 0.05	1.08 0.13	0.87 0.23	0.31 0.01	7.55 0.44
1.64 0.03	0.09 0.07	0.73 0.15	0.47 0.10	0.86 0.17	1.25 0.21	0.56 0.09	1.04 0.16	0.62 0.10	0.54 0.03	1.07 0.13	0.87 0.23	0.31 0.01	8.40 0.48
1.75 0.04	0.11 0.03	0.85 0.17	0.53 0.11	0.92 0.20	1.33 0.25	0.57 0.10	1.08 0.17	0.65 0.11	0.55 0.06	1.06 0.13	0.87 0.23	0.31 0.01	8.94 0.53
1.74 0.05	0.11 0.03	0.86 0.17	0.52 0.11	0.91 0.20	1.33 0.26	0.57 0.10	1.08 0.17	0.65 0.11	0.55 0.06	1.06 0.13	0.87 0.23	0.31 0.01	8.80 0.53
1.92 0.05	0.14 0.10	1.04 0.22	0.62 0.14	1.04 0.25	1.47 0.31	0.61 0.13	1.14 0.20	0.67 0.13	0.56 0.08	1.05 0.13	0.87 0.23	0.31 0.01	9.53 0.62
1.95 0.05	0.15 0.11	1.10 0.23	0.65 0.16	1.08 0.27	1.51 0.33	0.63 0.14	1.16 0.21	0.67 0.14	0.56 0.08	1.05 0.13	0.87 0.23	0.31 0.01	9.77 0.66
2.00 0.06	0.15 0.11	1.13 0.24	0.65 0.16	1.10 0.27	1.53 0.34	0.63 0.14	1.17 0.22	0.68 0.14	0.56 0.08	1.05 0.13	0.87 0.23	0.31 0.01	9.85 0.67
2.24 0.09	0.19 0.13	1.39 0.31	0.79 0.21	1.27 0.35	1.72 0.43	0.69 0.18	1.25 0.28	0.72 0.14	0.57 0.09	1.04 0.13	0.87 0.23	0.31 0.01	10.82 0.83
2.30 0.08	0.20 0.15	1.45 0.33	0.82 0.22	1.31 0.37	1.77 0.45	0.70 0.19	1.27 0.30	0.72 0.19	0.58 0.08	1.04 0.13	0.87 0.23	0.31 0.01	11.06 0.89
2.38 0.09	0.21 0.17	1.54 0.36	0.86 0.24	1.37 0.39	1.83 0.49	0.72 0.20	1.30 0.32	0.74 0.21	0.55 0.09	1.03 0.13	0.87 0.23	0.31 0.01	11.38 0.94
2.50 0.10	0.23 0.19	1.67 0.40	0.93 0.26	1.46 0.43	1.92 0.55	0.75 0.23	1.34 0.35	0.75 0.23	0.59 0.09	1.03 0.13	0.87 0.23	0.31 0.01	11.37 1.03
3.00 0.12	0.37 0.27	2.23 0.56	1.20 0.37	1.92 0.63	2.31 0.75	0.88 0.32	1.51 0.52	0.82 0.33	0.61 0.10	1.00 0.12	0.87 0.23	0.31 0.01	13.53 1.42

MULTIPLICITIES IN K-PLUS NUCLEUS INTERACTIONS AT 100 GEV/C

TABLE IV-7(f)

NU BAR	PSEUDORAPIDITY RANGE												AV MULT
	-0.67 -0.39	-0.38 0.56	0.55 0.92	0.92 1.33	1.33 1.99	1.99 2.25	2.25 2.75	2.75 3.08	3.08 3.38	3.38 4.08	4.08 5.28	5.28 7.00	
1.00 0.00	0.02 0.03	0.15 0.07	0.13 0.04	0.25 0.06	0.52 0.07	0.32 0.05	0.72 0.10	0.47 0.05	0.43 0.06	0.97 0.10	1.43 0.21	0.64 0.04	6.03 0.30
1.10 0.02	0.03 0.03	0.27 0.05	0.15 0.03	0.31 0.05	0.61 0.07	0.36 0.05	0.77 0.09	0.52 0.05	0.45 0.05	1.01 0.10	1.43 0.21	0.64 0.04	6.48 0.29
1.19 0.02	0.04 0.03	0.24 0.05	0.20 0.03	0.36 0.05	0.69 0.07	0.39 0.05	0.82 0.09	0.53 0.06	0.47 0.05	1.04 0.09	1.43 0.21	0.64 0.04	6.37 0.28
1.43 0.02	0.07 0.03	0.50 0.06	0.30 0.04	0.51 0.08	0.90 0.09	0.47 0.05	0.95 0.07	0.60 0.05	0.53 0.05	1.14 0.09	1.43 0.21	0.64 0.04	8.04 0.29
1.64 0.03	0.13 0.04	0.71 0.08	0.40 0.05	0.65 0.07	1.05 0.10	0.54 0.06	1.06 0.10	0.66 0.06	0.58 0.05	1.22 0.09	1.43 0.21	0.64 0.04	9.27 0.31
1.75 0.04	0.14 0.04	0.83 0.07	0.45 0.06	0.72 0.08	1.18 0.11	0.58 0.06	1.12 0.10	0.67 0.07	0.60 0.06	1.26 0.10	1.43 0.21	0.64 0.04	9.55 0.33
1.74 0.05	0.14 0.05	0.81 0.09	0.43 0.06	0.72 0.08	1.17 0.11	0.58 0.06	1.12 0.10	0.69 0.07	0.60 0.05	1.26 0.10	1.43 0.21	0.64 0.04	9.61 0.33
1.92 0.05	0.17 0.06	1.02 0.11	0.55 0.07	0.85 0.10	1.33 0.13	0.64 0.07	1.21 0.12	0.74 0.08	0.65 0.06	1.32 0.11	1.43 0.21	0.64 0.04	10.57 0.37
1.98 0.05	0.14 0.06	1.10 0.12	0.59 0.07	0.89 0.11	1.39 0.14	0.66 0.07	1.24 0.13	0.76 0.09	0.66 0.05	1.35 0.12	1.43 0.21	0.64 0.04	10.73 0.38
2.00 0.05	0.17 0.05	1.12 0.12	0.60 0.07	0.91 0.11	1.40 0.14	0.67 0.08	1.25 0.13	[illegible] 0.05	0.66 0.07	1.35 0.12	1.43 0.21	0.64 0.04	11.00 0.39
2.24 0.08	0.23 0.08	1.44 0.17	0.75 0.11	1.10 0.14	1.62 0.17	0.75 0.09	1.18 0.15	0.81 0.10	0.72 0.07	1.46 0.13	1.43 0.21	0.64 0.04	12.25 0.45
2.30 0.08	0.26 0.07	1.52 0.18	0.79 0.12	1.15 0.15	1.67 0.18	0.77 0.10	1.42 0.15	0.65 0.12	0.74 0.08	1.48 0.15	1.43 0.21	0.64 0.04	12.73 0.49
2.38 0.09	0.26 0.07	1.64 0.21	0.85 0.13	1.22 0.16	1.74 0.20	0.76 0.10	1.46 0.17	0.87 0.11	0.76 [illegible]	1.51 0.15	1.43 0.21	0.64 0.04	13.17 0.53
2.50 0.10	0.23 0.10	1.82 0.25	0.93 0.15	1.33 0.19	1.85 [illegible]	[illegible] 0.11	1.52 0.19	0.91 0.12	[illegible] 0.09	1.55 0.17	1.43 0.21	0.64 0.04	13.88 0.57
3.00 0.12	0.47 0.15	2.65 0.53	1.33 0.36	1.65 0.33	2.10 0.29	0.96 0.17	1.79 0.25	1.05 0.16	0.91 0.13	1.75 0.22	1.11 0.21	0.94 0.04	17.32 0.90

MULTIPLICITIES IN PI-PLUS NUCLEUS INTERACTIONS AT 50 GEV/C

TABLE IV-7(a)

NU BAR	PSEUDORAPIDITY RANGE												AV MULT
	-0.67 -0.34	-0.34 0.56	0.56 0.92	0.92 1.39	1.39 1.99	1.99 2.25	2.25 2.76	2.76 3.04	3.04 3.38	3.38 4.03	4.03 5.28	5.28 7.33	
1.00 0.00	-0.01 0.03	0.10 0.06	0.14 0.04	0.33 0.05	0.75 0.07	0.40 0.05	0.87 0.05	0.55 0.04	0.51 0.04	1.07 0.07	0.78 0.09	0.31 0.01	5.77 0.23
1.26 0.01	0.04 0.01	0.29 0.04	0.22 0.02	0.45 0.05	0.85 0.07	0.45 0.04	0.94 0.05	0.59 0.05	0.52 0.04	1.06 0.07	0.78 0.09	0.31 0.01	6.50 0.13
1.35 0.02	0.05 0.01	0.36 0.03	0.25 0.02	0.53 0.05	0.92 0.07	0.48 0.04	0.96 0.04	0.62 0.05	0.52 0.04	1.06 0.07	0.78 0.09	0.31 0.01	6.73 0.19
1.70 0.02	0.11 0.02	0.61 0.03	0.37 0.03	0.66 0.06	1.12 0.08	0.54 0.05	1.05 0.03	0.61 0.05	0.54 0.04	1.04 0.07	0.76 0.09	0.31 0.01	7.77 0.20
1.98 0.03	0.15 0.03	0.61 0.06	0.48 0.04	0.73 0.07	1.23 0.10	0.60 0.05	1.12 0.08	0.64 0.05	0.55 0.04	1.04 0.07	0.78 0.08	0.31 0.01	8.60 0.22
2.00 0.05	0.17 0.03	0.85 0.05	0.48 0.04	0.80 0.07	1.30 0.10	0.60 0.05	1.12 0.08	0.65 0.05	0.55 0.04	1.03 0.07	0.74 0.09	0.31 0.01	8.66 0.22
2.14 0.06	0.13 0.03	0.70 0.07	0.54 0.05	0.88 0.08	1.39 0.10	0.63 0.05	1.16 0.09	0.67 0.06	0.55 0.04	1.03 0.07	0.78 0.09	0.31 0.01	9.08 0.23
2.12 0.05	0.19 0.03	0.95 0.07	0.53 0.05	0.86 0.08	1.37 0.10	0.63 0.05	1.15 0.09	0.67 0.06	0.55 0.04	1.03 0.07	0.78 0.09	0.31 0.01	9.32 0.23
2.40 0.05	0.24 0.04	1.14 0.08	0.64 0.05	1.01 0.09	1.54 0.12	0.68 0.06	1.22 0.09	0.72 0.06	0.56 0.04	1.02 0.07	0.78 0.09	0.31 0.01	9.82 0.25
2.48 0.05	0.23 0.03	1.25 0.09	0.67 0.05	1.05 0.10	1.59 0.13	0.70 0.06	1.24 0.10	0.73 0.06	0.55 0.04	1.02 0.07	0.78 0.09	0.31 0.01	10.13 0.25
2.45 0.09	0.32 0.05	1.57 0.12	0.82 0.08	1.25 0.12	1.82 0.15	0.78 0.07	1.34 0.11	0.74 0.07	0.56 0.04	1.01 0.07	0.75 0.09	0.31 0.01	[illegible]
2.95 0.09	0.34 0.05	1.66 0.13	0.87 0.09	1.31 0.13	1.88 0.15	0.80 0.07	1.35 0.11	0.73 0.07	0.58 0.04	1.00 0.07	0.79 0.09	0.31 0.01	11.65 0.33
3.30 0.10	0.34 0.05	1.72 0.14	0.88 0.09	1.33 0.13	1.91 0.16	0.80 0.08	1.39 0.12	0.73 0.07	0.54 0.04	1.00 0.07	0.78 0.09	0.31 0.01	11.78 0.34
3.07 0.10	0.35 0.07	1.73 0.15	0.91 0.10	1.37 0.14	1.95 0.17	0.82 0.08	1.39 0.12	0.75 0.08	0.56 0.04	1.00 0.07	0.74 0.09	0.31 0.01	12.01 0.35
3.50 0.12	0.43 0.08	2.23 0.23	1.10 0.15	1.61 0.18	2.21 0.23	0.90 0.09	1.50 0.14	0.83 0.09	0.50 0.04	0.93 0.07	0.78 0.09	0.31 0.01	13.43 0.45

MULTIPLICITIES IN PI-PLUS NUCLEUS INTERACTIONS AT 100 GEV/C

TABLE IV-7(h)

NU BAR	PSEUDORAPIDITY RANGE												AV MULT
	-0.67 -0.31	-0.31 0.56	0.56 0.92	0.92 1.39	1.39 1.99	1.99 2.25	2.25 2.75	2.75 3.04	3.04 3.36	3.36 4.04	4.04 5.28	5.28 7.33	
1.03 0.00	0.02 0.01	0.18 0.05	0.17 0.03	0.34 0.05	0.65 0.05	0.38 0.04	0.85 0.07	0.56 0.03	0.54 0.04	1.23 0.07	1.49 0.05	0.65 0.02	5.91 0.18
1.25 0.02	0.04 0.01	0.24 0.03	0.26 0.02	0.46 0.04	0.86 0.05	0.44 0.03	0.93 0.06	0.62 0.04	0.58 0.04	1.28 0.06	1.49 0.08	0.48 0.02	7.69 0.15
1.36 0.02	0.05 0.01	0.32 0.03	0.27 0.02	0.51 0.04	0.90 0.05	0.46 0.03	0.95 0.06	0.64 0.04	0.63 0.04	1.30 0.05	1.50 0.08	0.49 0.02	7.99 0.15
1.73 0.02	0.08 0.02	0.53 0.04	0.35 0.03	0.68 0.05	1.13 0.07	0.54 0.04	1.05 0.07	0.72 0.05	0.65 0.04	1.36 0.06	1.50 0.08	0.53 0.02	9.08 0.18
1.95 0.03	0.11 0.03	0.67 0.06	0.44 0.04	0.61 0.07	1.31 0.08	0.61 0.05	1.15 0.07	0.72 0.05	0.65 0.04	1.40 0.07	1.51 0.08	0.56 0.02	10.01 0.20
2.00 0.04	0.11 0.03	0.58 0.06	0.65 0.04	0.82 0.07	1.33 0.08	0.61 0.05	1.16 0.08	0.75 0.05	0.68 0.04	1.41 0.07	1.51 0.08	0.56 0.02	10.08 0.20
2.14 0.04	0.13 0.03	0.76 0.06	0.49 0.04	0.93 0.07	1.42 0.09	0.65 0.05	1.21 0.08	0.77 0.05	0.70 0.04	1.43 0.07	1.51 0.08	0.57 0.02	10.56 0.21
2.12 0.05	0.13 0.03	0.77 0.06	0.49 0.04	0.88 0.07	1.41 0.08	0.64 0.05	1.20 0.08	0.77 0.05	0.70 0.04	1.43 0.07	1.51 0.08	0.57 0.02	10.49 0.21
2.50 0.06	0.17 0.04	0.93 0.07	0.58 0.04	1.02 0.08	1.60 0.10	0.71 0.05	1.30 0.08	0.81 0.06	0.73 0.05	1.47 0.07	1.52 0.08	0.53 0.02	11.43 0.23
2.65 0.06	0.18 0.04	1.05 0.08	0.60 0.05	1.66 0.08	1.65 0.10	0.73 0.05	1.33 0.08	0.87 0.06	0.75 0.05	1.58 0.07	1.52 0.08	0.61 0.02	11.77 0.23
2.85 0.09	0.24 0.04	1.40 0.10	0.73 0.05	1.25 0.10	1.91 0.12	0.83 0.06	1.48 0.09	0.86 0.06	0.77 0.05	1.53 0.08	1.52 0.08	0.65 0.01	13.20 0.27
2.96 0.09	0.26 0.05	1.50 0.10	0.77 0.05	1.30 0.11	1.97 0.13	0.86 0.07	1.52 0.09	0.84 0.06	0.78 0.05	1.54 0.08	1.53 0.09	0.66 0.03	13.58 0.29
3.00 0.10	0.27 0.05	1.54 0.11	0.79 0.07	1.32 0.11	2.03 0.14	0.87 0.07	1.53 0.09	0.90 0.06	0.78 0.05	1.55 0.08	1.53 0.09	0.66 0.03	13.74 0.29
3.07 0.10	0.21 0.05	1.61 0.12	0.81 0.07	1.36 0.12	2.05 0.14	0.89 0.07	1.55 0.10	0.91 0.07	0.78 0.06	1.56 0.08	1.53 0.09	0.67 0.03	14.03 0.31
3.50 0.12	0.38 0.04	2.08 0.14	0.98 0.11	1.48 0.18	2.34 0.21	1.01 0.11	1.76 0.14	0.90 0.11	0.81 0.09	1.61 0.10	1.56 0.10	0.77 0.03	15.75 0.45

MULTIPLICITIES IN PI-PLUS NUCLEUS INTERACTIONS AT 200 GEV/C

TABLE IV-7(i)

NU BAR	PSEUDORAPIDITY RANGE												AV MULT
	-0.67 -0.34	-0.36 0.55	0.55 0.92	0.92 1.34	1.34 1.99	1.99 2.25	2.25 2.75	2.76 3.09	3.09 3.38	3.38 4.08	4.08 5.28	5.28 7.00	
1.00 0.00	0.02 0.04	0.12 0.06	0.15 0.05	0.29 0.09	0.57 0.10	0.34 0.05	0.75 0.09	0.54 0.07	0.53 0.05	1.26 0.10	2.05 0.18	1.16 0.06	7.77 0.30
1.26 0.02	0.01 0.01	0.25 0.03	0.23 0.03	0.44 0.05	0.78 0.05	0.42 0.04	0.92 0.07	0.63 0.05	0.60 0.05	1.39 0.08	2.18 0.17	1.15 0.06	9.32 0.25
1.35 0.02	0.04 0.01	0.33 0.04	0.25 0.03	0.49 0.05	0.87 0.06	0.45 0.04	0.97 0.07	0.66 0.05	0.62 0.05	1.44 0.08	2.22 0.17	1.15 0.06	9.69 0.24
1.70 0.02	0.07 0.02	0.49 0.05	0.36 0.04	0.69 0.07	1.15 0.09	0.56 0.04	1.13 0.07	0.75 0.05	0.70 0.05	1.59 0.08	2.39 0.16	1.17 0.05	11.05 0.25
1.98 0.03	0.10 0.01	0.67 0.07	0.45 0.05	0.64 0.09	1.39 0.11	0.64 0.05	1.23 0.08	0.81 0.06	0.75 0.05	1.70 0.09	2.53 0.16	1.17 0.05	12.30 0.27
2.00 0.04	0.11 0.03	0.66 0.07	0.46 0.05	0.65 0.04	1.40 0.11	0.64 0.05	1.24 0.08	0.82 0.06	0.77 0.06	1.71 0.09	2.54 0.16	1.17 0.06	12.39 0.29
2.14 0.04	0.12 0.03	0.77 0.06	0.51 0.05	0.93 0.09	1.51 0.11	0.68 0.06	1.29 0.09	0.85 0.07	0.80 0.05	1.76 0.10	2.61 0.17	1.17 0.05	13.00 0.30
2.12 0.05	0.12 0.03	0.76 0.06	0.56 0.05	0.92 0.09	1.49 0.11	0.68 0.05	1.28 0.09	0.85 0.06	0.80 0.05	1.75 0.10	2.60 0.17	1.17 0.06	12.92 0.30
2.40 0.06	0.13 0.04	0.85 0.09	0.60 0.06	1.08 0.10	1.71 0.12	0.76 0.06	1.33 0.10	0.91 0.07	0.86 0.07	1.84 0.11	2.74 0.17	1.17 0.05	14.15 0.33
2.49 0.06	0.15 0.05	1.01 0.10	0.63 0.05	1.12 0.10	1.77 0.13	0.78 0.07	1.41 0.11	0.94 0.07	0.80 0.07	1.86 0.11	2.79 0.13	1.17 0.06	14.52 0.34
2.85 0.09	0.21 0.05	1.31 0.13	0.77 0.08	1.33 0.14	2.06 0.17	0.90 0.08	1.57 0.12	1.06 0.09	0.97 0.08	1.94 0.13	2.96 0.19	1.17 0.06	15.25 0.41
2.95 0.09	0.23 0.07	1.39 0.15	0.81 0.09	1.36 0.16	2.13 0.19	0.93 0.09	1.62 0.13	1.09 0.09	0.99 0.09	1.96 0.13	3.01 0.20	1.17 0.05	15.72 0.44
3.00 0.10	0.23 0.07	1.42 0.15	0.92 0.10	1.40 0.16	2.15 0.20	0.94 0.09	1.64 0.13	1.11 0.10	1.00 0.09	1.97 0.14	3.03 0.20	1.17 0.06	16.91 0.45
3.07 0.10	0.24 0.07	1.48 0.16	0.85 0.11	1.44 0.16	2.21 0.21	0.97 0.10	1.68 0.14	1.14 0.11	1.02 0.10	1.97 0.14	3.07 0.20	1.17 0.06	17.24 0.49
3.50 0.12	0.31 0.05	1.86 0.23	1.03 0.16	1.67 0.31	2.50 0.36	1.11 0.15	1.97 0.28	1.35 0.22	1.14 0.16	2.00 0.19	3.28 0.23	1.17 0.06	19.38 0.77

MULTIPLICITIES IN PI-MINUS NUCLEUS INTERACTIONS AT 200 GEV/C

TABLE IV-7(j)

NU BAR	PSEUDORAPIDITY RANGE												AV MULT
	-0.67 -0.35	-0.35 0.55	0.56 0.92	0.92 1.34	1.33 1.99	1.99 2.25	2.25 2.75	2.76 3.03	3.03 3.33	3.38 4.08	4.08 5.29	5.28 7.00	
1.00 0.00	0.02 0.02	0.13 0.04	0.13 0.03	0.30 0.05	0.64 0.06	0.36 0.04	0.77 0.07	0.59 0.05	0.49 0.05	1.16 0.10	2.02 0.27	1.04 0.05	7.61 0.33
1.26 0.02	0.03 0.01	0.24 0.02	0.19 0.02	0.40 0.04	0.79 0.06	0.43 0.04	0.89 0.07	0.60 0.05	0.57 0.05	1.36 0.09	2.11 0.26	1.06 0.05	8.68 0.31
1.35 0.02	0.04 0.01	0.29 0.02	0.22 0.02	0.44 0.04	0.84 0.06	0.45 0.04	0.94 0.07	0.63 0.05	0.60 0.05	1.42 0.09	2.15 0.26	1.07 0.05	9.33 0.31
1.70 0.02	0.07 0.02	0.47 0.04	0.32 0.03	0.59 0.05	1.05 0.08	0.55 0.05	1.10 0.08	0.73 0.05	0.70 0.06	1.61 0.10	2.27 0.25	1.07 0.04	10.55 0.33
1.98 0.03	0.10 0.02	0.65 0.05	0.41 0.04	0.74 0.07	1.27 0.10	0.63 0.05	1.24 0.09	0.81 0.05	0.75 0.06	1.73 0.11	2.37 0.27	1.11 0.04	11.32 0.35
2.00 0.04	0.10 0.01	0.66 0.05	0.42 0.04	0.75 0.07	1.29 0.10	0.64 0.05	1.25 0.09	0.81 0.06	0.77 0.06	1.74 0.11	2.35 0.27	1.11 0.04	11.91 0.35
2.14 0.04	0.11 0.03	0.76 0.06	0.47 0.04	0.83 0.08	1.40 0.11	0.68 0.06	1.32 0.10	0.85 0.06	0.80 0.06	1.79 0.12	2.42 0.28	1.12 0.04	12.56 0.37
2.12 0.05	0.11 0.03	0.74 0.06	0.46 0.04	0.82 0.07	1.38 0.10	0.67 0.06	1.31 0.10	0.85 0.06	0.79 0.06	1.79 0.12	2.42 0.28	1.12 0.04	12.46 0.37
2.40 0.05	0.13 0.03	0.95 0.07	0.57 0.05	0.99 0.09	1.63 0.12	0.77 0.06	1.45 0.11	0.92 0.07	0.84 0.07	1.87 0.12	2.51 0.29	1.14 0.04	13.78 0.39
2.48 0.05	0.14 0.01	1.01 0.07	0.61 0.05	1.04 0.09	1.70 0.12	0.80 0.07	1.49 0.11	0.94 0.07	0.85 0.07	1.87 0.12	2.54 0.29	1.14 0.04	14.16 0.40
2.86 0.09	0.21 0.04	1.33 0.10	0.73 0.07	1.30 0.12	2.01 0.16	0.93 0.08	1.65 0.13	1.02 0.08	0.91 0.07	1.95 0.13	2.68 0.32	1.16 0.05	15.04 0.46
2.96 0.09	0.21 0.05	1.42 0.11	0.83 0.07	1.15 0.13	2.19 0.17	0.97 0.09	1.73 0.13	1.05 0.09	0.92 0.07	1.95 0.13	2.71 0.32	1.17 0.05	16.54 0.48
3.00 0.10	0.23 [illegible]	1.46 0.12	0.85 0.07	1.41 0.13	2.22 [illegible]	0.99 0.09	1.76 0.14	1.05 0.09	0.92 0.07	1.95 0.14	2.73 0.33	[illegible] [illegible]	16.74 0.49
3.07 0.10	0.23 0.04	1.52 0.12	0.85 0.08	1.45 0.14	2.30 0.19	1.02 0.09	1.74 0.14	1.07 0.09	0.93 0.08	1.95 0.14	2.75 [illegible]	1.18 0.03	17.10 0.50
3.50 0.12	0.32 [illegible]	1.76 0.18	1.11 0.12	1.82 0.22	2.50 0.29	1.19 0.12	2.02 0.15	1.15 0.13	0.95 0.11	1.32 0.70	2.93 0.37	1.21 [illegible]	19.36 0.65

TABLE IV-8

Summary of Average Charged Multiplicities

Beam Energy	Target		<n>	
		p	K^+	π^+
50 GeV	H	5.24±.27	5.82±.56	5.77±.20
	C	6.40±.23	6.31±.52	6.54±.18
	Cu	9.27±.43	9.26±1.45	9.76±.30
	Pb	11.67±.57	11.35±1.29	11.26±.36
100 GeV	H	6.24±.16	6.03±.30	6.91±.18
	C	7.72±.16	6.92±.33	7.86±.15
	Cu	11.00±.32	8.89±1.10	10.29±.26
	Pb	14.75±.38	12.92±.79	13.21±.30
	U	15.94±.50	12.93±1.33	14.57±.39
200 GeV	H	6.94±.20	---	7.77±.30
	C	9.34±.18	---	9.48±.27
	Cu	14.01±.34	---	13.61±.77
	Ag	14.95±.34	---	14.31±.70
	Pb	18.47±.40	---	16.17±.61
		$\bar{p}$	K^-	π^-
200 GeV	H	7.41±.66	---	7.61±.33
	C	9.19±.35	---	8.99±.29
	Cu	13.49±2.23	---	12.60±.52
	Ag	17.96±2.12	---	13.86±.48
	Pb	16.04±2.83	---	16.31±.49

TABLE IV-9

Comparison of Average Multiplicities in Hadron-Proton Reactions. HBC Refers to Hydrogen Bubble Chamber.

Beam		Average Multiplicity
50 GeV/c proton	HBC[a]	5.35±0.11
	this expt	5.24±0.27
100 GeV/c proton	this expt	6.24±0.16
	HBC[b]	6.49±0.10
102 GeV/c proton	HBC[c]	6.32±0.07
200 GeV/c proton	this expt	6.94±0.20
205 GeV/c proton	HBC[d]	7.68±0.07
50 GeV/c π^+	HBC[e]	5.89±0.06
	this expt	5.77±0.20
50 GeV/c π^-	HBC[e]	5.78±0.04
100 GeV/c π^+	HBC[b]	6.80±0.14
	this expt	6.91±0.18
100 GeV/c π^-	HBC[f]	6.79±0.08
200 GeV/c π^+	this expt	7.77±0.30
200 GeV/c π^-	this expt	7.61±0.33
205 GeV/c π^-	HBC[g]	8.02±0.12
100 GeV/c K^+	HBC[h]	6.65±0.31
	this expt	6.03±0.30

TABLE IV-10

Comparison of Average Multiplicities in Hadron-Emulsion Interactions

Beam	$\langle n_s \rangle$	$\langle n \rangle$ this expt
50 GeV/c p	8.7 ± .1[a]	8.91 ± .27
67 GeV/c p	9.3 ± .2[a]	---
	9.7 ± .2[b]	---
100 GeV/c p	---	11.28 ± .22
200 GeV/c p	13.3 ± .3[b]	13.36 ± .25
	13.6 ± .5[c]	---
	13.8 ± .2[d]	---
	13.8 ± .2[a]	---
50 GeV/c π^+	---	9.02 ± .23
60 GeV/c π^+	8.6 ± .2[e]	---
100 GeV/c π^+	---	10.49 ± .21
200 GeV/c π^+	---	12.92 ± .30
200 GeV/c $^-$	11.9 ± .1[d]	12.46 ± .37
	11.9 ± .2[a]	---

TABLE IV-11

Comparison of 100 GeV Pion Results From the Two Parts of This Experiment

Target	Average Charged Multiplicity in $\theta < 110^\circ$	
	Part 1 of this Experiment	Part 2 of this Experiment
H	6.55 ± .2	6.89 ± .2
C	7.85 ± .1	7.81 ± .2
Cu	9.72 ± .1	10.16 ± .3
Pb	12.4 ± .2	12.[illegible]6 ± .[illegible]
U	11.7 ± .2	14.23 ± .4

TABLE IV-12

Results of Fitting to $R_A = a + b\bar{\nu}$

Beam	a	b	Error on R_A	χ^2
50 GeV/c p	0.51 ± .07	0.49 ± .04	2.8%	0.3
100 GeV/c p	0.45 ± .04	0.53 ± .02	1.4%	0.7
200 GeV/c p	0.39 ± .04	0.63 ± .02	1.2%	1.8
200 GeV/c $\bar{p}$	0.42 ± .16	0.57 ± .10	7.0%	0.7
50 GeV/c K^+	0.22 ± .23	0.75 ± .19	7.3%	0.1
100 GeV/c K^+	0.16 ± .12	0.83 ± .10	4.0%	0.3
50 GeV/c π^+	0.45 ± .06	0.53 ± .04	2.3%	2.7
100 GeV/c π^+	0.50 ± .04	0.48 ± .03	1.6%	1.3
200 GeV/c π^+	0.44 ± .07	0.57 ± .04	2.4%	0.4
200 GeV/c π^-	0.41 ± .07	0.58 ± .04	2.1%	0.1
All p and π	0.43 ± .02	0.56 ± .01	1.2%	2.3

TABLE IV-13

Results of Fitting to $R_A = R_1 A^{\alpha}$

Beam	R_1	α	Error on R_A	χ^2
50 GeV proton	0.89 ± .04	0.16 ± .01	2.7%	6
100 GeV proton	0.88 ± .02	0.18 ± .01	1.3%	19
200 GeV proton	0.92 ± .02	0.18 ± .01	1.1%	13
200 GeV anti-proton	0.93 ± .08	0.16 ± .03	7.0%	1.5
50 GeV kaon	0.89 ± .08	0.12 ± .03	7.1%	2.3
100 GeV kaon	0.91 ± .04	0.14 ± .01	3.6%	4.6
50 GeV π^+	0.89 ± .03	0.14 ± .01	1.7%	16
100 GeV π^+	0.87 ± .02	0.14 ± .01	1.7%	22
200 GeV π^+	0.92 ± .03	0.14 ± .01	2.1%	4.6
200 GeV π^-	0.89 ± .03	0.16 ± .01	1.6%	7
All p and π	0.90 ± .01	0.16 ± .003	0.6%	17

FIGURE IV-1

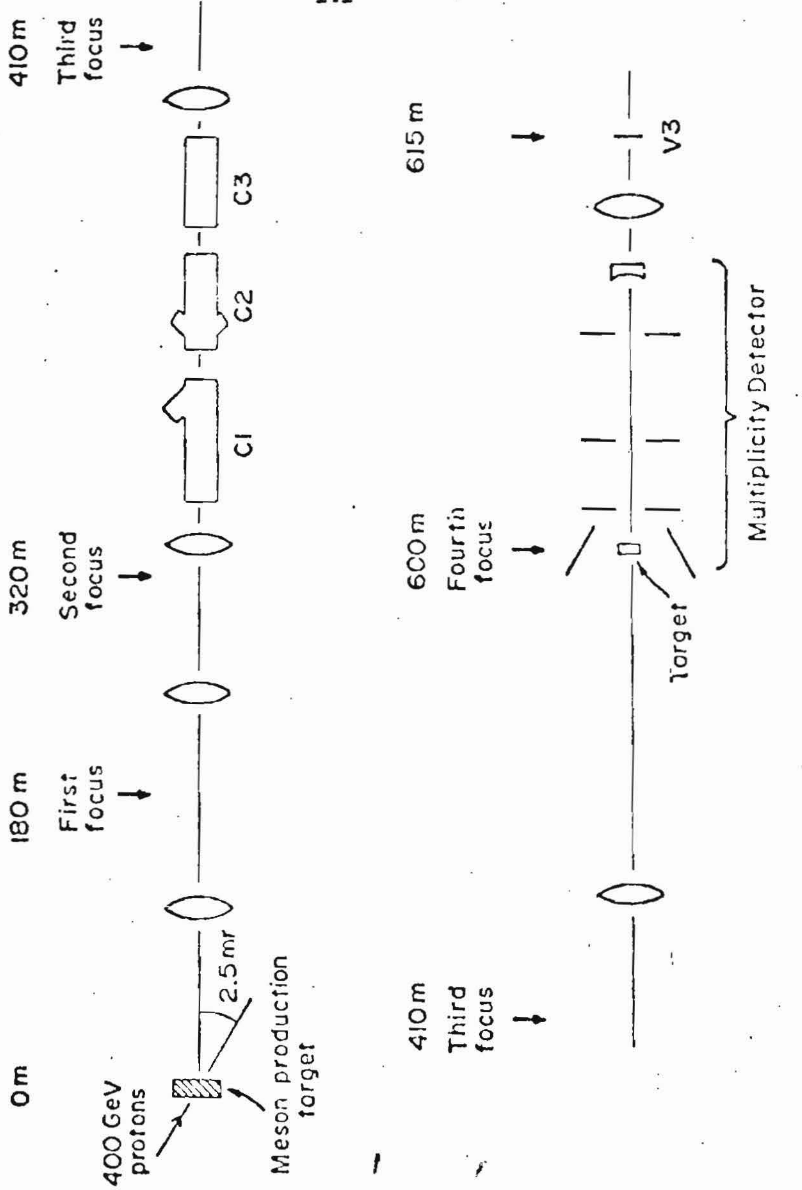

FIGURE IV-2

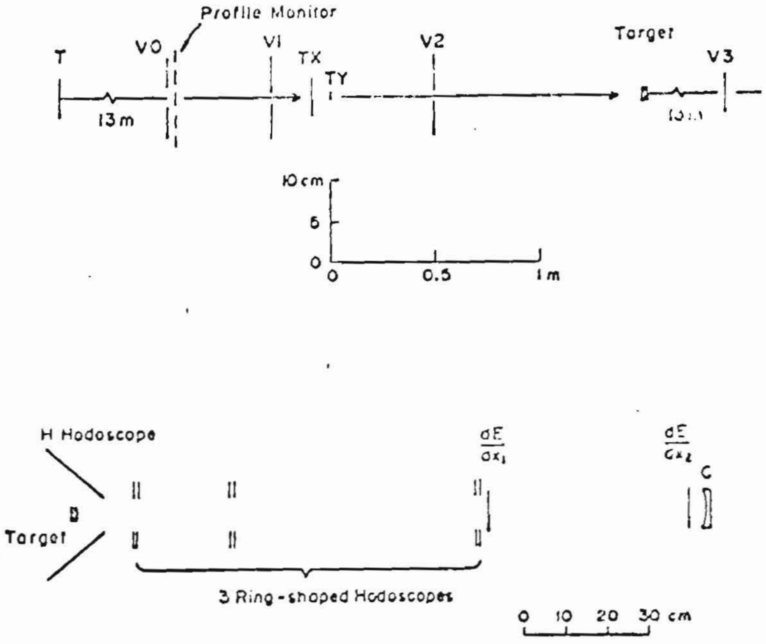

FIGURE IV-3

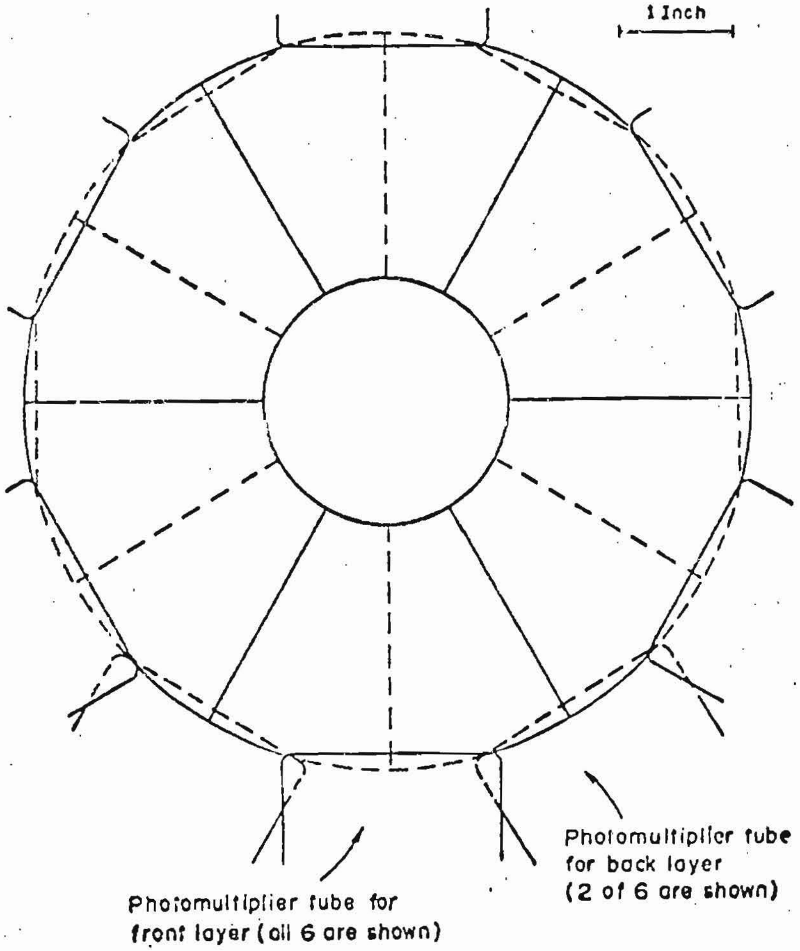

FIGURE IV-4

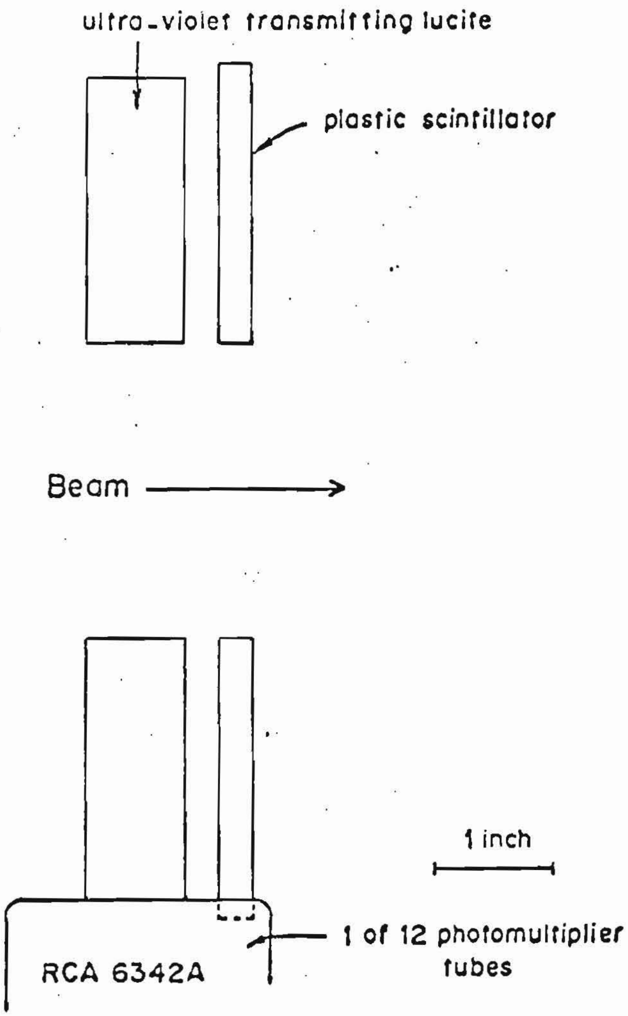

FIGURE IV-7

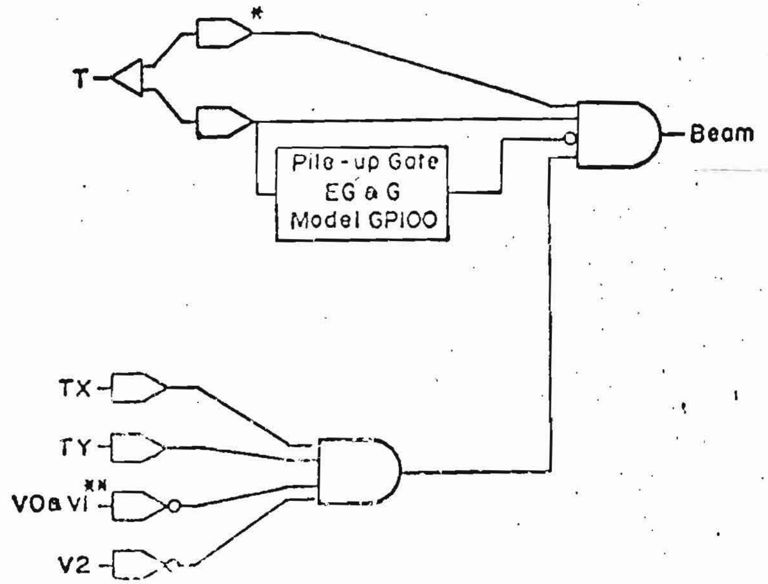

* This discriminator has a threshold of 1.5 times minimum ionizing.

** The outputs of the VO and VI counters have been added together.

Discriminator

Fan-out

Logical Inverse

AND

FIGURE IV-8

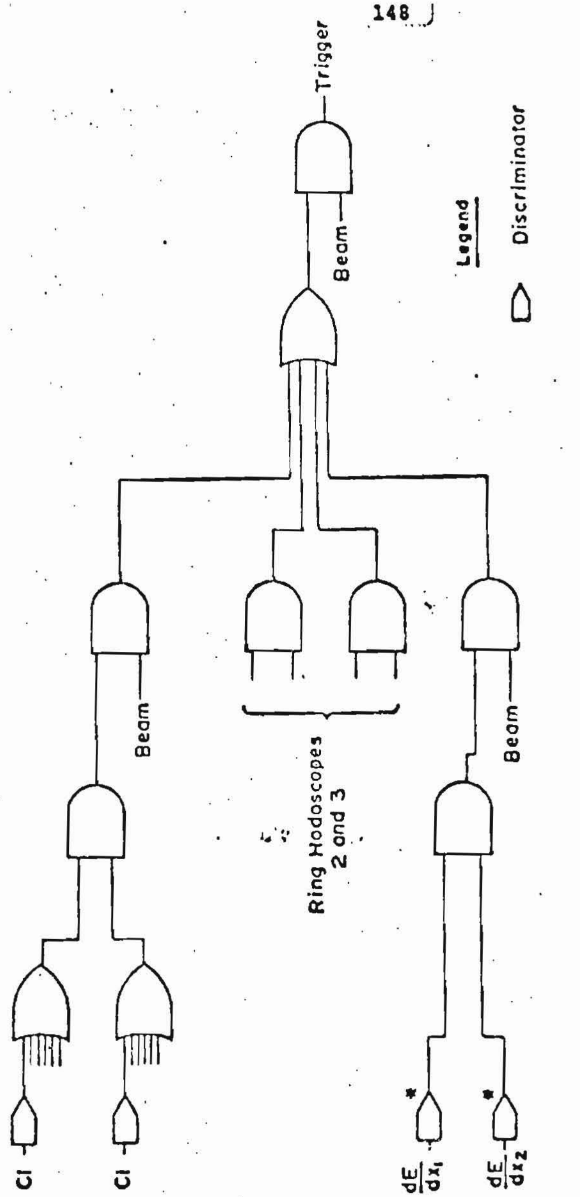

Legend

Discriminator

OR

AND

* These 2 discriminators have thresholds of 1.5 times minimum ionizing.

CI - 1 of 6 counters in front layer of the 1st. ring hodoscope.

SI - 1 of 6 counters in back layer of the 1st ring hodoscope.

FIGURE IV-9

$\langle n \rangle$ vs $\bar{\nu}$

50 GeV/c π^+A INTERACTIONS

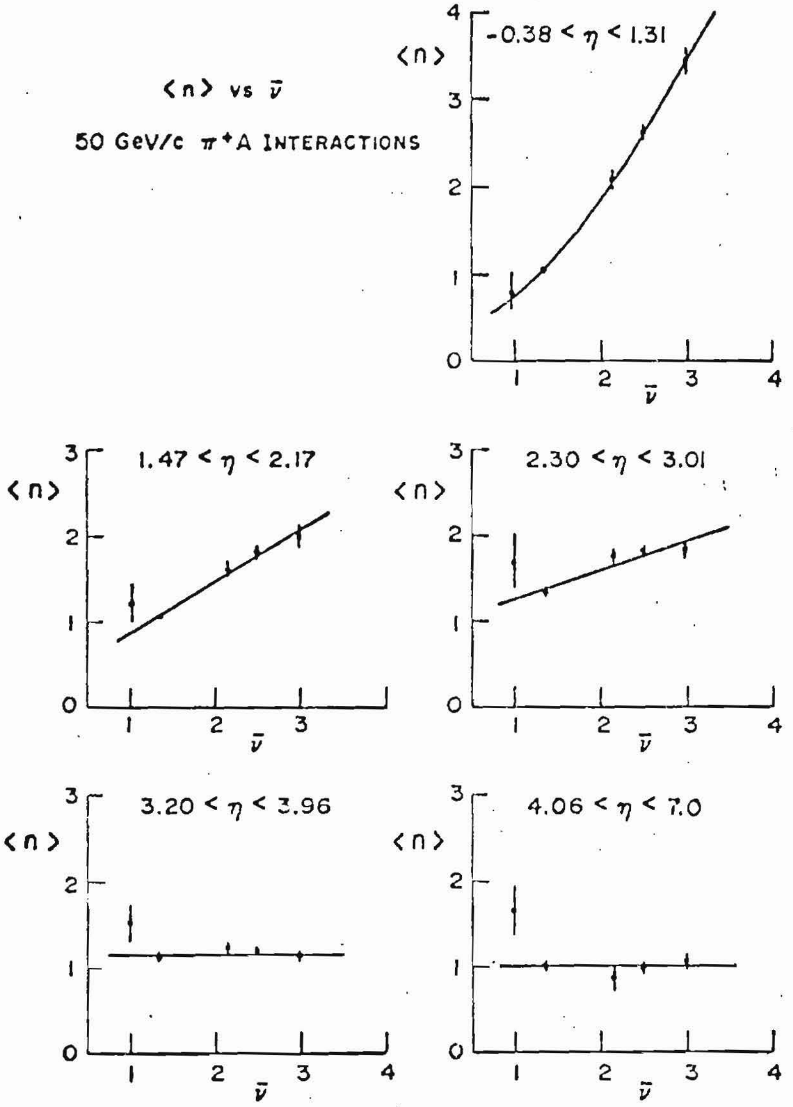

FIGURE IV-10

$\langle n \rangle$ vs $\bar{\nu}$

100 GeV/c π^+A INTERACTIONS

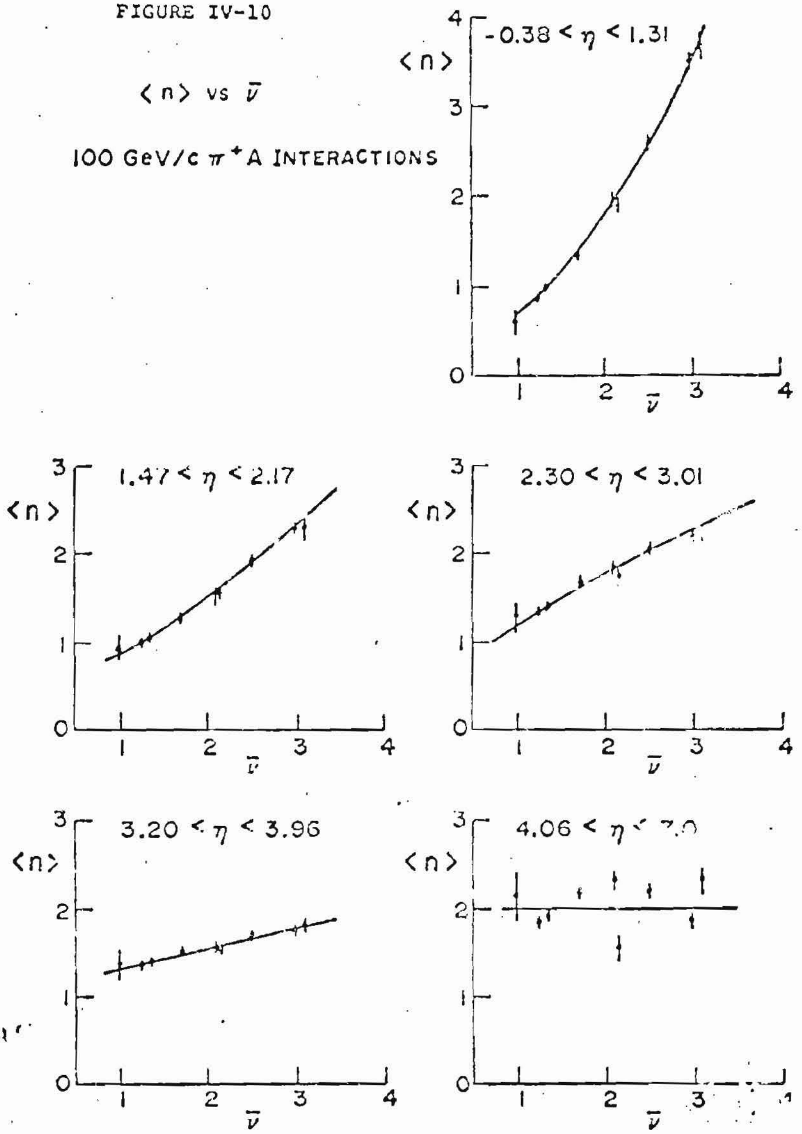

FIGURE IV-11

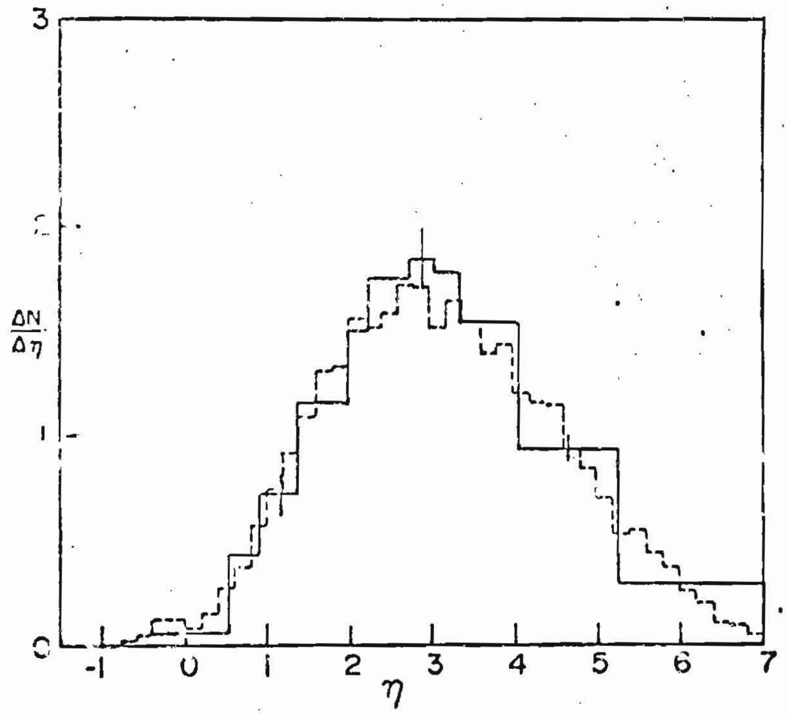

FIGURE IV-12

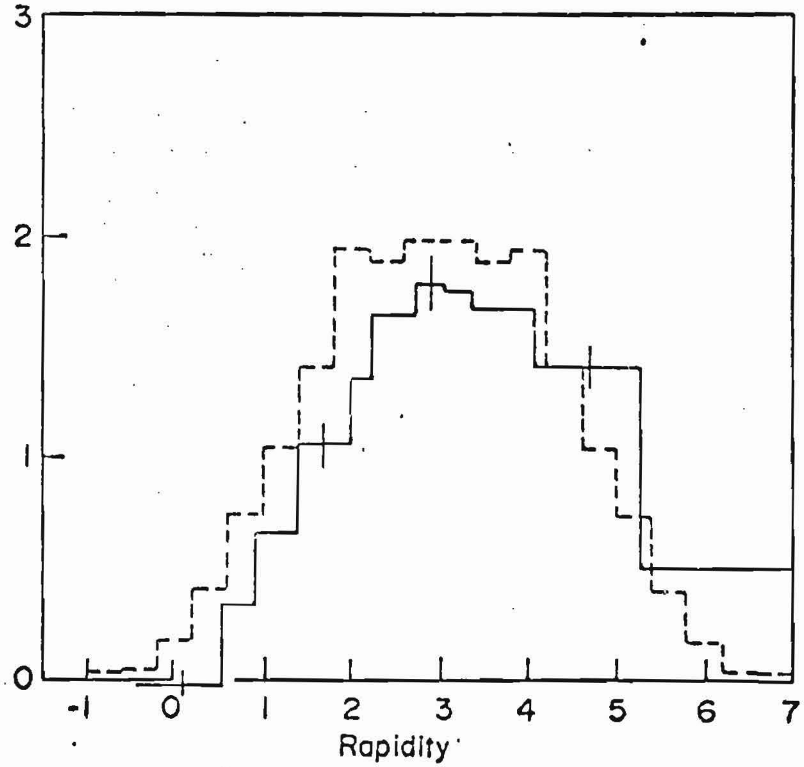

FIGURE IV-13

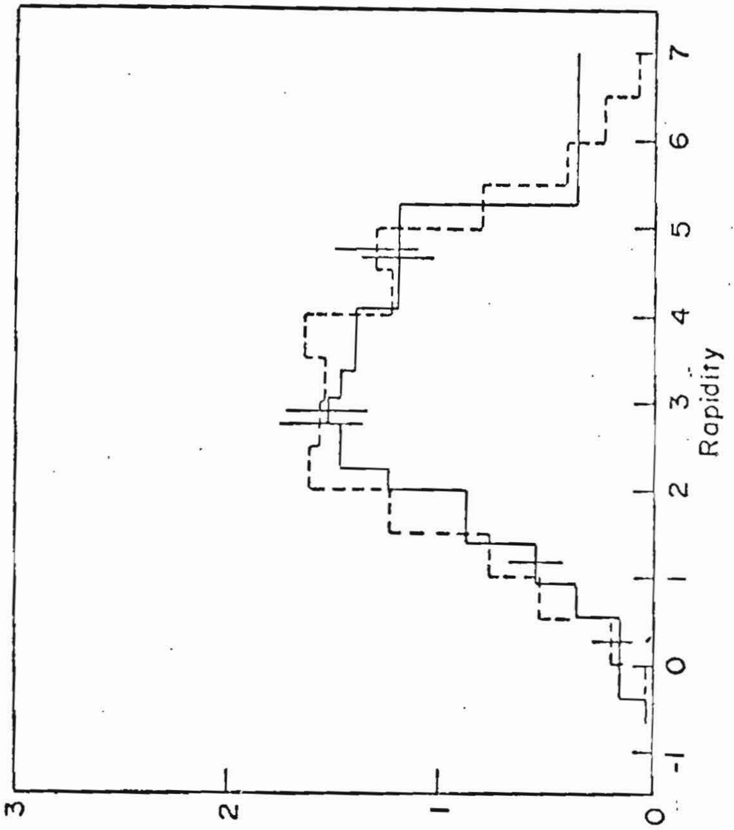

FIGURE IV-14

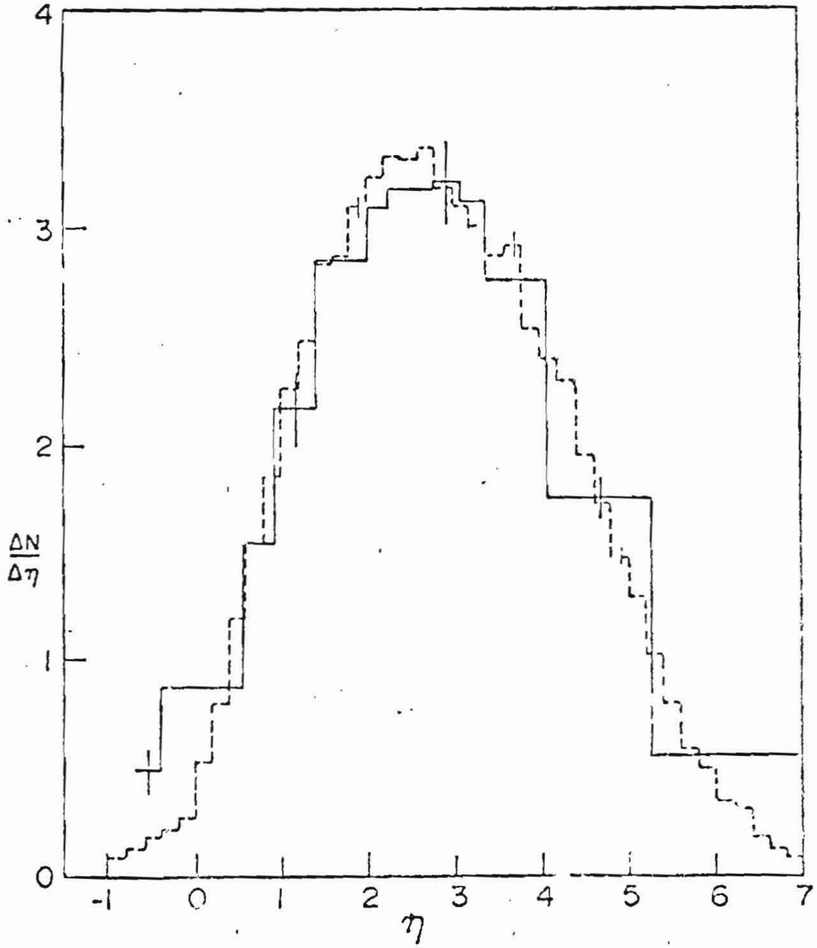

FIGURE IV-15

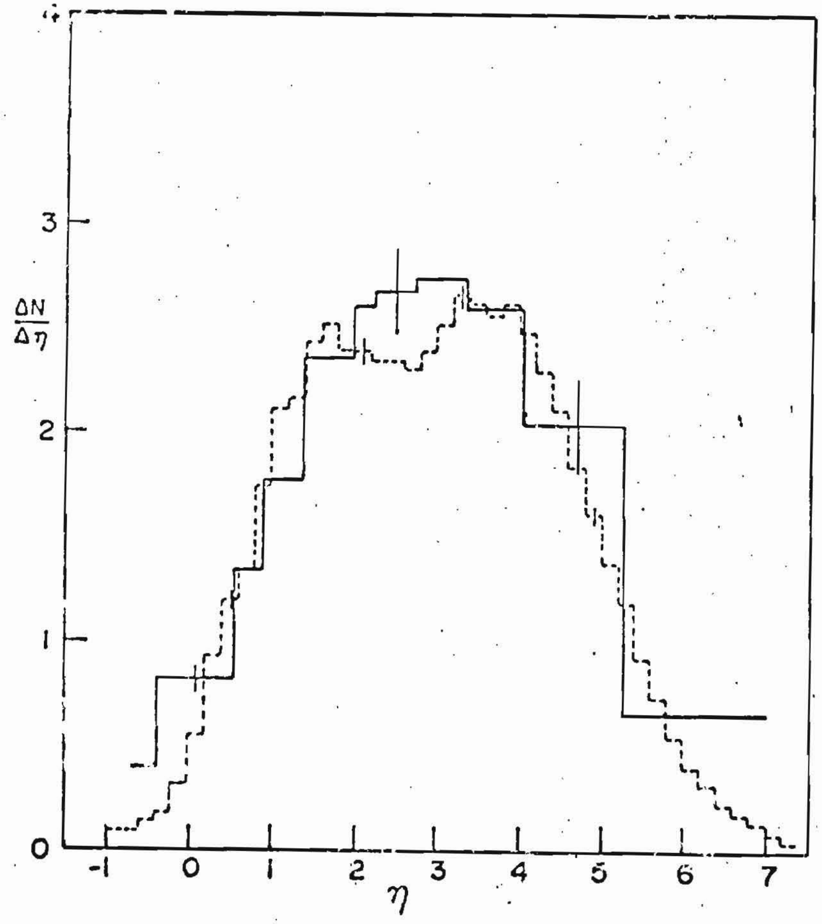

FIGURE IV-16

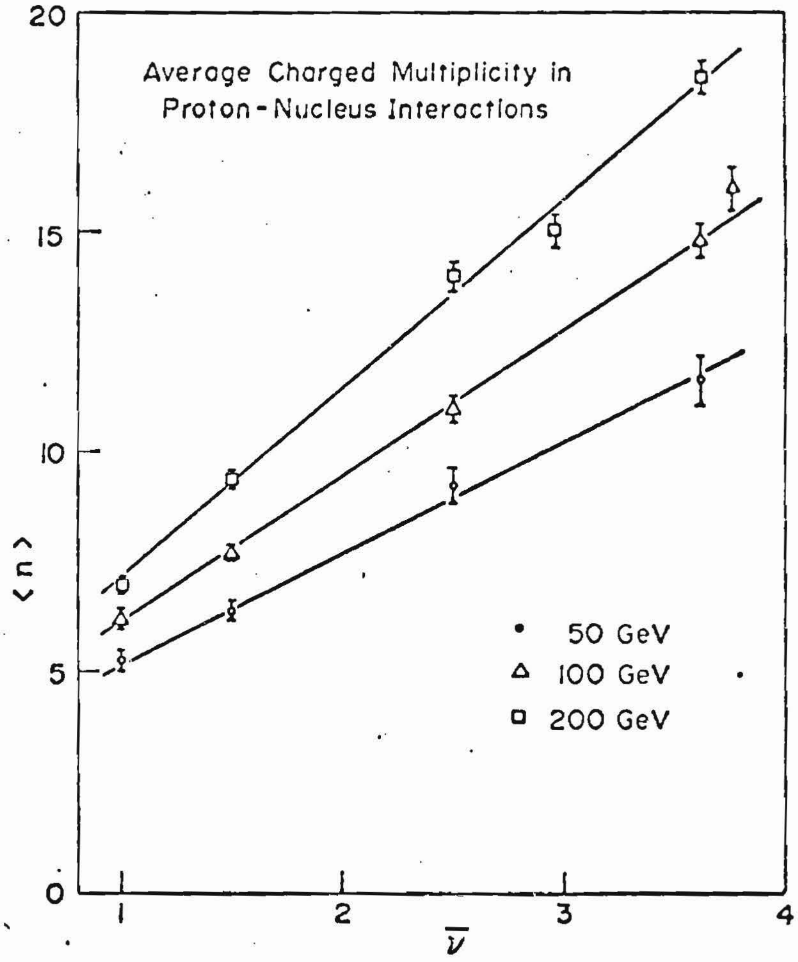

FIGURE IV-17

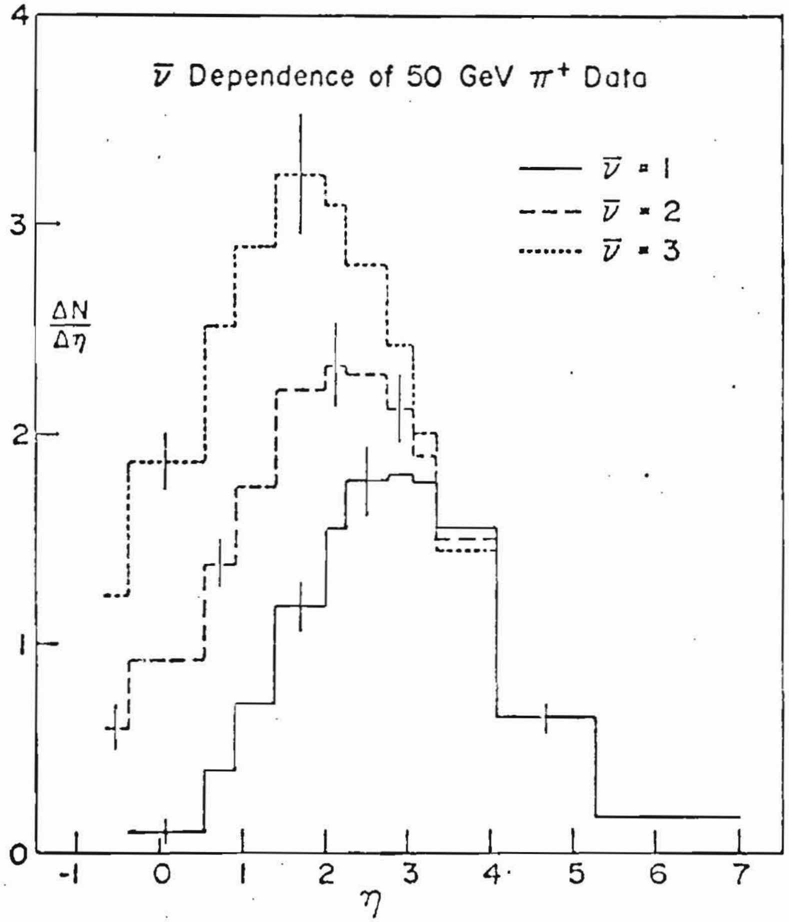

FIGURE IV-18

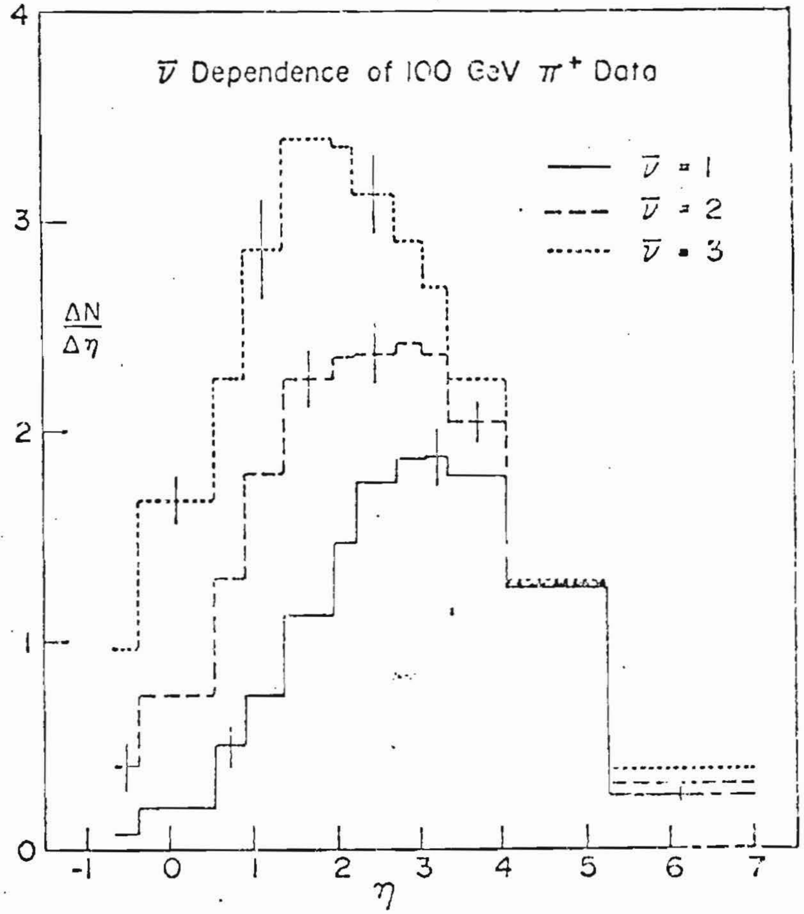

FIGURE IV-19

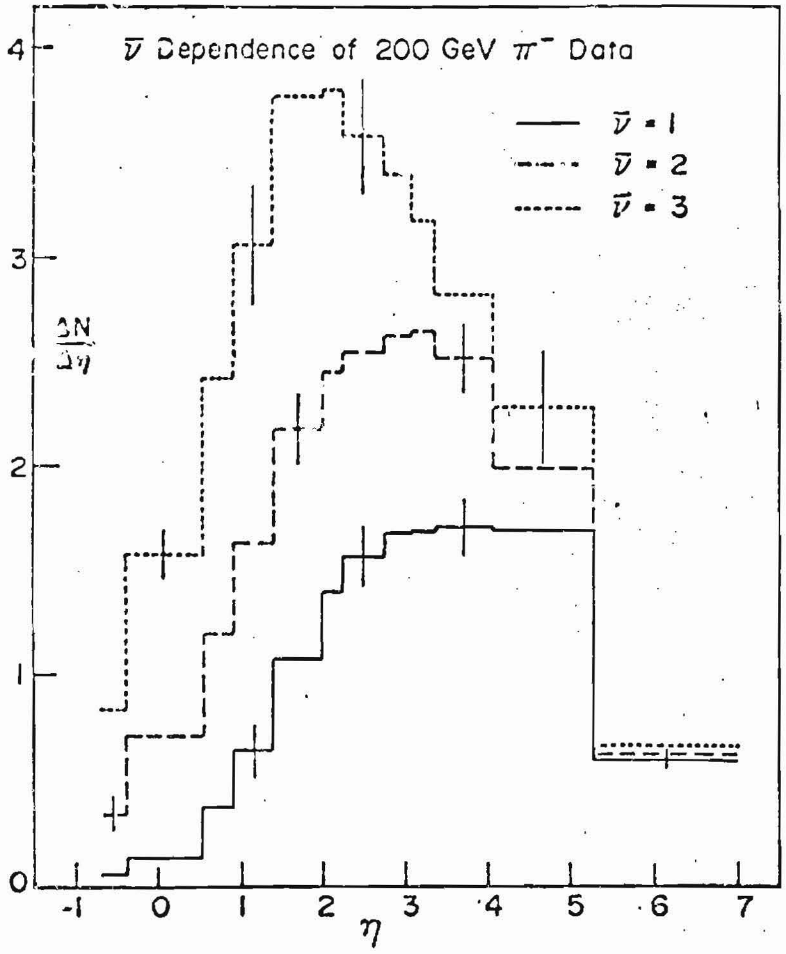

FIGURE IV-20

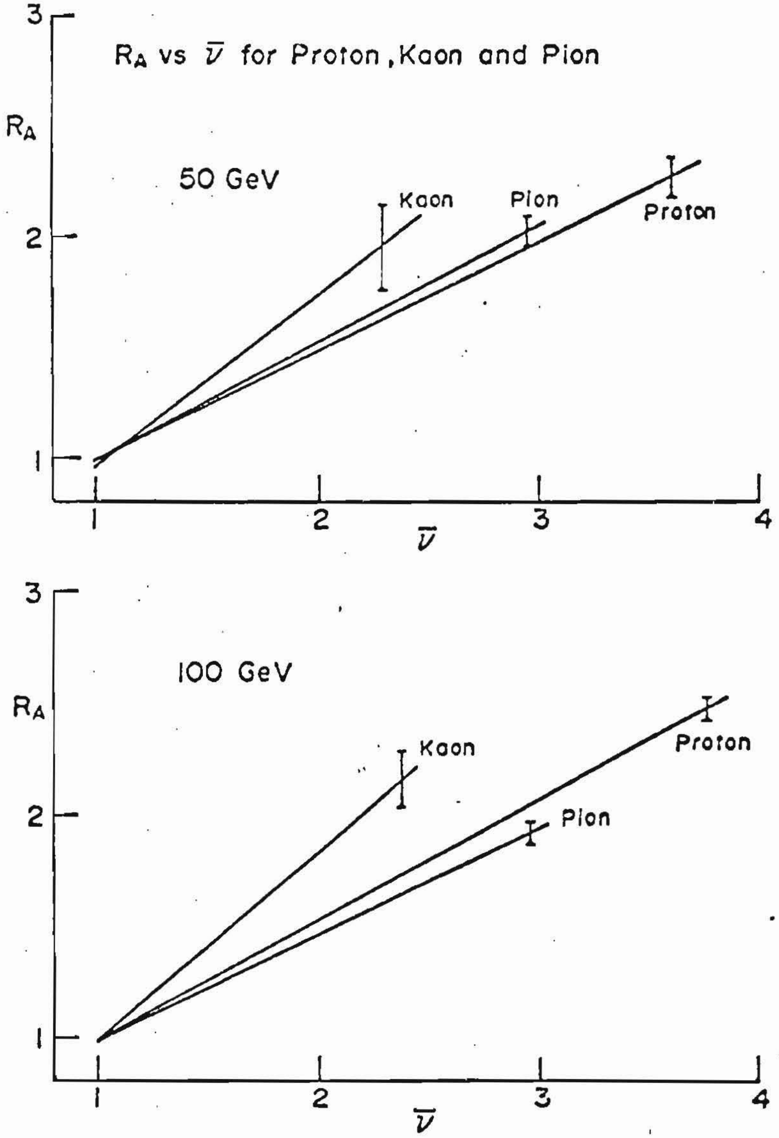

FIGURE IV-21

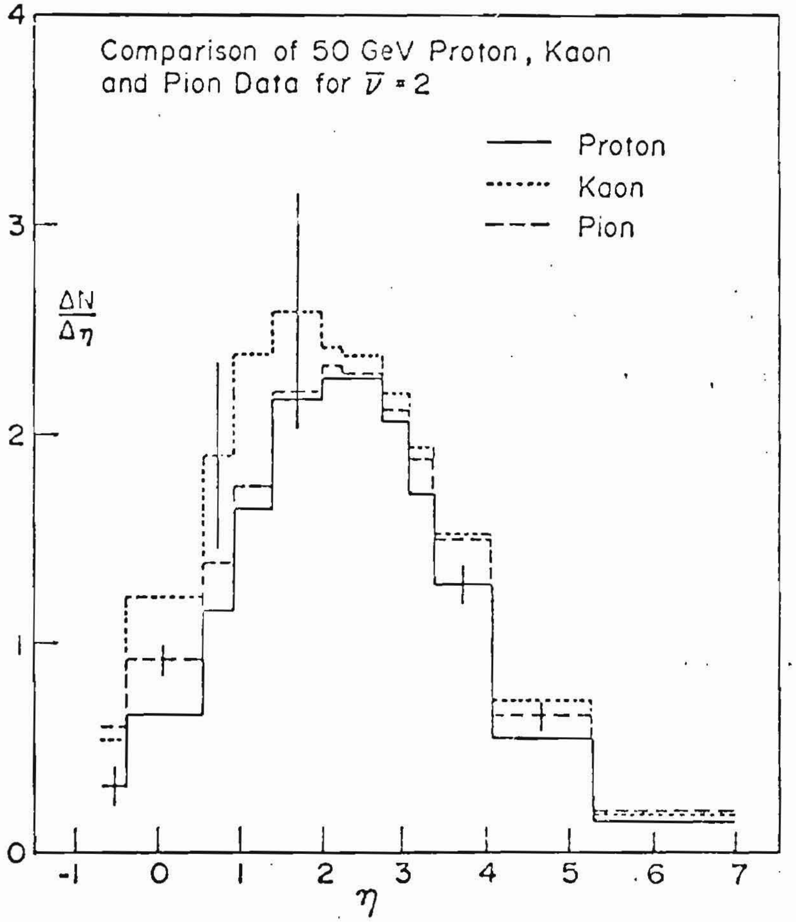

FIGURE IV-22

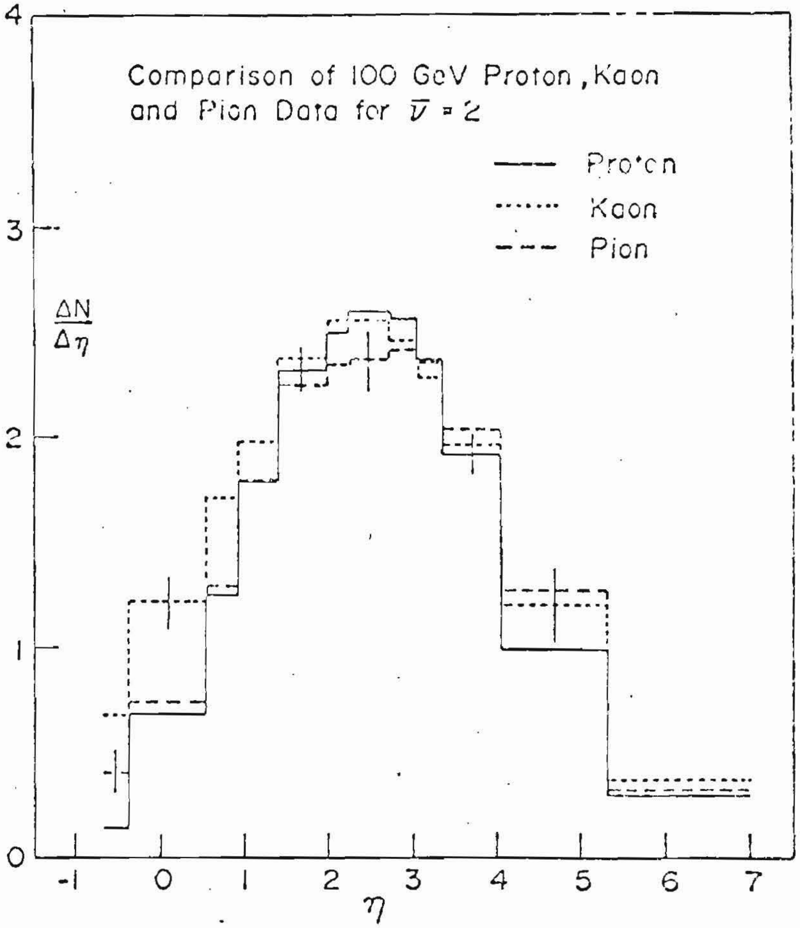

FIGURE IV-23

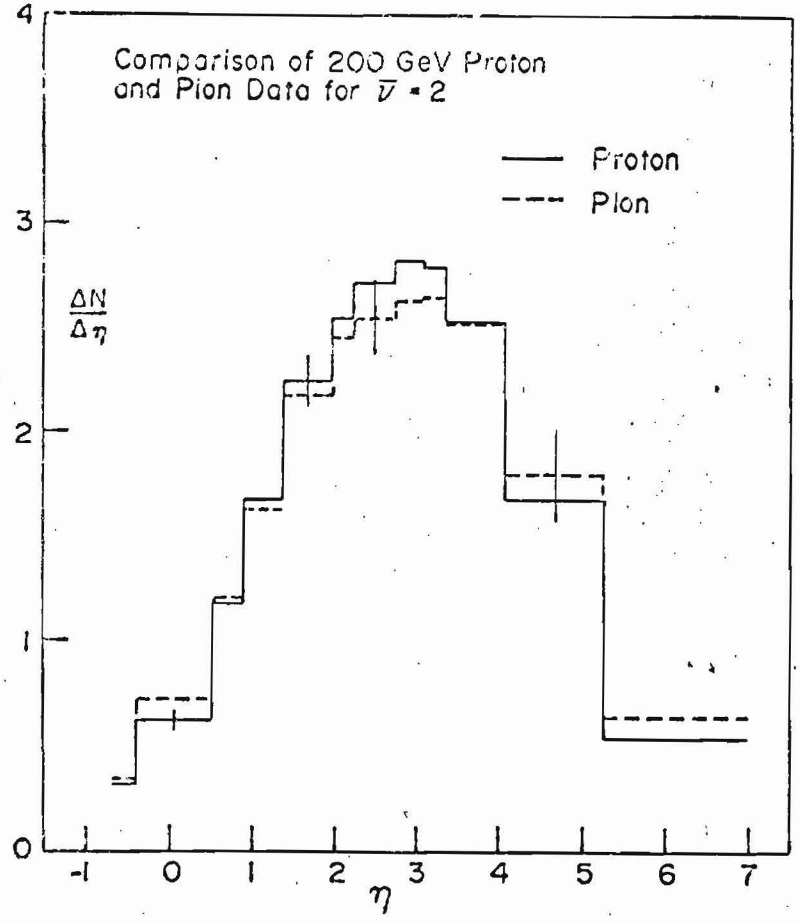

FIGURE IV-24

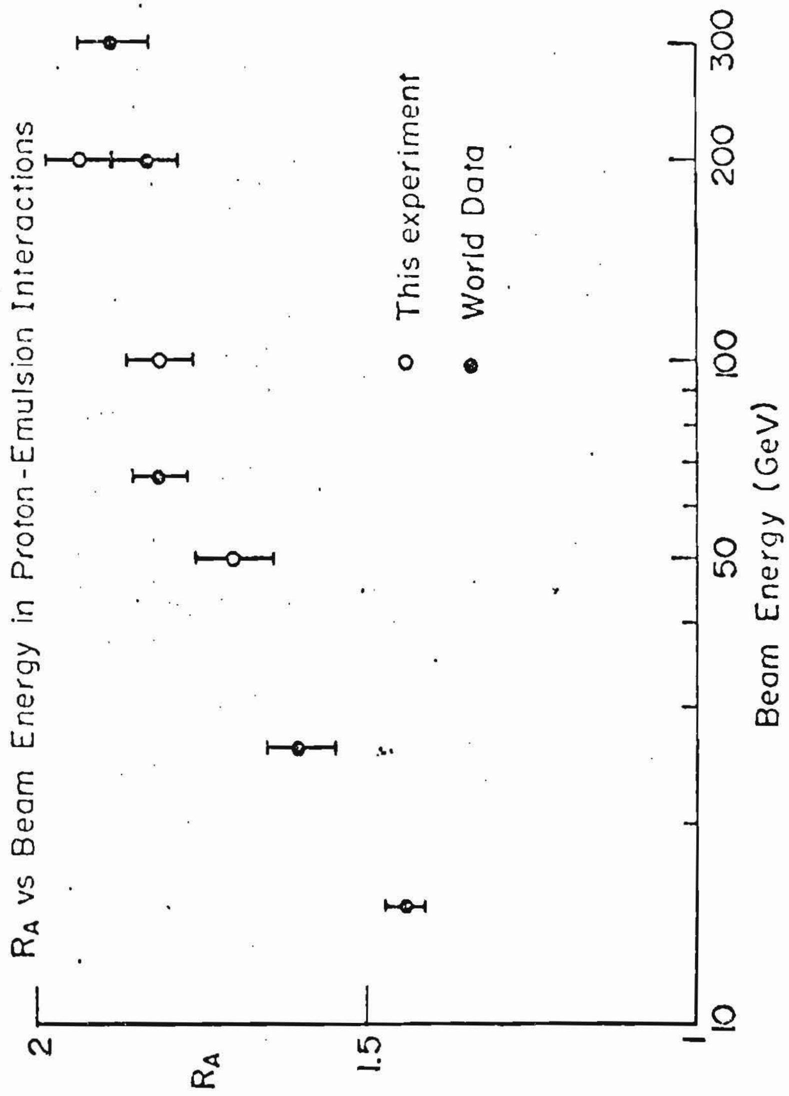

FIGURE IV-25

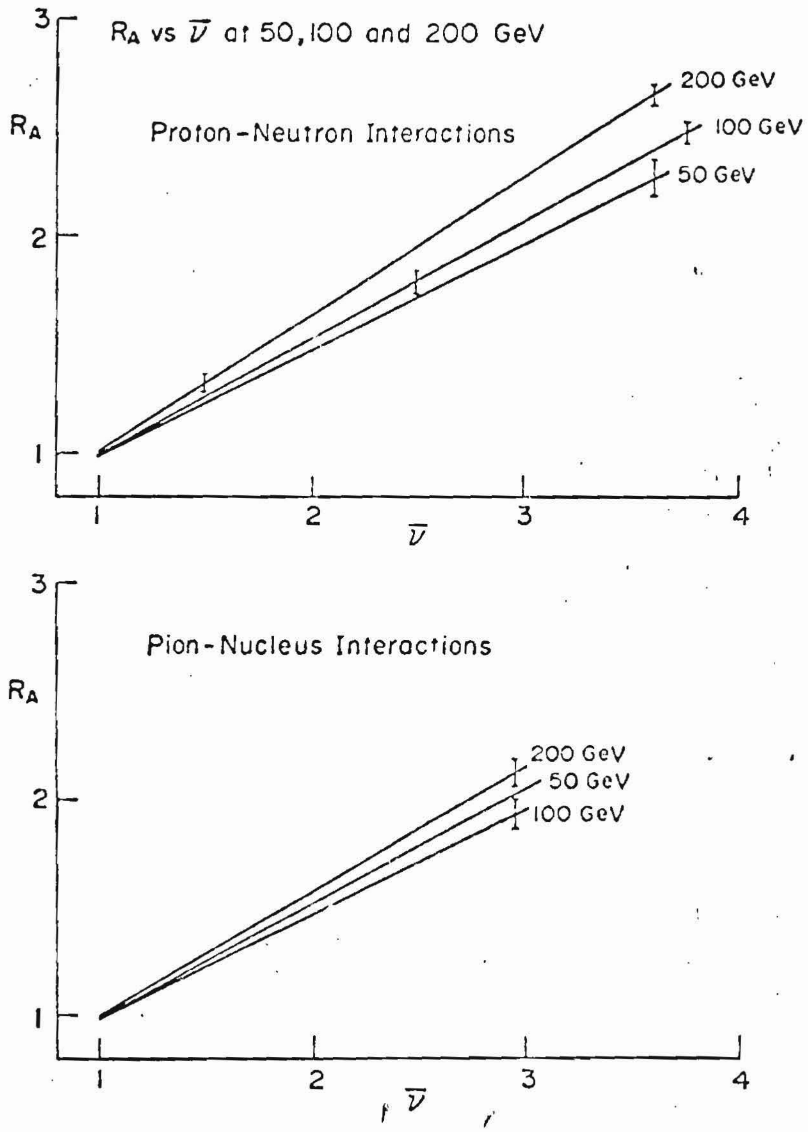

FIGURE IV-26

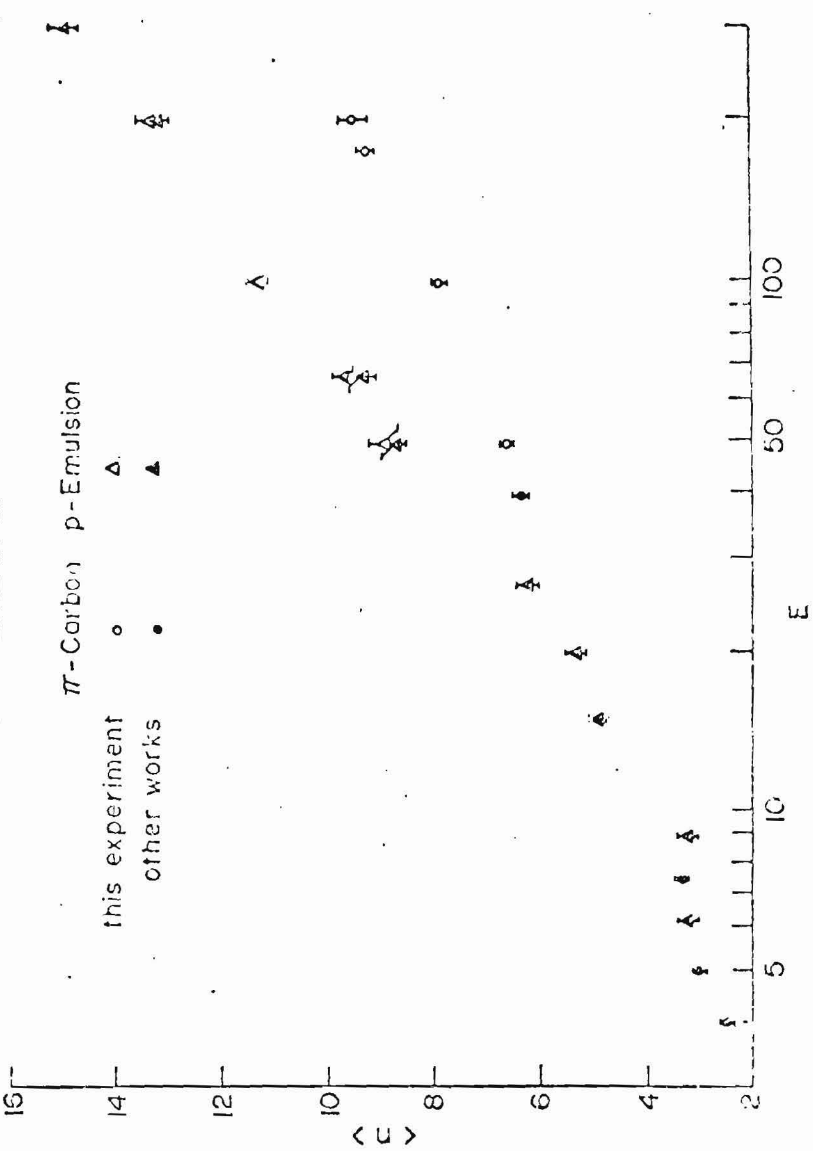

FIGURE IV-27

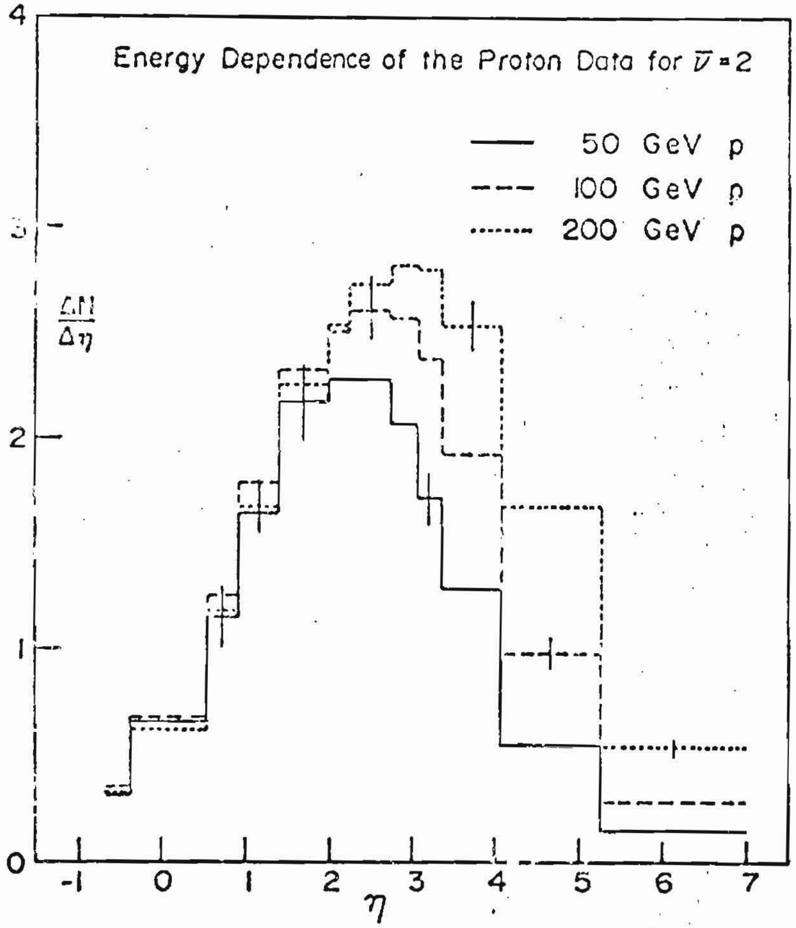

FIGURE IV-28

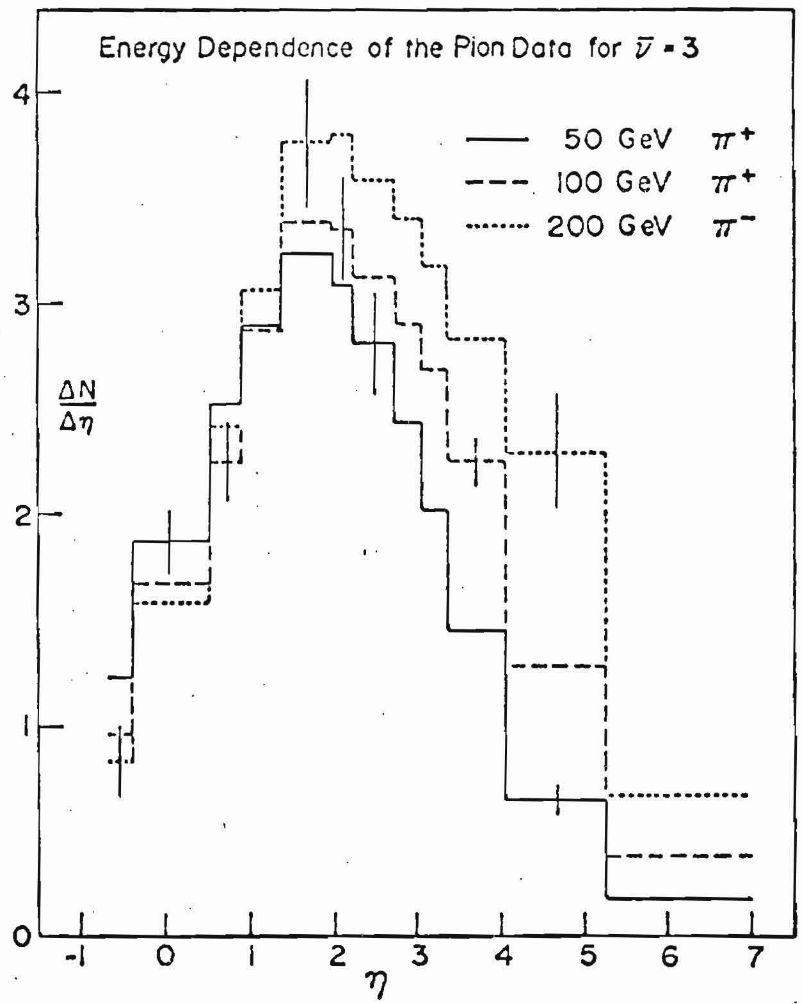

FIGURE IV-29

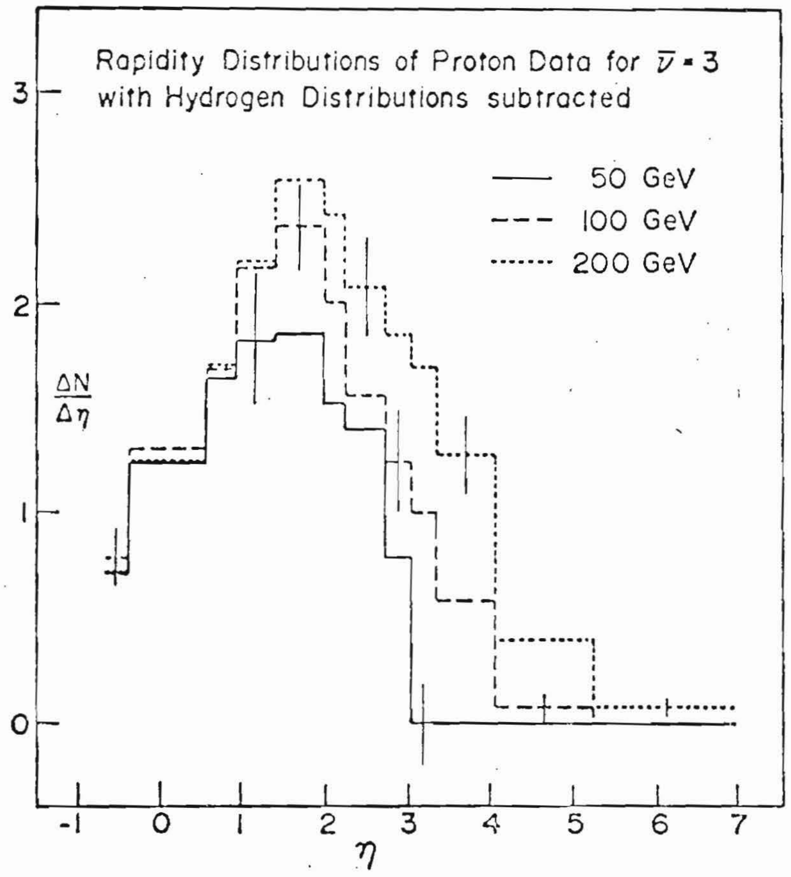
Rapidity Distributions of Proton Data for $\overline{\nu} = 3$ with Hydrogen Distributions subtracted
50 GeV
100 GeV
200 GeV
$\frac{\Delta N}{\Delta \eta}$
0
1
2
3
-1
0
1
2
3
4
5
6
7
η

CHAPTER V

COMPARISON WITH MODELS

The discussion here will be focussed on those models of hadron interaction that make definite predictions about hadron-nucleus collisions. They include the hydrodynamic[1] and energy flux cascade models,[7] the two-fireball model,[10] the parton[8] and multiperipheral models[3] and Reggeon field theory.[9] The last 3 are very similar in their simplified forms and will be discussed together as though they were identical. The coherent tube model[58] will be examined for the sake of comparison. An interesting idea due to Białkowski, Chiu and Tow[59] will also be discussed. The above by no means exhausts the list of all models.[60]

It should be emphasized that the discussion will be conducted almost exclusively at a qualitative and sometimes naive level. Only the simplified versions of the models will be considered. The discussion of the more sophisticated versions and the fitting of their free parameters have been undertaken by the proponents of these theories and can be found in the literature. Some of the results and their references are contained in Appendices X through XV. Until the models have been developed further and the data have become more precise, such a course of action is only marginally instructive.

Before a comparison of the theories with experimental data is undertaken, some cautionary remarks are in order. The assumptions of some theories are obviously invalid in the energy range of 100 GeV. These assumptions represent the belief, not always founded on solid evidence, of the authors of these models as to what should or might happen in the oft-mentioned but ill-defined asymptotic energy range.

One obvious example is the flat and constant rapidity plateau that is assumed to exist in proton-proton interactions. This is an input to the simplest version of the energy flux cascade model, and is an immediate result in the multiperipheral model. However, there is no obvious plateau even at the energies of the CERN Intersecting Storage Ring (ISR); furthermore, the height of the central region increases with energy.

Another example is the energy dependence of the proton-proton average multiplicity. It is often assumed to be given simply by $\langle n\rangle = b \ln s$. But at 100 GeV, the correction to this formula is substantial, i.e. $\langle n\rangle = a + b \ln s$ is a much better fit to the data and $\frac{a}{\langle n\rangle}$ is not small at 100 GeV.[61]

Models and theories tend to idealize and oversimplify situations as indeed they must. It then becomes important to examine the applicability of these idealized situations to actual experimental conditions. The hydrodynamic and energy flux cascade models assume some kind of central collision as the norm. The beam particle and the target nucleon coalesce into 1 single object which eventually evolves into the final state hadrons. The multiperipheral model and the two-fireball model assume that peripheral or grazing collisions are dominant. Something resembling the initial hadrons are present shortly after the collision. Nature's way of doing things is probably intermediate between these two extremes.

Hence, comparisons of theoretical predictions with the experimental data may pertain more to the assumptions of the model than its dynamics.

With the exception of the coherent tube model, all the models that are considered here have one property in common. They assume that there are multiple collisions in a hadrón-nucleus interaction. The identity and the properties of the object(s) that undergo(es) these collisions are, of course, model dependent. These models are sometimes known generically as models with "repeated collisions."

All the models have a built-in mechanism for suppressing the catastrophic cascading within a nucleus that necessarily results from the instantaneous production of the final state hadrons. This is achieved in various ways, which sometimes differ only semantically.

The hydrodynamic and energy flux cascade models postulate that the immediate product of a hadronic collision must act as a single object, which can only be described by collective variables since the many final state hadrons cannot fit into the space occupied by two Lorentz-contracted hadrons. The degrees of freedom are therefore suppressed and particle cascading avoided. The two-fireball model may be considered as a special case where the collective variables to be used are the same ones that described the initial state hadrons.

The parton model asserts that the constituents (partons) of the final state hadrons exist immediately after a collision. There is no packaging difficulties since the partons are assumed to be point-like. However, the time required for these constituents to re-arrange themselves into physical hadrons is large. And since the properties of the partons are different from hadrons, cascading can be easily avoided.

The coherent tube model neatly sidesteps the entire issue by equating a hadron-nucleus collision at one energy with a hadron-nucleon collision at another (higher) energy. Cascading within a nucleus is, by assumption, impossible.

Beyond this one common bond of a weak atomic number dependence of the average multiplicity in a hadron-nucleus collision, the models are different and few general statements can be made that apply to all of them. Attention will now be focussed on these models individually. Their predictions on hadron-nucleus interactions will be compared with the data of this experiment. Constraints imposed on these models by hadron-nucleon results can be found in the Appendices where the models are discussed in greater detail.

Landau's one-dimensional non-viscous hydrodynamic model predicts that $R_A=A^{0.19}$ and that R_A is energy independent. The data are best fitted by $R_A=0.9A^{.16}$ and exhibit a very slow but definite increase with energy. The pseudorapidity distributions can be fitted by letting the velocity of sound c_o to be a free parameter. $c_o^2=1/7.5$ yields a reasonable fit. Note that this value for the velocity of sound is not that used to predict an $A^{0.19}$ dependence; $c_o^2=1/3$ was used. In its simple form, the model predicts that all hadrons behave alike and should have the same multiplicities and inclusive distributions. This is a result of not considering the conservation and other effects of quantum numbers (besides energy-momentum). Further discussions on the hydrodynamic model can be found in Appendix X.

The energy flux cascade model predicts an energy independent $R_A=2/3+1/3\bar{\nu}$. The data are best fitted by $R_A=0.43+0.56\bar{\nu}$ with a weak energy dependence. The extra multiplicity from the repeated collisions are expected to populate only the lower 1/3 of the rapidity distribution

at all energies. This is in disagreement with the data. However, the predictions are sensitive to some input parameters and the model cannot be ruled out. See Appendix XI for a more detailed discussion on the energy flux cascade model and the variations in its predictions for different input parameters.

The family of parton-multiperipheral models make mostly qualitative predictions, which are in reasonable agreement with the data. For example, the increase in multiplicity as a function of the atomic number of the target nucleus is expected to be distributed over essentially the entire rapidity range with the enhancement being most prominent in the target fragmentation region. Even though the data have no obvious central and fragmentation regions, the pseudorapidity distributions can be described this way. More definitive comparisons can only be made with specific versions of these models. This is done in Appendix XII.

The two-fireball model predicts an energy-independent $R_A=1/2+1/2\bar{\nu}$ which is compatible with experimental results. However, it would be very surprising that the asymptotic prediction should hold at the energy range under consideration. In principle, R_A as a function of $\bar{\nu}$ should be different for p, K and π beams, but the predicted differences are smaller than the experimental uncertainties. See Appendix XIII for further comments on this model.

The coherent tube model predicts $R_A = A^{1/12}$, which is to be compared with the experimental result of $R_A = 0.9A^{.16}$. The predicted rapidity distributions are much flatter than the observed pseudorapidity distributions. However, the model cannot be completely ignored for two reasons. First, the model's predictions concern only the produced pions and cannot be expected to include the effects of fast knockout protons. Secondly, because of its unique assumptions concerning the target nucleus, the approximation of y with η is expected to be much worse than in a proton-proton collision. See Appendix XIV for a further discussion of this model.

These comparisons of theoretical predictions with experimental data have been summarized in Table V-1. Only the predictions at "asymptotic" energies have been tabulated. The multiperipheral model is omitted from the table because of the qualitative nature of its predictions.

It will be noticed that none of the models is in complete agreement with the data. This is not surprising. It appears that all the models can be made compatible with the data by judicious modifications to the theory, as noted in Appendices IX through XIV. These modifications are, of course, more serious with some models than others. Suffice it to say that none of the above models can be definitely ruled out, nor is there a clear favorite.

An interesting and novel hypothesis has been put forward by Białkowski, Chiu and Tow.[59] Hadrons are assumed to be produced instantaneously but cannot initiate a hadronic cascade because they are "immature." The maturity rate, which is characterized by some time scale τ, is enhanced in the presence of strongly interacting particles. This is assumed to be an intrinsic property of hadrons, whose cross-sections now have a time-dependent factor $(1-e^{-t/\tau})$. The data of this experiment can be fitted by picking an appropriate "induced maturity rate." Appendix XV contains a further discussion of this hypothesis.

TABLE CAPTIONS

V-1 Comparison of data with the asymptotic predictions of models. Only the simple versions of the models are considered here. More detailed discussions and comparisons can be found in Appendices X through XIV.

TABLE V-1

Comparison of Data With Predictions of Models

	Data	Hydro-dynamic	Energy Flux Cascade	Two-Fireball	Coherent Tube
R_A versus $\bar{\nu}$	$(0.43 \pm .02)$ $+(0.56 \pm .01)\bar{\nu}$	---	$\frac{2}{3} + \frac{1}{3}\bar{\nu}$	$\frac{1}{2} + \frac{1}{2}\bar{\nu}$	---
R_A versus A	$0.9A^{.16}$	$A^{.19}$	---	---	$A^{1/12}$
R_A versus E	increasing slowly	independent	independent	independent	independent
p versus π beam (same $\bar{\nu}$)	indistinguishable	identical	identical	very similar	identical
Location of extra multiplicity as $\bar{\nu}$ increases	confined to region of low pseudorapidity	can be fitted by $c_o^2 = 1/7.5$	restricted to rapidities less than 1/3 of maximum	restricted to rapidities less than ∼1/2 of maximum	input to the theory
Location of extra multiplicity as E increases	moves to region of higher pseudorapidity	same as above	same as above	same as above	same as above

CHAPTER VI

CONCLUSION

The results of this experiment (in the energy range 50 to 200 GeV) can be summarized as follows:

(1) The average charged multiplicity in hadron-nucleus collisions depends linearly on the parameter $\bar{\nu}(=\frac{A\sigma_{hp}}{\sigma_{hA}})$, i.e. $\langle n\rangle_{hA}=c+d\bar{\nu}$ where the values of c and d depend on the identity of the beam particle as well as the beam energy.

(2) In proton and pion initiated reactions, the relation between the multiplicity ratio $R_A(=\frac{\langle n\rangle_{hA}}{\langle n\rangle_{hp}})$ and the parameter $\bar{\nu}$ can be adequately represented by a universal energy-independent function: $R_A = (0.43\pm0.02) + (0.56\pm0.01)\bar{\nu}$. The kaon and anti-proton data are also consistent with this parameterization.

(3) The shapes of pseudorapidity distributions appear to depend only on the parameter $\bar{\nu}$.

(4) The increase in multiplicity as a function of beam energy is predominantly in the region of high pseudorapidity.

(5) The increase in multiplicity as a function of the size of the target nucleus is confined to the region of low pseudorapidity.

(6) The region of this enhancement increases with beam energy and extends to higher values of pseudorapidity.

(7) The dispersion and the average charged multiplicity in pion-nucleus collisions are linearly related: $D\sim0.5\,\langle n\rangle$. This parameterization is also consistent with π-p data. Heavy liquid bubble chamber results and the data from emulsion experiments suggest that this relationship also holds for other beam particles.

While these results are not explicit confirmation or refutation of any particular model, they impose constraints on the theoretical pictures of strong interaction. The first three points indicate that $\bar{\nu}$ is probably a relevant parameter. This favors models which have repeated collisions between nucleons and a projectile that retains the quantum members of the beam particle throughout the entire interaction.

The last point argues for a non-zero rapidity correlation. f_2 $(=D^2-\langle n\rangle)$ would be zero in the absence of all correlations. The fact that R_A does not decrease with energy (point (2)) and the fact that the target-dependent part of the pseudorapidity distribution goes out in η as the energy increases (point (6)) are indications that there are explicit long-range rapidity correlations.

It appears that hadron-nucleus experiments offer a unique way of probing the early development of hadronic interactions and are capable of putting constraints on models of hadron-hadron collisions. It is unfortunate though expected that a "first generation" experiment cannot completely refute any of the models.

Future experiments on this subject should be more sophisticated. However, the general approach should still be dictated by an attitude of searching for information as opposed to attempting to confirm or refute one particular theory -- there is little evidence that any theory at present deserves such attention. This may be contrasted with one's attitude towards quantum electrodynamics (QED).

Several approaches are possible and there is no a priori reason for picking one over another. For example, the properties of one of the secondaries can be examined in great detail and the associated pseudorapidity distribution measured. The leading particle or a high p_t particle appears to be a logical candidate for the one secondary studied in detail.

Another possible approach would involve identifying the protons among all the secondary particles, since models are usually incapable of predicting the behavior of these knock-out protons and concentrate instead on pions. Such an experiment has been proposed[62] for the SPS facility

at CERN.

The study of 2 particle correlations is useful. However, it probably needs to be done with rapidity as the variable; pseudorapidity is not necessarily a reasonable approximation. There is no fundamental reason to believe that the correlation function in pseudorapidity should at all resemble the correlation function in rapidity. In fact, the validity of such an approximation requires a knowledge of the rapidity correlation function and the transverse momentum distribution.

The simultaneous measurements of 2 sets of 4-momenta are certainly within the capabilities of present-day techniques. However, such an undertaking may not be practical. One could use large acceptance spectrometers. However, the existing devices do not have the resolution required by the high average multiplicities (≥15-20 charged secondaries per event). Two spectrometers with small acceptances can avoid this problem. The low rates of such a set-up are unacceptable for experiments intended as surveys. It appears that the measurements of 2-particle rapidity correlations as well as rapidity distributions have to await the development of new detectors.

A third approach is the measurement of multiplicity distributions. The widely-held belief that KNO scaling[63] is satisfied in hadron-nucleus interactions is founded on less-than-overwhelming evidence.

Obtaining the (pseudo)rapidity distributions for low- and high-multiplicity events can serve to test and differentiate between the various versions of 2-component models. This is possible with the data from this experiment. However, the conclusions will probably be clouded by the ambiguities in the definition of a "low-multiplicity" event.

However, before embarking on any of the proposed experiments, one needs an answer to the important question: Is there anything to be learned from the short-time behavior of a hadronic system that cannot be learned by studying only the asymptotic final state? An unambiguous and unequivocable answer is highly model-dependent and involves pure speculation. It will be argued, with the aid of an analogy, that such an investigation has great potential.

Consider the (almost) elastic scattering of a ping pong ball from a ping pong table. By observations of the unaided eye as well as by examining the pictures of this interaction taken with the aid of strobe lights, it is generally believed that the ping pong ball and the table actually make contact. The ball becomes squashed in the process. It then regains its spherical shape as it rebounds from the table. The scattering is a result of actual physical contact between the objects and momentum is transferred in the deformation process.

If the people who investigated this phenomenon were restricted to examining the asymptotic states (i.e. the ping pong ball approaching and receding from the table) our understanding of the scattering process might be quite different. If these early investigators were so restricted (say, by the lack of stroboscopic equipment and/or poor eyesight) and if they were equipped with today's models of hadronic interactions, it is not inconceivable that they might conclude that the scattering is best described by the exchange of a Pomeron or some equivalent object. This would set physics (and the game of ping pong) back many years.

Few people today subscribe to the view that ping pong ball-ping pong table scattering is mediated by a Pomeron, because the immediate vicinity of the interaction can be and has been examined in detail. The results of these investigations have led us away from such a picture of the scattering process.[64]

The analogy with hadronic interactions is, of course, not perfect, but this example of an everyday scattering process serves as a rather persuasive argument for continued research into the early behavior of hadronic systems.

ACKNOWLEDGEMENTS

This experiment started in 1973 and is now coming to an end. Although it is a relatively modest project, many people have been involved in it and I would like to thank every one of them.

My thesis supervisor, Dr. W. Busza, first conceived of the experiment. Without his novel pulse height technique for measuring the charged multiplicity, the experiment could not have been done. His help and instruction during the various stages of my graduate career are greatly appreciated.

E. Druck, G. Krey, T. Lyons, S. Redner and Dr. M. Sogard were of great help in the initial design of the apparatus. I thank the staff of the Brookhaven National Laboratory for help in the testing of the equipment.

Other participants in the first part of the experiment include Dr. J. Elias, Dr. D. Jacobs and P. Swartz, without whom the experiment could not have been completed. The aid of the Fermilab staff, especially Dr. S. Ecklund, Dr. P. Koehler and other Meson Laboratory personnel, is gratefully acknowledged. Special thanks are due to my fellow graduate student P. Swartz for many useful discussions and much help in the analysis. I would like to express my thanks to the collaborators in Experiment Numbers 69 and 96 at Fermilab for their cooperation.

There were several new participants in the second part of the experiment. Dr. D. Luckey was of great help, especially during the set-up and data-taking stages. Dr. C. Halliwell wrote the on-line computer programs and was also of assistance in the analysis. Their help is greatly appreciated. Also involved in this part of the experiment was my fellow graduate student L. Votta, without whom the experiment could not have been carried out.

I would like to thank the staff in the Laboratory for Nuclear Science at the Massachusetts Institute of Technology for their aid throughout the experiment. The author is indebted to S. Anand for her indefatiguable secretarial work. C. Bolon's help in the data analysis was invaluable. The assistance of D. Dubin, Dr. B. Nelson and Dr. R. Verdier is also appreciated. I would like to thank M. Jacob and R. Strong for their technical support throughout the experiment. G. Rowe and C. Tourtellote's cheerful preparation of the many drawings in this thesis is gratefully acknowledged. C. Smith's help is deeply appreciated.

I would like to thank Dr. B. Andersson, Dr. C. DeTar, Dr. K. Gottfried and Dr. L. Rosenson for many useful discussions, and the members of my thesis committee, Dr. W. Busza, Dr. V. Kistiakowsky and Dr. L. Osborne, for many discussions and suggestions.

My fellow graduate students, W. Aitkenhead and

W. Toy, offered much help and encouragement, and made my years at the Massachusetts Institute of Technology more enjoyable. The encouragement of Dr. D. Barton, Dr. G. Brandenburg, Dr. J. Friedman and Dr. H. Kendall is gratefully acknowledged.

Finally, I would like to thank Dr. F. Sciulli of the California Institute of Technology for introducing me to the field of high energy physics.

APPENDIX I

Definition of $\bar{\nu}$

$\bar{\nu}$ is defined as the average number of absorption mean free paths that a given target nucleus presents to an incident particle. Equivalently, it is defined as the average number of absorption collisions that the incident particle undergoes as it traverses the nucleus, provided that the incident particle (or an exact replica of it) re-emerges from each of these collisions. The proviso appears to be incompatible with an absorptive collision, but it is essential for the two definitions to be equivalent. The proviso simply states that there are no screening effects.

Let σ_N be the absorption cross-section of the incident hadron on a nucleon, and let σ_A be the absorption cross-section of the same incident hadron on a nucleus of atomic number A. The probability that the incident particle will interact with any given nucleon in the nucleus is proportional to σ_N. The average number of such collisions is therefore proportional to $A\sigma_N$. The proportionality constant is simply σ_A, the probability that the incident particle will interact at all with the nucleus. Hence[65]

$$\bar{\nu} = \frac{A\sigma_N}{\sigma_A}$$

Notice that the definition of $\bar{\nu}$ involves only the classical concept of a mean free path. One should therefore be able to calculate $\bar{\nu}$ by considering a purely classical experiment. Take the following. Fill a box (the nucleus) with A ping pong balls (nucleons). Let high-velocity bullets (incident beam) scatter off this box. Further assume that the box itself is transparent to the bullets. Translated to the language of hadron-nucleus interactions, this simply states that the nucleus is made of nucleons, which are bound to one another without an extraneous retaining wall. The bullets emerge from each "absorption" collision essentially unscathed because of their high velocity. The average number of shattered ping pong balls is, by definition, $\bar{\nu}$. In this particular experiment, it is obvious that $\bar{\nu}$ is given by the ratio of areas (which are also the cross-sections), i.e.

$$\bar{\nu} = \frac{\text{A x (cross-section of a ping pong ball)}}{\text{(cross-section of the box)}}$$

When translated to the language of hadron-nucleus collisions, this gives the formula derived above.

The actual number of absorption mean free paths that an incident hadron sees at a given impact parameter is, in general, different from $\bar{\nu}$. Let this value be ν. Let $P(\nu)$ be the (normalized) probability of having the value ν.

Then

$$\bar{\nu} = \sum_{\nu=1}^{A} \nu P(\nu)$$

While $P(\nu)$ depends on the nucleon distribution within the nucleus, $\bar{\nu}$ depends only on the ratio of cross-sections, as demonstrated above. Given the nucleon distribution, one could calculate $P(\nu)$ and also $\bar{\nu}$.

Let the nucleus be represented by a continuous nuclear density $\rho(\vec{r})$. Note that the discrete nature of the nucleons is ignored. At an impact parameter $\vec{b}$, the target thickness is $l(\vec{b})$, where

$$l(\vec{b}) = \int_{-\infty}^{+\infty} \rho(\vec{r})\, dz .$$

The probability of interacting exactly ν times at this impact parameter is then given by the Poisson distribution of mean $\sigma_N l(\vec{b})$, where σ_N is the absorption cross-section on a nucleon. Integrating over all impact parameters, one obtains the (unnormalized) ν distribution

$$P(\nu) = \int_0^{\infty} \frac{(\sigma_N l(\vec{b}))^{\nu} \exp(-\sigma_N l(\vec{b}))}{\nu !}\, d^2b$$

Obtaining the normalized distribution is straight forward.

This calculation has been carried out for a Wood-Saxon distribution of nuclear matter:[66]

$$\rho(r) = \rho_0 \left(1 + \exp\left(\frac{r-R}{s}\right)\right)^{-1}$$

where $s = 0.54$ fermi

$R = (0.978 + 0.0206\, A^{1/3})\, A^{1/3}$ fermi

$$\rho_0 = \frac{3A}{4\pi R^3}\left(1 + \frac{\pi^2 s^2}{R^2}\right)^{-1}$$

The form of ρ_0 is chosen to yield the proper normalization:

$$\int_0^\infty \rho(r)\, d^3r = A$$

σ_N is assumed to be 32.3 and 21.2 millibarns (mb) for a proton and a pion beam respectively. The results of this calculation are shown in Figures A-I-1 and A-I-2. The lines are hand drawn curves to guide the eye. A Monte-Carlo simulation technique was used to confirm these values of P(ν). The two calculations agree. Note that even for the heaviest element available (uranium) P(1) is the peak of the distribution. In other words, the most likely value of ν is always 1. This is a result of the diffuse edge assumed in the nuclear matter density ρ(r). The distributions P(ν) would, of course, be different if one assumes some other form for the nuclear matter density or if one takes a model of the nucleus with discrete nucleons.

Knowing P(ν), one could then calculate $\bar{\nu}$. The values of $\bar{\nu}$ so obtained are within 5 % of those obtained using the formula $\frac{A\sigma_N}{\sigma_A}$, where σ_A is taken from Reference 19. The values of $\bar{\nu}$ used in the analysis of this experiment are obtained from the latter formula.

In general, both P(ν) and $\bar{\nu}$ are functions of energy. However, in the limited range of 50 to 200 GeV, σ_N is effectively independent of energy. Therefore it follows that P(ν) and $\bar{\nu}$ are also independent of energy. The formulae for calculating $\bar{\nu}$ are given in Table A-I-1, and the values of $\bar{\nu}$ for the various targets and projectiles are presented in Table A-I-2. Since there are no published $\bar{p}$-nucleus absorption cross-sections at high energy, they have been arbitrarily taken to be the same as proton-nucleus cross-sections.

TABLE CAPTIONS

A-I-1 Formulae for $\bar{\nu}$. The proton-nucleon cross-sections are the average of 102 and 205 GeV/c data from References 43 and 31 respectively. The K-p cross-section is an average of 32 GeV/c data (Reference 20) and 100 GeV/c data (Reference 44). The π-p cross-section is an average of the results given in References 20, 22, 41 and 42. The hadron-nucleus cross-sections are from Reference 19.

A-I-2 $\bar{\nu}$ as a function of beam particle and target nucleus. The tabulated errors do not include the error on σ_N, which is an overall scale factor for each of the different beam particles.

FIGURE CAPTIONS

A-I-1 $\bar{\nu}$ distributions in proton-nucleus interactions calculated with a Wood-Saxon distribution of nucleons -- see text for details. The lines are drawn to guide the eye.

A-I-2 Same as above but for pion-nucleus interactions.

TABLE A-I-1

	$p/\bar{p}$	K^+	π^+/π^-
σ_N(mb)	$32.5\pm.5$	15 ± 2	$21.2\pm.5$
Fit to σ_A(mb)	$(46.5\pm0.6)A^{(.691\pm.004)}$	$(22.6\pm.9)A^{(.767\pm.013)}$	$(30.7\pm1.2)A^{(.728\pm.012)}$
Formula for $\bar{\nu}$	$0.695A^{.309}$	$0.664A^{.233}$	$0.692A^{.272}$
Scale uncertainties due to errors on σ_N	2%	13%	3%

TABLE A-I-2

Element	Atomic No.	$\bar{\nu}(p,\bar{p})$	$\bar{\nu}(K^+)$	$\bar{\nu}(\pi^+,\pi^-)$
H	1	1.00	1.00	1.00
Be	9	1.37±0.2	1.10±.15	1.26±.04
C	12	1.50±.03	1.19±.16	1.36±.04
Al	27	1.92±.03	1.43±.19	1.70±.05
Ti	48	2.29±.04	1.64±.22	1.98±.06
Cu	64	2.50±.04	1.75±.24	2.14±.07
Mo	96	2.84±.05	1.92±.26	2.40±.08
Ag	108	2.95±.05	2.98±.27	2.48±.08
W	184	3.47±.07	2.24±.31	2.86±.11
Pb	207	3.61±.07	2.30±.32	2.96±.12
U	238	3.76±.08	2.38±.33	3.07±.12
Emulsion		2.45±.05	1.74±.24	2.12±.06

FIGURE A-I-1

ν DISTRIBUTION FOR P-A INTERACTIONS

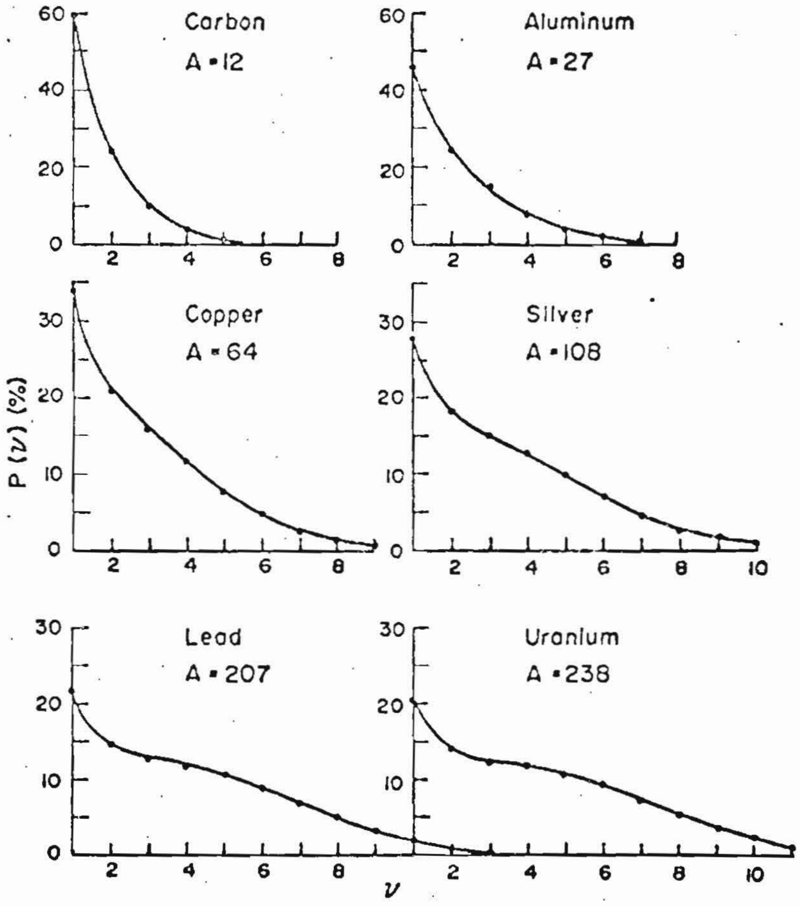

FIGURE A-I-2

ν DISTRIBUTION FOR π-A INTERACTIONS

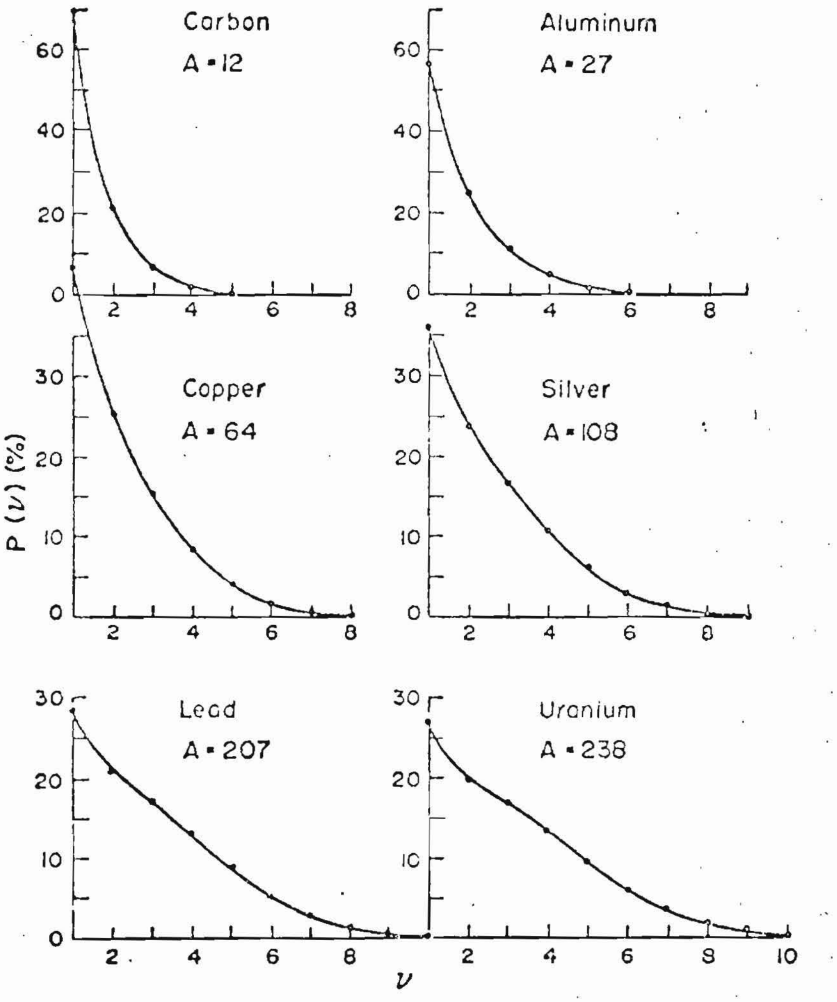

APPENDIX II

Rapidity and Pseudorapidity

The longitudinal kinematic variable used in many models on hadronic interactions is the rapidity y defined as

$$y = \frac{1}{2} \ln \left(\frac{E + P_{11}}{E - P_{11}}\right)$$

The transverse variable is $P_{\perp}$, the transverse momentum. The invariant cross-section is $Ed^3\sigma/dp^3$, which can also be written as $(1/\pi)d^3\sigma/dP_{\perp}{}^2dy$. Integrating over $P_{\perp}$, one obtains $d\sigma/dy$, the one-particle inclusive cross-section as a function of rapidity. It satisfies the normalization

$$\int \frac{1}{\sigma} \frac{d\sigma}{dy}\, dy = \langle n \rangle$$

where <n> is the average multiplicity.

While the Feynman scaling variable $x = 2P_{11}{}^{*}/\sqrt{s}$, where $P_{11}{}^{*}$ = longitudinal momentum in the center-of-mass frame and $\sqrt{s}$ = energy in the center-of-mass frame, is useful for examining the high momentum region (i.e., $x \sim 1$), the rapidity y is useful for looking at the central region (i.e. $x \sim 0$). Figure A-II-1 shows the relationship between x and y for various values of the transverse mass μ in a 100 GeV/c proton-proton collision, where $\mu = \sqrt{m^2+P_{\perp}{}^2}$. For

μ = 0.4 GeV, the average value in a p-p collision, the region $x>0.5$ is mapped into just 1 unit of rapidity; while the region $0<x<0.1$ is mapped into 1.5 units of rapidity. In other words, the rapidity variable opens up the central region while x expands the high-momentum region.

While rapidity has the advantage of magnifying the central region, it has, in practice, a serious drawback. From its definition, it is obvious that one needs to determine the 4-momenta of a particle in order to find its rapidity. To do this in a multiparticle experiment, where there may be as many as 30 prongs, is extremely difficult. It requires the ability to track all the particles through magnetic fields to find their momenta. Mass (or velocity) determinations would also have to be made. Therefore one needs a system of Cherenkov counters, time-of-flight counters, electron shower counters, muon counters, etc., capable of resolving some thirty particles. The system must also be able to recognize decay products of unstable secondaries. This is a formidable task.

Fortunately, the pseudorapidity variable, η, is a good approximation to y, and its determination involves only the measurement of the polar angle:

$$\eta = -\ln \tan \left(\frac{\theta}{2}\right)$$

The approximation is valid whenever $<P_\perp^2> >> m^2$, which holds on the average. The use of this variable greatly simplifies the experiment. Neither momentum nor mass determination are necessary.

The connection between y and η will now be derived. Their Lorentz transformation properties will also be discussed.

The rapidity y is defined as

$$y = \frac{1}{2} \ln \left(\frac{E + P_{11}}{E - P_{11}}\right)$$

Taking the exponential and re-arranging terms, one obtains the equivalent definitions:

$$y = \sinh^{-1} \left(\frac{P_{11}}{\mu}\right)$$

$$y = \cosh^{-1} \left(\frac{E}{\mu}\right)$$

and

$$y = \tanh^{-1} \left(\frac{P_{11}}{E}\right) = \tanh^{-1} (\beta_{11})$$

where $\mu = \sqrt{m^2 + P^2}$ = transverse mass.

The definition of pseudorapidty

$$\eta = -\ln \tan \left(\frac{\theta}{2}\right)$$

can be manipulated to give:

$$\eta = \sinh^{-1}\left(\frac{P_{11}}{P_\perp}\right)$$

$$\eta = \cosh^{-1}\left(\frac{P}{P_\perp}\right)$$

and

$$\eta = \tanh^{-1}\left(\frac{P_{11}}{P}\right).$$

It should be apparent that the definitions of y and η are equivalent in the limit $m^2/P_\perp^{\,2}$ becoming very small. To examine this in greater detail, use the definitions involving inverse hyperbolic tangents.

Expand the inverse hyperbolic tangent in a power series:

$$\tanh^{-1}(Z) = Z + \frac{1}{3} Z^3 + \frac{1}{5} Z^5 + \ldots \qquad |Z|<1$$

$$\text{So } \eta = \left(\frac{P_{11}}{P}\right) + \frac{1}{3}\left(\frac{P_{11}}{P}\right)^3 + \frac{1}{5}\left(\frac{P_{11}}{P}\right)^5 \ldots$$

$$\text{and } y = \left(\frac{P_{11}}{E}\right) + \frac{1}{3}\left(\frac{P_{11}}{E}\right)^3 + \frac{1}{5}\left(\frac{P_{11}}{E}\right)^5 \ldots$$

$$= \left(\frac{P_{11}}{P}\right)\left(1 - \frac{m^2}{2P^2} + \frac{3m^4}{8P^4}\right)$$

$$+ \frac{1}{3}\left(\frac{P_{11}}{P}\right)^3\left(1 - \frac{3m^2}{2P^2} + \frac{15m^4}{8P^4}\right)$$

$$+ \frac{1}{5}\left(\frac{P_{11}}{P}\right)^5\left(1 - \frac{5m^2}{2P^2} + \frac{35m^4}{8P^4}\right)$$

$$+ \text{ terms of order } \left(\frac{m}{P}\right)^6$$

$$= \eta - \frac{1}{2}\left(\frac{m}{P}\right)^2 \sum_{n\ \text{odd}} \left(\frac{P_{11}}{P}\right)^n + \frac{1}{8}\left(\frac{m}{P}\right)^4 \sum_{n\ \text{odd}} (n+2) \left(\frac{P_{11}}{P}\right)^n$$

$$+ \text{ terms of order } \left(\frac{m}{P}\right)^6$$

The evaluation of an infinite geometric series is well known:

$$S = \sum_{n\ \text{odd}} \left(\frac{P_{11}}{P}\right)^n$$

$$= \left(\frac{P_{11}}{P}\right) / \left(1 - \left(\frac{P_{11}}{P}\right)^2\right)$$

$$= \left(\frac{P_{11}}{P}\right)\left(\frac{P}{P_\perp}\right)^2$$

To evaluate the other infinite series, notice that

$$\sum_{n\ \text{odd}} (n+2)\left(\frac{P_{11}}{P}\right)^n = \left(2 + \left(\frac{P_{11}}{P}\right) \frac{d}{d(P_{11}/P)}\right) S$$

$$= \left(\frac{P_{11}}{P}\right)\left(\frac{P}{P_\perp}\right)^4 \left(3 - \left(\frac{P_{11}}{P}\right)^2\right)$$

Therefore

$$y = \eta - \frac{1}{2}\left(\frac{m}{P_\perp}\right)^2 \left(\frac{P_{11}}{P}\right) + \frac{1}{8}\left(\frac{m}{P}\right)^4 \left(\frac{P_{11}}{P_\perp}\right)\left(3 - \left(\frac{P_{11}}{P}\right)^2\right)$$

$$+ \text{ terms of order } \left(\frac{m}{P}\right)^6$$

Since $\left|\frac{P_{11}}{P}\right| \le 1$, η is a good approximation to y, provided that $(m^2/P_\perp^2) \ll 1$. To check for the validity of this inequality, one needs to find $m^2/\langle P_\perp^2\rangle$. For pions, this ratio is about 1/12,[16] and therefore the approximation of η for y is acceptable. The approximation is worse for heavier particles. Since hadronic products are predominantly pions, the use of η is justifiable. Note that one should compare m^2 with $\langle P_\perp^2\rangle$, not with $\langle P_\perp\rangle^2$.

The relative magnitudes of y and η can be most easily discerned by examining $P_{11} = \mu \sinh(y) = P_\perp \sinh(\eta)$. η is greater (smaller) than y when P_{11} is positive (negative), i.e. the absolute value of η is always greater than the absolute value of y.

This has an interesting consequence. Consider the center-of-mass rapidity of a proton-proton collision. If this distribution is indeed flat as the multiperipheral model would have it, its corresponding pseudorapidity distribution can be obtained if one assumes some transverse momentum distribution and can be shown to exhibit a dip in the central region if transverse momentum is limited. Carruthers and Duong-van[67] have shown that this dip may not "heal" for as much as 2 units of rapidity. Similarly, if the rapidity distribution is Gaussian in shape as predicted by the hydrodynamic model, then the corresponding pseudorapidity distribution would appear much flatter.

Under a Lorentz transformation along the direction

---

of P_{11}, it can be shown that

$$y \rightarrow y^* = y + u$$

where $u = \tanh^{-1}(\beta)$
and β = transformation velocity.

It follows that the rapidity distribution has the same shape and normalization regardless of the reference frame. Indeed its simplicity under a Lorentz transformation is one of the most attractive features of the rapidity variable. The proof is as follows.

Let $P_\pm = E \pm P_{11}$.

Using the definition of y, it can be re-written as

$$P_\pm = \mu e^{\pm y}$$

The transformed quantities, by definition, satisfy the equation

$$P_\pm^* = \mu^* e^{\pm y^*}$$

Under a Lorentz transformation along P_{11},

$$P_\pm \rightarrow P_\pm^* = \gamma(1 \pm \beta)\, P_\pm$$

$$P_\perp \rightarrow P_\perp^* = P_\perp$$

So $\mu^* = \sqrt{m^2 + P_\perp^{*2}} = \sqrt{m^2 + P_\perp^2} = \mu$

Now, $u = \tanh^{-1}(\beta) = \frac{1}{2} \ln (\frac{1+\beta}{1-\beta})$

Therefore, $e^{+u} = \sqrt{\frac{1+\beta}{1-\beta}} = \gamma(1+\beta)$

and $e^{-u} = \sqrt{\frac{1-\beta}{1+\beta}} = \gamma(1-\beta)$

Inserting into the equations for $P_\pm^*$, one obtains

$$\mu e^{\pm y^*} = P_\pm^* = e^{\pm u} P_\pm = e^{\pm u} \mu e^{\pm y}$$

It follows that $y^* = y + u$

The Lorentz transformation properties of η are more complicated, but become greatly simplified when certain assumptions are true. In general,

$$\eta = \sinh^{-1}(P_{11}/P_\perp)$$

transforms to $\eta^* = \sinh^{-1}(P_{11}^*/P_\perp^*)$

$$= \sinh^{-1}(\gamma \sinh \eta \ (1+\beta E/P_{11}))$$

where γ and β are the usual Lorentz factors associated with the transformation. If $(\mu^2/P_{11}^2) \ll 1$, then

$$\sinh(\eta^*) \simeq \gamma(1 + \beta \ (1 + \frac{1}{2} \frac{\mu^2}{P_{11}^2}) \ ) \sinh \eta$$

$$= (\gamma(1+\beta) + \frac{\gamma\beta}{2} \frac{\mu^2}{P_{11}^2} \ ). \sinh \eta$$

The assumption $(\mu^2/P_{11}^2) \ll 1$ implies that η is large, i.e. $\sinh(\eta) \approx e^\eta/2$. This approximation is good to 1% (5%) for particles within 11.4° (25.2°) of the forward direction.

In general, η^* need not be very large. One can still solve for η^* by successive approximation. Taking the natural logarithm on both sides, the lowest order solution is

$$\eta^* = \eta + \ln (\gamma(1+\beta) + \frac{\gamma\beta}{2} \frac{\mu^2}{P_{11}^2})$$

$$\simeq \eta + \ln (\gamma(1+\beta) \ ) + \frac{\beta}{2(1+\beta)} \frac{\mu^2}{P_{11}^2}$$

Note that $u = \tanh^{-1}(\beta) = \ln (\gamma(1+\beta))$

$$\text{So } \eta^* = \eta + u + \frac{\beta}{2(1+\beta)} \frac{\mu^2}{P_{11}^2}$$

Making use of this zeroth order solution, one can then find the first order solution:

$$\eta^* = \eta + u - (1-e^{-2u})e^{-2\eta} + \text{terms of order } (\frac{\mu}{P_{11}})^2$$

In the average 100 GeV/c proton-proton interaction, $\langle\mu^2\rangle \sim 0.4$ GeV^2 and $P_{11}^2 \gtrsim 100$ GeV^2; so the last term can be safely ignored.

Therefore, provided that the energy is dominated by the longitudinal momentum P_{11}, η and y transform the same way:

$$y \rightarrow y + u$$

$$\eta \rightarrow \eta + u$$

where $u = \tanh^{-1}(\beta)$.

The kinematically allowed range of y is most easily determined in the center-of-mass frame:

$$P^*_{11max} = \frac{1}{2}\sqrt{S} = \mu \sinh(y^*_{max})$$

$$y^*_{max} = \sinh^{-1}(\sqrt{S}/2\mu)$$

Therefore the full width in rapidity $Y = 2y^*_{max} = 2 \sinh^{-1}(\frac{\sqrt{S}}{2\mu})$.

For $Y \gg 1$, $\sinh(\frac{Y}{2}) \approx \frac{1}{2} e^{Y/2}$

So $Y \approx 2 \ln(\frac{\sqrt{S}}{\mu}) = \ln(\frac{S}{\mu^2})$

The maximal value of Y is attained when $\mu = m$, i.e. when

$P_\perp = 0$. This value of Y is given in Table A-II-1 for pions, kaons and protons at various beam energies. The approximate formula for Y shows that the kinematic limits for different particles differ by an energy-independent amount. Table A-II-1 shows that this is indeed true.

Figure A-II-2 shows contours of constant y and η in the P_{11}-$P_\perp$ plane. Figure A-II-3 shows contours of constant (η-y). The momenta scales are in units of the rest mass of the particle. When $P_\perp \gtrsim 2M$, y and η agree to within 0.1 unit of rapidity. Also shown in Figure A-II-3 is the line corresponding to $\beta = 0.85$. Particles with momenta lying within that quadrant of a circle are outside the velocity acceptance of this experiment.

To test the validity of the approximation of y with η in actual practice, 100 GeV/c proton-proton data[46] were examined. Figure A-II-4 shows the rapidity and pseudorapidity distributions of the relativistic secondaries ($\beta \geq 0.85$) of those events which have 4 or more charged prongs. These cuts are applied to simulate the conditions of this experiment. The two distributions have similar shapes. The psuedorapidity distribution is displaced slightly to the right of the rapidity distribution. To better illustrate the similarity between y and η, the frequency distribution of their difference, (η-y), is plotted in Figure A-II-5. Figure A-II-6 is the integral distribution. For 90% of the particles, η and y agree to within 0.3 units of rapidity, and only two percent of the secondaries have their rapidity and pseudorapidity differ by more than 1 unit.

TABLE CAPTIONS

A-II-1 The kinematically allowed range of rapidity for pions, kaons and protons as a function of the center-of-mass energy $\sqrt{s}$. E is the equivalent beam energy in a proton-proton collision. Note that $(Y_\pi - Y_K)$ and $(Y_\pi - Y_p)$ are independent of energy.

FIGURE CAPTIONS

A-II-1 The Feyman scaling variable x versus rapidity (pseudorapidity) for different values of μ $(P_\perp)$.

A-II-2 Contours of constant rapidity (dashed lines) and pseudorapidity (solid lines) in the $P_{11}-P_\perp$ plane. Note that the momenta scales are in units of mass.

A-II-3 Contours of constant $(\eta - y)$ in the $P_{11}-P_\perp$ plane. The quadrant of a circle enclosed by the dashed line corresponds to particles with velocity below 0.85 and are therefore outside the acceptance of this experiment.

A-II-4 Comparison of the pseudorapidity distribution (Δ) and rapidity distribution ($\cdot$) in 100 GeV/c proton-proton interactions. A velocity cut of $\beta > 0.85$ has been applied to the data. Also events with any

FIGURE A-II-3

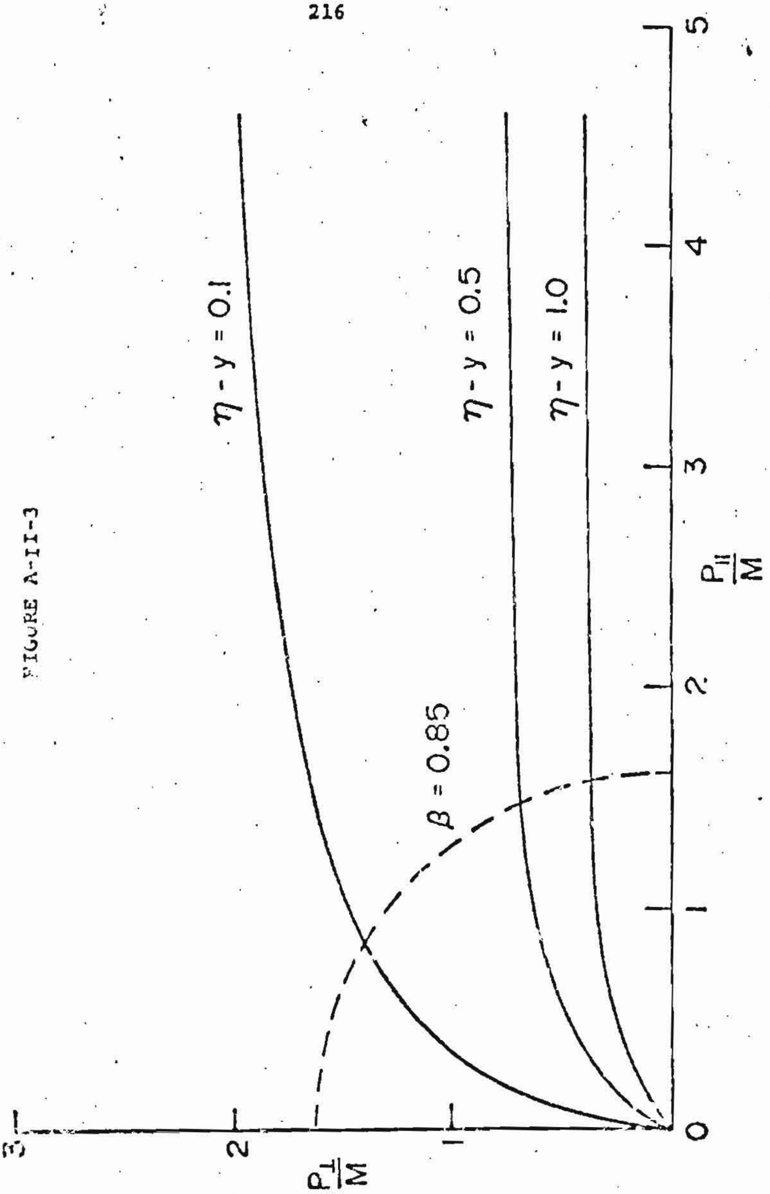

FIGURE A-II-4

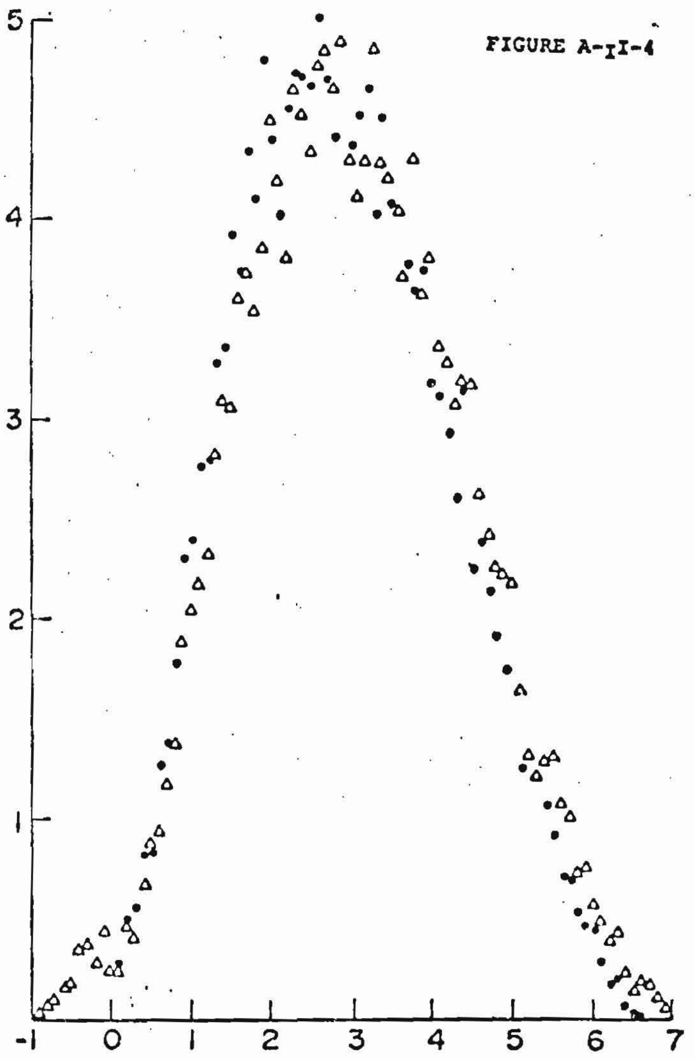

FIGURE A-II-5

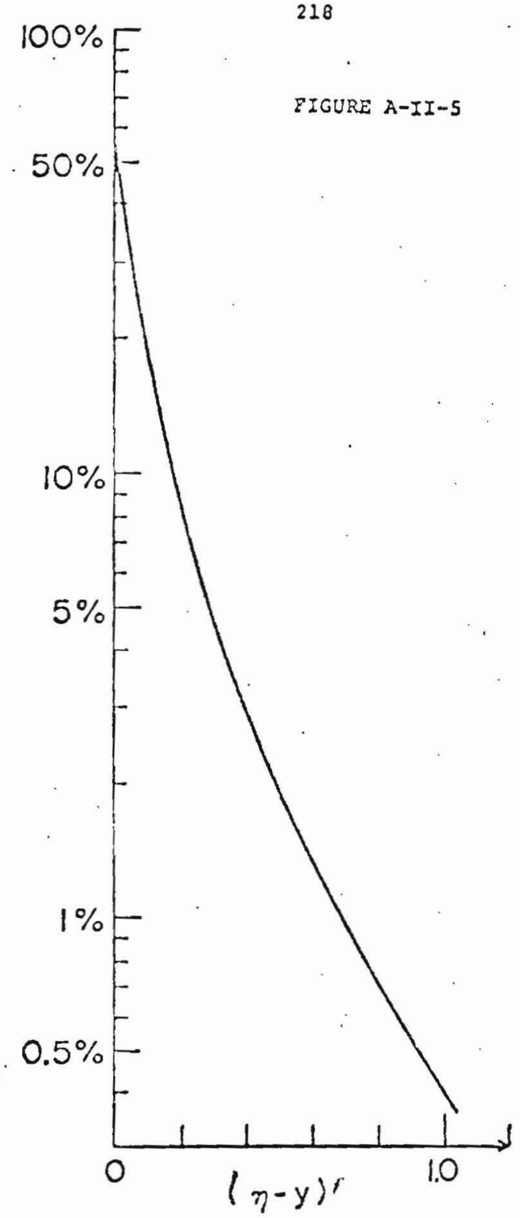

FIGURE A-II-6

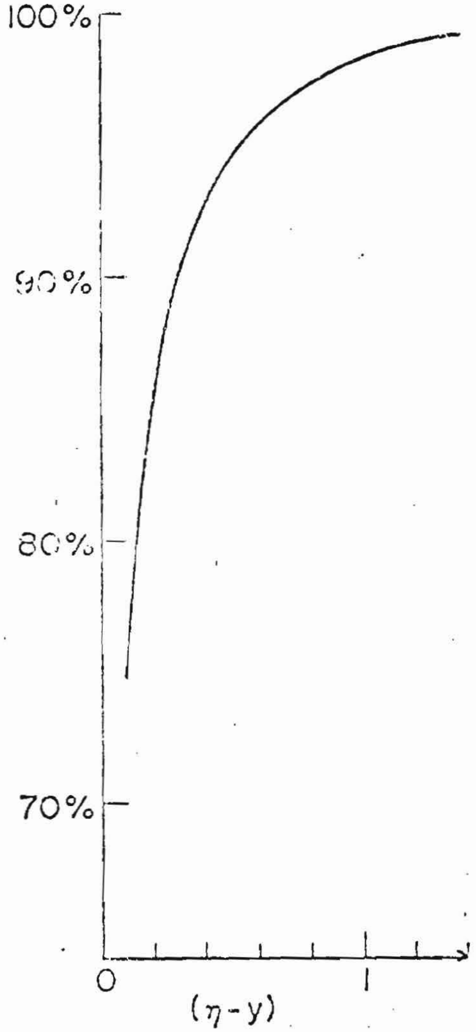

APPENDIX III

The C Counter

The C counter counts particles through a pulse height technique. If on the average one particle yields a certain amount of light, then two particles will, on the average, yield twice that amount of light, and so on. Therefore, knowing the pulse height distribution of some events, one can determine the average multiplicity of these events. The algorithm is presented in Appendix IV.

A scintillation counter appears to be a logical choice for this counter. The light yield is large, hence the pulse height resolution is good. However, it has a serious drawback for this experiment. While all relativistic particles give roughly the same amount of light, a nonrelativistic particle cannot be distinguished from a large number of fast particles. This is a consequence of the $1/\beta^2$ dependence of the ionization rate at low values of β.[62] Since one might reasonably expect some slow multiply-charged nuclear fragments in a high-energy hadron-nucleus collision, this is a serious problem.

The properties of Cherenkov radiation are well-known.[63] The light output as a function of velocity is illustrated in Figure A-III-1. The existence of a threshold prevents slow particles from masquerading as many fast ones.

The rapid saturation of light output above threshold is also important. All fast particles can be assumed to produce about the same amount of light. In other words, the light output curve can be well approximated by a step function.

The choice of radiators depends on several factors. The amount of light produced, the ease in handling and shaping the radiator, and the index of refraction are some important ones.

A gaseous radiator gives the experimenter control over the index of refraction and hence the threshold velocity. This attractive feature is negated by the long lengths of radiators (and the associated optics) required in order to produce enough light. The typically low indices of refraction result in a small number of photons being produced, which gives rise to a very poor pulse height resolution.

Liquid radiators can be made much smaller. The need for the radiator to be shaped and uniformly filled poses a serious problem.

Solid radiators are the easiest to shape and use. The level of light output is also acceptable. The major drawback is in having a fixed index of refraction.

The actual radiators used in this experiment were made of ultra-violet transmitting (UVT) lucite, which is a solid at room temperature with an index of refraction of about 1.50. Its threshold and saturation characteristics are shown in Figure A-III-1. For the sake of simplicity, the lucite was assumed to impose a velocity selection of $\beta \gtrsim 0.85$.

Since this counter was to be used for counting particles through their pulse height, uniformity of response as well as linearity of response were important.

Uniformity of response over the entire cathode surface of the photomultiplier tube was achieved by shaping the radiator so that it was thicker around the circumference where the cathode is less efficient. See Figure A-III-2 for the design of a typical radiator. Radiators of different thicknesses were used in the experiment in order to determine their effects on the observed multiplicity. None were observed. With these radiators, the variation in pulse height across the surface of the tube was less than 10%.

The linearity of response depends on the choice of the photomultiplier tube. The RCA Model 4525 photomultiplier tube with a 5-inch diameter photocathode was chosen. This is a 10-stage tube with bialkali photocathode for high quantum efficiency. The response curves and the manufacturer's specifications are given in Figure A-III-3 and Table A-III-1. A special voltage-dividing resistor chain was used -- see Figure A-III-4. It had several special features. The voltage between the cathode and the first dynode was maintained at, or near, the maximum rated

value to increase efficiency as well as resolution. This was done with the aid of Zener diodes. A second regulated DC power supply was connected to dynode number 7 in order to supply the extra current needed in the last few stages. Capacitors were put between all dynodes to prevent sagging in high current running. Note that unlike usual applications high current could result from not only high event rates but also from a high multiplicity per event.

The signal from the anode was sent into a LeCroy Research Systems Model 124 Gated Stretcher. This device integrates the charge during the period of the gate and then gives an output pulse whose height is proportional to the total charge. This pulse was then digitized by the pulse height analyzer.

For the first part of this experiment, a Tracor-Northern Model NS700 4096-channel pulse height analyzer was used. For the second part of this experiment, the pulse height analysis was performed by a LeCroy Research Systems Model 2249 1024-channel analog-to-digital converter. A typical pulse height spectrum is shown in Figure A-III-5. In both cases the linearity of the entire system was determined to be better than approximately 3% (integral) up to 25 particles. This was done with the aid of pulsed light emitting diodes (LEDs). This calibration was performed before and after each part of the experiment and was found to reproduce itself.

According to the manufacturer's specifications, the RCA 4525 has a rise-time of 18 nano-seconds (nsec). It was experimentally observed that the voltage at the anode returned to the quiescent level after approximately 100 nsec. Since the counter was situated in the beam and therefore responded to all beam particles, this set an upper limit on the beam intensity.

Whatever radiation damage the cathode and the dynodes might have suffered during the course of this experiment was not observable in tests on gain and linearity of response.

In the construction of the base, care was taken to keep all the components out of the beam in order to maximize transmission of the beam -- see the text for triggering requirements. Nevertheless, the counter still presented 10% of an interaction length to incident hadrons. This was experimentally determined by measuring the transmission of the beam with the counter in and out of the beam.

All the counters used in this experiment to measure multiplicities (as opposed to trigger counters) were made of UVT lucite. Therefore, these counters also had a velocity acceptance of $\beta > 0.85$.

TABLE CAPTIONS

A-III-1 Specifications of the RCA 4525 photomultiplier tube.

FIGURE CAPTIONS

A-III-1 Cherenkov light output per unit thickness of UVT lucite as a function of the velocity (or momentum) of the charged particle traversing it.

A-III-2 Front and side view of the design of one of the UVT lucite radiators used on the C counter.

A-III-3 Relative sensitivity and quantum efficiency of the RCA 4525 photomultiplier tube.

A-III-4 Design of the voltage-dividing resistor chain for the C counter.

A-III-5 A typical pulse height spectrum obtained with the C counter. Notice the clear 3-particle peak.

TABLE A-III-1

Specifications of the RCA 4525 Photomultiplier Tube

Quantum efficiency	25% at 4000 Å
Cathode material	Cesium-Potassium-Antimony
Dynode material	Beryllium oxide
Dynode structure	Venetian blind
Cathode area	> 15.1 inches^2
Wavelength of maximum response	4000 ± 500 Å
Number of stages	10
Pulse height resolution	7.5% (Cs^{137} source, 3"x3" NaI(Tl) scintillator)

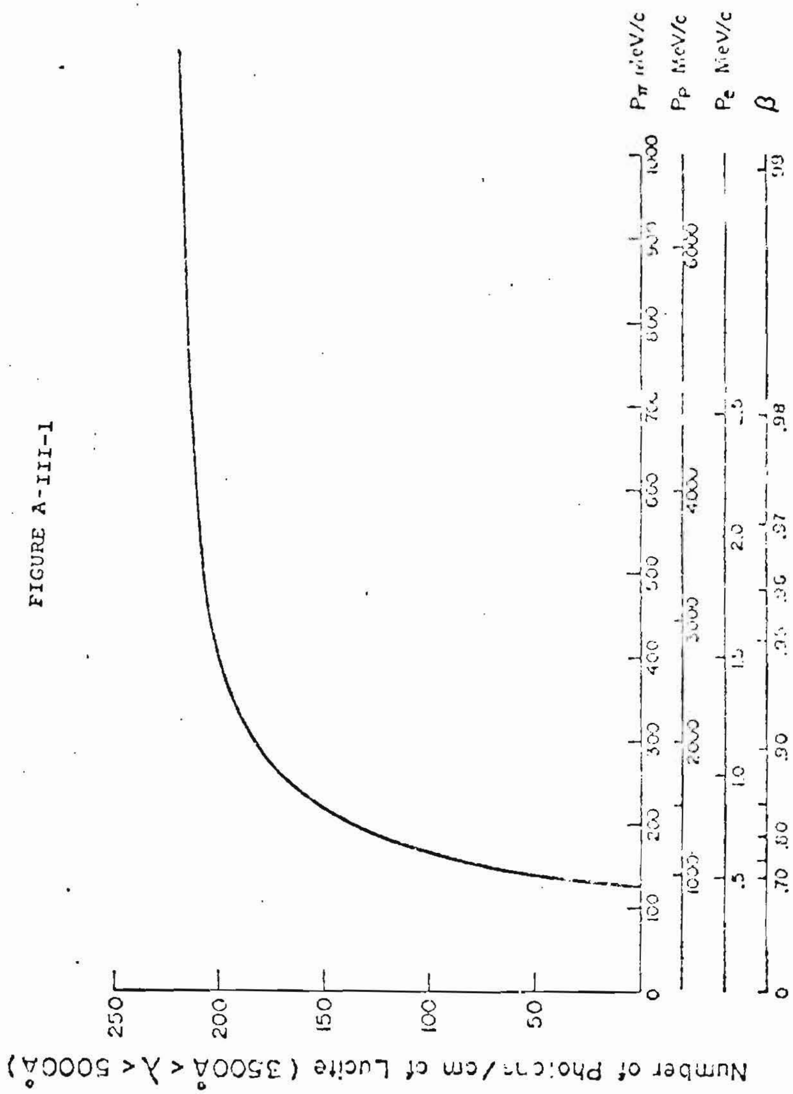

FIGURE A-III-1

FIGURE A-III-4

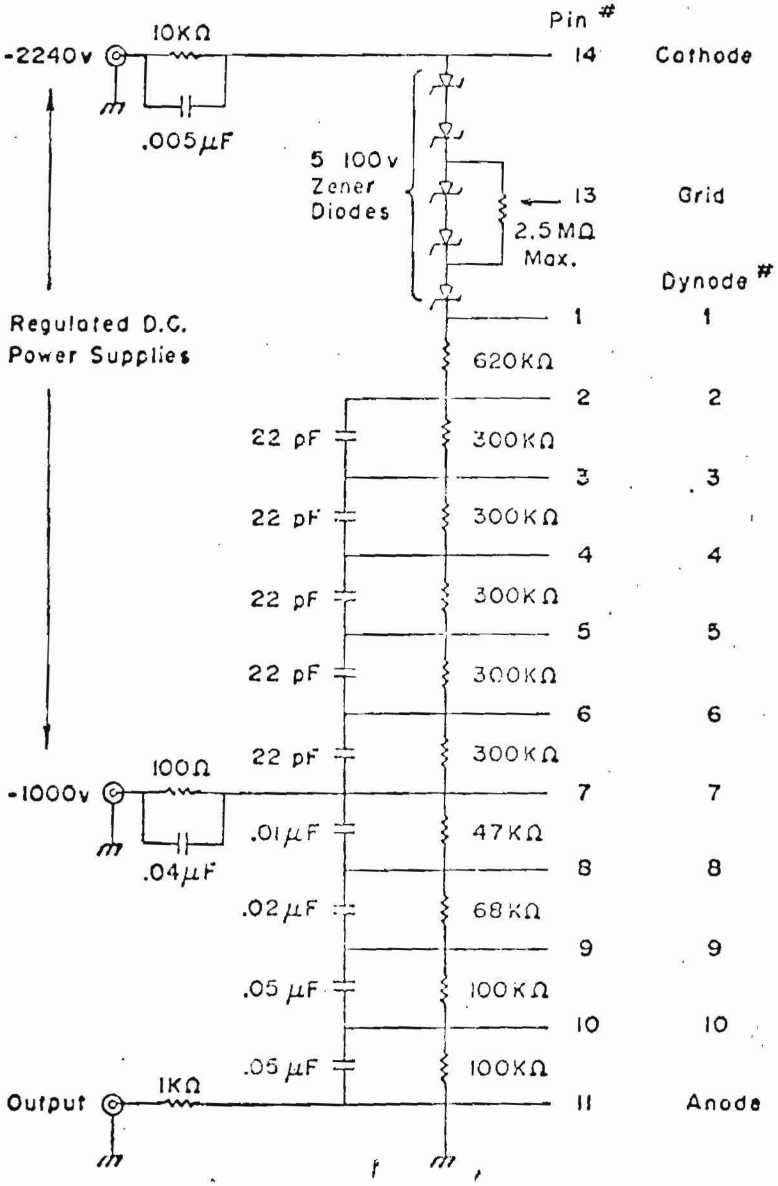

FIGURE A-III-5

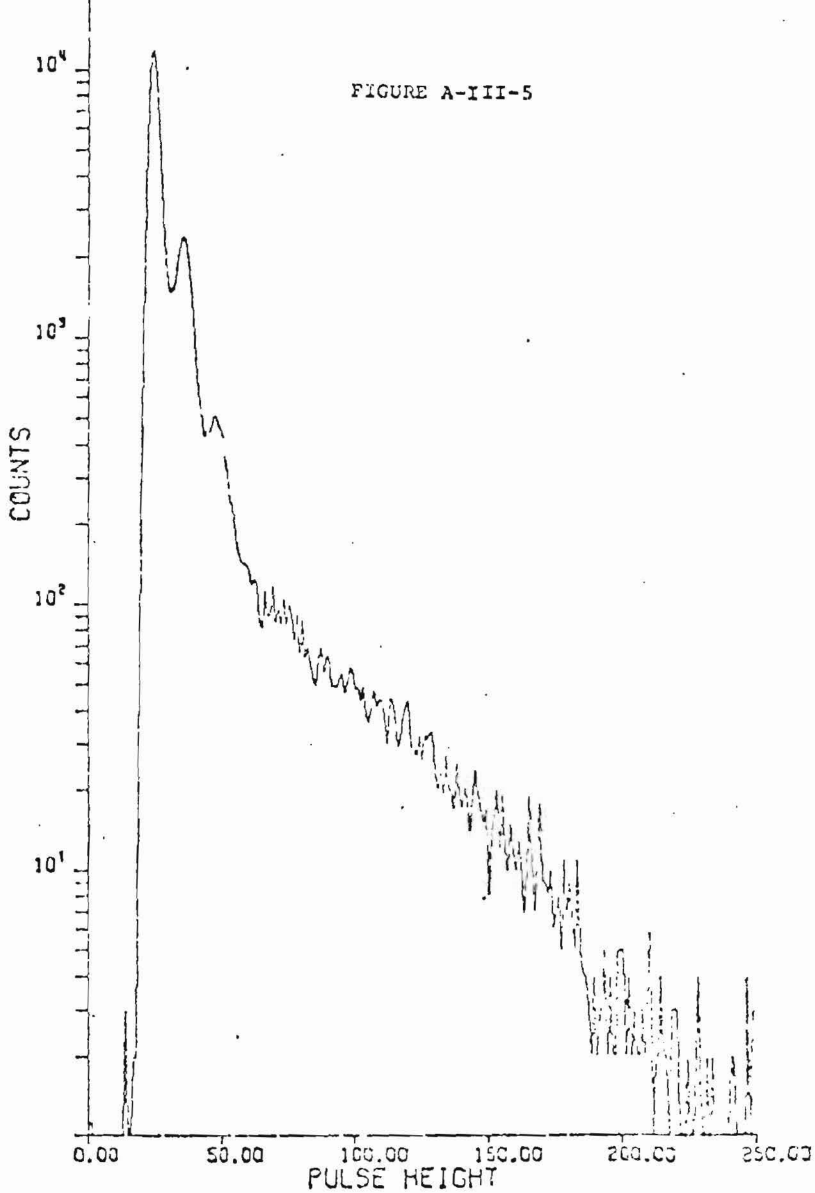

APPENDIX IV

Obtaining Multiplicity Moments from a Pulse Height Distribution

Let $P_1(x)dx$ be the probability that the pulse height from a singly-charged relativistic particle -- the only kind of particle that will be considered here -- is between x and (x+dx). Then the probability that two such particles will together yield a pulse height x is given by

$$P_2(x) = \int_0^\infty P_1(x-t)P_1(t)\ dt$$

Note that $P_1(x)$ is identically zero when x is negative; so the limits of integration are as shown. And in general, the probability that N particles will give a pulse height x is

$$P_N(x) = \int_0^\infty P_1(x-t)P_{N-1}(t)\ dt$$

Therefore a knowledge of the one-particle spectrum enables one to find the pulse-height distribution of an arbitrary number of particles. However, the precision with which these distributions are known decreases with the number of particles N.

Consider a sample of M events. Suppose that each of

a_1 of these events has one singly-charged relativistic particle, each of a_2 events has two such particles and so on. Then for this sample of events, the average multiplicity is defined as

$$\langle n\rangle = \frac{\sum_i i a_i}{\sum_i a_i} = \frac{1}{M}\sum_i i a_i$$

and the second multiplicity moment is defined as

$$\langle n^2\rangle = \frac{\sum_i i^2 a_i}{\sum_i a_i} = \frac{1}{M}\sum_i i^2 a_i$$

Note that the second moment, $\langle n^2\rangle$, is needed to calculate the dispersion of the multiplicity distribution, which is given by

$$D = \sqrt{\langle n^2\rangle - \langle n\rangle^2}$$

To find $\langle n\rangle$ and $\langle n^2\rangle$, one would (naively) have to obtain the a_i's first. This could be done by fitting to the pulse height distribution of these M events with a linear superposition of the various $P_i(x)$'s. These a_i's can then be inserted into the definitions of $\langle n\rangle$ and $\langle n^2\rangle$. This procedure is correct in principle, but runs into a host of practical problems.

First note that the distribution $P_1(x)$ is the only experimentally accessible quantity among the many $P_i(x)$'s. This one-particle spectrum cannot be known perfectly. The uncertainties propagate and multiply as one performs the convolutions needed to generate the $P_i(x)$'s. Errors on the pedestal of the distribution, i.e. the uncertainties in the zero of the pulse height scale, have two effects on the $P_i(x)$'s. First, these derived spectra will be shifted along the pulse height scale by an amount proportional to i. In other words, the Nth spectrum will have an error in its pedestal N times that in the one-particle spectrum. More importantly, the pulse height scale becomes distorted -- an error on the pedestal also reflects itself as an uncertainty in the gain of the system. Actual uncertainties in the gain used in measuring $P_1(x)$ will also manifest itself. Fitting procedures must be capable of determining the pedestal and gain. This simply introduces two more unknowns. However, these two unknowns are highly correlated with one another as well as with the a_i's being determined. Moreover, the problem is not linear in these 2 additional variables as it is in the a_i's. An unambiguous solution is often in doubt.

Secondly, the maximum number of spectra $P_i(x)$'s that are generated and used in a fitting procedure is limited.

Thirdly, a simple least-squares fitting procedure will, in general, yield some negative values of a_i's. The interpretation of these a_i's and the validity of such a

fitting procedure are in doubt. More complicated algorithms can and have been devised to find non-negative values of a_i's. The "fix-ups" in these algorithms are difficult to justify.

It will now be shown that there is a much simpler algorithm. A knowledge of the pulse-height moments of $P_1(x)$ and the spectrum under consideration is sufficient. No fitting is required. It will be argued that in addition to being a more direct and faster calculation this algorithm affords a more manageable way of taking into account the uncertainties in the pedestal and the gain.

Define the average pulse height of any spectrum f(x) by

$$\langle x\rangle_f = \frac{\int_0^\infty x\, f(x)\, dx}{\int_0^\infty f(x)\, dx}$$

and the dispersion in pulse height by

$$D_f^2 = \frac{\int_0^\infty (x^2 - \langle x\rangle_f^2)\, f(x)\, dx}{\int_0^\infty f(x)\, dx}$$

Apply the first formula to $P_N(x)$ and obtain:

$$\langle x\rangle_N = \int_0^\infty x\, P_N(x)\, dx$$
$$= \int_0^\infty x\left(\int_0^\infty P_1(t)\, P_{N-1}(x-t)\, dt\right) dx$$
$$= \int_0^\infty P_1(t) \left(\int_0^\infty (y+t)\, P_{N-1}(y)\, dy\right) dt$$
$$= \int_0^\infty P_1(t)\, (\langle x\rangle_{N-1} + t)\, dt$$
$$= \langle x\rangle_{N-1} + \langle x\rangle_1 .$$

Therefore, $\langle x\rangle_N = N\langle x\rangle_1$. Similarly, it can be shown that $D_N = ND_1$.

Let $f(x)$, the spectrum to be analyzed, be made up of a_1 one-prong events, a_2 two-prong events and so on. It can be written approximately as a linear superposition of the $P_i(x)$'s:

$$f(x) \approx \sum_i a_i\, P_i(x)$$

The equality becomes exact in the limit of infinite statistics. The a_i's are, of course, unknown at this point. The average pulse height of this spectrum is given by:

$$\langle x\rangle_f = \frac{\sum_i a_i \int_0^\infty x\, P_i(x)\, dx}{\sum_i a_i \int_0^\infty P_i(x)\, dx}$$
$$= \frac{\sum_i a_i \langle x\rangle_i}{\sum_i a_i}$$

$$= \langle x\rangle_1 \frac{\sum_i a_i i}{\sum_i a_i}$$

Therefore $\langle n\rangle = \frac{\langle x\rangle_f}{\langle x\rangle_1}$.

So the average multiplicity represented by the pulse height spectrum $f(x)$ is the average pulse height of that spectrum divided by the average pulse height of the one-particle spectrum.

It can be shown similarly that the dispersion of the multiplicity distribution is related to the dispersions of the spectrum $f(x)$ and the one-particle spectrum $P_1(x)$:

$$D^2 = \langle n^2\rangle - \langle n\rangle^2 = \frac{D_f^2 - \langle n\rangle D_1^2}{\langle x\rangle_1^2}$$

These formulae greatly facilitated the analysis of the data. The three above-mentioned difficulties in connection with fitting procedures have been avoided.

The calculation of the errors on the multiplicity moments are also straight forward. Uncertainties in the pedestal lead to an additive error in $\langle x\rangle_1$ and $\langle x\rangle_f$. Changes in the gain of the pulse height analyzing system lead to a scale change between $\langle x\rangle_1$ and $\langle x\rangle_f$. This uncertainty can be taken care of by introducing a percentage error on the multiplicity moments.

During the course of this experiment, the pedestal was observed to be stable to within about half a pulse height channel out of a full-scale 512 channels. This was true (independently) for the two parts of the experiment. Since 0.1% is much smaller than the statistical uncertainties of the experiment, this effect was ignored.

Similarly, there was no observable gain change. This was determined by examining the one-particle spectra taken at regular intervals throughout the experiment. This uncertainty was also ignored in the analysis.

For this algorithm to work, two criteria must be satisfied. First, the entire pulse height analyzing system must be uniform and linear. This is essential for the $P_i(x)$'s to be calculated correctly by the convolution method. The response must not saturate, otherwise the average pulse heights would be systematically biased. These two conditions were met by shaping the radiator (so that the response is independent of the trajectory of the particle), by selecting a photomultiplier tube with good linearity, and by using a specially designed base to avoid saturation and ensure linearity. See Appendix III for details.

APPENDIX V

Details of the Analysis for Part I of the Experiment

For each run, the eight pulse-height distributions were fitted to obtain the frequency distribution of the low-multiplicity events, i.e. those events with less than 7 prongs. These fits were restricted to low-multiplicity events for several reasons. First, low-multiplicity events were quite abundant and that part of the pulse-height distribution was statistically well determined. Hence the fits were well behaved. Secondly, the average multiplicity and dispersion would eventually be determined by a different and more reliable method -- Appendix IV -- so there was no need to obtain the complete multiplicity distribution. Lastly, restricting the domain of the fits resulted in a much faster calculation.

Using this information, those events with 3 or fewer prongs were removed. The resulting data were then analyzed to give the multiplicity moments. <n> and D were obtained for each of the 8 spectra using the technique discussed in Appendix IV.

Results for the angular region covered by the C counter were obtained by summing the information from the 8 spectra. The region covered by the 12 H counters was treated as in Appendix VI. For information on the combined angular region, the 2 results were added together.

The following corrections were applied. First, the contributions from empty-target interactions were statistically removed. During the experiment data were regularly obtained with the targets removed in order to find the background contributions to the data and the effects of a possibly over-efficient trigger. To obtain data on a hydrogen target, carbon was treated as the "empty" target for polyethylene data. In the construction of targets, care was taken to insure that the corresponding pairs of carbon and polyethylene targets had the same number of carbon nuclei per unit area.

The angular region covered by the H hodoscope needed an acceptance correction. The 12 H counters formed a cone but there were necessarily cracks between the counters. Consistent with the assumption used in the analysis that there was no azimuthal correlations, the observed multiplicities were increased by an amount proportional to the fraction of the solid angle not covered. This amounted to a ∿5% correction.

The possibility of hadronic interactions in the 3/4" of lucite in the H counters was significant, but resulted in only minute changes in the multiplicities. The hadronic products were most likely contained within individual H counters. No corrections were applied for this effect.

The calibration of the C counter was systematically biased. The algorithm used in the analysis (Appendix IV) required the knowledge of the average pulse height of a hadron coming from an interaction of a beam particle in the target. The average pulse height of a beam particle was used in this calibration. Particles incident on the C counters would not only be counted but might also interact in the radiator. Should such an interaction occur, more particles were produced and hence the light output would increase. Since beam particles had higher energy than those produced in the target, they would also produce more secondaries in the radiator. So the observed multiplicity had to be corrected upwards.

Another correction needed to be made in connection with the C counter. Consider an interaction in the target. In general π^0s are produced as well as charged pions. The resulting photons can produce pairs in the air or in the radiator of the C counter. These charged pairs will increase the pulse height, leading to an apparently higher multiplicity. Making the assumption that the average number of neutral pions is half the number of total charged particles, the correction factor can be calculated.

The combined correction from these two competing effects was estimated independently by three people. The results were consistent, and averaged 3%. Therefore, the observed multiplicity for the C counter was lowered by 3%.

The observed cross-sections had to be corrected for the presence of kaons, anti-protons and muons in the beam. Note that there were effectively no electrons in the beam because of the 4/3 radiation lengths of lead inserted at the first focus of the beam. Since muons did not interact significantly in the thin targets used, the effect was to change the beam rate. The effects of K^- and $\bar{p}$ were slightly more complicated but smaller in magnitude. The beam composition as well as the estimated K^--A and $\bar{p}$-A cross-sections were used to calculate the correction. The combined effect was to raise the observed cross-section by 3%.

Their effects on the multiplicity moments were negligible provided that the π^--A, K^-A and $\bar{p}$-A multiplicity distributions are not too dissimilar. Since the fractional contamination of the beam was small, since the dependence of the mean multiplicity on the atomic number of the target was weak and since the $\bar{\nu}$ dependence of R_A appeared to be independent of the identity of the beam particle, the corrections to the multiplicity moments could be estimated. It was less than ~1%. No corrections were applied because the uncertainties in the correction were comparable to the correction.

Finally, the data had to be corrected for the low-multiplicity events which had been removed in the first

stage of the analysis. Two different approaches were taken and gave indistinguishable results. The first algorithm is as follows. From the initial set of fits, the number of 4 prong events is known. The numbers of 3, 2 and 1 prong events were assumed to be 1/2, 1/4 and 1/8 respectively of this value.

The second algorithm involved an iterative procedure. The observed mean multiplicity was used to determine the value of the parameter λ in the hypothetical multiplicity distribution $n^3 e^{-\lambda n}$. This functional form is known to fit proton-proton data satisfactorily.[70] Then the predicted numbers of 1-, 2- and 3-prong events were added to the data. This yielded a new mean multiplicity, which was used to find a new value of the parameter λ. This procedure was repeated until a consistent set of numbers emerged. Three iterations were usually sufficient.

As expected, the two algorithms gave different numbers of 1-, 2- and 3-prong events. But since they represent only a small fraction of the absorption cross-section, the corrected mean multiplicities were not very different. The difference was taken to be an estimate of the systematic errors introduced in this correction. It was less than 3%.

Finally, the data from different runs with the same target material were examined. The multiplicity, as expected, was higher for thicker targets, reflecting extra-nuclear cascades. This effect was eliminated by extrapolating the data to zero target thickness. Linear extrapolations were used throughout. The error introduced in the extrapolation procedure was also incorporated into the final results.

It would be more informative to have obtained and presented the multiplicity distributions instead of the first two moments. The calculations have been carried out but the results have such large uncertainties as to render the distributions practically useless. The reasons are given below.

A multiplicity distribution is by definition the frequency of having an n-prong event where n is any non-negative integer. To obtain this distribution from a sample of M events, one needs to make the best estimates of the numbers of 1-prong events, 2-prong events and so on. There are two ways of getting this set of numbers.

An extension of the technique presented in Appendix IV can be used to obtain successively higher moments of the multiplicity distribution. These moments can then be used to calculate the corresponding multiplicity distribution. However, there are practical problems. To calculate the n-th multiplicity moment, it is necessary to calculate the n-th pulse height moment:

$$\langle x^n \rangle = \frac{\Sigma x^n f(x)}{\Sigma f(x)}$$

where f(x) is the pulse height distribution. The higher multiplicity moments are progressively more sensitive to the region of large pulse height, which is the region where the statistical accuracy of the data is very poor. In short, this technique leads to results with large uncertainties, which become magnified in obtaining the multiplicity distribution.

Another technique involves fitting to the entire pulse height spectrum. The multiplicity distribution is obtained directly. However, the results of such fits have enormous errors (up to $\sim 10^4$%). Note that these errors are highly correlated so that the mean multiplicity can be determined with much greater precision.

Even if this difficulty could be overcome, there is another obstacle to be tackled. The above procedures yield the multiplicity distribution for the data obtained with a target of finite thickness. This distribution has to be extrapolated to zero tartet thickness. This can be done in several ways.

The extrapolation can be performed independently for each multiplicity. The high multiplicity results take on (what appears to be) random values with large errors so that they are consistent with any reasonable (and some not-so-reasonable) extrapolation of the low multiplicity results. The extrapolation to zero target thickness of these results is obviously not reliable.

Another approach would be to parameterize the distributions and then extrapolate the parameter values to zero target thickness. Note that this is a ridiculous procedure unless 3 or more parameters are used. If there are only 2 parameters, they can be determined by the values of <n> and D obtained in the analysis. The entire procedure becomes simply hypothesizing a functional form for the multiplicity distribution. In any event, the result would be sensitive to the functional form assumed for the distribution.

APPENDIX VI

Finding the Average Multiplicity in the H Hodoscope

To find the average and the dispersion of the multiplicity distribution in the angular region covered by the H hodoscope, one needs to impose certain assumptions. In particular, a knowledge of the azimuthal correlations is needed in order to correct for the possibility of multiple hits in individual counters.

The assumption used in this analysis is that there is no azimuthal correlation. No justification will be given, but several excuses will be offered. The observed azimuthal correlations in proton-proton interactions is quite small.[71] And since the H hodoscope only cover a small fraction of the entire solid angle, one might expect the effect to be even smaller. There is, of course, no reason why the proton-proton data should be at all like the hadron-nucleus data. The overriding reason for making this assumption is that it is easy to handle and the corrections are simple to apply. One could offer a further after-the-fact excuse. The results from the second part of this experiment indicate that the azimuthal correlations within a small bin of polar angle are negligible.

Under this assumption, one calculates the probability that two or more particles will hit the same counter. One can then find, on the average, the multiplicity distribution that gave rise to the observed frequency distribution of struck counters.

The formula for the above-mentioned probabilities will be derived. Let P(r,n) be the probability that n particles, distributed randomly, will hit r out of N counters. N has the value 12 for the case under consideration. It will be shown that

$$P(r,n) = \frac{N!}{(N-r)!N^n} \sum_{j=0}^{r-1} \frac{(-1)^j (r-j)^n}{(r-j)!\,j!}$$

The proof proceeds as follows.

In distributing n particles randomly into N boxes, there are N^n possible outcomes and there are $\frac{N!}{(N-r)!\,r!}$ ways of picking the r struck items out of N. So the desired probability is given by

$$P(r,n) = \frac{1}{N^n} \frac{N!}{(N-r)!\,r!}\, g(r)$$

where g(r) = the number of ways that n particles can hit all of the r given counters.

Now let $h(j) = j^n$ = the number of ways that n particles can hit any combination of the r given counters. Then

$$g(r) = h(r) - \sum_{j=1}^{r-1} \frac{r!}{(r-j)!\,j!}\, g(r-j)$$

But g(r-j) can be written in a similar series. After collecting terms, one obtains

$$g(r) = h(r) + \sum_{j=1}^{r-1} \frac{r!(-1)^j}{(r-j)!\,j!}\, h(r-j)$$

$$= \sum_{j=0}^{r-1} \frac{(-1)^j\, r!}{(r-j)!\,j!}\, (r-j)^n$$

Therefore the required probability is given by

$$P(r,n) = \frac{1}{N^n} \frac{N!}{(N-r)!} \sum_{j=0}^{r-1} \frac{(-1)^j (r-j)^n}{(r-j)!\,j!}$$

An equivalent recursive formula can be derived as below. If the first (n-1) particles had already struck r counters, then the last particle would be required to hit one of these r given counters. If the first (n-1) particles had struck (r-1) counters, then the last particle is constrained to hit one of the remaining counters. Any other combination of hits by the first (n-1) particles would lead to an outcome different from having exactly r struck counters. Therefore,

$$P(r,n) = \left(\frac{r}{N}\right)P(r,n-1) + \left(\frac{N-r+1}{N}\right)P(r-1,n-1)$$

Since P(1,1) is obviously 1 and P(r,n) is zero whenever r is greater than n or when either r or n is non-positive, this recursive formula can be used to generate all the desired P(r,n)'s.

For N = 12, and r and n not exceeding 12, the values of P(r,n) are given in Table A-VI-1.

For the first part of this experiment, there was no information on the frequency distribution of struck counters beyond 7; and for the second part of the experiment the distribution ended at 12. Except for this one difference, the corrections were applied in identical fashion, so only one case will be discussed.

Consider the second part of the experiment. If the assumption of no azimuthal correlations is correct, then the observed frequency distributions of struck counters is simply the (matrix) product of the probability P(r,n) and the actual multiplicity distributions. In this case, both r and n range from 1 to 12. Hence, the inverse of the 12x12 matrix P(r,n) multiplied to the observed frequency distributions of struck counters will give the actual multiplicity distributions. It is then straight forward to calculate the moments of this multiplicity distribution. Note that the inverse of P(r,n) needs to be calculated only once. It is possible (though extremely tedious) to do this inversion by hand, and avoid the inaccuracies that are incurred when the inversion is done numerically by a computer. The importance of this point becomes obvious when one inspects

the matrix P(r,n). Its elements differ by many orders of magnitude, precisely the situation when computers are most prone to round-off errors.

The drawback of this technique is obvious -- it's impossible to recover any information beyond n = 12 as the algorithm is constrained by the total number of counters available. In other words, having made 12 measurements, it is impossible to juggle these numbers to obtain more than 12 independent numbers. If one assumes some azimuthal correlation or if one assumes some functional form for the multiplicity distribution, then it is possible to go beyond n = 12.

A check of this method was available in the second part of the experiment. Event-by-event information was available here. Treating the H hodoscope exactly as one of the ring-shaped hodoscopes, its frequency distribution in the 322 bins was fitted. The results were indistinguishable from those obtained using the algorithm presented here. For details of the algorithm used in analyzing the ring hodoscopes, see Appendix VII.

TABLE A-VI-1

J =	1	2	3	4	5	6	7	8	9	10	11	12
I = 1	1.0E 00	8.3E-02	6.9E-03	5.8E-04	4.6E-05	4.0E-05	3.3E-07	2.8E-08	2.3E-09	1.9E-10	1.6E-11	1.3E-12
I = 2	0.0	9.2E-01	2.3E-01	4.5E-02	8.0E-03	1.4E-03	2.3E-04	3.7E-05	5.5E-06	1.1E-06	1.8E-07	3.3E-09
I = 3	0.0	0.0	7.6E-01	3.8E-01	1.3E-01	4.0E-02	1.1E-02	3.0E-03	7.7E-04	2.0E-04	5.1E-05	1.3E-05
I = 4	0.0	0.0	0.0	5.7E-01	4.3E-01	2.6E-01	1.2E-01	4.7E-02	1.9E-02	6.5E-03	2.3E-03	8.1E-04
I = 5	0.0	0.0	0.0	0.0	3.8E-01	4.8E-01	3.7E-01	2.3E-01	1.3E-01	6.5E-02	3.2E-02	1.5E-02
I = 6	0.0	0.0	0.0	0.0	0.0	2.2E-01	3.9E-01	4.1E-01	3.4E-01	2.5E-01	1.6E-01	9.9E-02
I = 7	0.0	0.0	0.0	0.0	0.0	0.0	1.1E-01	2.6E-01	3.6E-01	3.8E-01	3.4E-01	2.8E-01
I = 8	0.0	0.0	0.0	0.0	0.0	0.0	0.0	4.6E-02	1.4E-01	2.4E-01	3.2E-01	3.6E-01
I = 9	0.0	0.0	0.0	0.0	0.0	0.0	0.0	0.0	1.5E-02	5.8E-02	1.2E-01	2.0E-01
I = 10	0.0	0.0	0.0	0.0	0.0	0.0	0.0	0.0	0.0	3.9E-03	1.8E-02	4.5E-02
I = 11	0.0	0.0	0.0	0.0	0.0	0.0	0.0	0.0	0.0	0.0	6.4E-04	3.5E-03
I = 12	0.0	0.0	0.0	0.0	0.0	0.0	0.0	0.0	0.0	0.0	0.0	5.4E-05

APPENDIX VII

The Average Multiplicity in a Ring Hodoscope

The construction of a ring hodoscope is illustrated in Figures IV-3 and IV-4. The two layers of 6 counters each resulted in 12 distinct equal-size azimuthal bins. In any given event, each counter might be on or off, leading to a total of 2^{12} possible outcomes. Invoking rotational symmetry (by integral multiples of 30°), this number was reduced to 322. Reflection symmetry would have reduced this number even further, but it was ignored for computational ease. Therefore the data for each ring hodoscope were represented by a 322-bin frequency distribution.

In order to find the average multiplicity in a ring hodoscope, one needs to allow for the probability of more than 1 particle incident upon the same azimuthal bin. This was done by assuming that there was no azimuthal correlation within the pseudorapidity range covered by a ring hodoscope. The reasons for this assumption are the same as those offered in connection with the H hodoscope -- see Appendix VI. An after-the-fact excuse can also be given. The fits detailed below yielded chi-squared per degree of freedom close to 1, indicating that the assumptions were not outrageous. In any event, it is only reasonable that the same assumption be used throughout the analysis.

Under the assumption of no azimuthal correlations, single-prong events were generated. Their representation in the 322-bin histogram was recorded. Similar histograms were obtained for higher multiplicities. The possibility of delta-rays was also simulated. Since most delta rays were not energetic enough to completely penetrate the front layer of the ring hodoscope (a 3/4-inch layer of lucite), they would only register in the front layer. Its signature was different from that of a relativistic hadron which would be counted in both layers of the hodoscope. γ-rays producing e^+-e^- pairs in the front layer would not trigger the front counters if the conversion occurred too deep into the lucite radiator. However, the resulting pair would trigger the back layer of scintillation counters, leading to a different signature. These spurious signals were also simulated.

The observed 322-bin frequency distribution was then fitted with a linear superposition of these simulated events and the simulated spurious signals. The number of types of events allowed in the fit was increased until the chi-squared per degree of freedom no longer decreased with an additional type of event. The average multiplicity and its error were then computed. The quality of these fits is illustrated in Figures A-VII-1 and A-VII-2.

The chi-squared per degree of freedom ranged from

approximately 1 for low-multiplicity data to 2-3 for high-multiplicity data. This is a reflection of the inability of the apparatus to resolve a large number of particles.

When the statistical accuracy of the data was poor, e.g. for kaon induced events, the 322 bins were very sparsely populated and the resulting fits were unreliable. This was overcome by rebinning the data into a 73 bin histogram. The rebinning procedure was guided by the high statistics data and their fits. In the high statistics data, it was noticed that some bins were populated with equal frequency and were fitted by the same linear combination of the simulated events. These bins were grouped into one single bin. To check the validity of this procedure, small samples of the high statistics data were used and they gave results indistinguishable from that given by the standard procedure applied to the entire high statistics run. This procedure was used for all the kaon and anti-proton data as well as the data on π^+ at 200 GeV/c and the proton data at 50 GeV/c.

As discussed in the section on the C counter, a fitting procedure invariably leads to some negative values for the frequency of some types of events. This comment also applies to this algorithm here. No attempt was made to put a positivity constraint on the fitting procedure. It should, however, be noticed that these negative values typically had errors that were at least 100%, i.e. they were consistent with zero. Because of the high degree of correlation among the many fitted values, the error on the average multiplicity was usually quite small, 1-5%.

FIGURE CAPTIONS

A-VII-1 The average multiplicity in a ring hodoscope as given by the algorithm discussed in the text as a function of the maximum multiplicity per event allowed in the fit. For this particular sample of events, 7-prong events were needed to obtain an acceptable fit for the first ring hodoscope (0) while 8-prong events were needed for another ring hodoscope (Δ). Some typical errors on the fitted average multiplicities are shown.

A-VII-2 The number of events of a given number of prongs that are needed in the fit as a function of the maximum multiplicity allowed in the fit. Some typical errors are shown. These errors are highly correlated and are not fair estimates of how well the fits were determined.

(a) 1-prong events
(b) 2-prong events
(c) 3-prong events
(d) 4-prong events
(e) 5-prong events
(f) 6-prong events

FIGURE A-VII-1

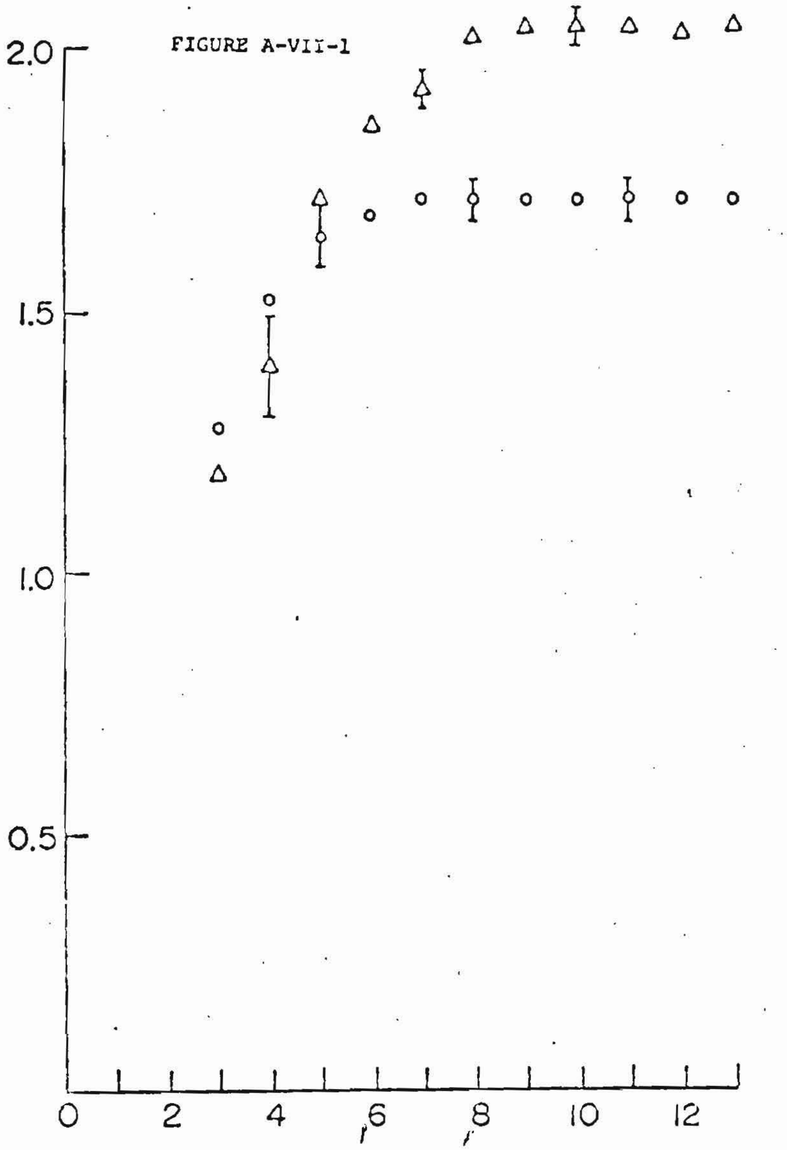

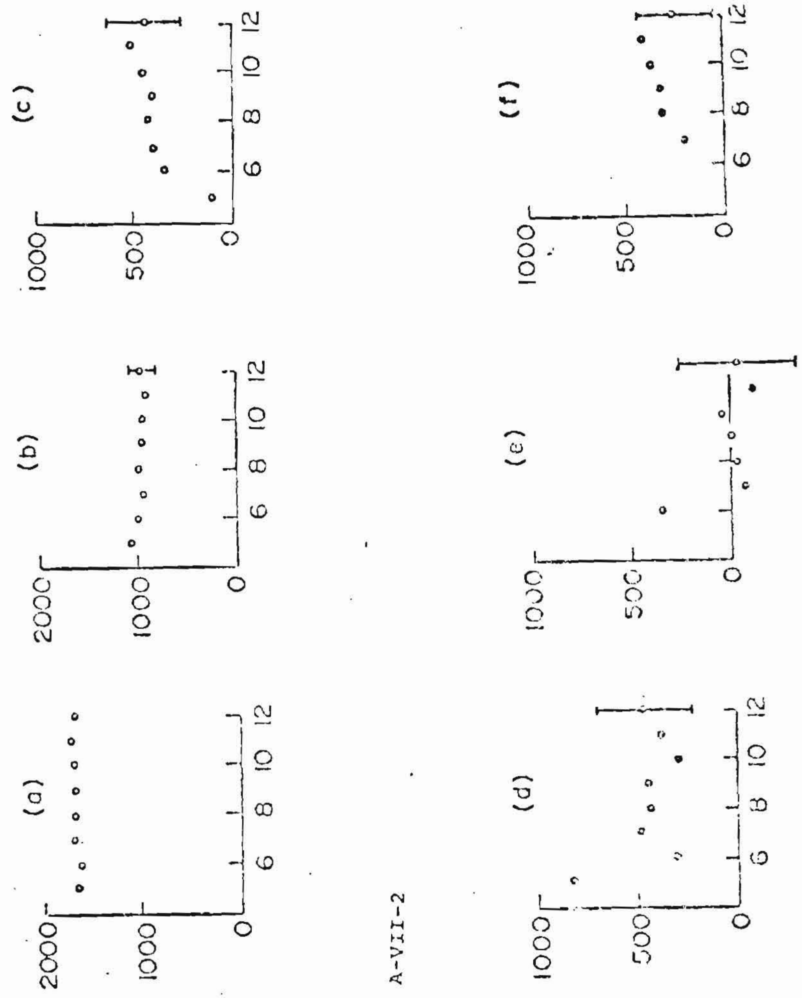

FIGURE A-VII-2

APPENDIX VIII

Corrections to the Data (Part II)

For each individual run, the missing 0-, 1- and 2-prong events were first corrected for. The number of such events was estimated from the difference between the known absorption cross-sections[19] and the measured ones. The latter have been corrected for decay in flight, muon contamination and doubly-occupied "RF buckets." The magnitudes of these corrections depend on the type of beam particle and on its momentum. They are summarized in Table A-VIII-1. Those runs that require corrections of greater than approximately 10% were removed from further analysis.

The missing events were assumed to have an average multiplicity of 1.25. The error introduced by this assumption was estimated by inspecting the results one would have obtained had one assumed an average multiplicity of 0.75. This ranged from about 3% for the data on Hydrogen target to about 0.3% for the data on Uranium target. The decrease of the error with the atomic number of the target is due to the fact that the 0-, 1- and 2-prong cross-sections become increasingly insignificant compared with the absorption cross-section. The errors resulting from the uncertainties in the known as well as measured cross-sections were also

taken into account.

These 0-, 1- and 2-prong events were further assumed to have the same pseudorapidity distribution as the higher multiplicity events. This assumption is almost certainly incorrect, but it was used for want of a better one. The low multiplicity events in a sample of hydrogen bubble chamber data[46] were examined to estimate the effects of this prescription. The pseudorapidity distribution of these events have a depleted central region. Even though the distribution is quite different from that of the higher-multiplicity events, their lower cross-sections make their effects on the shape of the pseudorapidity distribution much less noticeable. The multiplicity of each pseudorapidity bin is expected to be affected by less than 3%. These η dependent errors have not been included in the tabulated results or in the figures. This procedure is equivalent to keeping the pseudorapidity distribution unchanged in shape but normalizing its area to the corrected average multiplicity.

This correction was performed run-by-run. Then the data with the same target material were grouped together. For each pseudorapidity (or angular) bin, the average multiplicity was extrapolated to zero target thickness to eliminate extra-nuclear cascades, γ-conversions in the target and the production of (energetic) delta rays.

The data from the 3 different geometries were then combined to give the final results. This was done as follows. The data from each position were first smoothed. For a given range of η, the pseudorapidity distribution $dN/d\eta$ was approximated by a quadratic polynomial in η. This polynomial was constrained to give the measured average multiplicity for that pseudorapidity bin. Its end points were required to be those given by the average values of $\Delta N/\Delta\eta$ of the bin under consideration and its neighboring pseudorapidity bins. See Figure A-VIII-1. AB, DF and HI are the pseudorapidity bins of three adjacent sets of hodoscopes. The heights are the values of $\Delta N/\Delta\eta$ associated with these bins. Consider the central bin. The smoothing algorithm instructs one to find C and G such that they are the midpoints of BD and FG respectively. CEG is the quadratic polynomial which encloses an area equal to that under DF. This quadratic is unique. This procedure was repeated for all the pseudorapidity bins. The result was an approximation to $dN/d\eta$ which had the correct observed average multiplicity and was continuous in value but had several discontinuities in its slope. The three different approximate forms of $dN/d\eta$ obtained from the three different geometries were then averaged to yield the final pseudorapidity distribution. The average multiplicity is given by the area under the curve.

TABLE CAPTIONS

A-VIII-1 Corrections to the observed cross-sections. The fluctuations in the corrections for the effects of doubly occupied RF buckets are due to accelerator running conditions.

FIGURE CAPTIONS

A-VIII-1 An illustration of the procedure used in approximating the pseudorapidity distribution with quadratic polynomials. AB, DF and HI are three adjacent measurements of $\frac{\Delta N}{\Delta\eta}$. C and G are the mid-points of BD and FG respectively. The quadratic polynomial is given by CEG. The area CDE is equal to the area EFG. For details of the algorithm, see the text.

TABLE A-VIII-1

Corrections to the Observed Cross-Sections

Effect	Beam Condition	Correction to Cross-Section
Kaon decay	50 GeV/c	+5.3%
	100 GeV/c	+2.5%
Muon contamination of pions	50 GeV/c	+1.2%
	100 GeV/c	+1.5%
	200 GeV/c (positive)	+4.4%
	200 GeV/c (negative)	+0.5%
Doubly-occupied RF "buckets"	3 10^4/350 msec spill	+0.5 to +1.5%
	1 10^5/350 msec spill	+1 to +3%
	3 10^5/350 msec spill	+3 to +7%
	5 10^5/350 msec spill	+5 to +10%
	1.3 10^6/350 msec spill	+8 to +20%

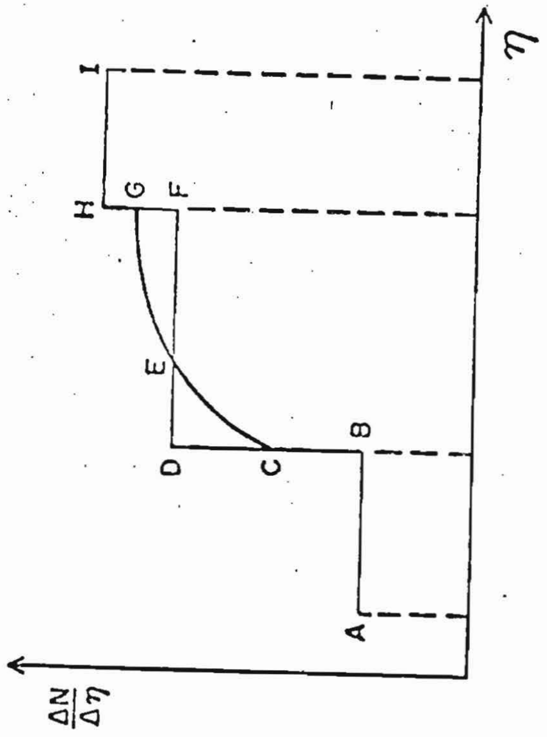

FIGURE A-VIII-1

APPENDIX IX

Emulsion

The composition of emulsion is given in Table A-IX-1. Since emulsion is a composite object, there is a need to define average quantities. Any quantity f, averaged over the constituents of emulsion, is given by

$$<f> = \frac{\Sigma\, n_i\, f(A_i)}{\Sigma\, n_i}$$

where n_i is the (relative) abundance of the element of atomic number A_i. Thus emulsion has an average atomic number of 32.9.

The averaging over the constituents of emulsion has to be carried out differently if the quantity f is only defined when there is an interaction, e.g. the average multiplicity and the quantity $\bar{u}$. See Appendix I for details on $\bar{\nu}$. The average is now given by

$$<f> = \frac{\Sigma\, n_i\, \sigma_i\, f(A_i)}{\Sigma\, n_i\, \sigma_i}$$

where σ_i is the absorption cross-section of the i-th species of nucleus. Carrying out this averaging, one finds that the average number of mean free paths seen by incident

hadrons are

$$\bar{\nu}_p = 2.45$$

$$\bar{\nu}_K = 1.74$$

$$\bar{\nu}_K = 2.12$$

An effective atomic number of 21.5 is needed to put the proton-emulsion absorption cross-section on the line $46.5A^{0.691}$, the best fit to proton-nucleus absorption cross-sections. Similarly, one needs to use an effective atomic number of 22.9 in order to place the pion-emulsion absorption cross-section on the line $30.7A^{0.728}$, the best fit to pion-nucleus absorption cross-sections.

Emulsion has been used for many years in high energy physics, both in accelerators and with cosmic rays. The emulsion serves simultaneously as a target and as a detector. An interaction occurs within the emulsion stack, and the resulting charged particles ionize the emulsion and leave tracks, which are rendered visible by a development process. These tracks can then be scanned for and measured under a microscope. These last two procedures are not unlike those in bubble chamber experiments.

Tracks are usually divided into two main categories: the shower tracks and the heavy tracks. The former are tracks with relatively low ionization, corresponding to velocities of $\beta > 0.7$. The heavy tracks are those with heavier ionization. These latter tracks are sometimes further subdivided into two groups: the gray tracks and the black tracks. The demarcation corresponds to $\beta \approx 0.3$. The shower tracks are generally believed to be mostly pions with an occasional fast proton. The heavy tracks are taken to be slow recoil protons and nuclear fragments.

The number of shower tracks in an interaction is denoted by the symbol n_s, while the number of heavy tracks is denoted by N_h. Averages are given by the same symbols in angle brackets, thus $<n_s>$ is the average shower track multiplicity.

It has been experimentally determined that the distribution of N_h is essentially independent of the beam energy, provided that it is above approximately 10 GeV. This fact is usually interpreted to mean that N_h is a reasonable measure of the identity of the struck nucleus and the severity of impact. However, it should be emphasized that at present there is no technique which can unambiguously identify the target nucleus on an event-by-event basis.

The typical N_h distribution[7] is illustrated in Figure A-IC-1. Half of the events have N_h greater than 7. Since the group of light nuclei in emulsion (C,N,O) have no

more than 8 protons each, the events corresponding to these nuclei are expected to populate almost exclusively the left half of the distribution. On the basis of known cross-sections, one expects the light nuclei to be involved in only 25% of the interactions. Thus one concludes that the heavy nuclei (Ag,Br) also contribute significantly to the region of N_h less than 7.

One could find the average shower track multiplicity for some given value of N_h. The result is a plot of $<ns>$ versus N_h. It has been observed that the data with beam energies ranging from 10 to 3000 GeV can be well approximated by a family of energy-dependent straight lines. This feature is reminiscent of the dependence of the average multiplicity on $\bar{\nu}$ in interactions of a hadron with targets of fixed atomic number. It is therefore tempting to postulate a one-to-one correspondence between N_h and $\bar{\nu}$. However, no such one-to-one correspondence has been established. Care ought to be exercised in comparing the results for some definite and selected values of N_h with data from experiments where targets of fixed atomic numbers are used.

The shower tracks in emulsion have a velocity cutoff similar to that used in this experiment ($\beta > 0.85$). In comparison with emulsion experiments, only the shower tracks are considered. The term "emulsion experiments" will be used to denote those experiments where the emulsion served both as the target and the detector. Hence the data from this experiment with an emulsion target would not qualify.

Emulsion experiments have several advantages over conventional high energy experiments. First, no other equipment is necessary, thus greatly simplifying the experimental setup. Until recently, no other equipment was used. Secondly, its compactness lends itself to high-altitude balloon experiments, which provide data on very high energy interactions -- 10 TeV proton-emulsion interactions are seen fairly routinely,[72] while present-day accelerators have yet to exceed 500 GeV. Thirdly, the high spatial resolution of emulsion (of the order of microns) is invaluable. It can be used to detect short-lived particles.[73] It can also be used to give a crude determination of momenta without the aid of magnetic fields -- the measured multiple scattering and the known radiation length furnish an estimate of the momentum of a particle. Attempts have also been made to measure momenta by undertaking the exposure of the emulsion stack in the presence of a strong external magnetic field.[74]

However, it is not without drawbacks. Because of the composite nature of emulsion, it is extremely difficult, if not impossible, to determine the identity of the target in any one given interaction; even though one could statistically separate the events into the so-called "light"

(C,N,O) and "heavy" (Ag,Br) groups. Recently, pellets[36] and wires[75] of metals have been successfully inserted into emulsion to remedy this. But success has only been met with a few metals, e.g. chromium and tungsten. These foreign objects degrade the spatial resolution in the vicinity of the interaction -- the pellets are usually of dimensions greater than the resolution of emulsion. See Figure 1 in Reference 36 for an example of a proton-tungsten interaction.

The statistics in emulsion experiments are usually quite poor -- too many beam tracks would make it difficult to locate interactions and measure the properties of the secondary particles. The number of events range from less than 100 (as in pellet-emulsion experiments) to several thousand.

In the case of cosmic ray experiments, the primary energy is poorly determined. Estimates on the average beam energy can be made, but the projectile's energy cannot be determined on an event-by-event basis. This problem of unknown incident energy is, of course, common to most cosmic ray experiments, land based as well as balloon borne.

There is one point about the data from emulsion experiments that ought to be investigated in greater detail. The data from emulsion experiments include the values of N_h and n_s for each event as well as the pseudorapidity

($\eta = -\ln \tan(\theta/2)$) of each of the shower tracks. One of the more interesting results is the observation that in the region $\eta > 5$, the average shower multiplicity $<ns>$ is a decreasing function of N_h.[52] And since N_h is often used as a guide to the identity of the target nucleus, it is therefore tempting to conclude that one ought to see a similar decrease in shower track multiplicity as the atomic number of the target increases.

Let $r(\eta,N_h)$ be the ratio of $\frac{dN}{d\eta}(\eta,N_h)$ to $\frac{dN}{d\eta}$ (η, hydrogen). Note that in emulsion experiments, "hydrogen" refers to those events where N_h is not greater than 1. The data can be parameterized by

$$r(5.5,N_h) \simeq 1 - 0.015\ N_h$$

for 200 GeV/c incident protons.[53] For $N_h = 25$, this ratio is about 1/2, indicating that the pseudorapidity distribution of $N_h = 25$ events is only half the height of the corresponding p-p distribution in the neighborhood of $\eta = 5.5$.

To estimate the effect that one might expect in reactions with a definite nucleus (but with no further separation of the data into different groups of N_h), one could make use of the N_h distribution (Figure A-IX-1) and the fit to the ratio $r(\eta,N_h)$. $r(\eta,N_h)$ has been parameterized in the form

$$r(\eta,N_h) = a(\eta) + b(\eta)\ N_h$$

where $a(\eta)$ and $b(\eta)$ are shown in Figure A-IX-2.[53]

Assuming that the Ag-Br data is that estimated by Babecki[7] -- also see Figure A-IX-1 -- it can be shown that averaged over all the (Ag,Br) data, $r \sim 0.9$ at $\eta = 5.5$. $\eta = 5.5$ is where the value of r is smallest in 200 GeV proton-emulsion interactions. One can also calculate the value of r at other values of η in the range $5.3 < \eta < 7$, the highest pseudorapidity bin in this experiment. Summing the results from the entire pseudorapidity range, one obtains an estimate of r greater than 0.95, i.e. the average multiplicity in a proton-(Ag,Br) interaction is expected to be no more than 5% lower than the proton-proton average multiplicity in the region $5.3 < \eta < 7$.

Two more observations are in order. First, the so-called proton-proton events in emulsion experiments are really $N_h = 0$ and 1 events. In other words, the denominator in the expression of $r(\eta, N_h)$ does not necessarily correspond to the results of proton-proton interactions. Secondly, the number of low N_h events included in the Ag-Br sample is no more than a guess. If one inspects the ν distribution -- Appendix I and Figures A-V-1 and A-I-2 --

one might reasonably conclude that the number of $N_h = 0$ and 1 events in the Ag-Br sample has been underestimated by the method of Babecki.

Thus the conclusion of this rather protracted discussion is that on the basis of emulsion data and some not unreasonable guesses the multiplicity in hadron nucleus collisions is expected to be approximately the same as in proton-proton interactions in the region of $5.3 < \eta < 7$. The data from this experiment for the range $5.3 < \eta < 7$ are shown in Figure A-IX-3; the average multiplicities are consistent with being independent of $\bar{\nu}$. Preliminary results from an optical spark chamber experiment[76] using targets of definite atomic number are in agreement with the observations of this experiment.

TABLE CAPTIONS

A-IX-1	Composition of emulsion.

FIGURE CAPTIONS

A-IX-1	N_h distribution for 25 to 200 GeV proton-Emulsion collisions. The numbers are from Reference 7.
A-IX-2	The fitted values of $a(\eta)$ and $b(\eta)$ in the formula $r(\eta, N_h) = a(\eta) + b(\eta)\, N_h$. The curves are from Reference 53.
A-IX-3	The average multiplicities measured in this experiment for the region $5.3<\eta<7$ at 50 GeV (O), 100 GeV (Δ) and 200 GeV (□). (a) Pion beam (b) Proton beam

TABLE A-IX-1

Composition of Emulsion

Element	Atomic Number	Relative Density (cm^{-3})
H	1	0.32519
C	12	0.13851
N	14	0.03183
O	16	0.09485
S	32	0.00131
Br	80	0.10039
Ag	108	0.10096
I	127	0.00057

FIGURE A-IX-1

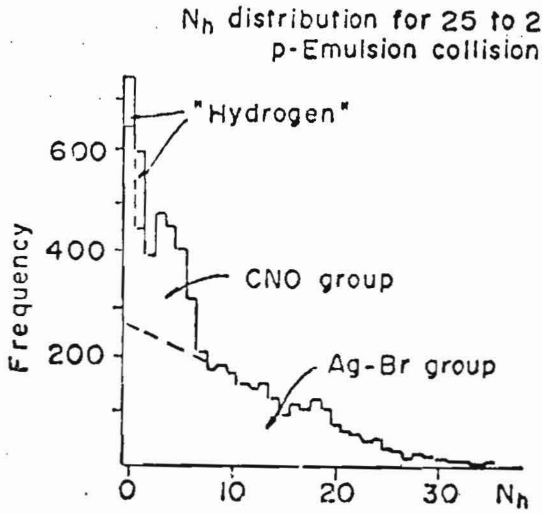

FIGURE A-IX-2

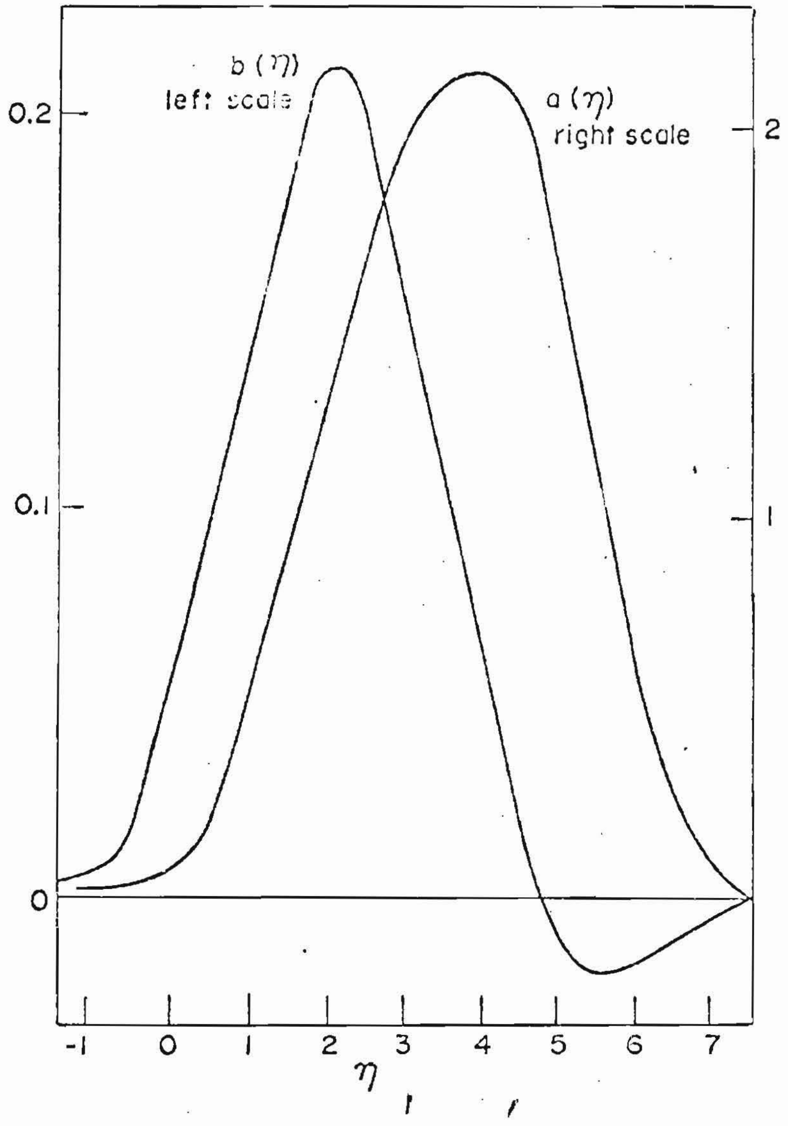

FIGURE A-IX-3

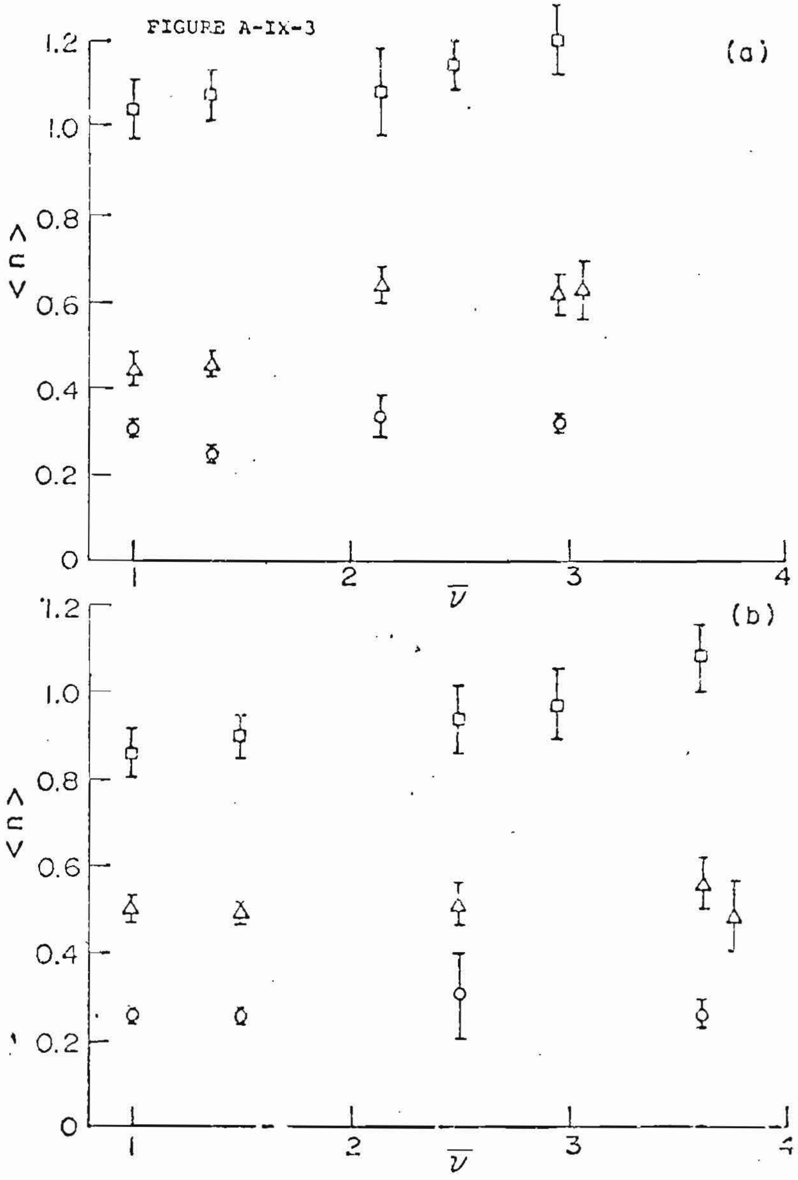

APPENDIX X

HYDRODYNAMIC MODEL

The hydrodynamic model[1,67,77,78,79,80] describes the dynamics of hadron-hadron interaction through their energy momentum tensor. It is assumed that the immediate result of a collision is a stationary (in the center-of-mass frame) flat disk of hadronic matter of very high temperature, the value of which is determined by the initial hadron energies. The volume of space that this hadronic matter occupies is a disk of thickness equal to the thickness of 2 Lorentz contracted hadrons. This highly compressed hadronic matter then expands according to the laws of (relativistic) hydrodynamics and cools down simultaneously. There is, by assumption, no viscosity. As the temperature reaches some critical value, pions condense out of this hadronic matter.

Most of the calculations have been carried out for the one-dimensional version of the model. The relativistic hydrodynamic equation in three dimensions is very difficult to solve and, in general, requires complicated numerical calculations. It is argued that the one-dimensional model is not unreasonable because the initial compression takes place longitudinally and the pressure gradient is therefore anisotropic. There is little or no

transverse compression. Within the context of the one-dimensional model, transverse motion is due to the thermal motion within the hot hadronic mass, which leads to an exponential $p_\perp$ dependence.

There are two free parameters in this theory. One is the speed of sound in nuclear matter, usually given the symbol c_o. It is specified once the equation of state is given:

$$c_o^2 = \frac{dp}{dE}$$

where p and E are the momentum and energy densities. The other parameter is the critical temperature at break-up, T_c. In the original version of this model put forward by Landau,[1] the equation of state is

$$p = \frac{1}{3} E$$

which is the same as for black-body radiation. It follows that the speed of sound is given by $c_o^2 = 1/3$. The breakup temperature is assumed to be of the order of the energy density of a physical pion. In other words, when the hadronic matter has expanded to the point where its energy density becomes comparable to that of physical pions, pions are expected to materialize. Indeed, the laws of hydrodynamics cannot be justifiably applied after this stage. In subsequent works by other authors, different equations of state are sometimes assumed. Others leave c_o as a free parameter to be determined from experimental data.

There are two prominent predictions of the hydrodynamic model concerning proton-proton collisions. First, the average multiplicity depends on the center-of-mass energy to some power:

$$<n>_{pp} \propto s^{\frac{1}{2}\frac{1-c_o{}^2}{1+c_o{}^2}}$$

In Landau's original version of the model, this becomes

$$<n>_{pp} \propto s^{1/4} \propto E^{1/4} .$$

The proportionality constant is, as far as can be ascertained, incalculable.

The other major prediction concerns the rapidity distribution. The hydrodynamic model predicts a Gaussian shaped rapidity distribution. In Landau's version, this distribution is given by:

$$\left(\frac{dN}{dy}\right)_{pp} = <n>_{pp} \frac{\exp(-y^2/2L)}{(2\pi L)^{1/2}}$$

where $L = \frac{1}{2} \ln \left(\frac{s}{4m_p^2}\right)$

and y = center-of-mass rapidity.

The average multiplicity in proton-proton collisions can be fitted by $2E^{1/4}$ in the energy range of 50 to 1000 GeV. In other words, Landau's assumption of $c_c{}^2=1/3$ is favored. However, this speed of sound leads to the above formula for the rapidity distribution, which is in disagreement with the data from the CERN Intersecting Storage Ring(ISR) on the width of the rapidity distribution. The data can be fitted much better by a Gaussian with a wider width. By allowing the breakup temperature T_c to be a free parameter, Andersson, Jarlskog and Damgaard[73] achieved a somewhat better fit with a single speed of sound. However, the inconsistency can only be reduced (but not eliminated) at the expense of limiting the range of rapidity and transverse momentum where the comparison is made. This is not very satisfactory.

The model can be applied to hadron nucleus collisions. As viewed in the laboratory, the first hadron-nucleon collision produces a hot hadronic mass which goes forward and interacts with other nucleons. Since the expansion time is long compared with the transit time between collisions (at ~100 GeV), the subsequent interactions are between nucleons and a slightly expanded hot hadronic mass. A new hot hadronic mass is generated at each collision. After the last collision, this mass is finally allowed enough time to expand to the point where pions condense out.

On the basis of Landau's hydrodynamic model, it has been predicted[77] that $R_A=A^{0.19}$, where A is the atomic number of the target. The quantity R_A is expected to be independent of energy. This is in apparent disagreement with the data, which show a weak but definite energy dependence.

The hydrodynamic model has no provision for the conservation and dynamical effects of quantum numbers besides energy and momentum. In particular, the model predicts no differences between reactions initiated by a proton, kaon or pion beam.

Masuda and Weiner[79] considered the pseudorapidity distributions of hadron-nucleus collisions and found adequate fits to the results of this experiment with $c_o^2=1/7.5$. This is significantly different from the value of the speed of sound required to give good agreement with the proton-proton multiplicities.

It appears that the one-dimentional hydrodynamic model cannot account for all the data with a single set of parameters. The three-dimensional model, which has been demonstrated to fit the proton-proton data quite satisfactorily,[78] has not been investigated in detail for its predictions on hadron-nucleus interactions.

APPENDIX XI

ENERGY FLUX CASCADE MODEL

The energy flux cascade model (EFC)[10] belongs to the class of models which attempt to describe a hadron-nucleus interaction through the properties of each of the many repeated independent collisions. It is close to Landau's hydrodynamic model in spirit:

> "The energy flux of hadronic matter is the essential variable that governs the early evolution of the system, and it is a cascade of this flux, and not of conventional hadrons, that occurs in a nuclear interaction."

The model views a hadron-nucleus interaction as a series of interactions with discrete nucleons. The first collision is "conventional" in the sense that it is a hadron-nucleon collision, while all subsequent collisions are between the generated energy flux and nucleons.

In order to obtain definite predictions, two postulates were put forward:

"(1) Subsequent to a p-p collision, hadronic matter is contained in a cylinder expanding uniformly from a disc at t=z=0; the stress tensor in the cylinder is determined by projecting the observed asymptotic flux backward in t via the classical trajectories of free particles.

(2) This flux scatters from nucleons as if it were a set H(t) of conventional hadrons, H(t) being determined by dividing the flux into slices each of which has the spatial thickness appropriate to a hadron moving with the mean rapidity of that slice."

The reasons for making these two particular postulates are discussed in Reference 10. Given these two postulates and a knowledge of the asymptotic properties of hadron-nucleon interactions, one could, at least in principle, predict all the properties of a hadron-nucleus interaction. Note that the model deals only with the longitudinal direction z and ignores the transverse directions.

Consider a proton-nucleus interaction where exactly ν nucleons are struck. Assume that the inter-nucleon distances are also given.

The first collision resembles in every respect a p-p collision at the same beam energy. The result of this collision is postulated to be the instantaneous creation

of an energy flux whose dynamical properties are the same as the asymptotic properties of the p-p final state. Its spatial property is, by assumption, characterized by a disc of zero thickness. The exact transverse dimensions are unimportant since the model only deals with the longitudinal dimension.

As this flux propagates toward the next nucleon, its thickness increases. This is due to the different velocity components in the energy flux. Thus at the instant of the second collision, the energy flux is an extended object. The second postulate instructs one as to how this energy flux-nucleon collision should be treated.

Consider the rapidity distribution of this flux. It is, by assumption, given by the observed rapidity distribution of p-p interactions. (That the rapidity is chosen as the dynamical variable instead of, say, the longitudinal momentum or the scaling variable x is for ease of computation as well as for convenience in comparing the predictions with experimental data.)

Figure A-XI-1 is a schematic illustration of the development of the energy flux. Consider the region in rapidity between y_2 and y_1. The energy of the enclosed flux is

$$E = \int_{y_2}^{y_1} \mu\left(\frac{dN}{dy}\right) \cosh(y)\, dy$$

where $\mu = \sqrt{m^2+p^2}$ is the transverse mass and is, in general, not a constant, while its longitudinal momentum is given by

$$P_{11} = \int_{y_2}^{y_1} \mu\left(\frac{dN}{dy}\right) \sinh(y)\, dy$$

So the longitudinal velocity of this energy-flux is

$$\beta_{11} = \frac{P_{11}}{E} = \frac{\int_{y_2}^{y_1} \mu\left(\frac{dN}{dy}\right) \sinh(y)\, dy}{\int_{y_2}^{y_1} \mu\left(\frac{dN}{dy}\right) \cosh(y)\, dy}$$

Now, that part of the flux with rapidity y_1 would have reached the point z_1 while the part of the flux with rapidity y_2 would have only reached the point z_2 as shown in Figure A-XI-1. The postulate instructs one to find the rapidity y_2 such that the thickness (z_1-z_2) is the Lorentz contracted thickness of a hadron moving at the velocity calculated above. The rest-frame thickness of hadrons is known to be about 1 fermi.

Having found y_2, the boundary between the first "hadron" and the second "hadron" within the energy flux, one could repeat the process and obtain y_3, and so on. Thus one obtains the set H(t) of "conventional hadrons" that exists at the second collision. Each of these "conventional hadrons," or slices of the original energy flux,

will undergo an "ordinary" hadron-nucleon collision and generate its own energy flux. Each of these new fluxes is again divided up into "conventional" hadrons at the third collision. This process is repeated until one has finished treating all the collisions.

Several features of this recipe are worthy of emphasis. First, it should be noted that the slicing procedure is not Lorentz invariant. In other words, an observer in a frame moving relative to the laboratory frame will decide, according to the same prescriptions as have been used in the laboratory frame, that the first slice should not terminate at a laboratory rapidity of y_2. It is easy to see that this is true. Gottfried has shown that when the maximum rapidity y_1 is large, then y_2 is approximately 1/3 of y_1 for a flat rapidity distribution. However, under a Lorentz transformation, the rapidity y changes by an additive constant.

One is therefore restricted to work in one particular frame of reference, say the laboratory frame. But there is still another problem. It is clear that as time progresses, the energy flux becomes more and more extended. Without any further restrictions, one could slice an infinite number of hadrons from it. This is a highly undesirable property of any model intended to describe nature as it is now known. It is therefore assumed that each slice must occupy some minimum thickness in rapidity. This thickness is chosen to be the average rapidity thickness of hadronic secondaries in p-p interactions.

A third point is that each of these slices will, in general, have an unphysical invariant mass. In itself, this is of no great concern. But it leads to a rather strange situation -- the second collision may have a center-of-mass energy higher than the first collision.

Another difficulty lies in the assumption that the immediate product of a hadron-nucleon interaction has no spatial thickness. While it may be small, this thickness cannot be zero. Since all longitudinal dimensions (e.g. the thickness of each of the slices of "hadrons") are Lorentz contracted, the initial thickness is not necessarily negligible in comparison. A somewhat more realistic picture of an initially extended object makes it impossible to calculate the boundary y_2 between the first and the second slice of "hadron" unless further assumptions are made concerning the correlations between the spatial and rapidity distributions.

While the exact consequences are dependent on the details of the assumptions, it is easy to see that drastic modifications to the predictions are possible. Consider a proton-proton collision where the incident proton has an energy E. It is reasonable to assume that the energy flux

has an initial thickness of the order of 1/E fermi, where E is expressed in units of GeV. A pion that eventually materializes from this hadronic flux may have an energy comparable to E; however, its thickness would be only 1/7E fermi. Therefore it appears that it is possible to have the fastest pion materialize quite early.

Two more questions may be raised. Where is the initial flat disc of energy flux located? When does the next collision take place? While these uncertainties on inter-collision distances probably do not exceed 1 fermi, they are not negligible compared with the mean free path. And since the boundary y_2 is time dependent, these uncertainties may affect the final results.

For the time being, one may disregard these objections and complications, and simply inquire into the consequences of such a simple picture of hadronic reaction. In principle, the model has been completely specified and calculations can be made; however, in practice, one needs a parameterization of the proton-proton final state configuration. In Reference 10, it is assumed that the asymptotic p-p final state is described by a flat rapidity distribution of height equal to the experimentally observed value (2.9) and that all successive collisions are separated by one mean free path. It is further assumed that the effects of leading particles can be approximated by delta-functions in the rapidity distribution. For this particular rapidity distribution, it can be shown that $y_2 \approx y_1/3$ and $\beta_{11} \approx \tanh^{-1}(\frac{y_1+y_2}{2})$. Furthermore, the energy contained in the first slice H_1 is

$$E_1 \approx E_{inc} \left(1 - \left(\frac{m^2}{s}\right)^{2/3}\right)$$

where m is the nucleon mass and E_{inc} is the energy of the beam particle. That is, the first slice contains essentially the full incident energy. Additionally, in the 100 GeV range, the rapidity distribution is too narrow to allow the existence of H_3.

The second collision is therefore between the target nucleon and a set of 2 hadrons, H_1 and H_2. H_2 has an energy

$$E_2 \approx E_{inc} \left(\frac{m^2}{s}\right)^{2/3} \approx \frac{s^{1/3}}{2}$$

where s is expressed in GeV^2. H_2 is, therefore, incapable of initiating its own energy flux. The second slice H_2 simply propagates through the nucleus and materializes into physical hadrons far outside the nucleus. The first slice, H_1, is practically identical to the initial hadron. A new energy flux is therefore produced. If $\bar{\nu}$ nucleons participate, then there are $(\nu-1)$ H_2's produced in addition

to the entire energy flux resulting from the last collision.

From the assumption that the multiplicity in hadron-nucleon collisions depends on the energy through a ln(s) dependence, it follows that the multiplicity is given by

$$n_{pA} \approx n_{pp}(s) + (\nu-1)\ n_{pp}(s^{1/3})$$

$$\approx n_{pp}(s)\ \left(1 + \frac{1}{3}\ (\nu-1)\right)$$

where n(s) is the p-p multiplicity at a center-of-mass energy of $\sqrt{s}$. Thus the ratio of multiplicities is given by

$$R_A = \frac{n_{pA}}{n_{pp}} = 1 + \frac{1}{3}\ (\nu-1)$$

Reference 10 then assumes that for a target of fixed atomic number A rather than a fixed number of collisions one simply replaces ν with the average value $\bar{\nu}$ in the equation for multiplicity ratios.

The predictions of the simple EFC model can be summarized as follows. The ratio of multiplicity in a p-A interaction to that in a p-p interaction is given by

$$R_A = 1 + \frac{1}{3}\ (\bar{\nu}-1)$$

which is obviously independent of energy. The rapidity distribution has an enhancement over the corresponding distribution in a p-p interaction. This enhancement is restricted to the region of rapidity less than 1/3 of the maximum rapidity. This factor of 1/3 is expected to be independent of energy.

Some unjustified assumptions will now be pointed out. First of all, the proton-proton rapidity distribution is distinctly different from that assumed in the calculation. Secondly, collisions are, in general, not separated by exactly one mean free path. The average multiplicity in a proton-proton interaction is better approximated by a+b ln(s) in the 100 GeV range. The final step of transforming the quantity ν in the formula for R_A into the parameter $\bar{\nu}$ cannot be justified without making some assumptions about the target nucleus. A more realistic calculation requires an averaging over the leading particle spectrum, which has been taken to be a delta function in this calculation.

The sensitivity of the model's predictions to some of the assumptions will now be examined. Consider the interaction of a 100 GeV proton with ν successive nucleons spaced apart by R_0, where R_0 is the rest-frame thickness of a hadron. The rapidity distribution is assumed to be flat as in Reference 10. And let the proton-proton average charged multiplicity be given by[60] $\langle n\rangle_{pp} = -0.5+1.27\ \ln(s)$. The enhancement in the rapidity distributions is indeed

confined to the region less than 1/3 of the maximum rapidity. However, if one parameterizes R_A as

$$R_A = 1 + c\ (\nu-1)$$

the parameter c has the value 0.42 instead of 0.33 as in the simple model.

If the rapidity distribution is assumed to be Gaussian in shape rather than rectangular, one would obtain 0.37 for the value of c. The enhancement in the rapidity distribution is still confined to some region of low rapidity. The form of the Gaussian is assumed to be

$$\frac{dN}{dy} = \langle n\rangle\ \exp\ (-y^2/2L)/\sqrt{2\pi L}$$

where $L = \frac{1}{2}\ \ln\ (\frac{s}{m_p^2})$

y = center-of-mass rapidity

$\langle n\rangle$ = average multiplicity in a p-p collision at a center-of-mass energy $\sqrt{s}$.

Repeating the calculations at 50 and 200 GeV shows that these observations are insensitive to the initial beam energy. The energy and ν dependence of the rapidity distributions are illustrated in Figures A-XI-2 and A-XI-3.

Notice in Figure A-XI-3 that $\frac{dN}{dy}$ is a slowly decreasing function of ν in the region $y \gtrsim 5$. The multiperipheral model expects a similar depletion -- see Appendix XII. However, this feature may be due entirely to the assumed s-dependence of the average multiplicity and rapidity distribution.

The predictions of the EFC model are quite sensitive to the inter-collision distance. If the inter-collision distance is increased from R_0 to $2R_0$, the value of c becomes 0.52 and 0.49 respectively for the flat and Gaussian rapidity distributions. The rapidity width of the enhancement also increases. And in the case of the Gaussian rapidity distribution, the extra multiplicity is not obviously confined to some region in rapidity. These effects are illustrated in Figure A-XI-4 for the case of $\nu=3$.

It is obvious that the predictions of the model change dramatically when the assumptions are modified. The model is actually not as parameter free as the author would have the readers believe.

The above discussions and calculations are intended only as guides to the different predictions of the model under various assumptions. They are not meant to be a fit to find the most appealing set of parameters. Thus, it can be concluded that a value of c different from 1/3 does not necessarily exclude the EFC model; nor does the absence of an abrupt change in the rapidity distribution

in the region of 1/3 of the maximum rapidity. Since all the known corrections to c increase its value, an experimental value of less than 1/3 would be incompatible with the EFC model. The best experimental value at this point is approximately 1/2.

There has been a lot of interest in this model and many discussions can be found in the literature.[81] More sophisticated calculations have also been made.[82] However, the most serious objection to the model, its failure to incorporate Lorentz invariance in the slicing procedure, has not been resolved.

FIGURE CAPTIONS

A-XI-1 Illustration of a hadron-nucleus collision in the energy flux cascade model.

(a) Just before the collision, the target nucleon has rapidity y_0 and the beam particle has rapidity y_1.

(b) Immediately after the first collision, there is a flat disk of hadronic matter -- the energy flux -- which has some distribution in rapidity. For simplicity, it is illustrated as a flat distribution from y_0 to y_1.

(c) Prior to the second collision, there are 2 "hadrons" H_1 and H_2.

(d) The H_1-nucleon collision results in a new energy flux. At an incident beam energy of $\sim$100 GeV H_2 is not energetic enough to initiate its own energy flux. The resulting rapidity distribution has an enhancement between y_0 and y_2.

A-XI-2 Results of a Monte-Carlo calculation of the rapidity distributions at 50 and 200 GeV. It is assumed that there are 3 participating target nucleons separated by R_0, the rest-frame thickness of a hadron. The top graph is the result

when the p-p rapidity distribution is assumed to be Gaussian. The lower graph is the result of a flat distribution.

A-XI-3 Results of a Monte-Carlo calculation of the rapidity distributions in 200 GeV hadron-nucleus collision as a function of the number of interactions ν. Successive interactions are assumed to be separated by the rest-frame thickness of a hadron. The upper and lower graphs are for Gaussian and flat p-p rapidity distributions.

A-XI-4 Rapidity distributions for $\nu=3$ in 200 GeV hadron-nucleus collisions as a function of inter-collision distance ΔZ. The upper and lower graphs are for Gaussian and flat p-p rapidity distributions. Notice in the top graph that there is no obvious "kink" when $\Delta Z=2R_0$.

FIGURE A-XI-1

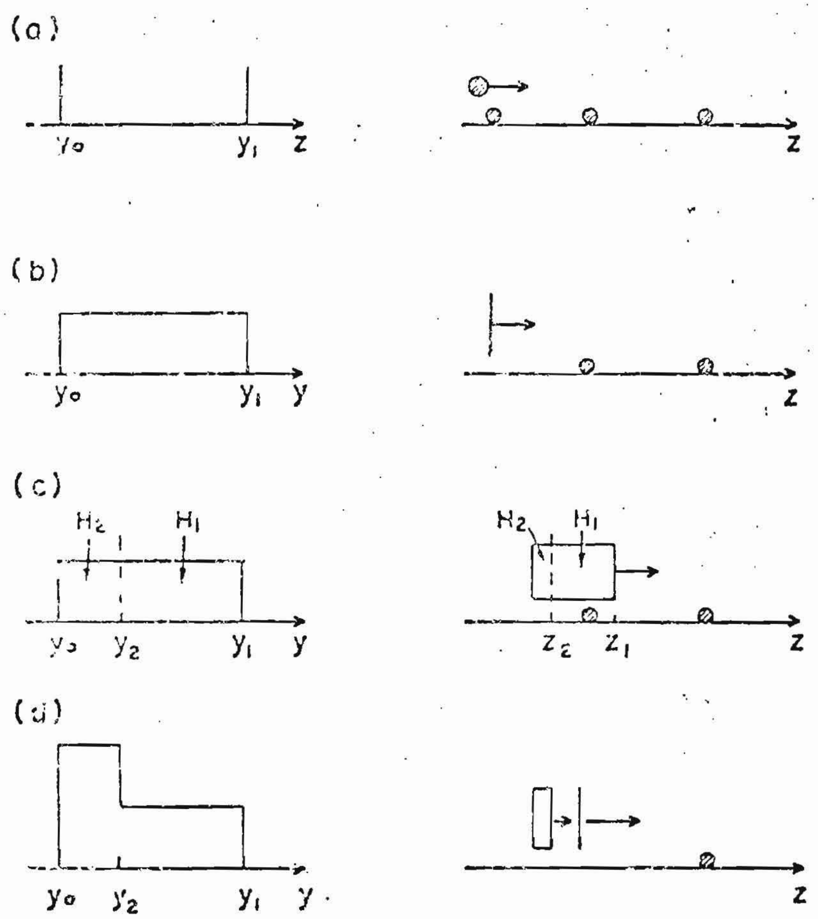

FIGURE A-XI-2

Energy-Dependence of the Energy Flux Cascade Model for $\nu = 3$

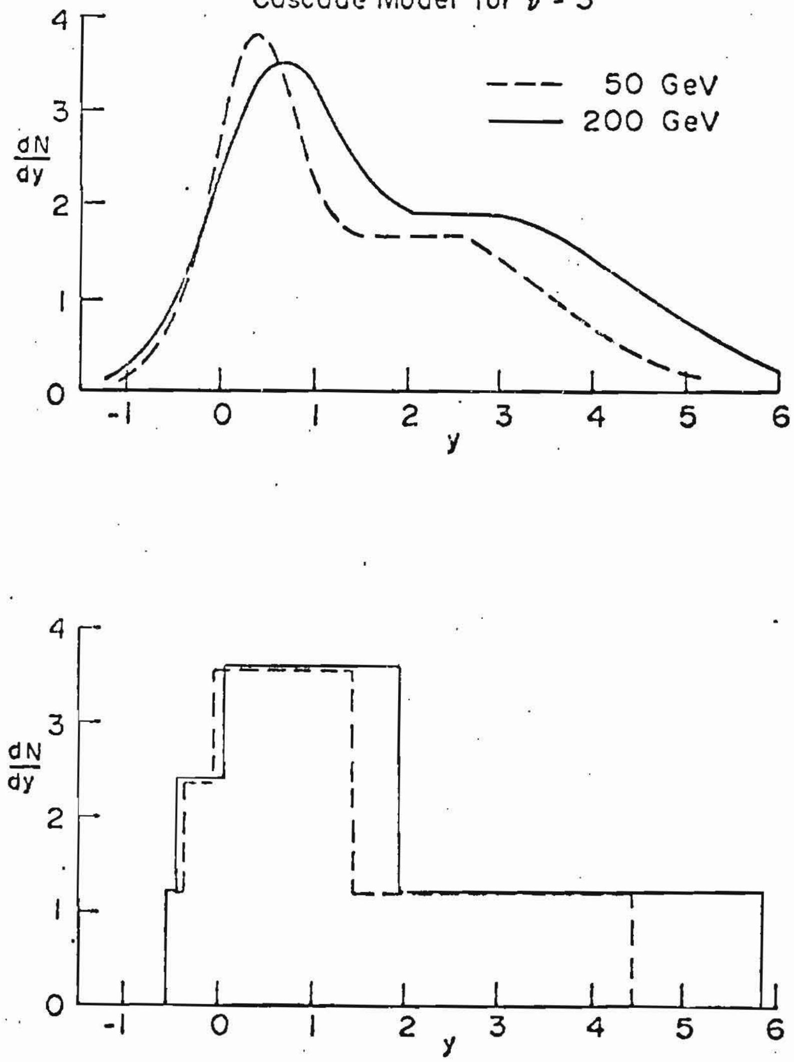

FIGURE A-XI-3

ν-Dependence of the Energy Flux Cascade Model

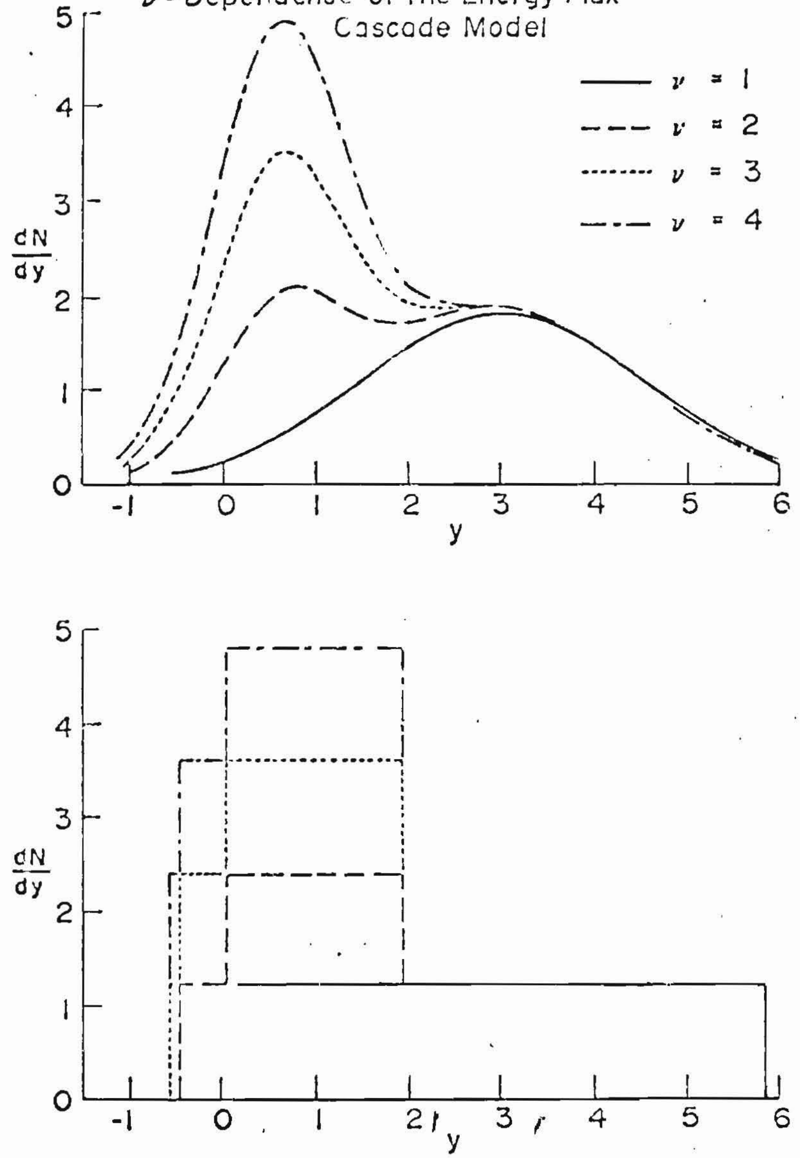

FIGURE A-XI-4

Predictions of the EFC Model for $\nu = 3$ as a Function of Inter-collision distances

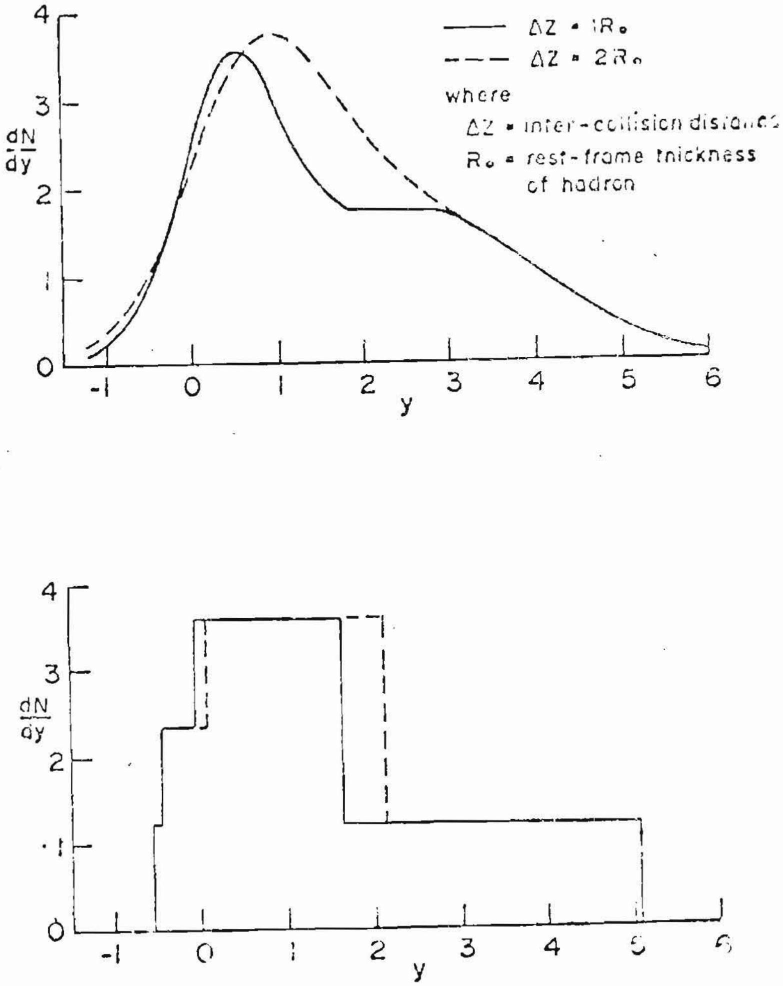

APPENDIX XII

MULTIPERIPHERAL MODEL, PARTON MODEL AND REGGEON FIELD THEORY

For the purposes of this discussion, which will be carried on at the qualitative level, the multiperipheral model,[3] the parton model[11] and Reggeon field theory[12] are essentially equivalent. The detailed mathematics of various versions of these models are obviously different, but they will not be entered into here, for they are beyond the scope of this thesis as well as the ability of its author. In the following the jargons of these three classes of theories will be used interchangeably and fairly loosely.

A hadron can be viewed as a superposition of point-like partons or as one or more multiperipheral chains. It is a basic assumption that only small momentum transfers are involved at each step of the ladder. Equivalently, only partons with similar momenta can interact, i.e. only the "wee partons" can interact significantly with the target. The energy E_i of the i-th parton is a fraction of the energy of the (i-1)-th parton, i.e.

$$E_i = k E_{i-1}$$

where k is a constant fraction independent of i.

An immediate consequence of this is that in hadron-hadron interactions, the rapidity distribution of final state particles will be flat and of a height independent of energy. These two conditions should be satisfied at asymptotic energies. It is, of course, not definite what "asymptotic" means. It should be noted that the rapidity distribution

$$\frac{dN}{dy} = \frac{1}{\sigma_{in}} \frac{d\sigma}{dy}$$

is neither flat nor constant in height up to ISR energies, $s \sim 2500$ GeV^2. Since the width of the rapidity distribution grows logarithmically with energy, the model also predicts a ln(s) dependence of the average multiplicity. The experimental data on proton0proton multiplicities can be fitted much better by the form a+bln(s).[61]

The multiperipheral ladder is depicted in Figure A-XII-1 in the form of a conventional Feynman diagram. However, the space-time development of the ladder is obscured. Figure A-XII-2 shows the same ladder in a space-time picture. It illustrates the evolution of the beam hadron into a set of partons in the target's rest frame. An estimate of the time scale is given by

$$\tau = \frac{E}{m} \tau_0$$

where E and m are the energy and mass of the beam particle and τ_0 (of the order of fermis) is the characteristic strong interaction time scale. Since $E_{i+1}=kE_i$, the time interval between the emission of successive partons decreases as one approaches the "wee partons." This is illustrated in Figure A-XII-2. This time τ is of the order of 10 fermis at 100 GeV and is the explanation for the relative unimportance of the 2 Reggeon diagram in high energy elastic scattering, Figure A-XII-3. The so-called Mandelstam diagram, Figure A-XII-4, may still contribute. It is topologically different from the diagram of 2 sequential elastic scatterings.

Now consider an inelastic hadron-hadron collision. This is shown schematically in Figures A-XII-1 and A-XII-2. The identities of the exchanged and produced objects, corresponding to the vertical and horizontal lines in Figure A-XII-1, depend on the particular model under consideration. The class of multiperipheral models generally assumes that the produced objects which eventually become the final state hadrons are produced in some independent emission process. This leads to a Poisson-shaped multiplicity distribution. The data are in drastic disagreement with this prediction. See Figure III-11.

This problem can be easily remedied by the so-called 2-component models. The high multiplicity component is

given by a multiperipheral process while the low-multiplicity part is accounted for by a diffractive process, e.g. the mechanism invoked in the 2-fireball model. However, if one intends to stay within the multiperipheral picture and to not invoke other processes, this can be interpreted as an indication that a single chain is not compatible with data. The possibility of multiple chains has to be entertained if the model is to survive.

Another consequence of the presumed dominance of a single Regge pole is that the inelastic cross-sections should factorize, i.e.

$$\frac{\sigma_{in,\,pA}}{\sigma_{in,\,\pi A}} = \frac{\sigma_{in,\,pp}}{\sigma_{in,\,\pi p}}$$

The right hand side is approximately 3/2, while the left hand side approaches 1 for heavy nuclei. So the data tend to refute factorization and therefore require that multi-Regge poles be included in calculations with the model.

For the time being, assume that the dissociation of the beam hadron into multiple chains is relatively unimportant. Applying the basic ideas to a hadron-nucleus collision, one arrives at the following situation.[4] A beam hadron of energy E approaches the target nucleus, which is at rest in the laboratory frame of reference.

This target nucleus occupies some region of space from z_1 to z_2, as shown in Figure A-XII-5. Recalling that only "wee partons" may interact with the target, one can conclude that if there is to be an interaction at all. the beam hadron must start dissociating into its constituent partons at a time $-\tau$, where $t=0$ has been chosen to be the time when the beam particle is coincident with the target nucleus.

Suppose that the first collision occurs at z_1. This information propagates back toward the fast partons at the rate indicated by the dashed line in Figure A-XII-5. It is the time when recombination is expected if the scattering were elastic. Until after this time, each parton must remain as a constituent of the original beam particle in the sense that it is incapable of generating its own multiperipheral ladder. This property has been endowed exclusively upon hadrons; indeed it may be viewed as the definition of a hadron. This can be cast in a slightly more sophisticated language. The emission of a multiperipheral chain by a parton is governed by the triple-Regge coupling constant, which is usually taken to be very small. However, after the partons have re-arranged themselves into physical hadrons, the emission of a chain is no longer suppressed by this small coupling constant. Therefore, the size of the target (z_2-z_1) determines which group of partons (or produced hadrons) could conceivably

take part in rescattering. The cutoff rapidity is denoted by y_c in Figure A-XII-5. Those partons with rapidity $y>y_c$ simply traverse the nucleus without interacting at all, identical to those in hadron-nucleon scattering. Therefore the rapidity distributions for nucleon and nucleus targets are expected to be different only in the region $y<y_c$. See Figure A-XII-6. The value of y_c should increase with the size of the target but is expected to be independent of energy as illustrated in Figure A-XII-7. The height of the rapidity distribution in the region $y<y_c$ is higher than that in hadron-nucleon interactions.

An estimate of the amount of increase in multiplicity over a proton-proton collision can be made easily by comparison with the energy flux cascade model (Appendix XI). Translated to the language of the parton model, the EFC model assumes that the fast partons rescatter and give rise to an extra multiplicity. Its predictions on the atomic number dependence of the multiplicity are weaker than that observed. The above multiperipheral picture would have the slow component rescatter. And since the average multiplicity is lower when the beam energy is lower, the predicted atomic number dependence of the multiplicity is much too gradual to be compatible with experimental results.

This difficulty together with the difficulties the model has in connection with p-p interactions leads one to the conclusion that if the multiperipheral model is to be valid, graphs with multiple ladders are important and cannot be ignored. The inclusion of multiple chains (but excluding Reggeon interactions) have been studied by many authors.

J. Koplik and A. Mueller[83] have investigated the connection between elastic and inelastic processes in hadron-nucleus interactions. In the simple picture where one is restricted to a single ladder, the central plateau in rapidity (if it exists) should be the same for hadron-nucleon and for hadron-nucleus interactions. An increased height in this central plateau for hadron-nucleus interactions is a measure of the probability of having multiple chains in existence simultaneously. These coexisting Reggeons are the generalizations of the Mandelstam graph shown in Figure A-XII-4, and they can contribute to the elastic cross-section, unlike Reggeons that exist sequentially. Thus Koplik and Mueller were able to derive bounds on the ratio of elastic to total cross-sections as a function of the height of the central plateau in hadron-nucleus interactions.

Let r be the ratio of elastic and diffractive cross-sections to the total cross-section, and let R_c be the ratio of the heights of the central plateaux in pA and pp collisions, i.e.

$$R_c = \frac{\left(\frac{1}{\sigma_{in}} \frac{d\sigma}{dy}\right)_{pA}}{\left(\frac{1}{\sigma_{in}} \frac{d\sigma}{dy}\right)_{pp}}$$

The connection between r and R_c is given as follows. If n is such that

$$\frac{1}{2}\left(\frac{1-2^{2-n}}{1-2^{1-n}}\right) \leq r \leq \frac{1}{2}\left(\frac{1-2^{1-n}}{1-2^{-n}}\right)$$

then $R_c \geq n+1 + 2^{n-1}\left(\frac{2r-1}{1-r}\right)$

The black disk limit, r=1/2, is achieved when n becomes infinite. R_c also becomes infinite. It follows that if the data shows that $r \approx 1/2$ and $R_c \approx 1$, multiperipheral model need major modifications to remain viable.

Present data indicate that nuclei, especially heavy ones, are quite black to incident protons, therefore the model predicts that the rapidity distribution in pA interactions should be as illustrated in Figure A-XII-6. The projectile fragmentation region may be depleted as a result of momentum conservation. Some cascading may occur in the target fragmentation region. The central region, which has so far not been observed to exist, should show a distinct enhancement when compared to a p-p interaction. J.H. Weiss[84] and C.A. Winbow[12] have arrived at similar conclusions.

In another version of the multiperipheral model, A. Capella and A. Krzywicki[85] made the assumptions (1) that the incident hadron dissociates into several equivalent ladders, the number of which is determined by the number of interactions that the projectile actually undergoes as it traverses the nucleus, and (2) that the partition of energy among the chains is completely random. The assumptions simply state that a proton-nucleus interaction involving ν collisions at a beam energy E can be viewed as ν parallel proton-proton collisions each with an energy E_i such that the total beam energy is E. This picture has been used to fit the 200 GeV proton data of this experiment and has succeeded remarkably[85] -- the predicted pseudorapidity distributions are in almost perfect agreement with the data.

Some objections to the model will now be raised. The partition of energy among the many hypothetical "protons" has been taken to be random, and these sub-energies add up to E. Then the leading particle effect should be greatly suppressed for heavy nuclei because it would require a partition of energy that is highly asymmetric. This is difficult to reconcile with the fact that intense high-momentum secondary beams can be made from a tungsten target. More definitive statements could only be made when there are additional data on the multiplicity associated with a high-momentum leading particle.

This problem can be avoided if one first partitions the energy into a share for the leading particle and another share for the multiple collisions. Then the sum of the sub-energies should not add up to the incident beam energy E.

There appears to be a further difficulty with the differences between a proton beam and a pion beam. To argue that a proton-nucleus collision may be equated with many parallel proton-nucleon interactions, it is necessary to assume that the number of virtual multiperipheral chains is large, i.e. much larger than $\bar{\nu}$. It follows that the cross-section of each chain on a nucleon is smaller than the hadron-nucleon cross-section by a factor of the order of the number of chains. Since the quantum numbers of the beam particle reside mostly in the fast components (in order to have a leading particle) and since only "wee" partons interact with the target, a proton and a pion beam differ mainly in the numbers of virtual chains that each one has. In the limit of a large number of chains each with a small probability of interaction, one would expect the same A-dependence for the absorption cross-sections of p-A and π-A interactions. Different A-dependences have been observed experimentally.

The ability of this particular model to fit the data of this experiment cannot be denied, but its difficulties with hadron-nucleus cross-sections and with the leading particle effect are disturbing.

FIGURE CAPTIONS

A-XII-1	Feynman diagram for an inelastic reaction in the context of the multiperipheral model.
A-XII-2	A space-time diagram of the same reaction.
A-XII-3	Two sequential elastic interactions. There is a minimum value for the spatial separation of the two interaction points.
A-XII-4	Two parallel elastic interactions. There is no constraint on the spatial separation between the two interaction points.
A-XII-5	Re-scattering of the slow component. The dashed line represents an estimate of the times at which the partons become hadrons and start emitting their own multiperipheral chains. The critical rapidity y_c is a function of the distance between the two scatterings.
A-XII-6	The expectations of the hadron-nucleus rapidity distribution as a result of the re-scattering of the slow component.
A-XII-7	The energy and target dependences of the hadron-nucleus rapidity distribution as a result of re-scattering of the slow component.
A-XII-8	Illustration of the predictions of the multi-peripheral model in the presence of multiple chains.

FIGURE A-XII-1

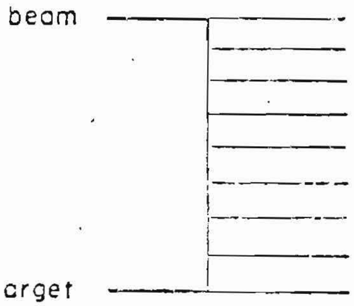

FEYNMAN DIAGRAM

FIGURE A-XII-2

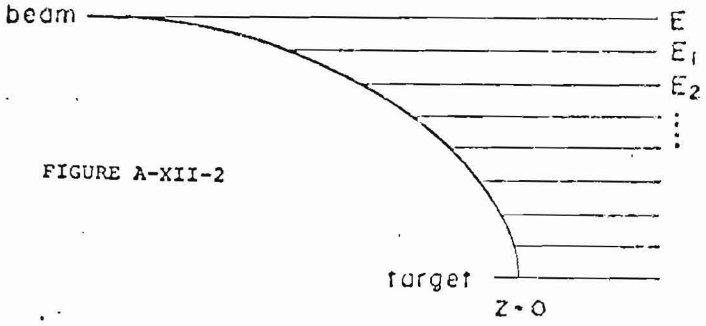

SPACE-TIME PICTURE

FIGURE A-XII-3

Two Sequential Interactions

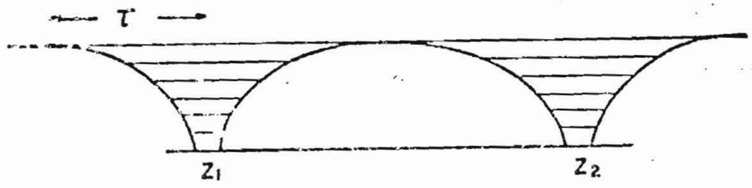

$(Z_2-Z_1) \gtrsim \tau$

Two Parallel Interactions

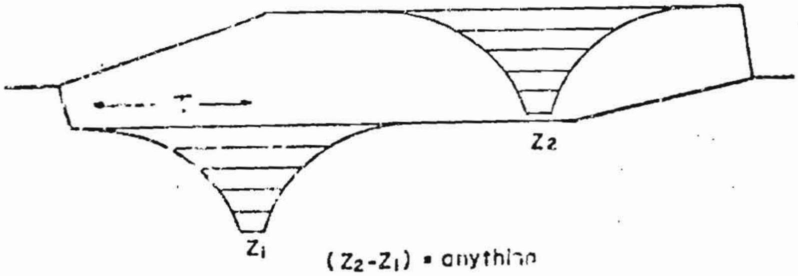

(Z_2-Z_1) = anything

FIGURE A-XII-4

FIGURE A-XII-5 RE-SCATTERING OF THE SLOW COMPONENT

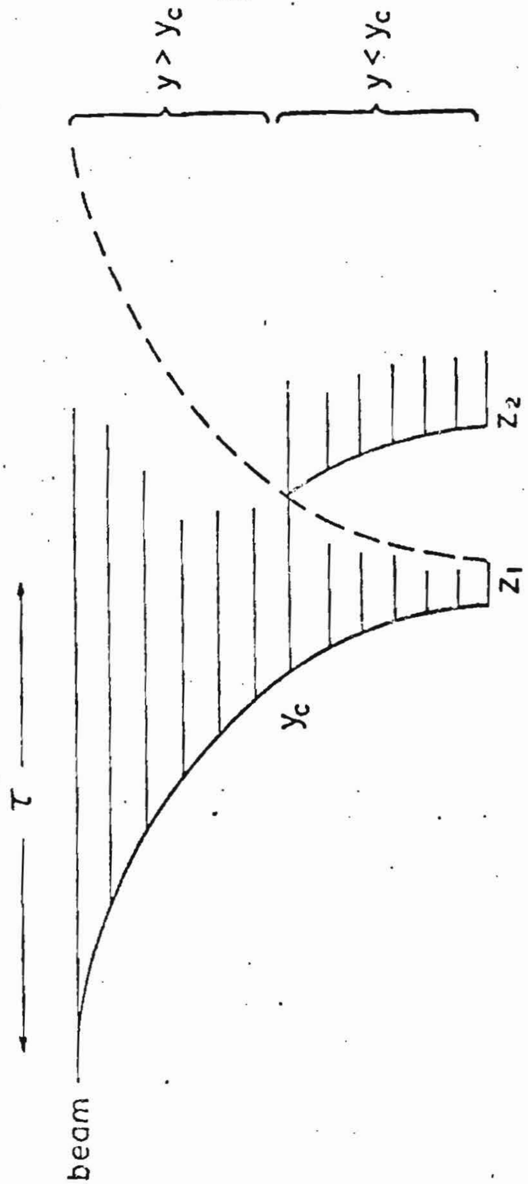

FIGURE A-XII-6

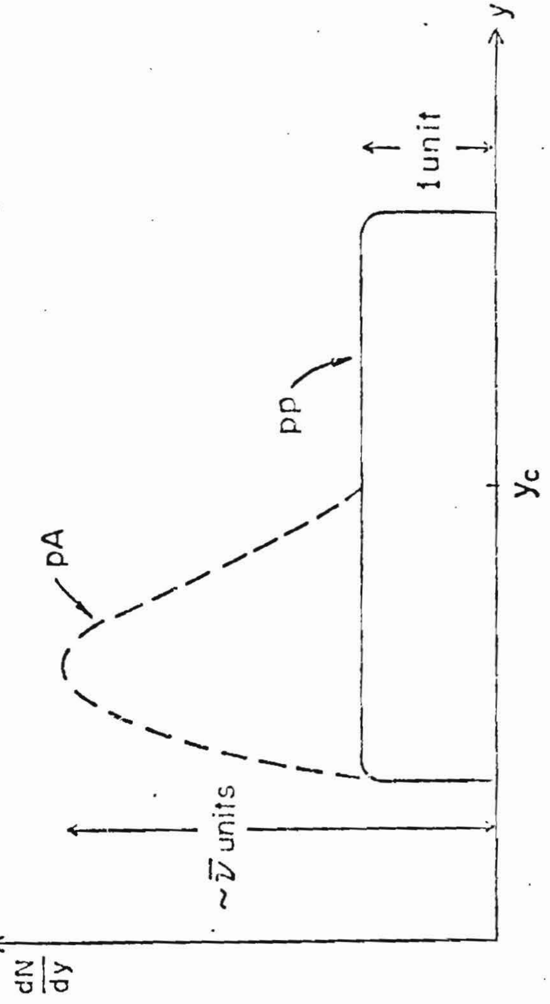

FIGURE A-XII-7

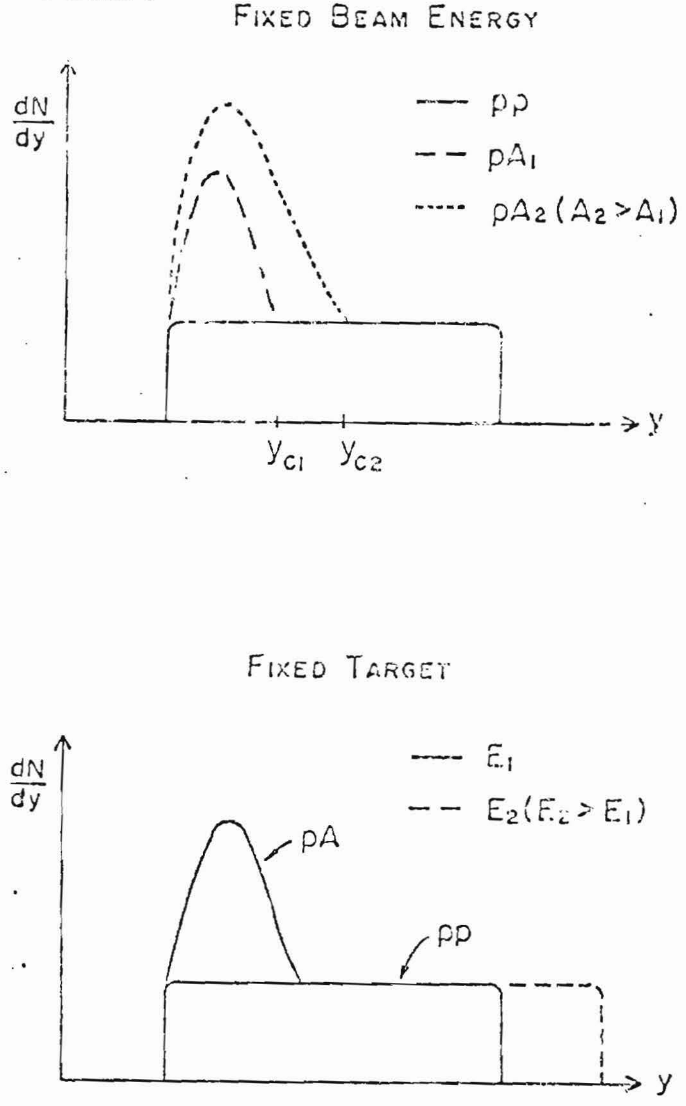

FIGURE A-XII-8

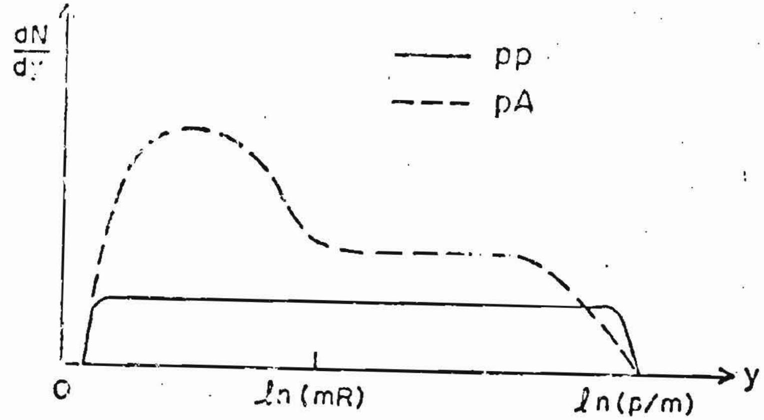

APPENDIX XIII

TWO-FIREBALL MODEL

The two-fireball model[13] assumes that in a proton-proton collision, one or both of the protons becomes highly excited. After a comparatively long period of time, the excited object decays into the final state hadrons. This decay is usually assumed to be isotropic in the rest frame of the excited object. These excited objects are assumed to retain the quantum numbers of the beam and target, i.e. a Pomeron is exchanged in the interaction, and have all the properties of initial particles until they decay.

It predicts that in hadron-nucleon collisions the cross-section for producing n particles approaches an asymptotic limit as the energy increases. It is expected that the low multiplicity part will reach this limit earlier than the high multiplicity part. This is in apparent contradiction to data. The 4- and 6-prong cross-sections are decreasing with energy after attaining a maximum.[86] Another prediction concerns the topological cross-sections for large values of n, i.e. n greater than the average multiplicity. These cross-sections are predicted to behave like $1/n^2$. The data exhibits a much faster fall-off.[86] These predictions on the topoligical cross-sections are similar to those in the hypothesis of limiting fragmentation.[87]

In a proton-proton collision at sufficiently high energies, the model expects to see two distinct peaks in the rapidity distribution corresponding to the two fireballs going off in opposite directions. The data from the ISR display only one central peak. Cosmic ray data at an average beam energy of ~1 TeV appear to have a dip in the central region of the pseudorapidity distribution.[88] Because of the transformation properties between rapidity and pseudorapidity -- See Appendix II -- this observation is consistent with a flat or slightly peaked rapidity distribution. In other words, the cosmic ray data are not definitive on this point.

All these difficulties could be attributed to a non-asymptotic energy. If that is the case, the model has no relevance to present-day accelerator data and its efficacy can neither be confirmed nor denied. Less drastic measures to salvage the model include the introduction of asymmetric decay of the fireballs. Another approach involves changing an input assumption. The average multiplicity has been assumed to have a ln(s) dependence. Modifying this will change the predictions.

This model can be applied very simply to hadron-nucleus collisions. The first collision between the beam hadron and a target nucleon produces 1 or 2 fireballs.

The beam hadron or its daughter fireball has not decayed by the time it has traversed one mean free path. It then undergoes another collision. By assumption, the beam fireball has the collisional properties of the original beam hadron. Therefore the second collision resembles the first. This process is repeated until the beam hadron or fireball exits from the nucleus. After a sufficiently long time, all the fireballs decay to yield the final state hadrons.

Consider the simple case where two fireballs are always produced in any one collision. If there are a total of ν collisions, there will be $(\nu+1)$ fireballs. A hadron-nucleus collision produces two fireballs which decay into $\langle n \rangle_{hp}$ particles, therefore, these $(\nu+1)$ fireballs will decay, on the average, into $(\frac{\nu+1}{2})\ \langle n \rangle_{hp}$ particles. It has been tacitly assumed that the energy is high enough that all fireballs have attained their asymptotic properties. This leads to a prediction of

$$R_A = \frac{1}{2} + \frac{1}{2}\,\bar{\nu}$$

The data are compatible with this prediction.

This agreement is rather surprising. At Fermilab energies, it is known that the leading particle (or fireball) has an energy which, on the average, is half the incident beam energy. The second collision is therefore between a target nucleon and a beam hadron of only half the initial beam energy. The fireballs produced in this second interaction should, on the average, have a lower multiplicity than the first interaction. In other words, the fireballs are not all identical. The predictions of R_A would have to be appropriately modified.

The predictions of R_A depend on the identity of the beam particle. For a proton beam, all fireballs have the same quantum numbers and the above prediction holds. However when a pion or kaon beam is used, one fireball has a different set of quantum numbers. This effect can be estimated. Consider 100 GeV/c beam particles. The average charged multiplicity of 6.5 in proton-proton interactions implies that each proton-like fireball gives rise to 3.25 charged particles. A π^+-proton average charged multiplicity of 6.8 implies that a pion-like fireball gives rise to 3.55 charged particles on the average. This leads to a prediction of

$$R_A = (3.55 + 3.25\,\bar{\nu})/6.8$$
$$= 0.52 + 0.48\,\bar{\nu}$$

for a pion beam. The difference between the 2 predictions are probably smaller than the finite energy corrections. And in any event, the accuracy of the data is not sufficient

to pinpoint this small effect.

Since the decay of the fireballs are independent, the multiplicity distribution in a hadron-nucleus interaction is expected to be simply convolutions of the multiplicity distribution in hadron-nucleon interactions. However, the multiplicity distribution predicted for hadron-nucleon interactions appears to be wrong. If the theory can be modified to give agreement with the proton-proton multiplicity distribution, then one should attempt a comparison for hadron-nucleus interactions.

At asymptotic energies, the rapidity distribution in hadron-nucleus collisions is expected to resemble that in hadron-nucleon interactions for the region $y_{cm}>0$. The region $y_{cm}<0$ is expected to be $\bar{\nu}$ times higher than in hadron-nucleon collisions. This simple-minded picture where each participating target nucleon behaves as the target nucleon in a hadron-nucleon collision is not in agreement with data. The increase in multiplicity is not confined to the lower half of the rapidity distribution.

The simplicity of the two-fireball picture is very appealing, but it appears that it cannot account for data in the 100 GeV range without modifications.

APPENDIX XIV

COHERENT TUBE MODEL

There is a model which attempts to describe hadron-nucleus data using the results of hadron-nucleon collisions as input. It makes predictions on the atomic number dependences of various processes, but makes no statements on the properties of the basic dynamics of hadronic interaction. This model is included here only for the sake of completeness.

The so-called coherent tube model[58] is based on two assumptions. In a high energy hadron-nucleus collision, those nucleons that lie within a tube of cross-sectional area σ along the path of the projectile are assumed to be the only ones to interact with the beam particle, and they do so coherently, i.e. they act as a more massive "proton" target. σ is taken to be the p-p total cross-section. If a beam proton of energy E is incident on such a tube with i nucleons inside, the center-of-mass energy-squared is now given by $s_i = 2iM_pE$. The second assumption states that the results of this collision are identical to the results of a proton-proton collision at the center-of-mass energy $\sqrt{s_i}$.

After performing an average over the possible tubes for a nucleus of definite atomic number A, one obtains:[89]

(1) $\langle n(s)\rangle_{pA} \sim \langle n(A^{1/3}\,s)\rangle_{pp}$

So if the average multiplicity in proton-proton interactions can be parameterized by $\langle n(s)\rangle_{pp} \sim s^{\alpha}$ then $R_A \sim A^{\alpha/3}$. The data favors a value of 1/4 for α in the equation for the average multiplicity.

(2) KNO scaling is satisfied in hadron-nucleus interactions if it is satisfied in hadron-nucleon interactions. In particular

$$D_{pA}(s) \sim D_{pp}\,A^{1/3}s)$$

If $D_{pp}(s) \propto \langle n(s)\rangle_{pp}$, as it appears to be the case, then $D_{pA}(s) \propto \langle n(s)\rangle_{pA}$ should hold for interactions with nuclear targets.

(3) $\left(\frac{dN}{dy}(s,y)\right)_{pA} \sim \left(\frac{dN}{dy}(A^{1/3}\,s, \frac{1}{6}\ln A+y)\right)_{pp}$

A value of 1/4 for α gives rise to $R_A \propto A^{1/12}$ which is in violent disagreement with the data. The predicted rapidity distributions are also in poor agreement with the data.

On the positive side, KNO scaling appears to hold,[32,33,34] and the dispersion and the average of the multiplicity distributions seem to be linear.[37] Note that if the prediction on KNO scaling is satisfied, the prediction on the dispersion is a necessary consequence. The converse is not necessarily true.

The failures of the model's predictions on the multiplicity and on the rapidity distributions can be overcome by making some not unreasonable assumptions about fast knock-out protons. Their frequency and angular distribution are such that the predictions and the data are more compatible. These detailed manipulations of the model will be left to its ardent proponents. If this model proves to be of merit, questions are raised concerning the general properties of the strong force and our understanding of special relativity. The presumed coherence of the target nucleons, over distances of as much as 10 to 15 fermis, is hard to reconcile with the range of the strong force ($\sim$several fermis) and the concept of causality.

Conventional arguments insist that nuclear binding is too weak to be of any consequence when the beam energy is of the order of 100 GeV. The first episode in a hadron-nucleus interaction is well approximated by the projectile striking a free nucleon.

Consider the unlikely case where the nucleons are not effectively free. Then the nuclear bonds cannot be ignored. One would then expect the entire nucleus to react coherently. (Coherent-ball model?) It is not obvious why the coherent tube model assumes that the longitudinal

nuclear bonds are important whereas the transverse bonds may be ignored. Any mechanism that is invoked to explain this asymmetry must also be compatible with the existing knowledge on nuclear physics.

APPENDIX XV

The Model of Białkowski, Chiu and Tow[59]

A model has been proposed where the properties of hadrons are time dependent. This hypothetical "maturity" time is of the order of the strong interaction time scale. Thus the cross-section of a hadron is given by

$$\sigma(t) = \sigma_0 \, (1-e^{-t/\tau})$$

where τ is the maturity time scale.

Such a time dependence is very familiar in classical physics and appears quite plausible. Since the properties of hadrons are measured long after their creation, there are no explicit data contradicting this point of view. It appears that the only tests of this model will have to come from hadron-nucleus interactions.

The model attempts to explain the small value of R_A on the basis of this time dependence. It is hypothesized that the final state hadrons are produced instantaneously in a hadronic collision. However, these produced particles are "immature" in the sense that their interactions cross-sections are smaller than the asymptotic values. A full-fledged hadronic cascade is therefore avoided.

The model, as stated above, cannot be reconciled

with the data of this experiment. However, by assuming that the maturity rate is enhanced in the presence of nearby strongly interacting material (as inside a nucleus) and by treating this "induced maturity rate" as a free parameter, an adequate fit to the results of this experiment has been obtained.

It is not obvious why the maturity rate should depend on the environment, nor is it obvious why the enhancement should take on the form assumed by the authors:

$$\tau \to \left(\frac{1}{\lambda} + \frac{1}{\tau}\right)^{-1}$$

where λ is the induced maturity path.

If the detailed mechanisms and mathematics are ignored, it will be noticed that the model is quite similar to some of the models mentioned earlier, except for semantic differences. Consider the parton model. The immature hadrons may be regarded as the partons before the latter re-arrange themselves into physical hadrons. The time dependent cross-section may be regarded as a particular way of parameterizing this re-arrangement.

In the language of the energy flux cascade model, $\sigma(t)$ can be considered as a way of partitioning the flux into some number of hadrons each with the correct asymptotic cross-section. In the framework of the two-fireball model, σ(t) gives a particular parameterization of the decay of the fireballs.

However, unlike the other models, the time dependence is assumed to be an intrinsic property of hadrons. This is a rather novel assumption that deserves further investigation.

REFERENCES

1. L.D. Landau, Collected Papers of L.D. Landau, ed. D. Ter Haar, Gordon and Breach, New York (1965).

2. M. Gell-Mann, Physics Letters 8, 214 (1964).

3. D. Amati, S. Fubini and A. Stanghellini, Nuovo Cimento 25, 626 (1962).

4. L. Bertocchi, Invited Talk at the VI International Conference on High Energy Physics and Nuclear Structure, Santa Fe and Los Alamos (1975).

5. L. Stodolsky, presented at the VII International Conference on Multiparticle Reactions, Oxford (July 1975).

   N.N. Nikolaev, Landau Institute Preprint (1976).

   A. Bialas and L. Stodolsky, Acta Physica Polonica B7 845 (1976).

6. L.D. Landau and I. Ya. Pomeranchuk, Doklady Academii Nauk 92, 535 (1953) and 92, 735 (1953).

7. J. Bakecki, Acta Physica Polonica, B6, 435 (1975).

8. K. Gottfried, CERN Preprint TH-1615 (1973).

9. P.R. Vishwanath et al, Physics Letters 53B, 479 (1975).

10. K. Gottfried, Physical Review Letters 32, 957 (1974).

11. R.P. Feynman, Photon-Hadron Interactions, Benjamin (1972).

12. See for example G.A. Winbow, Physical Review D15, 303 (1977).

13. R. Hwa and C.S. Lam, Physical Review Letters 27, 1098 (1971).

14. P.M. Fishbane and J.S. Trefil, University of Virginia Preprint (1974).

15. For a review see S. Mandelstam, Physics Reports 13C, 259 (1974).

16. E. Fermi, Progress in Theoretical Physics 5, 570 (1950), Physical Review 81, 683 (1951).

I. Ya. Pomeranchuk, Doklady Adad. Sci. USSR 78, 889 (1951).

R. Hagedorn, Nuovo Cimento Supplement 3, 147 (1965).

R. Hagedorn and J. Ranft, Nuovo Cimento Supplement 6, 169 (1968).

17. For example, B. Andersson, Invited Paper at the VII International Colloquium on Multiparticle Reactions, Munich (1976), also available as University of Western Ontario Preprint (1976).

18. J. Fines, Ph.D. thesis, Massachusetts Institute of Technology (1977), unpublished.

19. S.P. Denisov et al, Nuclear Physics B61, 62 (1973).

20. G.A. Adopdjanov et al, Nuclear Physics B75, 401 (1974).

21. E.L. Berger et al, Nuclear Physics B77, 365 (1974).

22. D.G. Fong et al, Physical Review Letters 37, 736 (1976).

23. D. Bogert et al, Physical Review Letters 31, 1271 (1973).

24. V.S. Barashenkov, Nuclear Physics 14, 522 (1959).

25. H. Meyer, Nuovo Cimento 28, 1399 (1963).

26. J. Babecki et al, Physics Letters 47B, 268 (1973).

27. S.A. Azimov et al, Nuclear Physics B107, 45 (1976).

28. A. Wroblewski, Acta Physica Polonica B4, 857 (1973).

29. A. Bialas and W. Czyz, Physics Letters 58B, 325 (1975).

30. G.D. Kaiser, Daresbury Preprint (1973).

31. S. Barish et al, Physical Review D9, 2689 (1974).

32. P. Slattery, Physical Review Letters 29, 1624 (1972) and Physical Review D10, 2304 (1974).

33. J.W. Martin et al, Nuovo Cimento 25A, 447 (1975).

34. J.R. Elliot et al, Physical Review Letters 34, 597 (1975).

35. G. Calucci, R. Jengo and A. Pignotti, Physical Review D10, 1468 (1974).

36. J.R. Florian et al, Physical Review D13, 558 (1976).

37. W. Busza et al, Physical Review Letters 34, 836 (1975).

38. Experiment No. 96 at Fermilab observed that less than 1/2% of RF buckets were doubly occupied at an equivalent beam rate of 0.5 10^9 particles per 1 second spill. Private communications J. Fines.

39. M. Benot, J. Litt and R. Meunier, Nuclear Instruments & Methods 105, 431 (1972).

40. J. Butler, Ph.D. thesis, Massachusetts Institute of Technology (1975), unpublished.

41. This effect was estimated with a sample of hydrogen bubble chamber events (Reference 46) and the details are given in Appendix VIII.

42. V.V. Ammosov et al, Nuclear Physics B75, 401 (1974).

43. J. Erwin et al, Physical Review Letters 32, 254 (1974).

44. C. Bromberg et al, Physical Review Letters 31, 1563 (1973).

45. V.E. Barnes et al, Physical Review Letters 34, 415 (1975).

46. I thank T. Ferbel for kindly furnishing a sample of 100 GeV/c proton-proton events obtained by the Michigan-Rochester Collaboration.

47. Y. Cho et al, Physical Review Letters 31, 413 (1973).

48. Alma-Ata-Gatchina-Moscow-Tashkent Collaboration, contributions to the XVIII International Conference on High Energy Physics, Tbilisi (1976).

49. S.A. Azimov et al, contribution to the XVIII International Conference on High Energy Physics, Tbilisi, (1976).

50. P.L. Jain et al, Physical Review Letters 34, 972 (1975).

51. I. Otterlund, Invited Talk at the Topical Meeting on Multiparticle Production at Very High Energy, Trieste (1976).

52. M.I. Tretyakova, preprint of the P.N. Lebedev Physical Institute of the Academy of Sciences of the USSR, Moscow (1974), also reported by K. Zalewski, Invited Talk at the XVII International Conference on High Energy Physics, London (1974).

53. J. Babecki et al, Physics Letters 52B, 247 (1974).

54. I. Otterlund, Invited Talk at the VI International Conference on High Energy Physics and Nuclear Structure, Santa Fe and Los Alamos (1975).

55. H. Winzeler, Nuclear Physics 69, 661 (1965).

56. E. Lohrmann et al, Physical Review 122, 672 (1961).

57. R. Barbaro-Galtieri et al, Nuovo Cimento 21, 469 (1961).

58. C. Berlad, A. Dar and G. Eilam, Physical Review D13, 161 (1976).

59. G. Bialkowski, C.B. Chiu and D.M. Tow, University of Texas (Austin) preprint (1976).

60. For example: Meng Ta-Chung, Physical Review D15, 197 (1977)

I.G. Bogatskaya, S.M. Eliseev and G.M. Zinovjev, preprint number E2-9958 of the Joint Institute of Nuclear Research, Dubna (1976).

S. Sohlo, Acta Universitatis Ouluensis, Series A, No. 26 (1974).

A.S. Goldhaber, Physical Review Letters 33, 47 (1974).

M. Fukushima, Nuovo Cimento 34A, 445 (1976).

61. E. Albini et al, Nuovo Cimento 32A, 101 (1976).

62. CERN SPS Proposal Number 79 (1976).

63. Z. Koba, H.B. Nielsen and P. Olesen, Nuclear Physics B40, 317 (1972).

64. The logical question is: what makes up this round thing called a ping pong ball? The analogous question in hadronic physics is: What makes up hadrons or the "bag" that surrounds the constituents of hadrons? These questions cannot be answered satisfactorily at this stage. However, it is important to know whether there is a "bag" or not. Until its existence has been demonstrated, questions concerning its properties are irrelevant.

65. The formula $\bar{\nu} = \frac{A\sigma_p}{\sigma_A}$ was first pointed out to the collaborators of this experiment by A. Bialas.

66. J.W. Negele, Physical Review C1, 1260 (1970).

67. P. Carruthers and M. Duong-van, Physical Review D8, 859 (1973).

68. B. Rossi, High Energy Particles, Prentice Hall, New Jersey (1952).

69. D. Perkins, Introduction to High Energy Physics, Addison-Wesley, Massachusetts (1971).

70. The topological cross-sections reported in Reference 31 for 205 GeV/c p-p interaction can be fitted by $\sigma_n = \sigma_0 n^3 e^{-\lambda n}$ where $\sigma_0 = 0.75$ mb and $\lambda = 0.52$.

71. C. Bromberg et al, Physical Review D9, 1864 (1974).

72. See, for example, the review article: E.L. Feinberg, Physics Reports 5c, 237 (1972).

73. W. Bozzoli et al, Fermilab Experiment Numbers 419 and 462, paper submitted to Nuovo Cimento Letters.

74. Alma-Ata-Dubna-Dushanbe-Leningrad-Moscow-Tashkent Collaboration, paper submitted to the XVIII International Conference on High Energy Physics, Tbilisi (1976).

75. Bucharest-CERN-Cornell-Lund Collaboration, reported by I. Otterlund, Invited Talk at the Topical Meeting on Multiparticle Production at Very High Energies, Trieste (1976).

76. A. Abrosimov et al, paper submitted to the XVIII International Conference on High Energy Physics, Tbilisi (1976).

77. S.Z. Belenkij and G.A. Milekhin, Journal of Experimental and Theoretical Physics (USSR) 29, 20 (1955), Soviet Physics JETP 2, 14 (1956).

78. B. Andersson, G. Jarlskog and G. Damgaard, Nuclear Physics B112, 413 (1976).

79. N. Masuda and R.M. Weiner, University of Marburg preprints (1976).

80. S. Chadha, C.S. Lam and Y.C. Leung, Physical Review D10 2817 (1974).

81. For example: R. Holynski, S. Krzywdzinski and K. Zalewski, preprint from the Institute of Nuclear Physics, Cracow, Poland (1974).

L.J. Gutay et al, Physical Review Letters 37, 468 (1976).

J.E. Lys et al, Fermilab Preprint FERMILAB-PUB-76/89-EXP-7200.194 (1976), to be published in Physical Review.

82. B. Andersson, CERN Preprint TH-2004 (1975).

83. J. Koplik and A.H. Mueller, Physical Review D12, 3638 (1975). Also see A.H. Mueller, lectures at the Summer Institute for Theoretical Physics in Bielefeld (1976) available as Columbia University Preprint CO-2271-91 (1976).

84. J.H. Weiss, Acta Physica Polonica B7, 851 (1976).

85. A. Capella and A. Krzywicki, Physics Letters 67B, 84 (1977).

86. See compilation of data in: J. Whitmore, Physics Reports 27C, 187 (1976).

87. J. Benecke, T.T. Chou, C.N. Yang and E. Yen, Physical Review 138, 2159 (1969).

88. F. Abraham, Proceedings of the International Conference on Cosmic Rays, London, 2, 844 (1965).

89. A. Dar, Invited Talk at the Topical Meeting on Multiparticle Production at Very High Energies, ICTP, Trieste (1976).